Synthesis and mechanical properties of iron-filled carbon nanotubes

Dissertation

zur Erlangung des akademischen Grades
Doctor rerum naturalium (Dr. rer. nat.)

vorgelegt

der Fakultät Mathematik und Naturwissenschaften der
Technischen Universität Dresden

von

Diplom-Naturwissenschaftler
Uhland Weißker

geboren am 16.01.1980 in Dresden

Die Dissertation wurde in der Zeit vom 01.08.2006 bis 31.10.2010 am Leibniz-Institut für Festkörper- und Werkstoffforschung (IFW) angefertigt.

1. Gutachter:
   Prof. Dr. B. Büchner, Technische Universität Dresden

2. Gutachter:
   Prof. Dr. G. Cuniberti, Technische Universität Dresden

Einreichung am 05.11.2012

Tag der Verteidigung 16.10.2013

Contents

Recurring abbreviations and symbols

abbreviation	**description**
AFM	atomic force microscope
BSED	back-scattered electron detector
CAEM	controlled atmosphere electron microscopy
CNT	carbon nanotube
CVD	chemical vapor deposition
DFT	density functional theory
EBID	electron beam induced deposition
EBM	Euler-Bernoulli beam model
EDX	energy dispersive X-ray spectroscopy
MD	molecular dynamics
hr-MFM	high resolution magnetic force microscope / microscopy
MWCNT	multi-walled CNT
PLL	phase locked loop
SEM	scanning electron microscope
SQUID	superconducting quantum interference device
SWCNT	single-walled CNT
TEM	transmission electron microscope
VLS	vapor liquid solid
XPS	x- ray photoelectron spectroscopy

symbol	**unit**	**description**
E	$\mathrm{N/m^2}$	elastic modulus
F	N	force, load
σ	$\mathrm{N/m^2}$	stress
ϵ		strain
α	Nm/rad	spring constant of elastic mounting
I	$\mathrm{m^4}$	moment of inertia
k	N/m	cantilever spring constant
m	kg/m	mass density
A	$\mathrm{m^2}$	cross section
ν or f	1/s	frequency
ω	rad/s	angular frequency
Q		quality factor
k_B	$1.38 \times 10^{-23}\,\mathrm{J/K}$	Boltzmann constant
R	$8.3145\,\mathrm{J/(mol\,K)}$	gas constant
T	K, °C	temperature
E_a	J/mol	activation energy
D	$\mathrm{m^2/s}$	diffusion coefficient
p	$\mathrm{N/m^2}$	pressure
μ_0	$4\pi \times 10^{-7}\,\mathrm{N/A}$	magnetic constant (permeability of free space)
A	J/m	exchange stiffness constant
B	T	magnetic flux density
K	$\mathrm{J/m^3}$	anisotropy energy
K_n	$\mathrm{J/m^3}$	n-th uniaxial anisotropy constant
K_s	$\mathrm{J/m^3}$	shape anisotropy energy
M	A/m	magnetization
M_s	A/m	saturation magnetization
m	$\mathrm{Am^2}$	magnetic dipole moment
q	A m	magnetic monopole moment

Introduction and motivation

Carbon forms the basis of a variety of compounds whose number is larger than for any other element. The allotropic forms of carbon include graphene, fullerenes, graphite, carbon nanotubes and diamond. All these structures possess unique physical and chemical properties. The existence of carbon nanotubes (CNT) was first experimentally confirmed by Iijima et al. in 1991 [1]. The structural diversity of CNT initialized extensive research in many different fields of fundamental and applied science, since CNT offer unique properties such as high electrical and heat conductivity as well as an exceptional tensile strength. Single-walled CNT are especially interesting for micro electronics due to their either metallic or semiconducting electrical properties. Multi-walled CNT are dedicated for many different applications enhancing the electrical, thermal and mechanical properties of composite and lightweight materials.

However, not only the carbon shell but also the hollow interior of CNT offers great research and application potential. This encapsulated cavity of CNT can be filled with foreign materials reaching from single molecules, clusters, small particles to extended nanowires. CNT have been investigated as drug delivery material in medical applications [2, 3] and also nano temperature sensors have been developed [4]. Depending on the kind of application, filled carbon nanotubes with tailored and tuned properties are necessary. CNT filled with ferromagnetic material are of particular interest. Carbon nanotubes filled with magnetic material have been studied as an alternative contrast agent for magnetic resonance imaging and they might also be used for hyperthermia treatment of cancer [2, 3, 5]. Furthermore, for the development of magnetic recording media having increased storage density nanoscale magnetic particles show great potential [6]. All these applications require rather partially filled CNT with short ferromagnetic nanowires. The hollow core might be used as a multifunctional nano-container and the ferromagnetic filling is only one component inside the tube. By varying the synthesis conditions spherical particles and differing lengths of nanowires of ferromagnetic material can be fabricated inside CNT. The emphasis of research was mainly focused on iron as filling material. In contrast to the previous mentioned applications, a continuous filling is stringently required for using iron-filled tubes as probes for magnetic field sensors especially for magnetic force microscopy (MFM).

The usage of CNT in sensor and actuator applications is an area of intensive research and development. Due to their high aspect ratio single-walled CNT are especially interesting as tips in raster probe microscopy [7]. They have successfully been utilized as tips for atomic force microscopy (AFM). With these probes surfaces with steep structures can be investigated with a high resolution. Also multi-walled CNT were employed for raster scanning applications [8]. A special scanning probe method is the magnetic force microscopy, where besides the topographic information, the sample's magnetic stray field interacts with the magnetic moment of the scanning probe resulting in a magnetic contrast. A CNT filled with an extended and continuous iron nanowire constitutes an ideal magnetic force microscopy probe, possessing a sharp tip and high aspect ratio for good topographic imaging and in particular a high and defined magnetic moment perpendicular to the sample surface. The latter might be a dipole moment spatially confined in three dimension or a monopole moment. Moreover, the carbon shells provide an oxidation protection and ensure a high bending stiffness. For these tips the CNT stiffness and resulting resonance frequency is important in order to avoid resonant vibration of the CNT tip itself during scanning. Furthermore, these iron-filled CNT are thought to be a promising material for micro- and nanoscale actuators and sensors. A CNT under flexural bending represents a cantilever by itself. Especially the elastic properties and the bending stiffness of the CNT determine the properties of the *cantilever*.

This thesis addresses two issues which are deduced from the demands of CNT for MFM. These are first the synthesis of CNT encapsulating long and extended nanowires consisting of ferromagnetic iron and second their mechanical properties, especially the determination of their elastic modulus.

The present work consists of three chapters. In the first chapter selected properties of carbon nanotubes are briefly presented. The second chapter deals with the synthesis of carbon nanotubes filled with ferromagnet materials focussing on the preparation of iron-filled CNT for MFM. This chapter also includes a discussion about the synthesis of iron-carbide filled CNT and some of their magnetic properties. The influence of metallic interlayers and precursor mass flow is presented and the importance of these two parameters with respect to the filling morphology is revealed. A combined growth mode model is applied and adapted to explain the formation of filled CNT. Conditions for a *control* of the properties are identified. In chapter three selected mechanical properties of iron-filled CNT are investigated. In the mechanics section a new method for the measurement and evaluation of dynamic bending experiments is developed and applied to the synthesized material. Furthermore, a new method for the static bending of CNT inside a TEM is presented. The boundary conditions and their influence on the bending behavior of iron-filled CNT are discussed and their usability as mechanically stable probes is shown. The mechanical properties of iron-filled CNT determined in the present work are compared to values of unfilled CNT found in literature and the different structural aspects are discussed, showing a relation between the growth process and the mechanical properties.

The present work will show that CNT with a low defect morphology are required in order to achieve a sufficient stiffness for sensor applications. The results of the synthesis and the study of mechanical properties reveal the potential of such iron-filled CNT for application as raster probe MFM tips, which was recently published in the thesis of Franzika Wolny [9].

1 Structure and selected properties of carbon nanotubes

1.1 Carbon nanotubes - structure, selected properties and application

The element carbon forms several allotropic structures reaching from fullerenes (0D), carbon nanotubes (1D) over graphene (2D) and graphite (quasi-2D) to diamond (3D). This diversity is related to the atomic structure of carbon, which is the first element of the IV main group and has a $1s^2 2s^2 2p^2$ electron configuration. For carbon the hybridization energy is low in comparison to the binding energy and thus the mixing of orbitals occurs forming sp^n states. Diamond is formed by sp^3-hybridized carbon orbitals, while graphene, graphite, CNT and fullerenes are mainly based on the formation of sp^2 orbitals. However, in the case of carbon nanotubes and fullerenes there is, due to the diameter dependent curvature, a mixing of sp^2 and sp^3 orbitals. This influences the physical properties of this group of material.

Graphene is the most basic carbon structure built up by benzene rings. It is the basis for other carbon based structures such as graphite but also fullerenes and carbon nanotubes. Carbon nanotubes are often discussed as an allotropic form of carbon [10]. Their properties can be explained by the theory of graphene considering some additional effects as a consequence of their special structure. It is common to start with the description of graphene and expanding the results to CNT. As result of their one dimensional structure, cylindric shape and chirality, CNT show a wide spectrum of physical properties.

The following sections describe the properties of single-walled CNT and focus on the properties of multi-walled carbon nanotubes where necessary. Many properties of multi-walled CNT can be attributed to the structure of single-walled CNT. An ideal multi-walled CNT can be thought of a stack of single-walled CNT each with a different radius and chiral vector. Therefore, the structure of single-walled CNT will be briefly discussed.

1.1.1 Structure of carbon nanotubes

A single-walled CNT can be described as a graphene sheet rolled into a cylindrical shape. The resulting structure is an one dimensional tube with an axial symmetry and in general exhibiting a spiral conformation, called chirality [11]. The structural features of CNT can be very effectively described by different vectors. A graphene sheet with the relevant parameters is shown in fig. 1.1 based on [11]. A CNT might be constructed by rolling up a graphene sheet around a vector which is denoted by $\overrightarrow{OC}$ in the sketch. The direction of this vector concurs with the translational vector $\vec{T}$ of the CNT. The vector $\overrightarrow{OA}$ defines the circumference of the CNT and is rolled up around the long axis direction $\vec{T}$ of the CNT. It is also known as *equator* or chiral vector $\vec{C}_h$ of the CNT. The points O,A,B and C are crystallographically equivalent sites and they coincide O with A and C with B after rolling up the graphene sheet. The unit cell base vectors $\vec{a}_1$ and $\vec{a}_2$, which are not orthogonal, can be used to express the chiral vector $\vec{C}_h$.

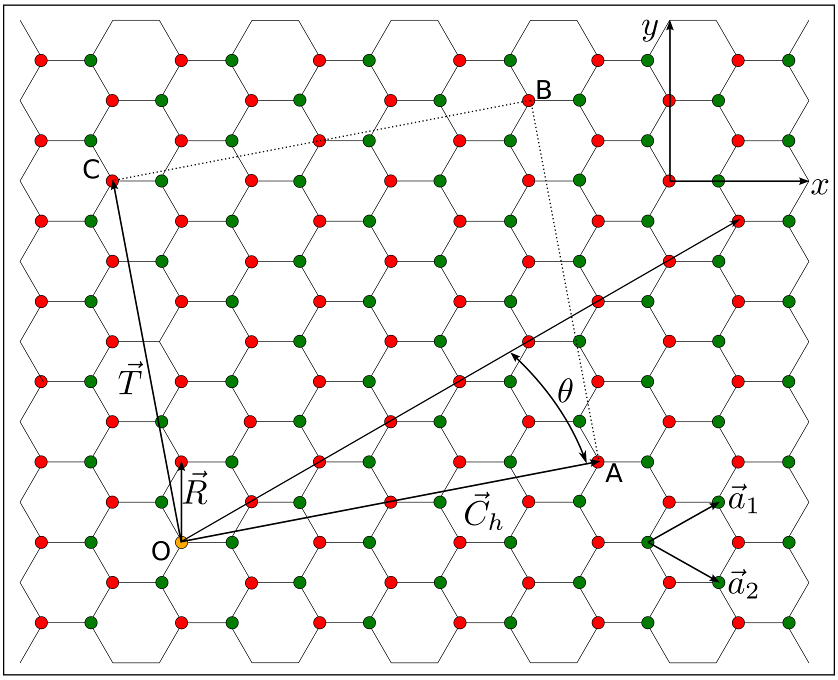

Figure 1.1: Graphene sheet based lattice of a carbon nanotube. The rectangle given by the sites O, A, B and C defines the unit cell of a single-walled CNT. When it is rolled up around the line $\overrightarrow{OC}$ a tube is formed. $\overrightarrow{OA}$ defines the chiral vector $\vec{C}_h$ and $\overrightarrow{OC}$ the translational vector $\vec{T}$ [11].

$$\vec{C}_h = n\,\vec{a}_1 + m\,\vec{a}_2 = (n, m), \quad (n, m \in 0 \leq |m| \leq n). \tag{1.1}$$

The chiral vector can be used to define a number of other quantities such as the tube diameter. The diameter (d_t) is given by the circumferential length (L) of the CNT divided by π.

$$d_t = L/\pi, \quad L = |\vec{C}_h| = \sqrt{\vec{C}_h \, \vec{C}_h} = a\sqrt{n^2 + m^2 + mn}\ ^{1} \tag{1.2}$$

The translation vector $\vec{T}$ is orthogonal to $\vec{C}_h$ and corresponds to the first crystallographically equivalent lattice point in the 2D graphene sheet through which the vector $\overrightarrow{OC}$ passes.

$$\vec{T} = t_1 \vec{a}_1 + t_2 \vec{a}_2 = (t_1, t_2), \quad (t_1, t_2 \in N). \tag{1.3}$$

The scalars t_1 and t_2 can be expressed in terms of n and m and the length is given by $T = |\vec{T}| = \sqrt{3}\, L/d_R$, where d_R is the greatest common divisor of the terms $(2m+n)$ and $(2n+m)$. An unit cell within a 1D nanotube is defined by a rectangle O, A, B and C which is spanned by the two vectors $\vec{C}_h$ and $\vec{T}$, whereas the surface is given by $|\vec{C}_h \times \vec{T}|$. The area of an unit cell in a 2D graphene sheet is defined by the vectors $\vec{a}_1$ and $\vec{a}_2$ and the area is given by $|\vec{a}_1 \times \vec{a}_2|$. With this two expressions the number of hexagons N per nanotube unit cell can be calculated by using eq. 1.4.

$$N = \frac{|\vec{C}_h \times \vec{T}|}{|\vec{a}_1 \times \vec{a}_2|} = \frac{2\,(m^2 + n^2 + nm)}{d_R} = \frac{2\,L^2}{a^2\, d_R} \tag{1.4}$$

Each hexagon contains 2 carbon atoms thus the number of atoms in a nanotube unit cell is $2\,N$. In order to determine the coordinates of a carbon atom within the nanotube unit cell the symmetry vector $\vec{R}$ is defined.

$$\vec{R} = p\,\vec{a}_1 + q\,\vec{a}_2 \quad = (p, q) \quad (p, q \in Z) \tag{1.5}$$

In a physical sense, the symmetry vector $\vec{R}$ consists of a rotation around the nanotube axis by an angle ψ combined with a translation τ in the direction of $\vec{T}$. The symmetry vector can be expressed as the projection of $\vec{R}$ on $\vec{C}_h$ and $\vec{T}$ which is given by eq. 1.6.

$$\begin{aligned} \psi &= \frac{2\,\pi}{N} \\ \tau &= \frac{(m\,p - n\,q)\,T}{N} \end{aligned} \tag{1.6}$$

A more detailed description of the SWCNT structure can be found in literature [10–12].

1.1.2 Electrical properties

The electrical properties of carbon nanotubes are closely related to graphene, which is a zero band gap semiconductor as result of its 2D-structure with an ideal sp^2

---

[1] $a = |\vec{a}_1| = |\vec{a}_2|$

hybridization of the carbon orbitals. The valence and conducting band are degenerated by symmetry at the special K point at the 2D Brillouin zone corner where the Fermi level in reciprocal space is located. While turbostratic graphite is a zero gap semiconductor as well, perfectly ordered graphite is a semimetal with a small band overlap that results in a metal-like conductivity.

The electrical properties of carbon nanotubes are influenced by the sp^2 hybridization but also by their sensitivity to the geometric structure especially the diameter and chirality which in turn depend on the parameters (n,m). The band gap properties depend on the chirality and the diameter which in turn results in a quantization of the electron wave vector along the circumferential direction of carbon nanotubes. As a consequence many properties are comparable to graphene but additional properties arise since only preferred k-states can exist. Semiconducting CNT have a real band gap at the K-point where no allowed wave-vector exist. Contrastingly, metallic CNT have properties very close to 2D graphene and can be classified as zero band gap semiconductors. They have an allowed wave-vector at the K-point. In both cases the electrical properties of CNT are defined by the k-states in the vicinity of the K point.

Interactions between electrical and mechanical properties of CNT have been experimentally and theoretically investigated. Liu et al. [13] simulated the bending of SWCNT caused by a sharp AFM tip resulting in a large local deformation of the CNT structure. For deflection angles of the CNT above 15° the break of the sp^2 hybridization and formation of sp^3 bonds were found. The electron π-system of the sp^2-structure, that is responsible for the high conductance, vanishes and the resistance increases significantly. It is expected that only highly bent CNT with sp^3-type bindings show a significant reduction of the conductance [13].

1.1.3 Optical properties

The optical properties of carbon nanotubes depend on the diameter and chirality and thus on the parameter set (n,m). They are also strongly correlated with the phonons and electrical properties. The peak absorption frequency ω is proportional to $1/d_t$ and this dependency of the diameter of a CNT can be measured by resonant Raman spectroscopy using different excitation energies. The so called Kataura plot [14] gives all allowed transitions for optical absorption as a function of the diameter (curve shape) and the chirality (curve). Raman spectroscopy can also be used to distinguish semiconducting and metallic single-walled CNT. In the case of multi-walled CNT the radial breathing mode (RBM) during resonant Raman scattering might indicate their concentric structure. For multi-walled CNT a peak frequencies upshift in comparison to single-walled CNT due to interaction with adjacent shells has been found [15].

1.1.4 Thermal properties

The thermal properties of CNT are different from that of graphene. While graphene has a 2D band structure, single-walled CNT have a 1D band structure due to their periodic boundary conditions. CNT show a behavior that is related to their graphitic nature as well as their unique size and structure. The behavior of the specific heat is similar to 2D graphene at high temperatures. At lower temperatures it is dominated by phonons and quantization effects due to the structure become visible. Carbon nanotubes are excellent 1D thermal conductors whereby the thermal conductivity κ of single-walled CNT depends on the diameter of the tube [16]. Multi-walled CNT can be thought of a stacking of single-walled CNT having different diameters. This results in a dispersion relation of the specific heat along the c-axis that is perpendicular to the cylinder surface. For multi-walled CNT a graphite like behavior is expected but due to the turbostratic structure the coupling could also be much weaker [16].

1.1.5 Mechanical properties

The carbon double bond in graphene is the strongest inter-atomic bond in nature and thus the in plane stiffness is expected to be very high. In the case of carbon nanotubes three forces are responsible for the characteristic elastic properties. The fundamental atomic forces consist of strong in plane σ- and π-bondings and, in case of multi-walled CNT, weaker interlayer bonding between adjacent layers. Single-walled carbon nanotubes are therefore widely regarded as the fiber material with the highest strength in direction of the tube axis. Furthermore, carbon nanotubes are rather flexible and possess interesting elastic properties. CNT can sustain large nonlinear deformations without failure and can relax into the original state without structural changes when the stress is released. Especially under axial compression CNT do not break easily but rather form kink-like ridges that often relax elastically. Due to their remarkable flexibility they can also bent around sharp edges with small radii without breaking. However, the electrical properties of such bent CNT can be different from the unbent state [13].

In addition, multi-walled CNT have unique properties that do not appear in single-walled CNT [17, 18]. The relatively weak interlayer interaction determines the stacking structure and since adjacent layers are generally incommensurable with each other a turbostratic structure is formed. This turbostratic structure affects the shear stress between the nanotube shells. The increase of the layer distance from 0.335 nm to 0.344 nm reduces the force between the shells so they can easier slight past one another in case each shell itself is perfectly pristine [10]. A stacking of carbon sheet comparable to graphite can in general not be expected and this influences the shearing between adjacent layers. In this sense, the shear between two graphite layers should be reduced in multi-walled CNT. One nanotube may move smoothly with respect to the adjacent layers in the attractive force between the walls. However, the resistance to shear might be increased by defects in the shells and sliding motion is hindered by the presence of end caps. In the limit of large outer nanotube diameter the properties should converge to those of bulk graphite, however, no clear criteria for a critical diameter has been reported yet. In section 3.1 on page 86 selected approaches for the theoretical description and experimental investigation of the mechanical properties of CNT are presented.

1.2 Filled carbon nanotubes

Due to the remarkable physical and chemical properties of carbon nanotubes intensive studies about the functionalization of their outer shell as well as their inner core have been conducted. Most of the functionalization methods are applied after the synthesis of the CNT. The functionalization can be based on covalent and non-covalent binding. The functionalization is performed in order to expand the usability of CNT in different fields [19]. In biomedical usage the functionalization is often necessary to enable biocompatibility for cell membrane penetration [20, 21]. In that case often non-covalent binding molecules are used. Another focus of the functionalization of CNT is a modification of the surface properties in order to clean, separate and select them depending on their physical properties [19]. Single-walled CNT can be separated depending on their electrical properties [22]. The surface functionalization of iron-filled CNT showed the separation of the nanowires which is a pre-requirement for building defined structures [23]. Besides the outer shell also the core of CNT can be functionalized. Depending on the synthesis method CNT encapsulate catalyst particles. In case of transition metals (Fe, Co, Ni) and depending on the size these particles lead to magnetic properties. Since these are often not desired the particles are removed using different approaches of heating and dissolving the CNT in acids. A post-synthesis functionalization of the interior of the CNT requires the opening of the shell structure which has been done by selective oxidation of the CNT caps in an oxygen atmosphere at elevated temperatures [24, 25] or acid treatment [26]. The subsequent filling with therapeutics such as carbo-platin was shown [27]. Also other compounds such as CuI and AgCl have been filled into the core of CNT after their synthesis [4]. Another possibility is the in-situ filling of CNT with transition elements Fe, Co and Ni during the synthesis using precursors having a significant amount of metal. Carbon nanotubes filled with ferromagnetic nanowires were obtained by this method [28–31].

1.3 Magnetic properties of Fe nanowires

Ferromagnetic nanowires are of great interest for both, fundamental research and applications like, e.g., high-density magnetic recording [32–34] and magnetic sensors probes for magnetic force microscopy [35, 36].
The transition element iron is a ferromagnetic material possessing a magnetic moment even though no external magnetic field H is present. The magnetic moment of iron results from unpaired electron spins within the d-shell of the atom. As a consequence of a strong exchange interaction between atomic moments a parallel alignment occurs giving a stable magnetic ordering. The magnetic ordering is thermally stable until the so called Curie temperature (1043 K for bulk iron) is reached at which a random orientation of the magnetic moments extinct the magnetization.
The magnetic properties of iron nanowires differ from those of bulk samples or other low dimensional systems such as small spherical particles and thin films. Investigations of interaction processes and magnetic reversal in low-dimensional magnetic structures have been performed on arrays of aligned nanowires [33, 37]. A common method to produce such nanowires is by self-assembly of porous alumina films and a subsequent electrochemical deposition of ferromagnetic materials into the pores.

The coercivity, magnetization reversal and interactions of the magnetic nanowires was studied [33]. Due to the high aspect ratio, the shape of the nanowires is the dominant contributor to the magnetic anisotropy, exhibiting the easy axis along the long wire axis [38, 39]. The shape anisotropy constant $K_s = \frac{1}{4}\,\mu_0\, M_s^2$ of an $\alpha-$iron nanowire at 300 K amounts to $\mathrm{K_s} = 9.1 \times 10^5\ \mathrm{J/m^3}$ and is significantly higher than the magnetocrystalline anisotropy constants $\mathrm{K_1} = 4.6 \times 10^4\ \mathrm{J/m^3}$ and $\mathrm{K_2} = 1.5 \times 10^4\ \mathrm{J/m^3}$. The saturation magnetization at 300 K equals to $\mathrm{M_s} = 1.7 \times 10^6\ \mathrm{\frac{A}{m}}$. The switching field for an iron nanowire with a diameter of 9 nm and a length of 1 µm is about $183\,000\ \mathrm{\frac{A}{m}}$. The remanence ratio is $M_r/M_s = 0.96$ but depends on the diameter and length [33]. The study of ensembles of magnetic nanowires considering also morphological imperfections give rise to localization of magnetization reversal and also its domination of the hysteresis behavior was revealed [33].

Ferromagnetic iron nanowires encapsulated within carbon nanotubes are ideal model systems for studying the magnetic behavior of isolated systems [40–42]. The covering carbon shells exhibit a negligible diamagnetic behavior [43] and provide both an appreciable mechanical stability and an effective protection of the ferromagnetic filling against oxidation. However, the carbon-metal interface influences the properties of the metal nanowire such as its lattice type or the lattice constant [40, 44].
The magnetic properties of ferromagnetic nanowires are predominately investigated by magnetometry of ordered nanowire arrays [33]. The magnetization reversal of single,

separated nanowires can be studied by means of submicron Hall magnetometry [45], microbridge dc superconducting quantum interference device (SQUID) [46, 47], cantilever magnetometry [41] or magnetic force microscopy [48, 49]. Thereby, MFM is a widely employed method to map magnetic stray field related properties of a sample [50–52].

1.4 Magnetic force microscopy

Magnetic force microscopy is a special raster probe method comparable to atomic force microscopy (AFM). A typical raster probe setup for investigations of micro-scale magnetic samples is shown in fig. 1.2 and represents a typical atomic force microscopy setup. The setup consists of a cantilever as probe, a laser for the cantilever deflection detection, a detector and a feedback controller. The ferromagnetic coated tip of the probe scans the sample and measures the interaction force between the tip and the sample surface. The total force contains different contributions such as Van der Waals forces, electrostatic and magnetic forces.

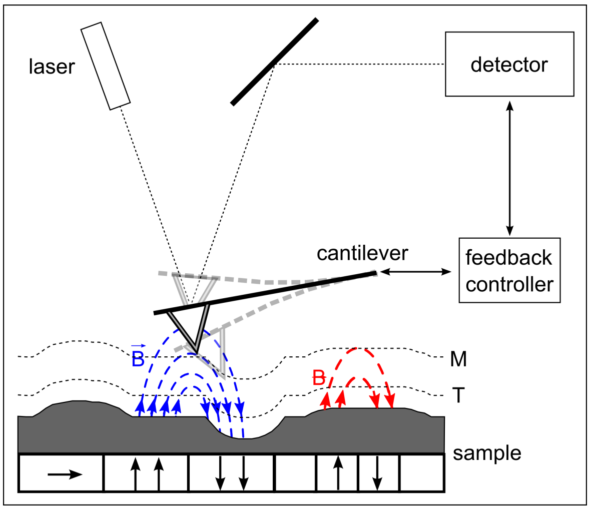

Figure 1.2: Setup of a tapping mode MFM consisting of a cantilever, laser, detector and feedback controller. The topography is imaged at height T and the magnetic contrast at height M.

Different measurement modes have been developed such as dynamic (tapping) mode MFM. The tip is dynamically excited by a periodic force at a height above the sample surface defined by the selected interaction force. Using a feedback loop the cantilever vibration amplitude is held constant. The scanning line of the tip is shown by the line denoted with T in fig. 1.2.

In dynamic mode MFM, local force gradients due to magnetostatic tip-sample interactions are measured. In order to exclude strong short range forces such as van der Waals forces the magnetic contrast is measured at a greater distance above the sample surface.

Raster scans are mostly conducted in constant height mode or lift-mode^{TM}, whereas the latter is illustrated by the line M in fig. 1.2. Performing raster scans such MFM maps

contain spatially resolved information on the magnetization direction and magnetic domain configurations. In hr-MFM measurements, the cantilever resonance frequency shifts are mapped in constant height mode, scanning in a plane above the sample surface. The resonance frequency shift is caused by tip-sample interactions, particularly by magnetostatic force gradients. The cantilever resonance conditions are ensured by, e.g., a phase locked loop (PLL) circuit.
In fig. 1.3 the topography and the corresponding magnetic contrast of a hard disk drive is shown. The magnetic contrast results from positive and negative force gradients due to the interaction of the magnetic moment of the probe tip with the magnetic stray field of the sample. In order to get a magnetic probe tip, often a conventional AFM cantilever covered by a thin magnetic film is used.

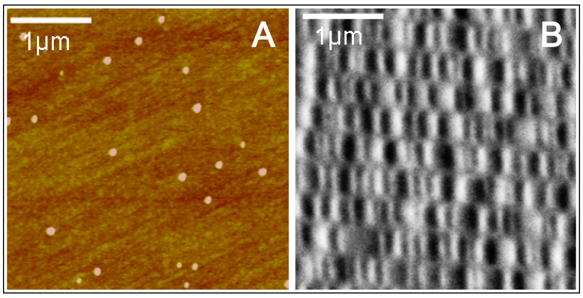

Figure 1.3: (A) shows the topography and (B) the magnetic contrast of a hard disk drive sample. [a]

---

[a] private communication Franziska Wolny, IFW Dresden

A challenge in magnetic force microscopy is a quantitative evaluation of the measured MFM signal. Hartmann et al. [53] proposed the point probe model where either a magnetic dipole moment $\vec{m}$ or a magnetic charge q is assumed to be localized at one particular point. In case of a pyramid-shaped tip this position is along the pyramid center line. Furthermore, the exact position of the point probe and the strength of the magnetic dipole moment or magnetic charge depend on the active volume of the probe that contributes to the signal. As illustrated in fig. 1.4(a) and (b) the effective probe volume depends on the decay length of the magnetic stray field of the sample. In order to avoid these problems another possibility is the usage of long and extended nanowires, as shown in fig. 1.4(c) and (d), where the distance between the two magnetic monopoles is much larger than the stray field decay length. Only the magnetic charge close to the sample stray field contributes to the interacting force. In fig. 1.4 the effective position and amount of a magnetic dipole moment or magnetic charge for a pyramid and an extended nanowire are shown. Different experimental approaches were developed in order to approximate the assumptions of the point probe model. Most concepts are based on the selective deposition of ferromagnetic material as narrow wires or by external coating of carbon nanotubes. However, these approaches lack of a long time chemical stability of the ferromagnetic coating against oxidation and are easily mechanically damageable. Iron-filled carbon nanotubes are a promising material to combine the advantages of extended nanowires contemporary protecting the wire

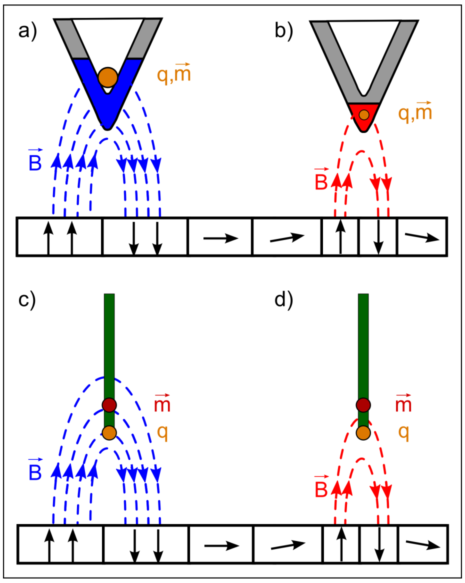

Figure 1.4: The point probe model [53] assumes the effective tip magnetization to be localized in a single point carrying the magnetic dipole moment $\vec{m}$ or magnetic charge q. The colored areas in (a) and (b) illustrate the effective probe volume that depends on the magnetic stray field decay length of the sample and contributes to the magnetic interaction force. In (c) and (d), the effective magnetic charge q is solely defined by the wires cross section and its magnetization. It does not depend on the characteristics of the sample strayfield. Its position is strayfield-independent too.

against oxidation and supporting the mechanical stability by the carbon shells. The successful usage of CNT filled with ferromagnetic iron nanowires has been proven by [35, 36, 54].

2 Synthesis of filled carbon nanotubes

2.1 Synthesis of carbon nanotubes by thermal CVD

The thermal chemical vapor deposition (CVD) is a convenient method for the synthesis of different types of carbon nanotubes ranging from the single-walled over the multi-walled to the metal-filled carbon nanotubes. CVD is suitable to produce large quantities with satisfactory quality and allows also an up scaling at moderate costs for industrial mass production. In this section we focus on the manufacturing of filled carbon nanotubes. A short overview about the synthesis of such tubes with defined properties as filling degree, length, diameter and form is given.

The CVD process can be schematically described by a sequence of temperature depending processes which are shown in fig. 2.1. For the description of these processes the concept of a *boundary layer* has been introduced. In general, it is assumed, that the rate of precursor consumption in a CVD process is higher than the diffusion of the precursor to the reaction side. But also the side products have to diffuse through this layer. In the 1^{st} step shown in fig. 2.1 the precursor compounds are delivered to the reaction site. In the 2^{nd} step they diffuse through the boundary layer. The adsorption of the reactants at the surface of the substrate takes place in the 3^{rd} step. In the 4^{th} step the precursor species gets activated and different products are formed. While a part of the products desorb and diffuse back through the boundary layer into the surrounding gas atmosphere other products diffuse at the surface as illustrated by step

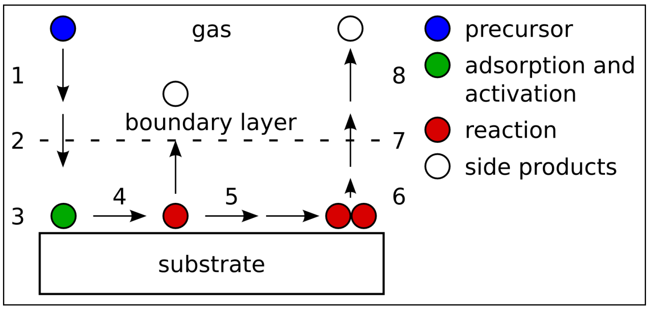

Figure 2.1: Basic steps of a thermal CVD process. 1.) Precursor delivery. 2.) Precursor diffusion through boundary layer. 3.) Adsorption on surface. 4.) Activation of the molecules. 5.) New compounds are formed by chemical reactions and diffuse along the surface. 6.) Desorption of products. 7.) Diffusion of by-products through boundary layer. 8.) Take away of the by-products.

5. Step 6 represents the formation of thin films or other structures at the surface. The steps 7 and 8 show the desorption of products that also diffuse into the gas atmosphere. These process steps are common for all chemical vapor deposition reactions. In the case of CNT formation the main product does not desorb but rather grow directly at the surface. Only by-products desorb during the process and are carried away by a carrier gas flow.

Since the governing processes are thermally activated and their kinetics depend on the temperature. Fig. 2.2 shows the dependency of a CVD process on the reaction temperature. At low temperatures (I) the supply with precursor material is larger than the consumption by the reaction. The process is kinetically controlled in that case and follows the Arrhenius-law

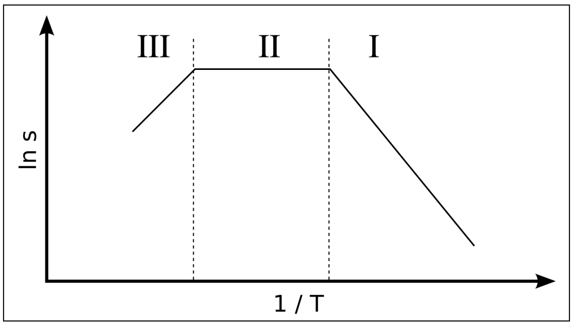

Figure 2.2: Dependency of the growth velocity s on the reaction temperature in a logarithmic scale.

$$s = A_k \exp\left(-\frac{E_a}{RT}\right) \tag{2.1}$$

where s denotes deposition or growth rate, A_k is the collision rate of reagents and E_a the activation energy within the exponential Boltzman distribution, which denotes the probability that two reagents have enough energy to react with each other. With increasing temperature (II) the kinetics of the reaction enhances and depletion zones are formed that can be described by the boundary layer model. The growth velocity now depends on the diffusion rate j of the precursor material through this boundary layer.

$$j = D\,\frac{n_r}{\delta_G} \tag{2.2}$$

The diffusion rate depends on the diffusion coefficient D, the thickness of the boundary layer δ_G and the concentration of the reactive species n_r. A further increase of the temperature (III) allows for reactions already in the gas phase with powder-like structures being formed.

Basically the methods for the synthesis of empty and filled carbon nanotubes are similar. Within both processes hydrocarbon precursor compounds are required delivering the carbon for the formation of the CNT walls. Additionally, since it is a catalytic process a catalyst, in this case a metal, is involved, that controls the kinetics of the reactions such as the decomposition of the precursor. It also acts as a geometric confinement for the forming CNT structure. The catalyst can be located on a substrate or is delivered via the gas phase. The latter is often called a floating catalyst process, which is in the focus of this work.

While for empty CNT besides the metal-organic compound an additional hydrocarbon (mostly liquid or gaseous) is very often used, the deposition of highly filled carbon nanotubes is realized by using only metal-organic compounds. The family of metallocenes (Me-$(C_5H_5)_2$ with Me = transition metals) accommodates both elements (C and Me) in their structure in a fixed ratio of 1:10. Because these compounds also possess a convenient temperature range for sublimation and thermal decomposition, the metallocenes ferrocene, cobaltocene and nickelocene are usually used as precursors for filled carbon nanotube synthesis. It is well known, that these metals have a low carbon solubility, form only metastable carbides and are so able to act as efficient catalyst.

By using only such metallocenes the formation of the CNT and its filling is a simultaneous process (the so-called in-situ filling process). Other strategies, e.g., for an ex-situ filling of empty, hollow nanotubes in a separate process have been discussed in literature as well [55, 56].

In the following we focus on the synthesis of filled CNT and discuss two different methods for in-situ filling processes. The first method starts with a metallocene powder as precursor and in the second method the metallocene is dissolved in a liquid hydrocarbon at the outset of the synthesis process.

2.1.1 Solid source chemical vapor deposition (SSCVD)

For the *solid source* CVD a horizontal quartz tube and a two zone furnace setup can be used. The typical setup for the SSCVD method is shown in fig. 2.3. In the first temperature zone ($T_{\mathrm{pre}} \ll T_{\mathrm{reac}}$) the metallocene powder is positioned in a quartz boat and is directly sublimated at a compound specific temperature (e.g. for ferrocene in the temperature range between 100 °C and 200 °C) [57, 58]. The metallocene vapor is transferred by a controlled gas flow into the second temperature zone (T_{reac}) where the decomposition of the metallocene and the growth of the filled carbon nanotubes occurs. As carrier gas argon, hydrogen, nitrogen or mixtures of those are used.

The chosen temperature (T_{pre}) determines the sublimation rate and combined with the carrier gas flow the amount of metallocene which is transported into the reaction zone. Thus the metallocene concentration is a function of temperature, gas flow and furnace geometry. As discussed in more detail later, the precursor concentration is a decisive factor for the properties of the obtained material.

For the deposition of iron-filled carbon nanotubes the T_{reac} is preferentially varied between 1020 and 1370 K. The deposition takes place on special substrates located in the hot zone of the reactor as well as on the inner wall of the quartz tube reactor. However, the reactor wall is more provided with undefined material compared to the aligned grown nanotubes on the substrate. Commonly, silicon substrates (semiconductor wafers) with a thin oxide layer are employed and an additional coating of these substrates with a few nanometer thin metal layer (the metal could be Fe, Co or Ni) leads to an improved deposition behavior and higher filling degrees, because these layers act as secondary catalysts.

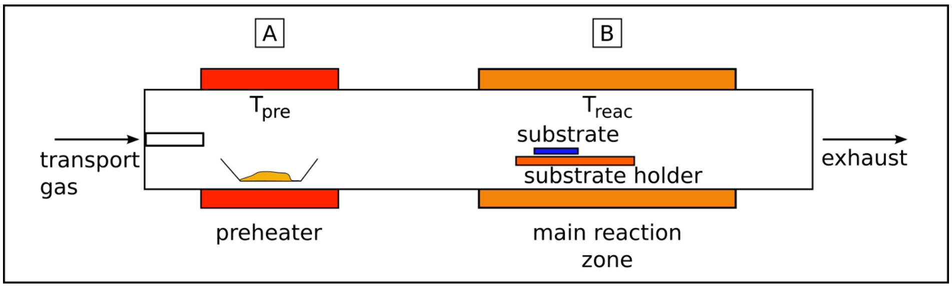

Figure 2.3: Setup of a typical SSCVD experiment. Ferrocene is sublimated in the preheater zone A at temperature T_{pre}. The decomposition of the precursor and the formation of CNT occurs in the reaction zone B at temperature T_{reac}.

2.1.2 Liquid source chemical vapor deposition (LSCVD)

The term *liquid source* CVD covers all methods employing solely liquid precursors as starting material for the deposition process. Because of its high flexibility and adaptability the LSCVD method is widely used in the synthesis of various empty and filled carbon nanotubes [29, 59–62]. The liquid precursor is either the only carbon source or it also acts as a solvent for other precursor compounds. In the case of carbon nanotube synthesis the liquid precursor is a hydrocarbon (benzene, acetonitrile, heptane etc.) in which the metal catalyst compounds (very often metallocenes) are dissolved. If such liquids are introduced into the CVD reactor both, the hydrocarbon and the metallocene decompose almost simultaneously. Caused by this high excess of carbon in the gaseous phase predominantly hollow carbon nanotubes with small spherical catalyst particles are formed but no filled CNT with long wires inside the tubes. The simplest experimental design for a LSCVD is a two zone furnace (horizontal or vertical) with an evaporation zone followed by a reaction zone. The principle setup is presented in fig. 2.4. The injection of the liquid precursor into the reactor can be realized in different manner, but often an additional inert gas flow such as argon or nitrogen is used. In the hot zone the decomposition of all precursor components takes place and the carbon nanotubes are formed. The attraction of the LSCVD method is its ability to control precisely the concentration of the used solution (the atom ratio between

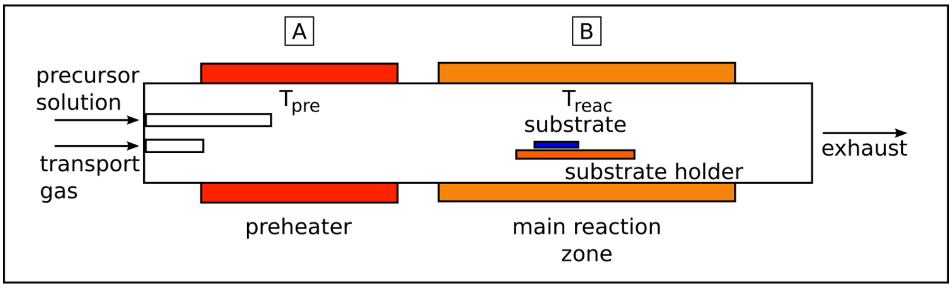

Figure 2.4: Setup of an aerosol experiment. The precursor solution is introduced by a nozzle and diluted by a transport gas flow. The solution evaporates in the preheater zone at temperature T_{pre}. In the reaction zone both the hydrocarbon and the metallocene decompose at temperature T_{reac} to form the CNT.

carbon and the metal component (catalyst) can be exactly regulated in a certain range (carbon/metal ratio $\gg 10$). Furthermore, the feeding amount can be adjusted using a flux pump (e.g. syringe pump) [30, 59, 61, 63]. A special injection method is the spray pyrolysis of the precursor solution by utilizing an aerosol generator, which e.g. can be a nozzle or an ultrasonic bath [60, 63–66].

2.1.3 Discussion of synthesis parameters

In this section the state of the art concerning the so far reached filling degree (and distribution) in dependence on the deposition conditions will be discussed. Beside the filling degree, other important properties of filled carbon nanotubes are their diameter and length. Both also determine significantly the application possibilities of these species. The so-called aspect ratio, i.e., length to diameter ratio strongly influences the physical and chemical properties of filled nanotubes. Furthermore, another often demand is that the tubes are grown straight and not wool-like entangled and bended. Straight grown nanotubes are easier to handle and show stronger anisotropic properties, which are very important for applications.An alike important criterion for the quality of all types of nanotubes is the crystallinity of the carbon shell, because a lot of properties depend on its purity.

Therefore, in the following the connections between these properties (filling degree, length, diameter, morphology and shell structure) and specific used process parameters are shown. They are mutually dependent and complement one another. First, the role of the precursor will be discussed followed by a description of the influence of different substrates, including additional interlayers and catalyst layers on the deposition process. Finally the effect of the reaction temperature and the gas atmosphere is presented. A critical analysis of the literature will give an overview about the current possibilities to produce filled carbon nanotubes with application-tuned properties.

2.1.3.1 Role of the precursor

The choice of appropriate precursors is important for a successful synthesis. This accounts for both, empty and filled carbon nanotubes. Fillings with ferromagnetic properties at room temperature are restricted to the elements iron, cobalt and nickel. The organometallic family of metallocenes, especially ferrocene, cobaltocene and nickelocene contain these metals and are therefore suitable as precursor for the synthesis of metal-filled CNT. Apart from their decomposition temperatures also their kinetics and the reactivity of by-products are convenient for a successful synthesis process [57, 67]. A further advantage is that metallocenes can be mixed. For example CNT with iron/cobalt alloys inside were obtained by mixing ferrocene and cobaltocene powders [68]. Metallocenes are solid crystalline powders at room temperature. Their structure is sandwich-like with the metal in the center and two cyclopentadiene rings as ligands. An example is shown in fig. 2.5. The material can be sublimated in a wide temperature range starting from below 100 °C up to 300 °C. The sublimation behavior especially for ferrocene was intensively studied [69–71]. For the synthesis often a value of 150 °C is given as an optimum temperature.

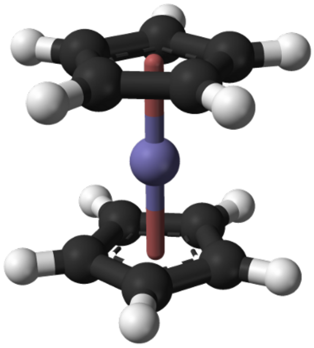

Figure 2.5: Ferrocene molecule as a representative of the general structure of metallocenes. Two cyclic organic molecules (ligands) bind to the central metal atom. In the center is the iron atom (blue), the carbon atoms are black and hydrogen atoms are white.

The concentration of the metallocene in the gas phase at a constant carrier gas flow can be controlled by the temperature T_{pre} of the preheater. By setting a higher temperature the concentration of the metallocene in the gas phase can be raised keeping the transport gas flow constant. An increase of the inner and outer diameter of iron-filled CNT was observed when the ferrocene concentration was hiked up [28]. The increment of the outer diameter occurred since more carbon shells were formed by larger particles. At higher temperatures the metallocenes decompose according to the equation (2.3)

$$Me(C_5H_5)_2(g) \rightarrow Me(s) + H_2 + CH_4 + C_5H_6 + ... \tag{2.3}$$

whereas the moieties depend on the reaction temperature and the composition of the gas atmosphere. The thermal stability of different metallocenes decreases from ferrocene over cobaltocene to nickelocene. Ferrocene decomposes above 1073 K whereas the nickelocene already above 550 K. In contrast, Dyagileva et al. [57] found a significant decomposition rate of ferrocene already at 823 K in a hydrogen-containing medium. Since hydrogen is formed during the CNT growth, the decomposition starts at 823 K and further heating will increase the decomposition rate and alter the composition of moieties in the gas phase.

Metallocenes can also be dissolved in liquid hydrocarbons as applied in the LSCVD method. The measured maximum solubility of ferrocene in selected solvents is given in tab. 2.1. The higher the solubility of ferrocene in the solvent is, the higher is also the possible concentration of metal in the reaction volume. But with the injection the solvent also evaporates and decomposes depending on its thermal stability. The chosen solvents (tab. 2.1) decompose in a wide temperature range (500 °C to 1100 °C) and thus during the synthesis process more and less intensively. That means, more active carbon is there in the reaction zone and the consequence is a lower filling degree. Finally only partially filled CNT are formed [59, 61, 72, 73]. The encapsulated particles can show a large variety of shapes such as spherical forms or small cylinders with low aspect ratio. In contrast by employing only ferrocene as precursor high filling degrees up to 50% per tube could be achieved [28]. It should be emphasized that a large fraction of the CNT is filled with long and continuous iron nanowires.

Table 2.1: Maximum solubility of ferrocene in selected liquid hydrocarbons that are often used as precursor in CNT synthesis. These organic compounds take part in the formation process and increase the carbon to iron ratio above 10:1.

compound	max. solubility of ferrocene in mg/ml at 293 K	boiling temperature in ˚C
Ethanol	2	78
1-Propanol	1	97
cyclopentane	71	49
n-hexane	36	69
cyclo hexane	56	81
benzene	222	80
toluene	160	111
xylene	146	138-144
1,2-dichlorobenzene	236	180

Wang et al. [30] used chlorinated hydrocarbons such as 1,2-dichlorobenzene as solvent for the ferrocene (Tab. 2.1 last row). The boiling temperature is 180 K and thus in the upper end of the sublimation range of ferrocene. Two further special features of 1,2-dichlorobenzene are important. In the presence of hydrogen hydrochloric acid can be formed which might interact with the iron or with carbon atoms. It was suggested that the etching effect of chlorine reduces the number of carbon shells and causes

CNT with thin walls and smaller outer diameters [30]. To understand the influence of the chlorine different chlorinated compounds were investigated [30, 74, 75]. The other point is the special thermal decomposition behavior of the chlorine-contained hydrocarbon, since thermal stable benzene might be formed and therefore less active carbon is supplied to the CNT formation. The kinetics of the decomposition also depends on temperature and the retention period of a gas volume element in the hot zone of the furnace. Thus the decomposition of stable aromatic systems is more reduced at high transport gas flow. This results in less active carbon which in turn leads to shorter or thinner CNT. Also the number of carbon shells is reduced.

By using ferrocene as sole precursor a high filling degree can be expected. Any addition of reactive hydrocarbons will lead to a decrease of the filling degree. Inferential, the ratio of reactive carbon to reactive iron in the gas phase is an important control parameter for the filling degree and filling distribution.

2.1.3.2 Role of the substrate

The condition of the substrates is also a very influential factor in the synthesis of carbon nanotubes [76–80]. The substrate supports the nucleation and growth of the CNT. It should be thermally stable under process conditions and should also be inert for reactions with the different metal catalysts and with carbon. The most simple and inert substrate is the inner surface of the quartz tube reactor. Due to the floating catalyst conditions catalyst particles can condense at the surface and nucleation and growth of CNT occur. However, growth conditions can be optimized if special substrates are located at defined positions within the temperature profile of a furnace. This is due to the growth conditions being strongly dependent on the location in the horizontal tube reactor [67, 81]. Kuwana et al. [67] investigated the formation of small iron particles by ferrocene decomposition. According to this work, best conditions for small and homogeneous particles are found to be in the center line of the furnace.

Aside from the position influence, substrates with defined preparations can alter the deposition process. The most common substrate types are silicon wafers having a thermal oxide layer on top. Furthermore, sapphire substrates are also very often used. Both substrates show the required thermal stability and chemical inertness. Not only the chemical properties but also the physical interaction between substrate surface and metallic catalyst are important since, e.g., the size of a catalyst particle is a function of the surface tension of both substrate and catalyst.

The deposition of CNT on defined substrates has also the advantage that the substrate surface can be changed by precoating and patterning of the catalyst material in order to obtain a better control of the deposition process.

As interlayers, one or more thin layers of additional material that should adjust the properties of the substrate and the catalyst are employed. The basic structure of a substrate with interlayers is sketched in Fig. 2.6. The substrate most often consists of a silicon wafer. One or more interlayers such as a thin silicon oxide layer, alumina, tantalum, copper or tungsten can be employed. On top a thin layer of catalyst is deposited. If needed, the catalyst can be structured. For the formation of alloys more than one catalyst layer can be deposited. Like the substrates the interlayers also have to be thermally stable and chemically inert. Most often the interlayers are used to enhance the activity of the catalyst in order to achieve long and defect-free CNT.

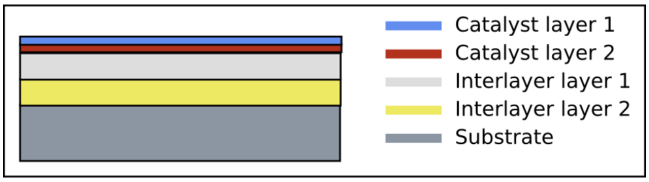

Figure 2.6: Schematic setup of typical CVD substrate for CNT synthesis

The size of the catalyst particles is a decisive factor in the CVD to control the CNT diameter. The diameter distribution and the density of catalyst particles can be varied by the properties of the interlayer. The important feature is the wettability behavior between the interlayer and the catalyst material.

To enhance the growth of CNT the element aluminum is often used as interlayer material in the synthesis of CNT either as pure metal film [78, 82, 83] or as alumina [84–86]. It was found, that these layers lead to a smaller mean diameter and more narrow diameter distribution of the CNT in the synthesis of unfilled as well as of filled CNT. The area density and the alignment of CNT increased. Furthermore, chemical reactions of carbon on the interlayer surface might be involved [85]. This interlayer should be thicker than 1 nm in order to completely cover the substrate. A thickness of 10 nm alumina was reported to give high quality iron-filled CNT [87]. Consequently, such interlayer can change the catalyst particle size as well as its distribution on the substrate and thereby the diameter of the nanotubes [88–90]. Ng et al. [82] investigated the catalytic activity of Fe, Co, Ni and Fe/Ni in combination with several interlayer materials such as Ti, Ta, W, Ir and Al. By using a combinatorial library Ng et al. found, that most of the combinations allow the growth of CNT. Except Al all used materials have a very high melting point in common. In a carbon containing atmosphere Ti, Ta and W form stable carbides. The best result in terms of length, alignment and purity of the CNT was obtained for Fe/Ni on Al. Iron gave good results on W and Al, however, the best results were achieved on Ti as interlayer. The Fe/Ni alloy showed the best results on all employed types of substrates. The combination of Ni and Al showed good results as well. For Fe and Co a high density of CNT was found with Ti as interlayer. In Tab. 2.2 the results are presented according to [82].

Another important feature of an interlayer is its possibility to act as an inhibitor in

Table 2.2: Synthesis results of the transition elements Fe,Co and Ni (as catalyst) on different metal interlayers. The classification into *best, good* and *bad* is related to the morphology of the obtained CNT. The CNT were grown on the different substrates under the same synthesis conditions. However, the results may differ to some extent if the growth conditions are optimized for each combination of interlayer and catalyst respectively [82].

catalyst	interlayer material		
	best growth conditions	good growth conditions	bad growth conditions
Fe	Ti	W, Al	Ta, Ir
Co	Ti	Ta, Al	W, Ir
Ni	Al	Ta, Ti	W, Ir

order to prevent the formation of CNT at defined areas on the substrate. Especially when using floating catalyst methods it is difficult to prevent a growth on special parts of the substrate because both the carbon and catalyst are delivered via the gas phase. This issue can be solved by employing additional interlayers. Thus non-inert layers are deliberately used to locally prevent the growth of CNT in special applications [91]. The growth of CNT based on ferrocene as precursor was successfully prevented by employing an amorphous carbon layer [92]. The iron from the gas phase falls onto the amorphous carbon and diffuses into the layer possibly forming carbides. It was also found that the iron diffuses through the amorphous carbon layer and accumulates at the interface between the silicon substrate and the amorphous carbon as small spherical iron-containing particles [92]. In principle, elements that form very stable carbides can be imagined as potential inhibitor materials. Of course the suppression of the CNT formation strongly depends on the interaction between the interlayer and the catalyst. In tab. 2.2 the last column lists catalyst-interlayer configuration that result in very low quantity or no CNT formation [82]. These materials could be used as inhibitor materials in the floating catalyst method. Nevertheless, it remains a challenge to grow ferromagnetically-filled CNT in well defined structures.

To conclude, due to their influence on the catalyst, interlayers can be used to control the density and alignment of CNT films. The interlayers support the formation of small particles with a narrow diameter distribution and a homogeneous particle area density.

2.1.3.3 Role of the catalyst

The most common catalyst materials are the VIIIb-metals of the periodic table of elements [82, 93]. They possess a low carbon solubility and form only meta-stable carbides, which are important properties of the catalyst material. However, an exclusive consideration of the influence of catalyst material on the CNT formation is somewhat artificial, since it is always in a strong interaction with the used substrate and interlayers [76]. For the fabrication of well-filled carbon nanotubes two sources of catalyst material are available. The first is a metallocene in the floating gas and the second is a thin catalyst layer on the substrate. The size of the catalyst particles is a very important control parameter. The interaction of the catalyst material with the substrate surface is a basic issue in the catalyst preparation. Demands on the catalyst are the following: Defined diameter and small diameter distribution, low mobility on the surface thus low agglomeration, possibility to solve carbon, ability to form meta-stable carbides and to allow for surface or bulk diffusion.

On the nanoscale the catalyst affects the reaction not only due to its chemistry but also by its geometry. The geometry of the catalyst in turn is affected by the interaction of the catalyst with its surrounding [76, 77, 79, 80, 93, 94]. The so-called size effect, caused by the nanodimension of catalyst particles is intensively discussed in the literature [77, 79, 80, 93, 95–100]. Thereby it is possible to synthesize CNT at temperatures far below the melting point of the VIIIb-metals, because nanoparticles have lower melting points than the bulk material.

A simple method for the production of catalyst particles is the deposition of thin films with thicknesses varying between 1 and 100 nm. A thermal treatment transforms such layers into small islands. Often, the growth of CNT by thermal CVD is performed on such catalyst precoated substrates.

It is advantageous if the catalyst particles are formed by the Volmer-Weber mode (island mode). Islands are formed since the thin layer material wants to interact with itself rather than with the substrate or interlayer surface. In contrast, if the catalyst interacts corresponding to the Frank-van der Merve mode, which is the layer-by-layer mode, no separated particles would occur. In a third mode (called Stranski-Krastanov mode) the two before mentioned are combined. In this mode first a layer is formed but with a raising amount of material the formation of islands starts. Therefore it is called the layer-plus-island mode. In the last situation also catalyst particles might be formed. In the synthesis of CNT by CVD most often the Volmer-Weber mode is assumed. However, the last mentioned can not be excluded. As will be discussed in the section about the growth mechanism the interaction between the catalyst and the substrate determines the growth mode. In the Volmer-Weber mode the catalyst particles can have a contact angle below or above 90°. In the first case there is a strong interaction between the particle and the surface and it broadens. In the second case the particle surface interaction is weak and it does not spread.

It is known, liquid Co forms smaller particles than Fe on a SiO_2 layer, because it has a higher surface tension [83]. A thin Co catalyst layer (2 nm) on SiO_2 resulted in a visual decrease of the inner diameter of the grown CNT in comparison to an 2 nm Fe layer. All other conditions were kept constant. It was suggested that a higher surface tension of the Co nanoparticles on the surface caused the smaller particle diameter.

Thus the diameter of CNT can be controlled by the choice of the catalyst material, furthermore, by the catalyst layer thickness and the pretreatment conditions.

The size of the catalyst particles defines the inner diameter of a CNT. The larger the particle diameter the larger the inner diameter is. Also the outer diameter depends on the catalyst particle size in a similar way, since it increases with increasing particle size. However, the outer diameter also depends on other parameters, e.g., the reaction temperature and concentration of active carbon in the gas phase.

Besides all influences, which are mentioned before, the particle size also strongly depends on the temperature of the pretreatment of the substrate and the gas atmosphere. It was shown, that an annealing of thin catalyst films in the presence of hydrogen produces smaller particles than in a pure argon atmosphere [101].

The properties of catalyst particles are comparable important for both, the growth of unfilled as well as filled CNT. At the deposition of unfilled CNT on prepared substrates the catalyst defines the growing site and the diameter of the CNT. However, before we will discuss the influence of an additional catalyst layer on the growth behavior of filled CNT, we present some remarks about the synthesis of CNT by using the floating catalyst method. In this case the decomposition of the precursor in the gas phase leads to the formation of metal clusters. These clusters agglomerate on the substrate in a random manner and form heterogeneous nucleation sites. The precursor concentration thereby defines the average size of the particles. In fig. 2.7 four different scenarios for the correlation between the diameter and its distribution depending on the synthesis method are shown. Case (A) represents the synthesis of unfilled multi-walled CNT on a substrate with a thin catalyst film. The synthesis of multi- walled CNT using a precursor that contains a small concentration of catalyst in the gas phase is illustrated in case (B). The comparison of floating catalyst experiments for the synthesis of filled CNT without and with additional catalyst layers on the substrates is shown in fig. 2.7 in case (C) and (D). In the former case (C) the average diameter of the CNT is smaller compared to the latter (D) but the diameter distribution is much higher. Without

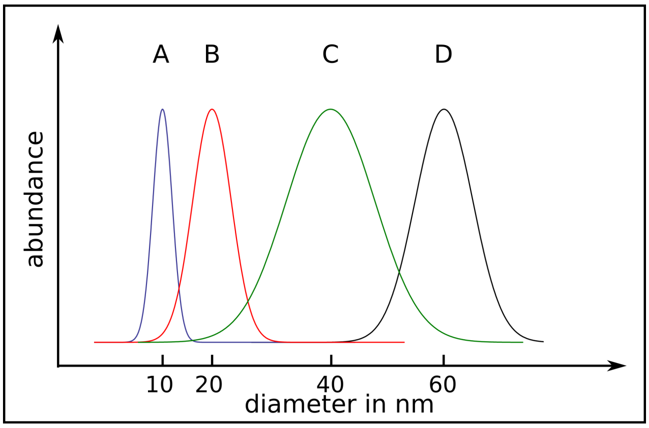

Figure 2.7: In the graph the mean outer diameter and the diameter distribution of CNT are sketched. Curve (A): small diameter and distribution of unfilled CNT grown on substrates with catalyst. The other curves (B,C,D) represent CNT grown by the floating catalyst method. Curve (B): almost unfilled CNT, Curve (C): well filled CNT, Curve (D): well filled CNT grown by the combination of catalyst supported substrates and floating catalyst. Based on data from [28, 29].

additional catalyst on the substrate (C) the diameter strongly depends on the ferrocene concentration in the gas phase [28]. In principle the CNT possess a broader diameter distribution for the floating catalyst method (C and D) in comparison to unfilled CNT (A and B). The given mean diameters are typical values for multi-walled CNT frequently found in literature [28, 29].

In the synthesis of metal-filled CNT by the LSCVD method normally no additional catalyst is supplied with the substrate. The filling degree is reduced not only because of the increased carbon to metal ratio but also due to the missing additional catalyst material on the substrate. However, substrates with additional catalyst can be used in the LSCVD as well [29, 66]. In the presence of an additional catalyst layer the mean diameter of the grown CNT increases, because the size of the primary catalyst islands are dominantly determined by the thickness of the catalyst film. Thus, the diameter depends less on the ferrocene concentration [28].

In addition the alignment of the CNT grown by the SSCVD method enhances if there is catalyst on the substrate [28]. It was further revealed that the density of catalyst islands and the density of CNT corresponds [101]. The combination of both sources, catalyst material from the gas phase and from the substrate, results in a high filling degree up to 50 wt% [28, 29, 83, 102, 103]. Without an additional catalyst layer a lower filling degree was found using the SSCVD method.

The catalyst is one of the most important parameter in the synthesis of CNT by CVD. Its activity does strongly depend on the synthesis conditions especially the reaction temperature and gas atmosphere. After selection of the catalyst the optimal temperature and gas conditions has to be found.

2.1.3.4 Role of temperature and gas composition

All reactions in the thermal CVD including sublimation, evaporation and decomposition of the precursors as well as the formation of CNT are temperature dependent. The influence of the temperature and gas atmosphere on the formation of CNT are strongly interlinked. The are discussed focussing on their effect on the CNT formation and resulting morphology. Intensive numerical simulation studies have shown how the reaction temperature influences the catalyst particle formation and the kinetics of the gas phase reactions [67, 81, 104–106]. It was found that the diameter of the catalyst particles, which are spontaneously formed in the gas phase or on a substrate, increases with raising temperature. It is experimentally confirmed that the results significantly differ depending on the substrate position in the reactor. This is related to the always existing temperature profile in a reactor (radial and longitudinal) which depends on the utilized particular setup. These results confirm the sensitive dependence of CNT growth on the temperature and gas atmosphere. Besides the temperature profiles, each reactor has specific flow conditions which also strongly influence the deposition [67]. Because of that a comparison of the experimental results in the literature is difficult.

The morphology of CNT is characterized by the length, the outer and inner diameter and the shell thickness. In the case of (in-situ) filled CNT also the structure of the filling has to be considered. The inner diameter and to some extent the outer diameter of a CNT are controlled by the diameter of the catalyst particle [89, 90, 107]. The diameter of the catalyst particles depends on the temperature but also on the gas atmosphere [101, 108]. For example a pretreatment of 2 nm Fe films in an Ar/H_2 atmosphere (30:1) at 1100 K produces smaller islands in comparison with a treatment under pure Ar at the same temperature. In the former case the surface roughness was higher than in the latter [101]. This is due to the different surface energies of the particles in the corresponding gas atmosphere. At a high temperature catalyst particles on the substrate surface coagulate into larger islands. At lower temperatures the islands are smaller due to a lower activation energy and hampered surface mobility. Thus the pretreatment conditions are important for the diameter of the grown CNT. However, using the floating catalyst method a random increase of the particle diameters should be considered because of metal clusters originating from the gas phase that accumulate on the substrate surface. Also in the floating catalyst method without additional catalyst on the substrate the formation of clusters and the rate of cluster deposition is related to the temperature and used gas phase. At low temperatures the metallocene decomposition is slow and only few metal clusters deposit on the substrate. However, the decomposition rate of the metallocenes increases in the presence of hydrogen which also increases the deposition rate [57, 69, 71]. For example the decomposition of ferrocene in vacuum starts at temperatures $\approx 1100\,\mathrm{K}$, using a hydrogen flow, the decomposition already at temperatures of $\approx 700\,\mathrm{K}$ occurs. However, there is a broad variation in the behavior within the group of metallocenes. The decomposition kinetics of hydrocarbons depends on the hydrogen concentration as well [57, 71]. Hence, the balance between the temperature and the hydrogen concentration controls the diameter of the CNT.

So far it was presented how the temperature and the gas atmosphere act on the catalyst particle and thereby on the CNT diameter. Now the influence of these two parameters onto the diameter, shell thickness and length of the grown CNT will be discussed.

The most common inert or transport gas is argon, but also nitrogen [109] is used. Hydrogen containing gases such as pure hydrogen (H_2) or ammonia (NH_3) are employed as well, but they cannot be considered as inert gases since they take part in the reaction. Wasel et al. [110] intensively studied the role of hydrogen on the formation of CNT. And Kamalakaran et al. [60] suggested, that hydrogen is able to etch excess carbon from catalyst particle surface. Furthermore, the role of hydrogen is to limit or alleviate the so called poisoning of the catalyst particle [111, 112]. The catalyst particle can be deactivated if its complete surface is covered by excess carbon. By the loss of its catalytical activity the growth process will stop. The removal of excess carbon is therefore crucial for a long active period of the catalyst and thus for the length of the CNT. If necessary, the growth of CNT can be stopped by a sudden increase of highly reactive hydrocarbons. If the diffusion of dissolved carbon through the particle is lower than the decomposition and deposition rate of carbon on the catalyst surface the growth will terminate. A finishing of the growth process can also be achieved by cooling which hinders the decomposition of hydrocarbons and diffusion of carbon.

Since hydrogen can have competitive effects on different occurring reactions its influence has to be carefully considered. The etching of the catalyst to maintain its activity is a desired effect. If the concentration of hydrogen is too high no CNT will be formed but oil-like deposits. Therefore the growth of CNT will also stop at a high concentration of hydrogen [113]. It was argued that with increasing hydrogen concentration the dehydrogenation of hydrocarbons is reduced and less active atomic carbon is available [110, 113]. Moreover, the role of hydrogen was discussed within a concept that explains its importance during the CNT formation by a so called free radical condensation mechanism [113]. Currently it is not completely clear whether such non-inert gases as hydrogen etch carbon from the deposited structure or if its influence is mainly to act on the gas phase reactions. Also the waiver of pure hydrogen can lead to a better growth behavior if only argon is used as transport gas [58]. It is suggested that the amount of H_2 produced by the ferrocene decomposition is sufficient. The total length of CNT did not increase with additional H_2 but the filling degree decreased [58].

Although filled CNT are grown using a relatively high metallocene concentration and consequently fresh catalyst material is added during the process, it has been observed, that the sudden growth stops after a certain time period [29]. This is valid for CNT grown by LSCVD as well as SSCVD, although the observed maximum length of CNT using the LSCVD is ≈45 µm and only ≈15 µm for SSCVD-technique. It was suggested that the continuous delivery of ferrocene (LSCVD) into the furnace allows an uninterrupted growth since there are no strong variations in the precursor concentration. Nevertheless, the final length as well as the diameter of the grown CNT are proportional to the ferrocene concentration [28]. However, it was proposed that the growth of very long CNT is due to the continuous feeding of iron catalyst that results from the ferrocene dissolved in xylene [61]. In that case the iron concentration was much lower in comparison to methods that solely employ ferrocene. Up to now, there is no conclusive explanation for these experimental observations.

It is difficult to grow short CNT by LSCVD (shorter 1 µm) because of the high amount of active carbon present in the reaction chamber. The high growth rates in LSCVD ($\approx$1000 $\frac{\text{nm}}{\text{s}}$) are sometimes unfavorable since the length and diameter can hardly be controlled. Depending on the nature of the precursor the growth rate can be controlled by adjusting the ferrocene concentration, the gas composition and temperature. For example, in the LSCVD the diameter and length was smaller at a low ferrocene concentration but both are increased with raising concentration [28]. The averaged growth rate which can be reached in the SSCVD method is in general lower ($\approx$20-50 nm/s) than in the LSCVD. Therefore, the SSCVD is better suitable for the synthesis of shorter CNT. The growth rate of a CNT, its diameter as well as its length depends on the decomposition rate of the precursor, which in turn depends on the temperature and the gas atmosphere. Above a certain temperature the diameter of the growing CNT increases. This limit temperature depends also on the exact composition of the gas atmosphere [114]. The optimal temperature for CNT formation increases with increasing concentration of additional NH_3 in the gas phase. For a higher temperature the precursor concentration should be increased. This is related to the balance between the precursor decomposition and the diffusion rate of dissolved carbon through the catalyst particle [114].

The outer diameter strongly depends on the reaction temperature, in contrast to the inner diameter of the CNT, which is mainly defined by the diameter of the catalyst particle. At higher temperatures, the number of carbon shells and also the deposition rate of amorphous carbon on the surface of already existing CNT increases. Juang et al. [114] found a significant increase of the CNT diameter above 900 °C. An increase of the reaction temperature, e.g., above 1000 °C did not lead to longer CNT but to an increase of the number of amorphous carbon coated particles especially in the synthesis of CNT from ferrocene precursor [28]. The wall thickness and thus the outer diameter is influenced by the reaction temperature. In principle the crystallinity of the carbon shells enhances with increasing temperature as confirmed by Raman spectroscopy [29]. By using a higher concentration of additional etching gases the growth temperature can be higher and still the wall thickness of a CNT can be reduced. In contrast, by using ferrocene the increased decomposition rate has to be considered since this could lead to an increase of the diameter. If the carbon supply at the decomposition site of the particle is at an identical rate as the diffusion rate of carbon through the particle CNT will grow with best quality [114]. The total flow rate can be adjusted using a mixture of an inert gas (argon) and a reactive gas (hydrogen, ammonia). However, for each compound used new optimal values for the parameters have to be determined.
Besides the etching effect of hydrogen also that of chlorine was investigated [30, 74]. Using 1,2-dichlorobenzene as solvent for ferrocene in the LSCVD method a significantly

smaller wall thickness for iron-filled [30, 74] and iron-carbide-filled CNT [66] was obtained compared to material grown by the SSCVD method [58, 102]. By studying different chlorinated hydrocarbons (benzene derivatives) it was suggested that the etching effect of chlorine, which is formed during the thermal decomposition of the solvent, is decisive for limiting the number of carbon shells [30, 74]. On the other hand it might also be possible that the chlorine reacts with hydrogen forming hydrochloric acid. Simultaneously the thermally stable benzene is forming. The benzene does not intensively react in the reaction zone due to its high thermal stability. Thus the low concentration of active carbon leads to relatively few carbon shells.

The structure of the filling also depends on the process temperature and the cooling rate. At high temperatures a large amount of carbon dissolves in the catalyst particle. As Ding et al. [115] have theoretically shown, it is most likely that the catalyst particle is highly saturated with carbon during the growth. After a highly supersaturated state it will oscillate around the saturation concentration. If the reaction is terminated by cooling down, structural transformations will occur according to the phase diagram. The structure of the filling can be changed by specific tempering the sample at temperatures close to phase transitions. For example it has been shown that annealing at 645 °C can transform γ-Fe into α-Fe [28, 74].

The phases of the filling also depend on the gas composition, gas flow velocity (retention period) and the method of the transfer of the precursor into the reaction zone. For example, Wang and Gui et al. [30, 74] used the LSCVD method and evaporated a 1,2-dichlorobenzene/ferrocene solution, with a concentration of 60 mg ferrocene in 1 ml of the solvent. A gas flow of Ar/H_2 with 2000 sccm was employed. Bundles of oriented CNT were obtained having mainly α- and γ-Fe filling. Employing the same precursor solution (same concentration) leads to mainly iron carbide filling when the solution was sprayed into the furnace with a nozzle at a transport gas flow of 1000 sccm Ar/H_2 [66]. However, the structures of the shells were quite similar and a significant limitation of the wall thickness was observed in both cases. If only the transport gas flow as well as the resulting precursor concentration are responsible for these differences can not be answered yet. The CVD-process is kinetically determined therefore the gas velocity is decisive for the deposition process. Because the gas velocity is strongly dependent on the geometry of the used reactor (diameter, length, volume) also the deposition process is influenced by the reactor geometry [67].

From the discussion above, some rules for the formation of in-situ filled CNT with different filling degrees can be concluded. Firstly, for the synthesis of long and continuous filled carbon nanotubes it is convenient to use a precursor with a low carbon to metal ratio, such as it exists in the metal organic compound family of the metallocenes. A metal catalyst layer as a secondary source for the filling material leads to higher filling degrees and a lower diameter distribution of the CNT. For partially filled CNT a higher carbon to metal (catalyst) ratio is needed, which can be realized by additional hydrocarbons in the precursor. A significant higher concentration of active carbon in relation to the metal catalyst will lead to less filled CNT. Nevertheless, it should be considered, that an additional catalyst layer leads to a smaller diameter distribution. For highly crystalline carbon shells rather high temperatures are advantageous. However, to avoid an increase in the wall thickness the amount of transport gas should be increased. That reduces the stationary concentration of the reactive precursor and balances the amount of active carbon. Due to the competitive reactions in the gas phase and on the substrate an optimum for the temperature has to be found for each used precursor. A reactive gas species takes actively part in the reactions. The gas velocity is important since it defines the retention period of the reacting species in the reaction zone.

2.2 Growth models

Understanding the growth mechanism of carbon nanotubes is a key requirement for the deliberated synthesis in order to obtain the special properties needed for their applications. Intensive studies were performed to find a mechanism describing the formation of carbon nanotubes. Up to now, there is no generally accepted growth mechanism and further research is necessary.

The mechanism discussed here for the formation of in-situ filled CNT is a phenomenological description. It is deduced from different experimental observations to explain the variety of observed structures of the CNT. The phenomenological mechanism is also the foundation for theoretical studies. These theoretical studies are mainly performed for the formation of single-walled CNT. However, many results are also useful for the understanding of multi-walled CNT formation.

The knowledge and understanding of the growth mechanism is under continuing development and several modifications were discussed during the last two decades. In this section selected features of the growth mechanism are discussed, that are especially suited for the synthesis of filled CNT by the CVD method.

2.2.1 VLS mechanism

The basis of the following discussion is the vapor-liquid-solid (VLS) mechanism, which was originally developed for the growth of silicon whiskers by Wagner and Ellis in 1964 [116]. It bases on the assumption that a gaseous phase, a liquid phase and a solid interact. The precursor is supplied as gas. The liquid phase is the molten catalyst particle situated on the solid substrate. During the growth process the precursor decomposes in a specific area of the surface of the liquid particle at the temperature T_1. The precursor material dissolves until saturation at concentration c_1 is reached. It is assumed that the particle possesses an area with a lower temperature T_2 and a lower concentration c_2. Thus the presence of both a concentration and a thermal gradient is assumed. The precursor material diffuses through the particle and precipitates at T_2. These very basic assumptions of the mechanism allow the application to other systems.

2.2.2 Base and tip growth mode

One of the first mechanism to explain the growth of carbon whiskers was initially developed by Baker et al. [117, 118] on basis of the VLS mechanism. They performed in-situ studies on the growth of carbon whiskers employing controlled atmosphere electron microscopy (CAEM). During the formation the (liquid) metal catalyst particles were found either on the tip or bottom of the formed whiskers [118]. Due to forces acting on the catalyst particles they deform during the process resulting in two growth modes. If there is a strong attractive interaction between the catalyst and the substrate a good wettability is found that lead to contact angles below 90 °C and the particle most likely remains on the substrate surface. Since the decomposition of hydrocarbons relies on the catalytical activity of the particle surface supplied carbon atoms can only connect to the already existing carbon structure at the particle whisker interface. Therefore the oldest part of the whisker is the tip and the youngest part is at the bottom. For this reason it is called base growth mode. If there is a repulsive interaction between the particle and the surface a contact angle above 90 °C will establish and the particle most likely detaches from the surface and lifts up. In this case the oldest part of the CNT is close to the substrate surface and the youngest part is the tip. Thus, this is called tip growth mode. Both growth modes were introduced to discuss the different occurrence of the metal particles in the as-grown carbon material.

Other groups adapted the mechanism of Baker et al. to explain their experimental results for unfilled carbon nanotubes [89]. In the modified mechanism it is assumed, that first of all the change in the size of the catalyst particles, from large dimensions down to diameters below 100 nm is the reason for the formation of the tubular carbon structures [89] instead of whiskers. The key features of the VLS mechanism like the decomposition, dissolving and diffusion of carbon species into the metal particle and precipitation due to supersaturation have been adopted and can be applied to describe the formation of carbon nanotubes. The base and tip growth mode of unfilled carbon nanotubes are shown in fig. 2.8 and fig. 2.9 respectively.

In the VLS mechanism a sufficient solubility and sufficient diffusion rate of carbon in the catalyst material is assumed. Esconjauregui et al. [93] investigated the catalytic effectivity of various metals depending on their electron configuration in detail. Elements

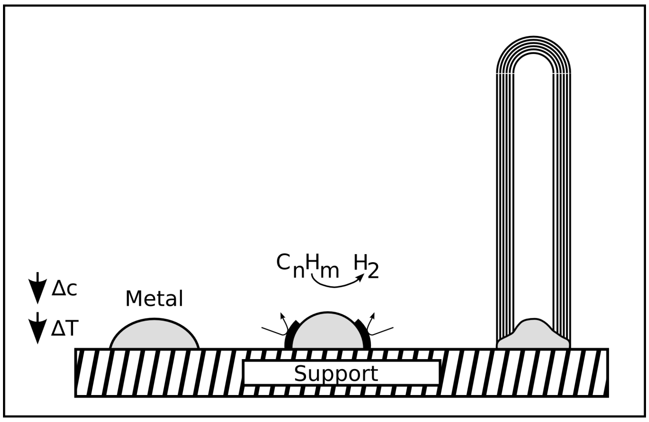

Figure 2.8: Base growth mode according to [118]: The metal particles on the surface are exposed to gaseous hydrocarbons, which decompose catalytically on the surface of the catalyst particle. An exothermic decomposition is assumed and a carbon concentration as well as a temperature gradient form. After its decomposition the carbon diffuses from the hot area with a higher concentration to the colder region of the particle and precipitates to form the graphitic structure of the CNT wall. The particle remains attached to the substrate.

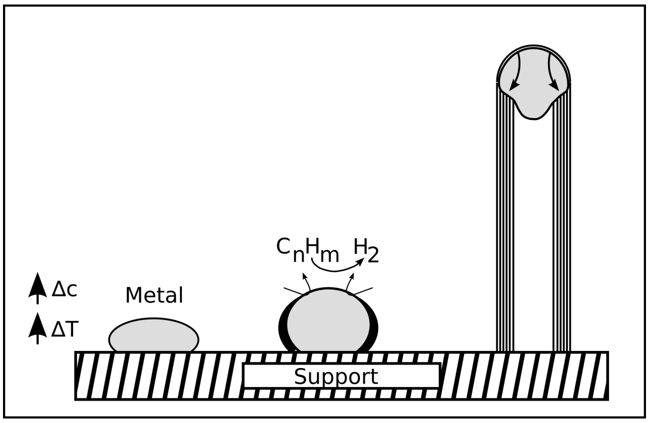

Figure 2.9: Tip growth mode according to [118]: The metal particle is only weakly bound to the substrate surface. The decomposition of the hydrocarbons takes place at the upper side of the particle. Again an exothermic decomposition is assumed and the temperature and carbon concentration increases at the top of the particle which gets deformed during this process and detaches from the substrate. The carbon now diffuses to the colder side of the particle and precipitates to form the CNT shells.

with few d-vacancies such as iron, cobalt and nickel were confirmed to be very active catalysts since they possess a high diffusion rate for carbon and form only metastable carbides. The decomposition of carbides is required for growing CNT.

The estimated growth rates suggested that the CNT formation strongly depends on the diffusion of carbon through the volume of the catalyst particle and its precipitation at an opposed side of the particle [101]. Other groups stated that only surface or subsurface diffusion takes place [119].

The dimension of the catalyst particle defines the inner diameter of the CNT but to some extend also the number of graphite shells. Sinnott et al. [89] investigated the influence of the catalyst particle size, the precursor composition and the temperature. They observed that the carbon shells precipitate from one half of the particle if its shape is spherical or pear shaped (on the lower curvature face for pear shapes). As the main driving force a carbon concentration gradient was assumed [89].

2.2.3 Base and tip growth mode for filled CNT

For filled CNT, not only the formation of the carbon shells but also the formation of the in-situ filling has to be explained. It is particularly difficult to describe the influence of the catalyst because it is applied on the substrate and additionally as floating catalyst from the decomposed precursor. During the whole growth process metal particles, most of them catalytically active, interact with the forming CNT. Nevertheless, several research groups adjusted the VLS mechanism and the concepts of the tip and base growth mode to explain the formation of in-situ filled CNT [61, 65, 89, 120].

From their experiments Zhang et al. [61] suggested a growth mechanism that could explain the in-situ filling of carbon nanotubes with iron during the synthesis. The scheme of the mechanism is shown in fig. 2.10. According to Zhang et al. [61], an open-tip tip growth mode and furthermore the existence of two different growth rates are present during growth. In the initial state the catalyst particles detach from the substrate surface, which results in a tip growth mode. Thereafter the growth slows down and stops eventually. An empty tube growth is explained by the reaction of carbon clusters from the gas phase with the open tip of the forming CNT. This is the slow growth stage. When a metal particle falls onto the tip the catalytic process takes place and the CNT walls grow much faster until the particle is surrounded with carbon again. This part is the fast growth stage. Both stages alternate with each other during the process. During the fast growth stage the iron particles are forced into cylindrical shape and form the filling. The necessary pressure originates from the comparatively faster growing carbon shells [61]. The filling progresses by subsequent addition of iron nanoparticles on the open tip of the growing CNT. However, the assumption of an open CNT during the growth is critical. There are different possibilities to define an open tip during the formation process and in fig. 2.11(B) and fig. 2.11(C) two cases are shown.

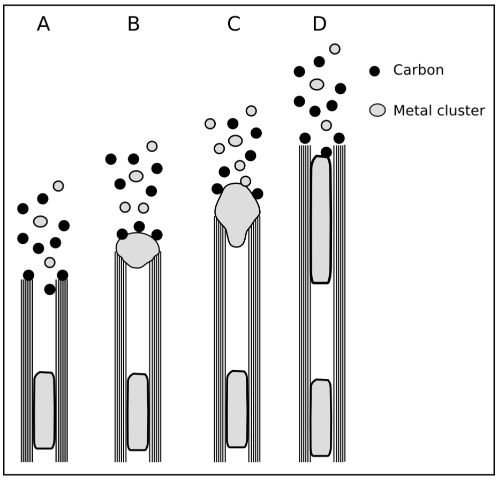

Figure 2.10: The figure presents the growth process of in-situ filled CNT after [61]. (A) shows the slow growth stage. The carbon shells at the open tip react with carbon clusters from the gas phase. In (B) a larger catalyst particle attaches to the open tip and the fast growth stage starts. The CNT grows fast and the pressure caused by the shells deforms the catalyst particle. In this stage (C) a filling section is formed. If the supply with catalyst material stops the slow growth stage continues.

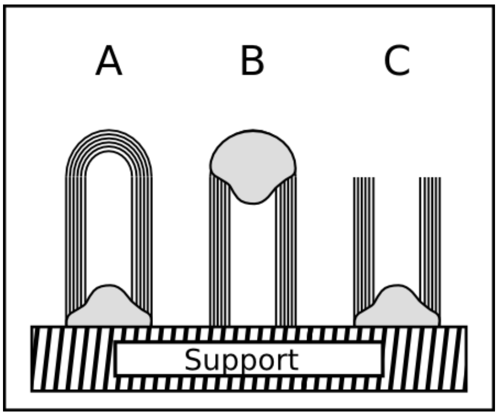

Figure 2.11: Three schematic cases for the tip of a growing CNT. Case (A) shows a closed tip since each shell is closed by a fullerene-like cap. Case (C) represents an open tip whereas this situation is only favorable under certain conditions. An open tip can be either stabilized by lip-lip-interaction [121] or as result of the so called "scooter" mechanism [122]. The case (B) is sometimes called open [123] because of the missing fullerene cap but it is also regarded as closed due to the particle.

Since the existence of open tips is a fundamental assumption in some of the growth mechanisms [61, 65] for filled CNT, we want to briefly discuss the possibility for their occurrence during the CNT formation. Most of the discussion in literature is related to unfilled and especially single-walled CNT. However, the understanding of these investigations can be transferred to some extend to the carbon shell formation of filled CNT.

Kwon et al. [121] simulated the growth of unfilled MWCNT without a metal catalyst involved. The basic idea is that dangling bonds at the open tip are stabilized by single atoms that form stable covalent bridge-bonds between adjacent layers which are called lip-lip interactions. The CNT grow by subsequent incorporation of carbon atoms into the shell structure. The formation of a cap requires more energy than the lip-lip interactions and excess carbon is needed for building pentagonal defects. This distinguishes the mechanism from others, because cap formation, in the lip-lip interaction mechanism interrupts and finishes the growth process. However, another type of simulation revealed, that the lip-lip interaction is not sufficient to keep the tip of a growing CNT open [124, 125]. In other mechanisms the formation of a cap is the initial step and often called nucleation of the CNT growth process [123].

An alternative mechanism to prevent the closure of the growing CNT is the "scooter"-motion. A fast moving small metal cluster on the open tip prevents the closure of the CNT cap [122]. In the CVD synthesis of in-situ filled CNT there is a relatively high concentration of small metal clusters in the gas phase [105] and the tip of a growing CNT interacts with these clusters. It is hardly possible that the lip-lip or scooter mechanism are stable under these conditions. It is therefore assumed that either the tip of the CNT is closed by a carbon cap or by a metal particle with a diameter at least of the inner diameter of the CNT [123]. In case of MWCNT the particle diameter should be as large as the outer diameter (see fig. 2.11(B)). Also Charlier et al. [126] found that a metal particle under their simulation conditions promotes a closure of the cap. Most of these simulations are restricted to the formation of single-walled CNT, but are also valid for multi-walled CNT.

An experimental evidence for an open tip growth was reported by Iijima et al. [88], where the material was synthesized by arc discharge. It was suggested that the continuous growth of long CNT results from addition of hexagons whereas heptagons together with pentagons lead to the formation of closed caps. The thickness of the CNT increases by subsequent addition of further carbon on existing basal planes. An open tip growth was also proposed to explain the experimental data [60, 61, 65, 101]. However, in the as grown material open caps were not exclusively observed.

According to Deck et al. [65] the formation of iron-filled carbon nanotubes can be explained by the open tip base growth mechanism which is shown in fig. 2.12. It is suggested that the long iron nanowires inside of the CNT are formed through the subsequent addition of iron nanoclusters that fall onto the open tip. The liquid-like metal clusters with diameters lower than the inner diameter of the CNT diffuse inside the cavity. They can contribute to an existing nanorod or form a new one. For diffusion, a liquid or at least highly mobile state of the clusters is required. In the work of Deck et al. [65] no slow and fast growth stage are assumed. Deck et al. Instead, the formation of small CNT embryos in the gas phase, which fall onto the growing CNT and contribute to the formation of the filling is proposed. The mechanism offers an explanation for micrometer long metallic wires encapsulated in carbon nanotubes. The presented mechanisms are capable of describing the formation of both, the filling and the carbon shells in a feasible manner. However, theoretical studies [115, 123–127] have shown, that an open tip in the sense of fig. 2.11(C) is energetically unfavorable in comparison to a closed cap.

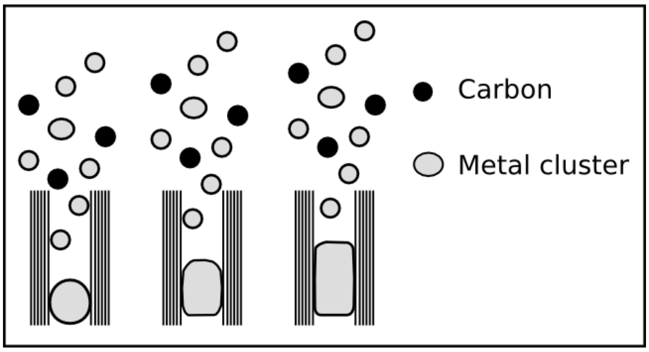

Figure 2.12: Open tip base growth according to [65]: The filling of the cavity results from the diffusion of small metal clusters that are produced in the gas phase. The clusters diffuse a certain distance, eventually forming a continuous filling.

2.2.4 Combined growth mode

An intensive discussion and interesting approach to explain the growth of metal-filled CNT was presented by Kunadian et al. [120]. They combined the tip- and base-growth mode explaining the formation of the filling in the context of a closed tip growth process in the sense of fig. 2.11(B). In the following section the mechanism is presented and discussed since it might explain the in-situ filling of CNT during synthesis as it was performed in this work.

In the mechanism (fig. 2.13) it is assumed that the initial state, i.e., the nucleation follows the base growth mode. Hydrocarbons decompose on the surface of the catalyst particles. In the continuous-feed CVD the precursor, which contains both, the carbon source and the catalyst material, is provided continuously during the process. Due to the floating catalyst conditions metal clusters are formed and hydrocarbons can already decompose in the gas phase. The catalytically active metal clusters and the carbon atoms fall onto the catalyst particles which remain anchored to the substrate surface.

In addition to [120] the author of the present work assumes, that this results in a continuing change of the catalyst conditions. Each cluster that connects to the catalyst particle modifies the volume, shape and the carbon concentration of the catalyst. Thus under floating catalyst conditions it is likely that the growth mode switches from the base to tip growth mode. After the switching the filling process as well as the shell formation occurs simultaneously at the tip. This mechanism could thereby explain many observed phenomena like the distribution of metal particles and wires along the hollow core of the CNT. Furthermore, structure specifics such as kinks and branches of CNT that are characteristic for filled CNT may be explained.

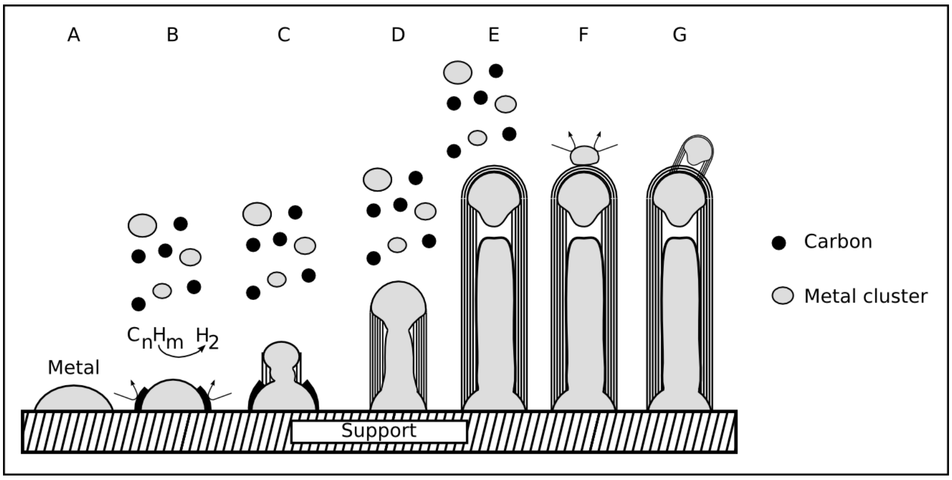

Figure 2.13: Steps of the combined growth mechanism according to [120]. In step A a catalyst particle is formed. Step B describes the decomposition of hydrocarbons on the particle surface. Due to the floating catalyst method catalytic processes occur also in the gas phase forming metal and carbon clusters. In step C the deposition of iron particles at the growing site takes place continuously. Thereby the growth mode changes from base to tip growth mode (step C→D). When further material deposits from the gas phase the growth continues (step E) until a stable cap is formed. If the cap is closed, a so called secondary growth might occur. This is often tip growth since the wettability of the metal catalyst is low and the particles easily detach (step F and G).

As mentioned above, the closed tip growth (see fig. 2.11(A) and especially (B)) is an important assumption in this mechanism [120]. After the CNT have stopped to grow a secondary nucleation can take place and further CNT are formed on the existing material. These new CNT are most often formed by the tip growth mode since the interaction between the metal particles with the already existing CNT material is low and particles detach [120]. The combined mode proposed can explain many experimental observations by only making a few assumptions, and taking theoretical findings into account.

Experimental results of the in-situ synthesis of metal-filled CNT [58, 83] support the idea of the combined growth mechanism. In these experiments different materials of the substrate catalyst and the floating catalyst were selected. At first, a Fe catalyst layer (2 nm) and cobaltocene as precursor was employed as carbon and metal source. Energy dispersive X-ray spectroscopy (EDX) investigations in the middle of the filling show resolvable amounts of iron [83]. Secondly, a Co layer (2nm) on a silicon substrate was employed and ferrocene was used as carbon and metal source. Vertically aligned iron-filled CNT could be achieved. Investigations by cross sectional EDX inside TEM revealed that there is no Co at volume sections along the Fe filling [83, 128]. The latter is an indication for switching from base to tip growth mode since only the material from gas phase (Fe) was catalytically active and found as filling phase.

2.3 Synthesis of iron-filled CNT for magnetic probes

Depending on the growth conditions different filling morphologies, as shown in fig. 2.14, can be formed. All types are found in literature, whereas type A and B are especially interesting for applications where the cavity shall be filled with foreign material. A long filling (C) was reported for iron by, e.g., [29, 30, 58, 74, 102], for cobalt [129, 130] and for nickel [56, 131], whereby one of the most promising application potential of iron-filled CNT are carbon nanotube encapsulated single iron nanowires as probes for

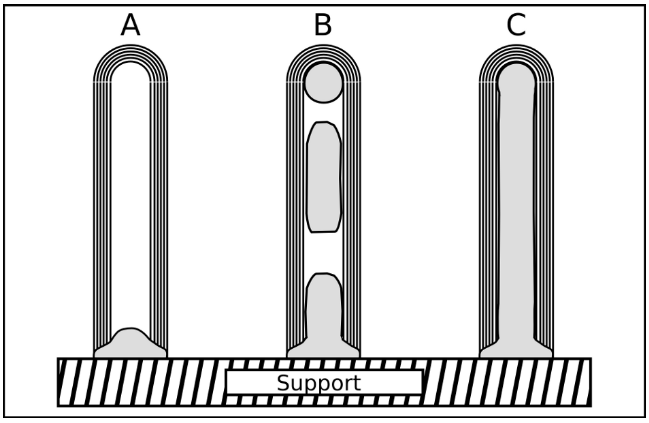

Figure 2.14: The sketch represents three types of filled CNT that possess different degree and distribution of the filling.

magnetic force microscopy. For this application CNT possessing a continuous iron filling (type C) are stringently required. The high aspect ratio of the filling leads to a geometrically extended magnetic dipole [35, 36].

In the synthesis of in-situ iron-filled CNT as tips for magnetic force microscopy the influence of three parameters was investigated. The first was the role of the temperature profile of the employed furnace, the second the influence of an aluminum interlayer and the third the mass flow of the precursor ferrocene. The influences of other parameters such as temperature and gas flow were investigated in previous works [132, 133]. The conditions that were reported as best were retained in the present experiments. Therefore, the reaction temperatures were set to $T_{\mathrm{reac}} = 800\,^{\circ}\mathrm{C}$ and $T_{\mathrm{reac}} = 830\,^{\circ}\mathrm{C}$, respectively. The reaction temperatures were achieved by placing the substrates on the related positions of the temperature profile of the furnace. An inert gas flow (argon) of 150 sccm was used. The aluminum layers were selected due to reported positive effects on the growth of carbon nanotubes [85]. But also promising results of preliminary testing with multilayer systems consisting of Al and Au were found [87, 133]. The influence of the precursor mass flow will be discussed in the context of the combined growth-mode model in section 2.3.5 on page 71.

2.3.1 Experiments

The employed setup for the SSCVD is presented in fig. 2.15. The setup consisted of an outer quartz tube and two furnaces. The furnace $\boxed{\text{A}}$ was used for the sublimation of the solid precursor powder. In the furnace $\boxed{\text{B}}$ the growth of the CNT took place. The gas was introduced into the furnace by an inlet tube (Inlet in fig. 2.15). The transport gas flow was used to transfer the sublimated precursor into the reaction zone. The exhaust gases were removed through the flue. The gas flows were controlled by mass flow controllers.

The metal-organic compound ferrocene (manufacturer: ACROS, purity: 98%) was purified by sublimation and condensation. The so purified ferrocene was further processed as precursor.

In order to place the quartz boat with the precursor and the substrates at the right position and to prevent the contamination of the outer furnace tube during the synthesis, an additional insertion tube was used. During and after the inner quartz tube was inserted into the furnace the whole system was flushed with argon to remove the air.

The powder-like precursor was placed into a quartz boat, equipped with two magnetic skids that were fixed to it using a thermally stable glue. Thus, it was possible to move the quartz boat inside the closed furnace from the outside with a strong permanent magnet. This was necessary for two reasons. In the beginning of the process the sublimation furnace $\boxed{\text{A}}$ was heated up to its nominal value at position C (fig. 2.15). To avoid a sublimation of the precursor before the synthesis process the quartz boat was placed in a cold region (position A in fig. 2.15) outside of the gas flow. To start the growth process the quartz boat with the precursor was moved to position B (fig. 2.15) as well as the sublimation furnace $\boxed{\text{A}}$. Consequently, the sublimation started at the selected temperature. To stop the growth process, the sublimation furnace $\boxed{\text{A}}$ was switched off and moved back to position C and the quartz boat was moved to position A where it cooled down. The experiments consisted of the following steps:

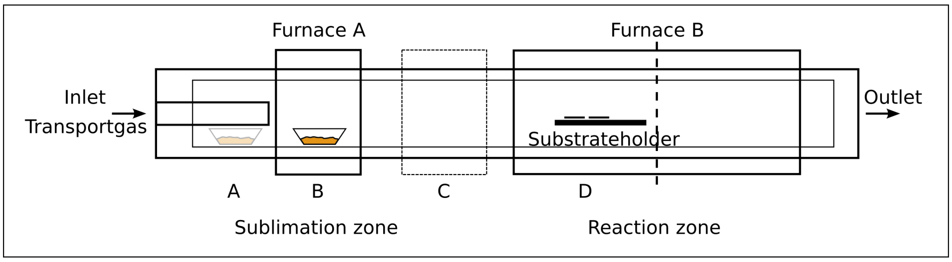

Figure 2.15: The sketch represents the basic elements and experimental steps. The dashed line marks the middle of the furnace. The moveable Furnace A is used for sublimation of the solid precursor. The decomposition of the precursor and the formation of CNT occur in furnace B. The samples are placed on a substrate holder. The quart boat with the precursor can be moved from the outside using a strong permanent magnet. The transport gas is introduced through a inlet steel tube.

- Flushing of the setup with Ar at 300 sccm for 10 min
- Positioning of the substrates in the inner quartz tube
- Filling of the quartz boat with the precursor
- Inserting the inner tube with the quartz boat and the substrates into the setup
- Flushing of the setup with Ar at 500 sccm for 10 min
- Setting the volume flow of the gases (argon and hydrogen)
- Heating of the reaction furnace B up to 870 K and holding for 10 min, treatment of the substrates in a mixture of argon and hydrogen
- Heating up of the sublimation furnace A
- Stopping the hydrogen flow and further heating up of the reaction furnace B to the final reaction temperature
- Reaching the nominal reaction temperature of 950 °C
- Sublimation furnace A is positioned over the precursor - beginning of the process (reaction temperature is hold for 10 min to 30 min)
- End of the process: sublimation furnace A is switched off and moved away from the precursor to position C, in addition the quartz boat with precursor is moved out of the gas flow to position A and cooled.
- Reaction furnace B is switched off and cools slowly down to room temperature ($20\,\frac{\mathrm{K}}{\mathrm{min}}$)
- Taking out of the samples

In fig. 2.16 the temperature of the reaction zone versus time is shown as a scheme. At first, the reaction furnace $\boxed{\text{B}}$ was heated up to a pretreatment temperature of 873 K, which was kept for 10 min (section A in fig. 2.16). During this time period a argon hydrogen gas mixture (50:50 sccm) was applied. At second, the temperature was increased to the set point temperature for the growth process. The temperature was kept constant for 10 or 30 min (section B in fig. 2.16). To finish the process the sublimation was stopped but the reaction temperature was hold for another 10 min (section C in fig. 2.16). In the end the furnace $\boxed{\text{B}}$ was slowly cooled down to room temperature at a cooling rate of about 20 $\frac{\text{K}}{\text{min}}$.

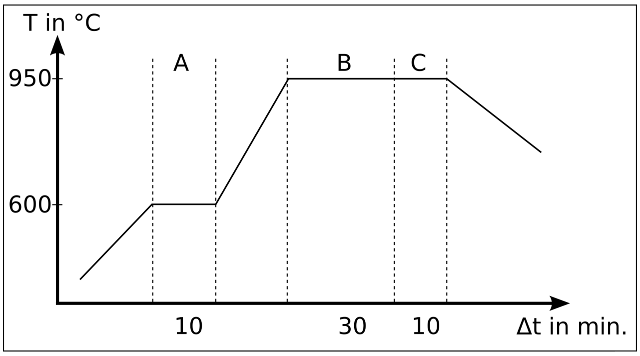

Figure 2.16: Course of time of the set point temperature of the reaction furnace.

The parameters used in the present work are shown in tab. 2.3. However, the optimal parameter values depend on the particular setup. And for each setup the optimal conditions have to be determined individually.

Table 2.3: The table shows the parameters that were used in the conducted experiments.

CVD reactor set point temperature	1223 K
temperature at sample position	1073 K to 1103 K
pressure reactor outlet	1.013×10^5 Pa
ferrocene sublimation temperature	343 K to 403 K
ferrocene mass flow	≈0.5 $\frac{\text{mg}}{\text{min}}$ to 10.0 $\frac{\text{mg}}{\text{min}}$
transport gas volume flow	100 sccm to 300 sccm
process time	3 min to 30 min
cooling rate of the reactor	20 $\frac{\text{K}}{\text{min}}$
substrate position	2 cm to 11 cm

In the following sections the results of the investigations on the influence of the temperature profile, the importance of the substrate and the role of the mass flow are presented. Experiment that combine the investigation of the two last-mentioned parameters were conducted. Each type of substrate was used for different time, substrate temperature and precursor mass flow.

2.3.2 Role of temperature profile

The influence of the temperature profile on the formation of iron-filled CNT can be shown by comparing the effect of two different heating coils whereas all other setup parameters and process conditions are kept constant. The experiments show a significant impact of the particular profile on the formation of iron-filled CNT.

The first heating coil possessed a homogeneous distance between two subsequent windings along the full length. The second heating coil had the same construction but a smaller distance between subsequent windings at the beginning and the end. The profiles were measured inside the furnace with a thermocouple every 10 mm at an argon gas flow of 150 sccm for several given set point temperatures. In fig. 2.17(a) and fig. 2.17(b) the temperature profile T1 of furnace 1 (red) and the profile T2 of furnace 2 (blue) for a set point temperature of 950 °C are shown. Additionally, the sketches at the bottom illustrate the characteristic deposition behavior of carbon and iron structures at the inner surface of the insert quartz tubes according to the temperature profiles T1 and T2, respectively. The dashed vertical lines mark the middle of the heating coils.

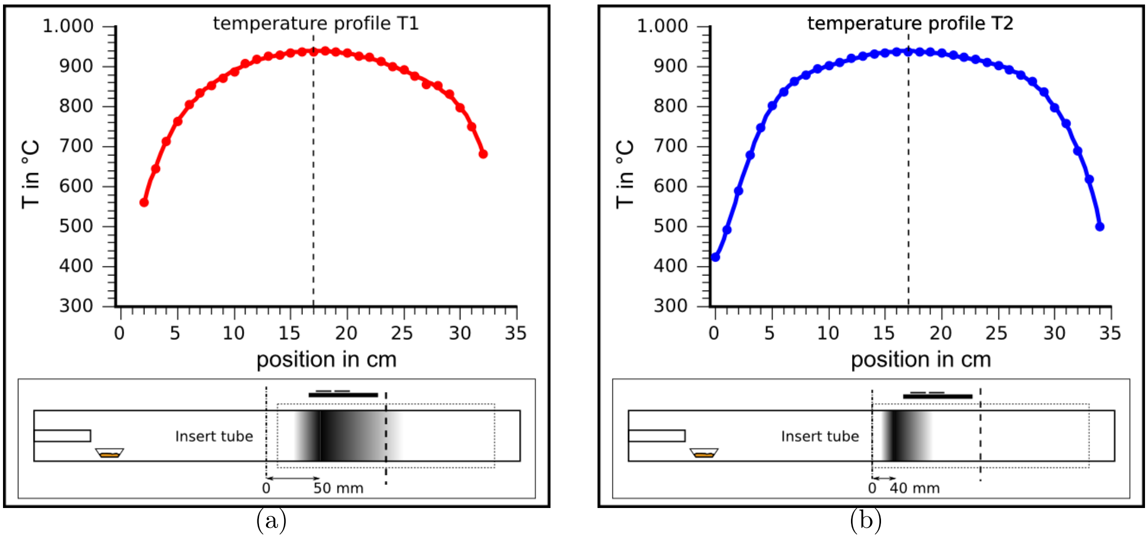

(a) (b)

Figure 2.17: The sketch fig. (a) shows the temperature profile T1 and the typical deposition behavior of carbon and iron structures at the inner wall of the insert tube for the heating coil 1. The sketch fig. (b) shows the temperature profile T2 and typical deposition behavior of carbon and iron structures at the inner wall of the insert tube for the heating coil 2. The positions of the substrate holders are shown for comparison. The dashed lines mark the middle of the heatings. The dashed and dotted lines mark the entrance of the heating. The dashed box represents the position of the heating coil and thus the region of the measured temperature profile.

The dashed and dotted lines mark the entrance of the furnaces which also defines the common reference point for comparison of the results. The dashed boxes indicate the position of the heating areas. The decomposition of the precursor and the deposition of the iron and carbon structures took place in the first half of this area and no deposition was found beyond the middle. The intensity of the black color corresponds to the deposition magnitude.

The temperature profile T1 enabled an *active* area in the range of 40 mm to 170 mm where the precursor decomposition and the subsequent deposition of carbon structures took place. As shown in fig. 2.17(a), the highest deposition intensity was at about 50 mm, whereas high quality CNT were obtained in the area ranging from 60 mm to 70 mm at 800 °C and 830 °C, respectively. An example of iron-filled CNT grown at a sample temperature of 800 °C is shown in fig. 2.18. Typically, the CNT were about 20 µm in length and possessed outer diameter in the range from 30 nm to 120 nm. The filling length varied between short sections of only few nanometers and extended nanowires up to several microns in length.

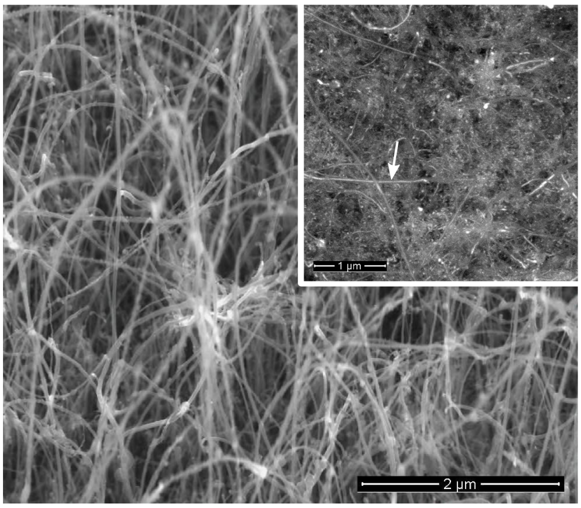

Figure 2.18: Iron-filled CNT grown at a sample temperature of 800 °C employing temperature profile T1. Insert shows the BSED contrast of iron-filling.

Employing the temperature profile T2 resulted in a different deposition behavior, which is schematically shown at the bottom in fig. 2.17(b). In that case, there was only a small region, starting at 40 mm, where the deposition of carbon at the wall was observed and which was only about 20 mm in its extend. However, there was no area at all where high quality CNT have been obtained.

Since reasonable results for the formation of iron-filled CNT were previously reported to grow at 800 °C and 830 °C [28, 29, 58, 133], in most cases the substrates were placed at the corresponding positions of the temperature profiles. However, in order to investigate the morphology of the deposited material when using the profile T2, substrates were placed in the region of the maximum material deposition at the wall at a temperature of 750 °C at 40 mm. In fig. 2.19 some results of the synthesis employing the temperature profile T2 are presented. The first column (fig. 2.19(a) and (c)) shows the results at 750 °C for the substrate and the insert tube wall, respectively. Even though the formation of low quality CNT was observed for this temperature at the reactor wall, no formation of CNT was observed on the substrates at the very same position. Instead, only large amorphous carbon encapsulated iron particles were formed. The second column (fig. 2.19(b) and (d)) gives an impression of the results at 800 °C for the substrate and the insert tube wall, respectively. On this position some CNT were found at the wall fig. 2.19(d). However, almost no CNT were formed on the substrate fig. 2.19(b). At the position of the optimal growth temperature of iron-filled CNT at 830 °C no deposition of carbon structures was observable, when using furnace 2. This indicated, that all sublimated material did decompose and react in a very small area between 700 °C to 800 °C. It was surprising, that the morphology of the carbon structures was that different, since all conditions except the heating were the same. It seems, that the difference in the temperature profile is responsible, which will be discussed in the part below.

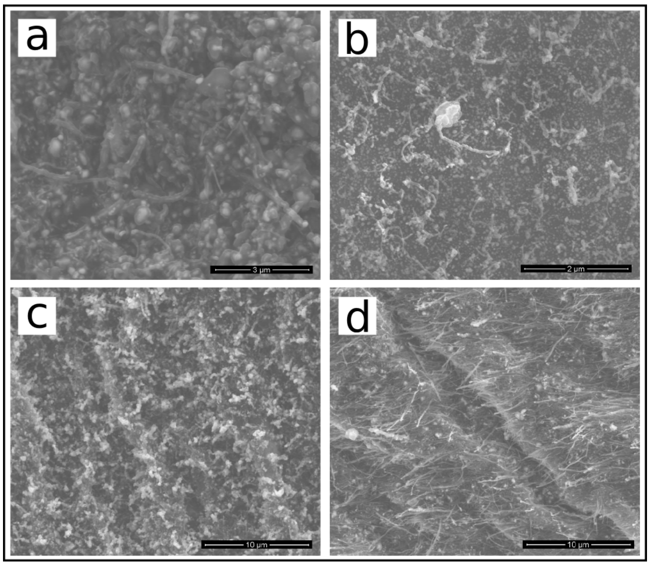

Figure 2.19: Results from the wall of the furnace in comparison with the substrate at the corresponding temperature. Fig. 2.19(a) and fig 2.19(c) show the CNT formation on the substrate and the tube wall at the first temperature of 750 °C. Fig. 2.19(b) and fig. 2.19(d) show the CNT formation on the substrate and the tube wall on the second temperature of 800 °C.

In the synthesis of unfilled CNT the temperature profile is of minor interest. While the decomposition and gas phase reactions of hydrocarbons depend on the local temperature of the profile, the formation of CNT is restricted to the area where the catalyst is localized. Hence, the growth of CNT occurs only at the position of the substrate borne catalyst. The reaction kinetics and quality of the CNT depends on the local temperature but not on the temperature profile. However, in contrast the temperature profile is especially important in the floating catalyst method, since the gas phase contains the catalyst itself. It will be activated as soon as the reaction conditions for any catalyzed reaction are satisfied.

Although the temperature profiles seem similar and result in the same set point temperature (fig. 2.20(a)) the absolute temperature values differ in the beginning and the end by up to 40 °C as shown in fig. 2.20(b). The reason is the deviating winding of the heating coils. While T1 has a lower slope, T2 is designed to have a broader temperature plateau. This differences give evidence, that the conditions at the heating

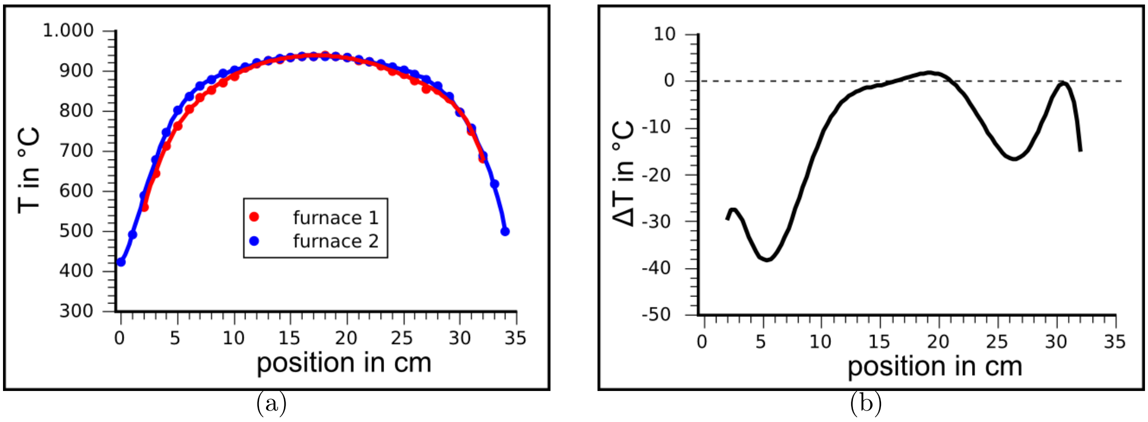

(a) (b)

Figure 2.20: The temperature profiles of two different furnaces 1 (red) and furnace 2 (blue) are shown in fig. (a). The corresponding temperature difference T1 minus T2 is shown in fig. (b).

entrance are decisively for the reaction products because of the reaction kinetics.

The collision model describes the reaction rate r of a bimolecular gas by eq. 2.4.

$$r = Z\,\rho\,[A]\,[B]\,\exp\left(\frac{-E_a}{R\,T}\right) \tag{2.4}$$

Where R is the gas constant, T the absolute temperature and E_a the activation energy for a new bond formation. The concentrations of the two involved species are denoted by $[A]$ and $[B]$. The Boltzmann factor considers the fraction of collisions with more energy than the activation energy where a new bond formation is possible. The collision frequency of the two species A and B is denoted by Z and ρ is the steric factor, which takes into account, that only a fraction of collisions with sufficient energy finally result in a new bond formation. The rate constant $k(T)$ can be deduced as given by eq. 2.5.

$$k(T) = Z\,\rho\,\exp\left(\frac{-E_a}{R\,T}\right) \tag{2.5}$$

In the present work ferrocene has been used as precursor for the synthesis of iron-filled CNT. The decomposition of ferrocene is given by eq. 2.6

$$Fe(C_5H_5)_2(g) \rightarrow Fe(s) + C_5H_5^{\bullet}(g) + ... \tag{2.6}$$

according to [57]. However, little is known about the chemical kinetic behavior of the ferrocene decomposition [104]. The studies of Kuwana et al. were primarily interested in the formation of iron catalyst particles [67, 104]. For the formation of carbon nanotubes, the reaction and decomposition behavior of the involved hydrocarbons is also important. In eq. 2.6 a cyclopentadienyl radical is produced which may be combined with a hydrogen atom to form a cyclopentadiene molecule. The crucial step in the reaction behavior of the cyclopentadienyl radical is the so called ring opening [134]. Mainly acetylene, ethylene and methane but also benzene were found as decomposition products [134].

Thus, in reality the complex synthesis process involves more than just two species and results in a complex reaction model with different reaction constants for each pair of species. The reaction rates for each pair are coupled via the concentration of the particular species and depend on each other.

In fig. 2.21(a) and fig. 2.21(b) the processes and reactions between the molecules that take place in the first part of the temperature profiles of the two employed furnaces are shown. The following assumptions are encountered. The same setup for both temperature profiles is used, as well as the same amount of carrier gas. Therefore, the gas flow velocity is constant and consequently there is the same retention period of a particular volume element in a certain area. The only difference between the

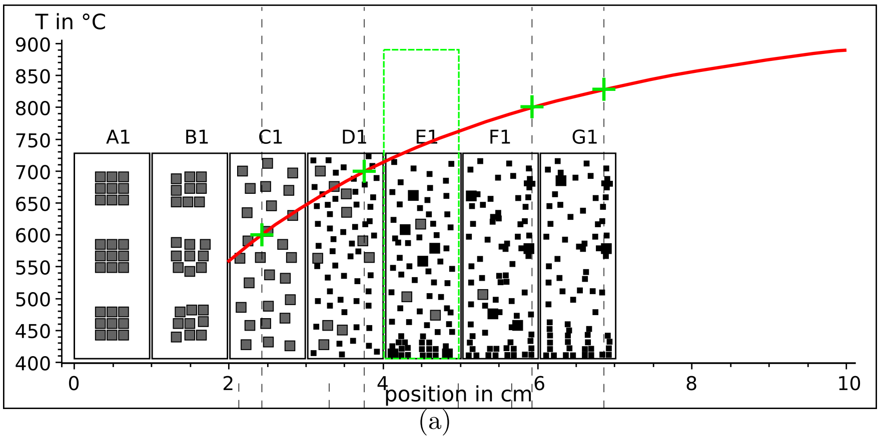

(a)

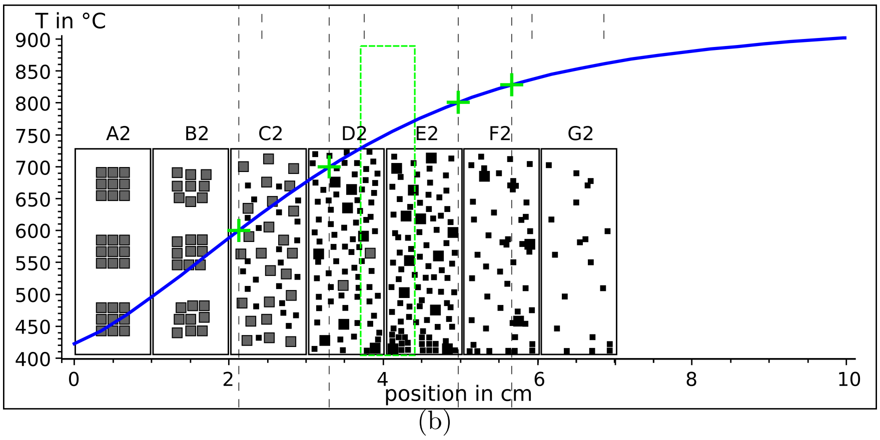

(b)

Figure 2.21: In fig. (a) part of the profile T1 of furnace 1 and in fig. (b) part of the profile T2 of the furnace 2 is shown. The black boxes represent the control volumes labeled from A to G. The light grey boxes illustrate the sublimated ferrocene. The small black squares symbolize different kinds of reactants and products. The large black squares stand for larger structures formed during the process. The green dashed box marks the area with the highest deposition rate of amorphous carbon structures.

setups is the spatial distance between points of equivalent temperatures. In order to compare the experimental results, the reactor volume is divided into segments with an identical control volume size, which run from A to G. In each volume the processes are interpreted by classical collision theory with the reaction constant and Boltzmann factor and consequently the reaction rates as functions of the local temperature per volume. The sublimated ferrocene molecules in the gas phase are represented by light grey boxes. The small black squares symbolize different kinds of reactants and products that can result from the ferrocene decomposition and reaction of fragments. The large black squares stand for larger structures that are formed by reactions of smaller molecules. It is assumed, that the products of the previous volume determine the reactants for the subsequent volume. Due to the deposition of material at the furnace wall or substrate surface the mass flow decreases.

Since an identical size of the volume elements has been chosen, different concentrations of particular species and chemical processes can be expected when comparing two volumes with the same label letter as illustrated in fig. 2.21(a) and fig. 2.21(b). At temperatures below 500 °C ferrocene is stable. The decomposition is initiated around 550 °C in a hydrogen containing atmosphere [57, 135]. In the temperature range 500 °C to 600 °C ferrocene gets activated and the decomposition starts. At 750 °C the decomposition rate reaches its maximum at the given process conditions. Because of the differences of the temperature profiles the precursor decomposition and subsequent reactions are initiated at different locations in the heating area. The temperature gradient in the decisive section B2 and C2 is higher than in B1 and C1 and hence the decomposition as well as the reaction constant $k(T)$ of the molecules is higher in the particular control segment. As consequence of the decomposition the concentration of reactants increases. Because the reaction rate $r(T)$ is a function of temperature and concentration the variety and output of possible reactants increases. Since both parameters are higher in D2 and E2 in comparison with D1 and E1, all reactions occur at higher rates. It also has to be taken into account that a variety of species result from the ferrocene decomposition. Consequently, there are always pairs of reactants which possess their specific activation energy at the local temperature. In case of furnace 2 the formation and deposition of large amorphous and spherical particles has its highest reaction rate at 750 °C in volume D2 and E2. This results in an effective reduction of the mass flow in the gas phase. The green dashed boxes mark the area with the highest deposition rate of amorphous carbon structures. Due to the high concentration of reactants the majority of material is used up in this particular region below the temperature range of 800 °C to 830 °C which is optimal for the growth of iron-filled CNT. The concentration of material in control volume F2 is lower in comparison to G1 and only very few CNT were found on the substrates. Consequently, no deposition of material is observed in volume G2. In contrast to the conditions in F2, the concentration and hence reaction rate in the control volume F1 in furnace 1 is lower. And in section G1 the concentration of material is suitable for the formation of iron-filled CNT with long and continuous filling since there is sufficient carbon structures and iron.

From that it was concluded, that a too high excess concentration of carbon and iron in close vicinity to the substrates is adverse to the formation of aligned and filled CNT. The experimental results give evidence for the impact of temperature profile on the floating catalyst synthesis of iron- filled CNT. As a result large amorphous spherical iron containing carbon structures were formed which have been frequently observed (fig. 2.19(a)). A higher transport gas flow could be used for dilution and to decrease the concentration. Nevertheless, a lower ascent of the temperature would extend the area of decomposition and thus lower the concentration of the decomposition products. Due to the concentration dependency this is also related to the total amount of precursor in the carrier gas flow, which is discussed in section 2.3.4 on page63. As consequence of the experimental observations, the profile fig. 2.17(a) with the lower temperature gradient is favorable and was selected for further experiments.

2.3.3 Role of the substrate

For all experiments substrates were employed to collect the material for further processing and investigation. Furthermore, substrates with additional iron catalyst material and aluminum interlayers were selected, in order to investigate the influence of this type of layer system on the growth of iron-filled CNT.

The general substrate structure was the same in all experiments and consisted of the following layer sequence starting from the bottom. For the experiments single crystalline silicon wafers with a thin thermal oxide layer of 1 µm were employed. The following layer was made of aluminum, whose thickness was 1 nm, 10 nm or 100 nm. As an additional catalyst a 2 nm thick iron layer was deposited on top. In the first case no closed Al-film could be expected. For the latter two it was anticipated, that a closed Al-film was formed.

The aluminum as well as the iron layer were deposited by electron beam evaporation under high vacuum conditions without interruption. However, the samples were always exposed to air before further processing. It has to be considered that aluminum layers cover them self with a thin natural alumina layer of approximately 1 nm when they are exposed to air.

In order to measure the oxidation state of the aluminum layers, angle-resolved X-ray photoelectron spectroscopy (AR-XPS) measurements at different incident angles were performed. The angle of incidence was measured relative to the normal vector of the substrate surface. Large angles correspond to surface and low angles to bulk measurements, respectively.

The results presented in fig. 2.22 show the XPS spectra of an as prepared 10 nm thick aluminum layer with 2 nm Fe on top. The colors correspond to the incident angle that was measured relative to the normal vector of the substrate surface. The carbon (a) and oxygen (b) peaks resulted from the cleaning process of the substrate with ethanol and from absorbances from the atmosphere. The Al layer (c) showed a metallic behavior at all incident angles. The signal maximum and curve shape of iron oxide is shown in fig. 2.22 (d). For the as prepared samples the absence of an alumina peak was observed. This confirmed, that the as-prepared aluminum layer was not oxidized. The aluminum was in the metallic state fig. 2.22 (c). As the presence of a thin aluminum oxide layer was expected, the 2 nm iron layer may have acted as a passivation layer.

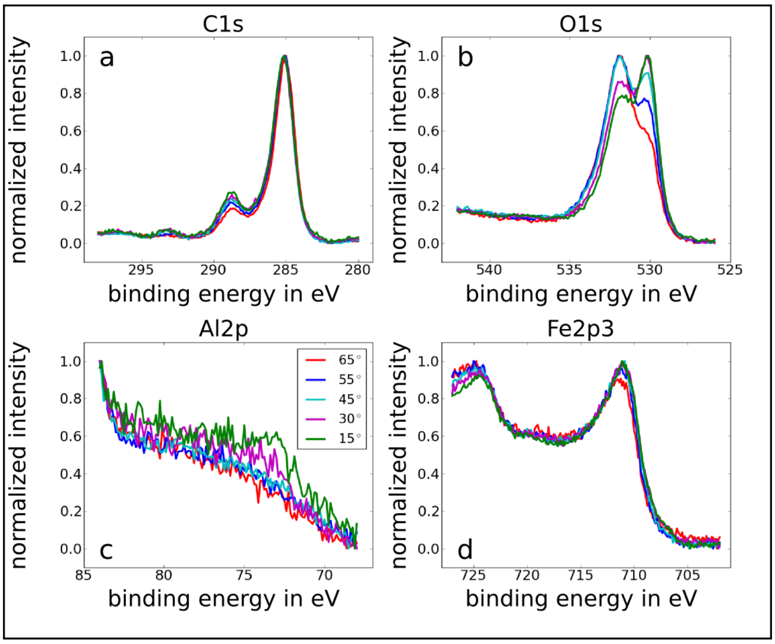

Figure 2.22: XPS spectra of an as prepared substrate with 10 nm thick Al layer.

In fig. 2.23 the XPS spectra of the same sample after a thermal treatment in an argon and hydrogen containing atmosphere at 800 °C for 10 min are presented. The gas atmosphere during the process was the same like during CNT synthesis, however no carbon source was involved. It can be seen that the oxygen peak (b) at 530 eV vanished. It was anticipated, that this was a consequence of the reduction of oxygen containing carbon species. Furthermore, a peak for alumina was formed during the thermal treatment. The metallic signal of the Al layer vanished and instead an alumina signal (c) was found. The signal (d) could be attributed again to iron oxide. Despite the reducing hydrogen containing gas atmosphere iron oxide was formed. However, the state of iron at 800 °C could not be determined by this examination. The oxygen spectrum in fig. 2.23 (b) showed no angle dependent variation of the signal shape after the thermal treatment. Within the penetration depth of the XPS method no evidence

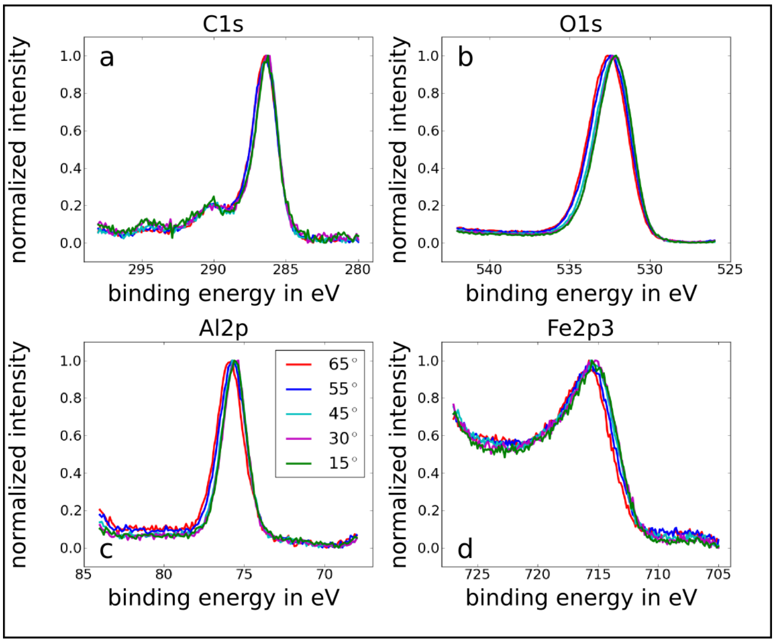

Figure 2.23: Substrate after thermal treatment at 800 °C in an argon atmosphere.

of a layer system could be found anymore. It was anticipated that the layer system was destroyed by the thermal treatment and the aluminum layer melted. Instead a mixture of small alumina and iron oxide volume elements may have formed possessing homogeneous properties.

There were two possible oxygen sources for the oxidation of the aluminum layers during the heating process. Part of the oxygen could have originated from the iron oxide and did diffuse into the aluminum at higher temperatures. The second source may have had its origin in the oxygen that was contained in the argon gas itself.

The aluminum interlayers were introduced to enhance the growth of highly vertically aligned CNT [84–86]. In order to investigate the influence of the interlayer thickness on the growth of in-situ iron-filled CNT, substrates with 1, 10 and 100 nm of aluminum were employed. Since the formation of in-situ filled CNT also depends on the precursor mass flow each type of substrate was used in experiments with different preheater temperatures (70, 100 and 130 °C). The influence of the precursor mass flow will be discussed in the following section 2.3.4 on page 63.

In fig. 2.24 samples produced at the same process conditions especially the same sublimation temperature of 70 °C but employing different substrates are shown. Each column represents a different thickness of the aluminum interlayer with 1, 10 and 100 nm, respectively. The samples were at different positions in the furnace but grown during the same experiment. In the first row the samples were produced at $T_{reac} = 800\,°C$. The samples in the second row were grown at $T_{reac} = 830\,°C$. The total reaction time was 30 min. As visible in fig. 2.24 iron-filled CNT were formed on all substrate types. However, the best results were obtained on a 10 nm thick Al interlayer. Also on 1 nm at 800 °C and 100 nm at 830 °C a certain amount of aligned CNT grew. However, they

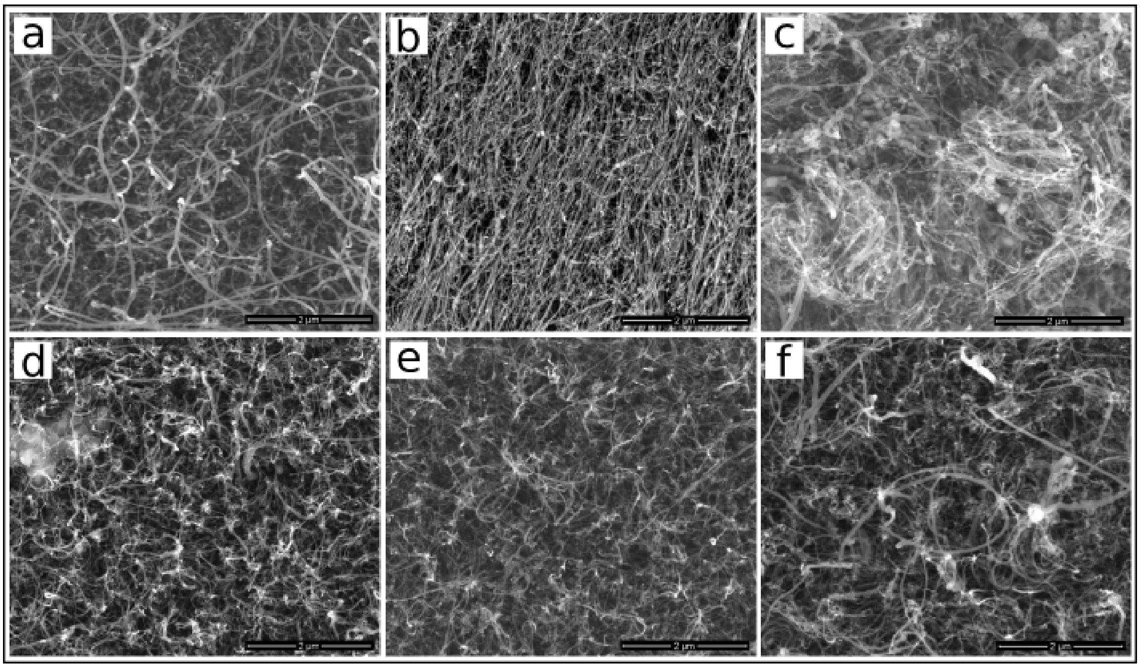

Figure 2.24: Samples produced at T_{reac} = 800 °C (a-c) and T_{reac} = 830 °C (d-f), Al-interlayer of 1 nm (a,d), 10 nm (b,e) and 100 nm (c,f). Sublimation temperature of 70 °C. The scale bar is 2 µm.

were of minor quality in comparison to the CNT grown on 10 nm aluminum layers independent of the temperature.

In fig. 2.25 the results for a sublimation temperature of 100 °C and a process time of 10 min are shown. All other process parameters were identical to the previously described experiment. Aligned iron-filled CNT grew on both 10 nm and 100 nm thick Al interlayers. However, the quality of CNT grown on the former were of better quality. On 1 nm aluminum layers only CNT of poor quality were formed.

In fig. 2.26 on page 63 the results for a sublimation temperature of 130 °C and a process time of 10 min are shown. All other process parameters were identical to the other two experiments. The formation of long and aligned iron-filled CNT was only obtained on 10 nm thick Al interlayers. In the two other cases the formation of amorphous structures and poorly shaped CNT dominated.

It has been reported [84–86], that aluminum layers enhance the formation of vertically aligned CNT. Iron as catalyst on alumina layers gave good yield of CNT and it was stated, that especially the catalyst particle size was stabilized by the interaction between the alumina and iron. It was also found that the thickness of the aluminum layers plays a role. The results gave evidence for the influence of the interlayer on the formation of the carbon structures. In the present work, the effect of the interlayer on the formation of in-situ iron-filled CNT was only indirectly regarded by evaluating the morphology of the CNT.

Depending on the thickness of the interlayer the results of the grown carbon structure

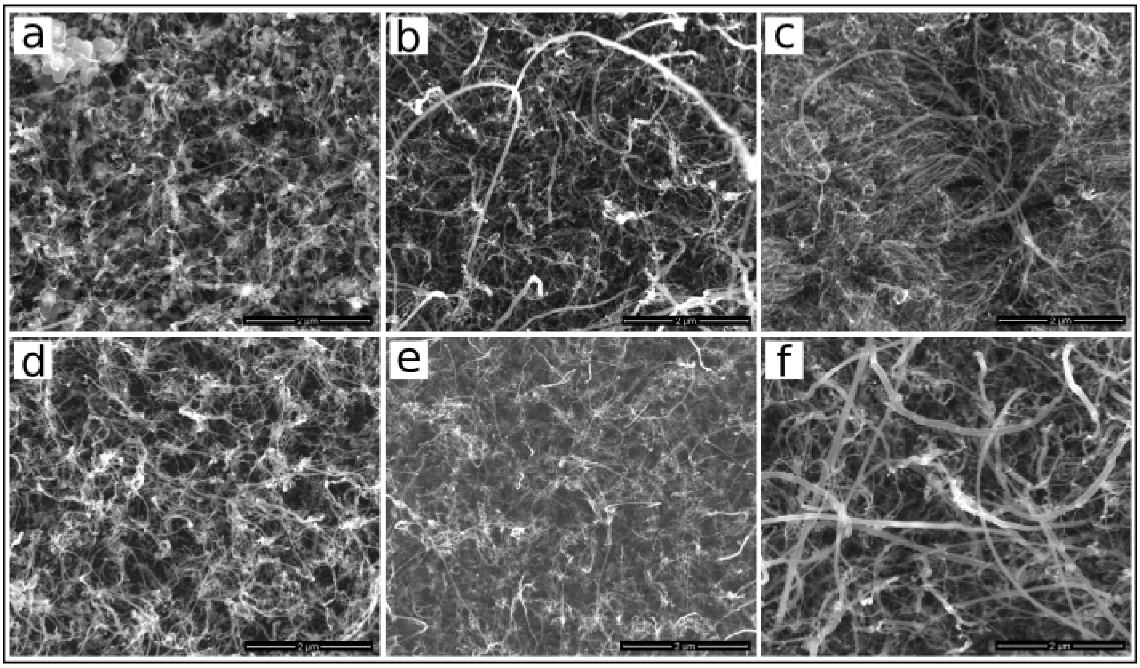

Figure 2.25: Samples produced at $T_{reac} = 800\,°C$ (a-c) and $T_{reac} = 830\,°C$ (d-f), Al-interlayer of 1 nm (a,d), 10 nm (b,e) and 100 nm (c,f). Sublimation temperature of 100 °C. The scale bar is 2 µm.

showed different morphologies. Almost no CNT formation was observed for 1 nm thick Al layers as can be seen in fig. 2.25(a),(d) and fig. 2.26(a),(d). Only for a longer reaction time and a low precursor sublimation temperature a significant amount of CNT was formed fig. 2.24(a),(d). It is likely, that such thin layers were not closed or partly vaporized during the CNT synthesis. The formation of amorphous structures suggested that these thin layers did not prevent the formation of larger metal catalyst islands on the substrate. These results showed, that the 1 nm Al interlayer did not enhance the formation of aligned in-situ iron-filled CNT. The results were comparable to the growth of iron-filled CNT on silicon substrates [136].

For 100 nm Al interlayer different results were observed and in fig. 2.24 (f) and fig. 2.25 (f) aligned CNT are shown. For other process conditions no CNT but rather amorphous carbon and iron containing structures were formed, as shown in fig. 2.26 (c) and (f). Since the melting temperature of aluminum is about 600 °C, one reason might have been the melting of the relatively thick layer due to the reaction temperature of about 800 °C. Thus, the formation process of highly crystalline CNT was disturbed and the CNT were of lower quality. Also on these substrates a relatively hight amount of amorphous structures was formed. As the XPS measurements showed, aluminum did convert into alumina during the heat treatment. However, since the XPS is a very surface sensitive method, investigations of the deeper bulk were not possible.

The best results were obtained on 10 nm thick aluminum layers, as can be seen in fig. 2.24(b),(e), fig. 2.25(b),(e) and fig. 2.26(b),(e). These layers were stable under

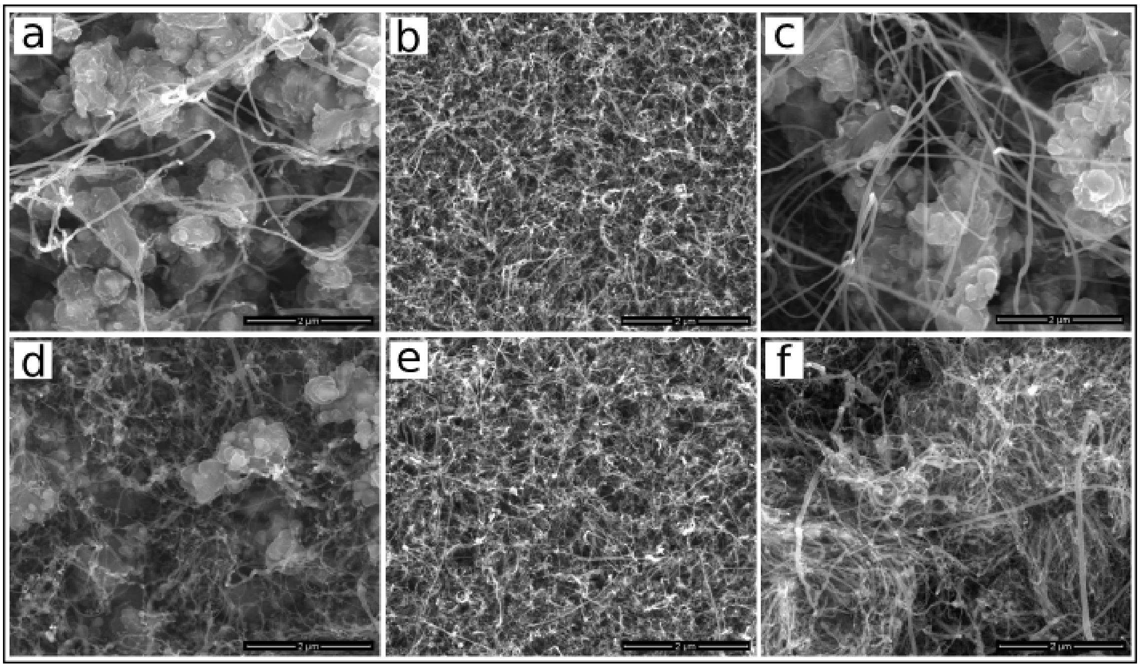

Figure 2.26: Samples produced at $T_{reac} = 800\,°C$ (a-c) and $T_{reac} = 830\,°C$ (d-f), Al-interlayer of 1 nm (a,d), 10 nm (b,e) and 100 nm (c,f). Sublimation temperature of 130 °C. The scale bar is 2 µm.

the given process conditions. Even though XPS could only measure the substrate surface, the complete oxidation during the growth process was likely. The synthesis on these layers showed the best results for all process conditions. It could be concluded, that these layers did support the formation of separated iron catalyst particles and enhanced the growth of aligned iron-filled CNT.

2.3.4 Role of the precursor mass flow

Besides the influence of the interlayer a significant effect of the precursor mass flow was anticipated. In order to investigate its influence the ferrocene precursor was sublimated at different temperatures. The morphology of the resulting CNT was assessed.

The average precursor mass flow was determined by measuring the difference between the initial weight and the weight after the synthesis divided by the sublimation duration. The mass flow was estimated from the Clausius-Clapeyron eq. 2.7.

$$ln\, p_{pre} = -\frac{B}{T} + A \tag{2.7}$$

Whereas B is defined by the enthalpy of sublimation $\frac{\Delta_{sub}H_m}{R}$ devided by the universal gas constant $R = 8.314\,\frac{J}{mol\,K}$. The term A is determined by $\frac{\Delta_{sub}H_m}{R\,T^*}$ were T^* represents the room temperature (298.15 K). The B and A value of ferrocene are 8830.89 K and 29.63 respectively. Their calculation was based on the sublimation enthalpy value of $\Delta_{\mathrm{sub}}\mathrm{H}_{\mathrm{m}} = 73.420\,\frac{\mathrm{kJ}}{\mathrm{mol}}$ [137]. The partial pressure p_{i} of the gaseous precursor is proportional to the mole fraction x_{i}.

$$p_i = x_i\,p = \frac{n_i}{n_i + n_T}\,p \tag{2.8}$$

In this relation n_{i} and n_{T} are the mole of the precursor and the mole of the transport gas (argon) respectively. Assuming an ideal gas the mole flow of the transport gas $\dot{\mathrm{n}}_{\mathrm{T}}$ is

$$\dot{n}_T = \frac{\dot{V}_T}{V_{mol}} \tag{2.9}$$

whereas V_{mol} is the molare volume. After converting eq. 2.8 to n_{i} and inserting eq. 2.9 the mole flow of the precursor can be calculated.

$$\dot{n}_i = \frac{\dot{V}_T}{V_{mol}}\,\frac{p_i}{p - p_i} \tag{2.10}$$

From this relation one obtains the mass flow by multiplying eq. 2.10 with the molare mass of the precursor (ferrocene $0.186\,\frac{\mathrm{kg}}{\mathrm{mol}}$). A comparison of the theoretical estimated and the experimental determined mass flow is shown in fig. 2.27. At temperatures below 363 K the theoretical and experimental values match quite well. For temperatures above the measured values (blue curve) are below the theoretical estimation (red curve).

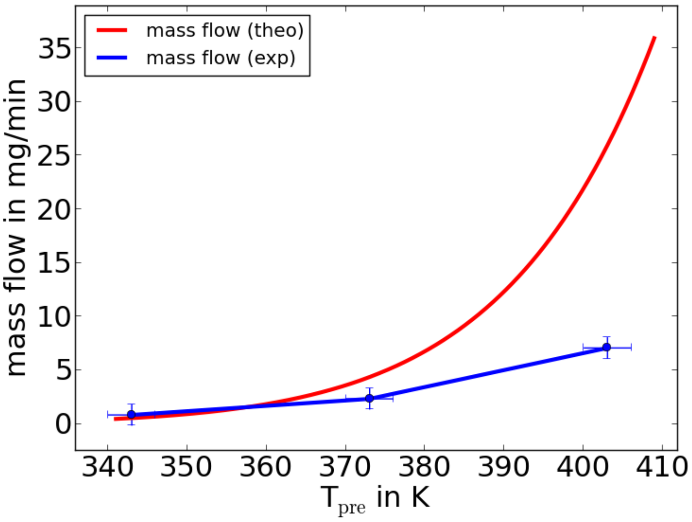

Figure 2.27: The image shows the theoretical estimated (red) and the experimental measured (blue) mass flow as a function of the preheater temperature.

In the following the results concerning the CNT morphology depending on the precursor mass flow are presented. The carrier gas composition and flow, the set point temperature and type of substrates were kept constant.

The sublimation behavior and the resulting mass flow depends on the specific setup used and especially the gas flow conditions [81, 105, 106]. In tab. 2.4 the gas flow, the temperature and the achieved mass flow between literature [133] and the present work are opposed. In both cases a geometrically comparable setup has been used. The experimentally obtained mass flow differs. That illustrates the necessity to determine the mass flow of the metallocene for each setup separately. Parameters such as the employed initial mass and the resulting surface to volume ratio do influence the sublimation behavior. Furthermore, the gas flow behavior above the solid powder does also alter the sublimation behavior. These effects were not studied in the present work in detail. However, it should be mentioned that the used setup might have produced a vacuum above the ferrocene containing quartz boat since the gas entered the furnace through a tube with a diameter of 1 cm. From the volume flow in the tube an average gas velocity of $v = 0.03\,\frac{m}{s}$ could be estimated. This might have been one reason for the higher sublimation rate in the present work in comparison to [133]. In tab. 2.5 the sublimation temperature and the resulting precursor mass flow of the present work are listed. The first column contains the aluminum interlayer thickness of the used substrates.

Table 2.4: Comparison of different sublimation temperatures and resulting ferrocene mass flows.

	literature [133]	present work
carrier gas flow	120 sccm	150 sccm
T in K	$\dot{m}$ in mg/min	$\dot{m}$ in mg/min
343	–	0.84
373	1.8	2.34
403	–	6.78
453	12	–

Table 2.5: The table corresponds to the samples shown in fig. 2.28. The field tabs contain the precursor mass flow in $\frac{mg}{s}$. The first column lists the thickness of the aluminum interlayer.

	$T_{pre} = 70\,°C$	$T_{pre} = 100\,°C$	$T_{pre} = 130\,°C$
Al1	0.012	0.03	0.083
Al10	0.02	0.03	0.09
Al100	0.013	0.05	0.167

In order to determine the influence of the precursor mass flow, the morphology of the filled CNT was investigated. Fig. 2.28 gives an overview about samples grown at the same reaction temperature of $T_{reac} = 800\,°C$ and a carrier gas flow of 150 sccm. The reaction time was 10 min. The arrangement of the sample images is similar to the entries of tab. 2.5. In the first row a substrate with an aluminum interlayer of 1 nm, in the second row 10 nm and in the third row 100 nm were employed. Moreover, the columns represent the results for the precursor sublimation temperatures of 70 °C, 100 °C and 130 °C, respectively. The insets show the corresponding top view of the sample. The samples show a dependency on the interlayer properties as discussed in the previous section (2.3.3). The growth on 1 nm thick interlayer did result in rather short and low quality CNT for a low and medium precursor mass flow of 0.012 $\frac{\text{mg}}{\text{s}}$ and 0.03 $\frac{\text{mg}}{\text{s}}$, respectively. At the highest mass flow of 0.083 $\frac{\text{mg}}{\text{s}}$ mainly amorphous and spherical particles with high diameter were formed. Only few CNT could be found on these samples. The same characteristics were observed for the growth on substrates with a 100 nm thick aluminum interlayer. Also the samples grown on a 10 nm aluminum interlayer showed, that with an increasing sublimation rate and thus increasing precursor mass flow the quality of the CNT diminished. However, the quality of the CNT was better than in comparison to the other two substrate types. With rising precursor mass flow the length of the CNT increased.

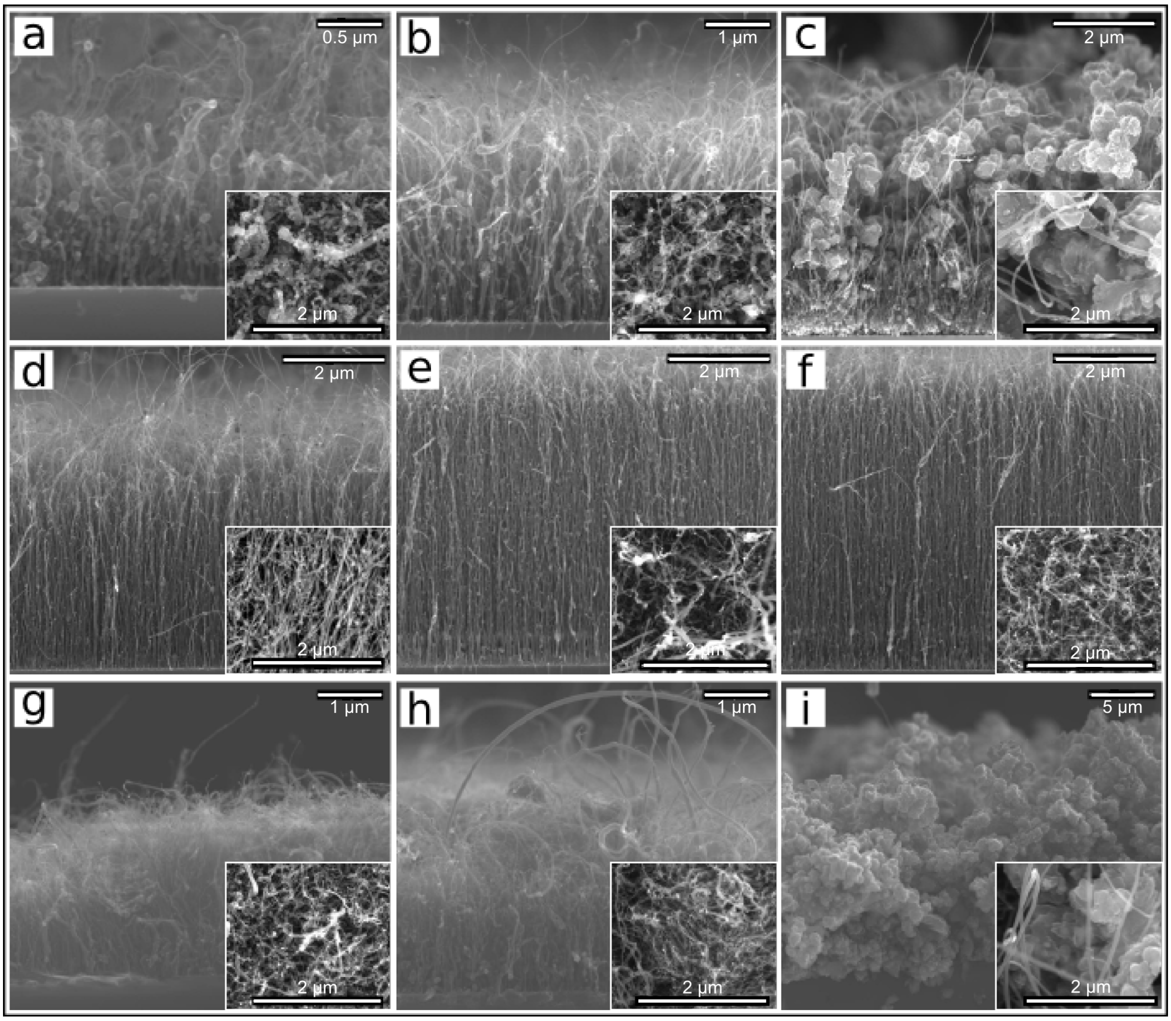

Figure 2.28: Samples produced at different precursor mass flow and aluminum interlayer thickness. Each column represents a different sublimation temperature of 70 °C, 100 °C and 130 °C respectively. Each row represents a different thickness of the aluminum interlayer of 1 nm, 10 nm, and 100 nm respectively. The samples were produced at $T_{\text{reac}} = 800\,^{\circ}\text{C}$. The inset shows the sample from top.

In order to gain further insight into the influence of the precursor mass flow on the morphology of the filled CNT especially the bottom part of the CNT carpet close to the substrate surface was investigated in detail. In fig. 2.29 a sequence of samples grown at a process time of 10 min is shown. The samples showed, that with increasing precursor mass flow the alignment of the CNT was reduced and the defect density increased. To provide a comparison between different samples the following defect density was defined. First, an area of 1×1 µm^2 was selected on each sample. Second, the *line density* of CNT within this area was determined by counting the CNT along the bottom line of the box. This was followed by counting defects within the selected area. At last the number of defects was related to the CNT line density. Only defects that could be resolved by SEM were taken into account. Furthermore, only one obvious defect per CNT was counted. As defects either kinks, spherical sections or branches were considered. The defect density is presented in tab. 2.6. The table shows the results of samples grown at 800 °C on substrates with 10 nm Al and 2 nm Fe, since these parameters corresponded to the best growth conditions.

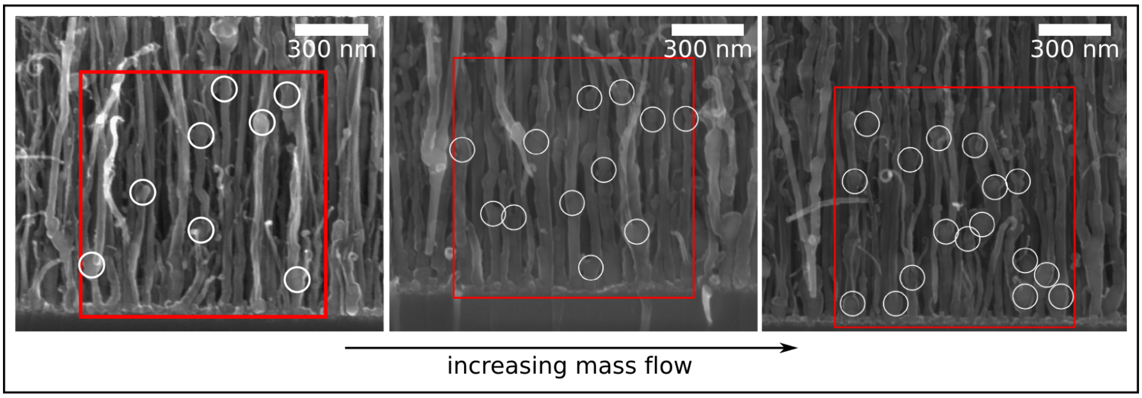

Figure 2.29: The image shows the bottom part of the CNT carpet near to the surface. The red box is equivalent to a 1×1 µm^2. The white circles mark significant defects.

Table 2.6: Comparison of different sublimation temperatures and resulting ferrocene mass flows (comp. fig. 2.29). Furthermore, the CNT density, defect density and the average CNT diameter is given.

sublimation temperature in °C	70	100	130
mass flow in $\frac{\text{mg}}{\text{s}}$	0.02	0.04	0.09
CNT density in 1/µm	18	16	19
defect density	8	12	17
average diameter in nm	55	63	53

In fig. 2.30 another sequence of samples is shown. Besides all synthesis parameters were kept constant, the total growth time was 30 min instead of 10 min. The samples showed, that with increasing precursor mass flow the alignment of the CNT was reduced. The average CNT diameter was slightly higher than in the immediately preceding example (tab. 2.6). Thus, the CNT line density is slightly less. As expected the total length of the CNT was higher. However, the process time did not affect the defect density of the in-situ iron- filled CNT.

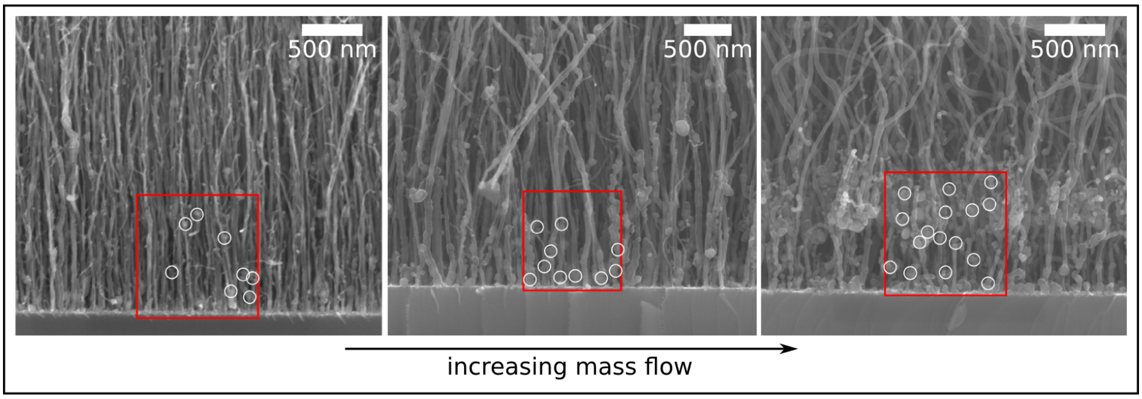

Figure 2.30: The image shows the bottom part of the CNT carpet near to the surface. The red box is equivalent to a 1×1 µm^2. The white circles mark significant defects.

Table 2.7: Comparison of different sublimation temperatures and resulting ferrocene mass flows (comp. fig. 2.30). Furthermore, the CNT density, defect density and the average CNT diameter is given.

sublimation temperature in °C	70	100	130
mass flow in $\frac{mg}{s}$	0.01	0.03	0.1
CNT density in 1/µm	16	12	16
defect density	8	10	16
average diameter in nm	63	83	63

The experimental results revealed an increasing defect density especially at the bottom part of the CNT carpet that could be correlated to the increasing precursor mass flow. The lowest mass flow was still sufficient to form highly iron-filled CNT which was proofed by BSED investigations. However, due to limitations of the setup the sublimation temperature could not be reduced further.

The issue of excess carbon in the initial phase of the CNT formation that occurs close to the substrate surface is shown in fig. 2.31. Large iron containing particles formed and this disturbance of the initial growth phase compromised the formation of aligned and continuously iron filled CNT. After the initial growth phase either the formation of CNT took place or further amorphous structures accumulate, as can be seen in fig. 2.32(c). The first two samples fig. 2.32(a) and (b) were synthesized at low precursor mass flows and the formation of aligned CNT was observed.

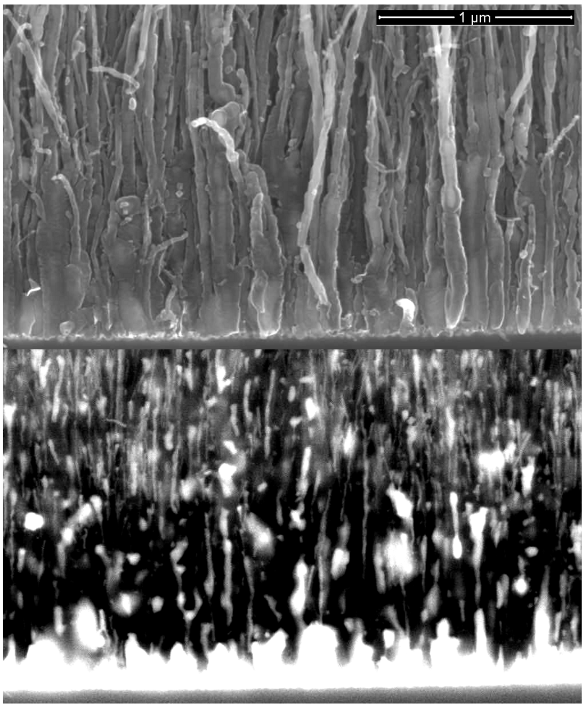

Figure 2.31: Excess iron on the substrate surface led to the formation of large spherical iron containing particles. The lower part of the image shows the atomic number contrast (back scattered electrons).

The effect of the precursor mass flow on the morphology and properties of iron filled CNT should not only be visible in electron microscopy studies. The crystallinity of the carbon shells was therefore also measured by Raman spectroscopy. For example, the crystallinity of the carbon shells of iron filled CNT increases with rising temperature [28, 29, 132, 133]. The influence of the mass flow however is not as straight forward. It is assumed by the author, that a low catalyst concentration in the gas phase is favorable for the growth of CNT. At high concentrations the catalyst tends to disturb the CNT formation process. At a too high concentration no formation of CNT occurs and instead large iron containing amorphous particles are formed which can be seen in fig. 2.32(c). The intensity ratio I_D/I_G between the G-band and D-band increased with an increasing mass flow indicating that for a given temperature the number of defects in the sample did accumulate. The images of the samples illustrate an enhanced formation of amorphous particles with increasing ferrocene mass flow. Still the crystallinity of CNT them self might not be reduced but amorphous structures accumulate on the sample. These defect rich structures intensify the signal of the defect band (D-band).

Besides the effect of the formation process on the carbon shell structure, the morphology and properties of the iron filling should also reveal a dependency on the precursor mass flow. The AGM measurements in fig. 2.33(a) and fig. 2.33(b) on page 71 show the in-plane and perpendicular normalized component of the magnetization, respectively. The data belongs to the same samples which were measured by Raman spectroscopy. An increasing inhomogeneity of the perpendicular and in-plane magnetization has been observed. This was due to the high amount of spherical, isotropic iron particles in the

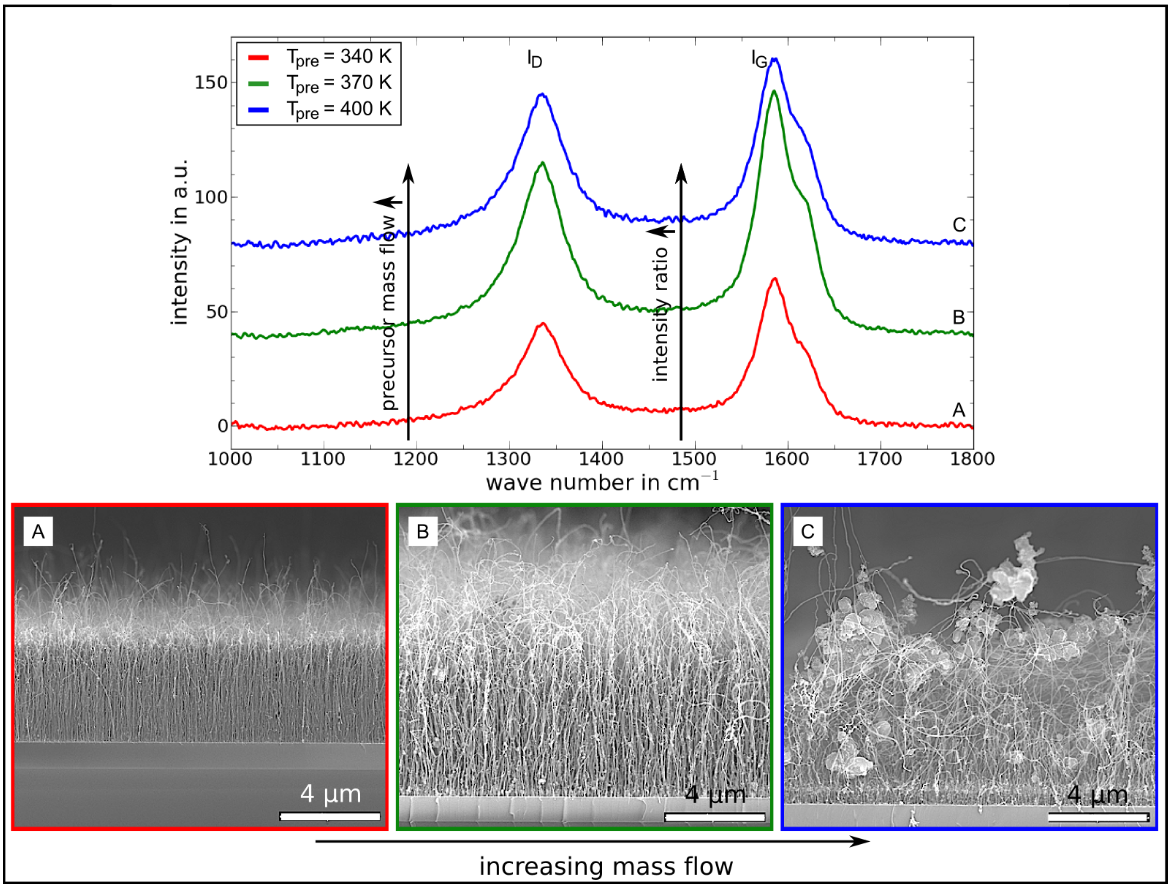

Figure 2.32: The figure shows the Raman spectra of samples grown at different ferrocene mass flows. The red, green and blue spectra correspond to the mass flows of 0.8, 2.3 and 6.7 $\frac{\text{mg}}{\text{min}}$ respectively. The ratios I_D/I_G are 0.69, 0.71 and 0.81.

sample. The AGM measurements indicated the increasing existence of spherical iron particles. The signals related to the magnetic properties of the iron filling show the same tendency that was found by electron microscopy and Raman spectroscopy.

As it turned out the mass flow of ferrocene had an important impact on the quality of both the carbon shell structure as well as the filling. Since both the formation of the carbon shell and the filling occurred at the same time they are strongly interlinked. For the formation of a completely filled CNT the carbon structure and the filling should grow at the same rate.

For discussing the influence of the precursor mass flow the term *effective mass flow* was introduced in order to describe the difference between the *absolute mass flow* that can be measured in the experiment and the mass flow the occurs at the position of the substrate. Unfortunately, the effective mass flow is hardly measurable. It depends inter alia on the actual gas flow behavior in the furnace and the temperature. The mass flow is especially important in the floating catalyst CVD since the catalyst is present at all positions in the reaction furnace. A very high concentration of the precursor in the

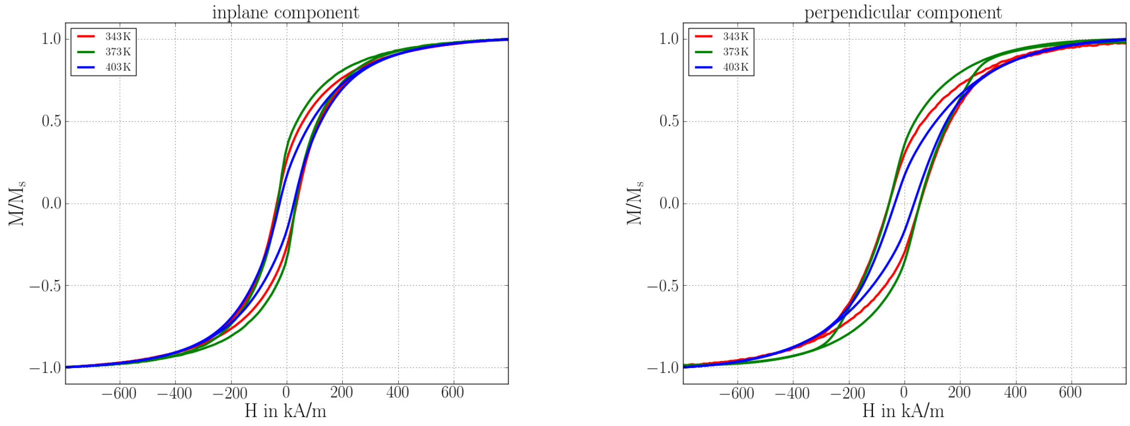

(a)

(b)

Figure 2.33: AGM measurements of samples produced at different ferrocene mass flows. In (a) the normalized in-plane components and in (b) the perpendicular components of the magnetization are shown.

gas phase leads to an increased collision probability of molecules and thus to reactions within the gas phase but also on the substrate. As the experimental results have shown, if the mass flow is to high the formation of CNT is disturbed or even hindered. Of course, if the mass flow is to high depends also on the employed substrates and the reaction temperature. However, the formation of CNT at a high precursor mass flow on suitable substrates (Al 10 nm) at appropriate temperatures (800 °C to 830 °C) showed a higher defect density in comparison to a lower mass flow.

Furthermore, it might be concluded that the defect enriched initial state of the in-situ iron-filled CNT resulted from a depletion of reactive carbon species at the CNT formation site. Even though the carbon to iron ratio in ferrocene (10:1) is preferable for the formation of a continuous filling, the amount of carbon might have been insufficient in the initial state. The depletion effect is further enhanced by the additional iron catalyst layer. Almost no unfilled CNT and amorphous structures were found and BSED contrasts near the substrate CNT interface always reveal a high amount of iron within the structures. Nevertheless, the additional catalyst layer is important for controlling the diameter and its distribution. But slightly more carbon for the initial state seems to be necessary. Thereby it should be possible to prevent the formation of spherical and v-shaped defects of the carbon shell around spherical iron particles.

2.3.5 Discussion of the combined growth mode

In this section the VLS mechanism together with the combined growth mode, as it was suggested by Kunadian et al. [120], will be used to discuss the formation of in-situ iron-filled CNT. Its applicability to the formation of in-situ filled CNT is examined and modifications are supposed that are motivated by experimental observations of the present work. Beyond this the influence of the mass flow will be considered in order to explain the formation of different morphologies of the filling.

For the formation of in-situ iron-filled CNT activation energies were determined to 0.4 eV/atom on bare and 0.5 eV/atom on catalyst supported substrates, respectively [101]. The growth rate as a function of temperature was measured and the data was evaluated by assuming a kinetically controlled behavior, so that the Arrhenius-law was applicable. However, the assumption of a kinetically controlled process should be discussed further. The Arrhenius-law can be applied if there is a *reservoir* of reagents and the reaction rate does only depend on the temperature. In this ideal case the reagents in the reservoir do not interact with each other but solely into the desired products at a temperature given rate. However, this can not be assumed in the case of the synthesis of filled CNT on the basis of ferrocene. The ferrocene starts to decompose at temperatures (≈700 °C) that are far below the temperature that is necessary for the formation of filled CNT (800 °C) by thermal CVD. The decomposition fragments do interact with each other forming new structures at the given temperature. That means, if the temperature and thus the kinetics for the formation of CNT is not high enough different structures will be formed. Moreover, if the concentration of reagents is very high, these reactions will also disturb the formation of CNT. For that reason prevailing amorphous structures instead of CNT were found at high precursor mass flows. In part, a higher reaction temperature and a lower effective precursor concentration could reduce these unwanted side reactions.

How are the experimental observations related to the growth mechanism of in-situ filled CNT? In advance, it should be stated, that no open tip growth (section 2.2.3 on page 44) is assumed in the present work since it is, in agreement to [115, 123–127], unlikely that under thermal CVD conditions an open tip growth process occurs. The following two possibilities fig. 2.11(A) and (B) (page 45) are available for the formation of CNT with closed tips. If a closed fullerene-like carbon cap forms a closed tip (A) the CNT can not be filled anymore. In contradiction to this in the tip growth mode the catalyst particle is located at the tip of the growing CNT (B). Its exposed surface allows for the decomposition of hydrocarbons which dissolve in the particle and diffuse on the surface or through the volume of the particle. Now, under floating catalyst conditions, it is assumed that besides hydrocarbons also metal catalyst particles get in contact with the particle on the tip. The particles volume can increase and while carbon shells are formed also the catalyst particle grows and elongates. That means a tip-growth mode like behavior is proposed in the present work, where the filling is formed by subsequent addition of filling material to a existing particle at the tip. Furthermore, it is suggested that the filling and the carbon shells have to grow at the same rate in order to get a continuous filling. This proposed mode, that is a particular case of the VLS mechanism should be discussed, whether to explain the observed experimental results and should furthermore be able to predict new experimental results.

A number of different kinds of defects have frequently been observed in the growth of in-situ filled CNT. The most obvious characteristics of the filling is the *discontinuity* of the metal nanowires inside of a CNT. Other observations are *branches* and *v-shaped* defects in the CNT morphology that were found especially close to the substrate but also in the middle and top of CNT structures. Typical examples investigated by SEM and TEM are presented in fig. 2.34. These defects are most likely to occur in floating catalyst methods and especially in the synthesis of filled CNT. In the following the morphological particularities will be explained in the frame of the discussed growth mechanism.

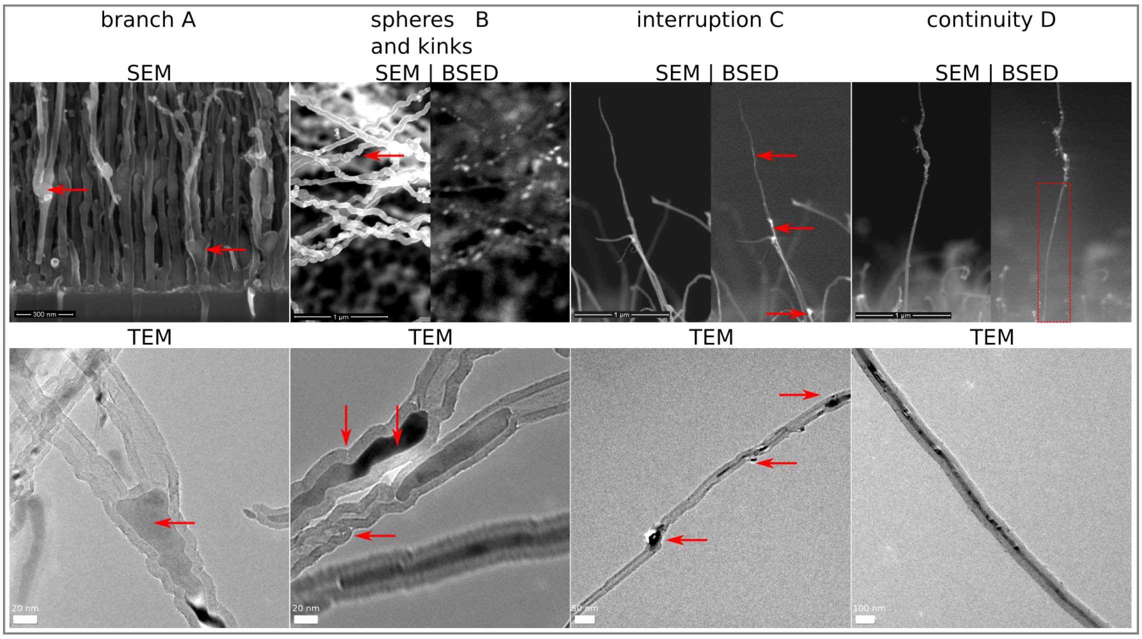

Figure 2.34: The image shows some impressions of typical defects that have been observed. The first row are SEM and the second row TEM images, respectively.[a]

In the very beginning of the formation process, which is also called the nucleation state, the catalytic decomposition of hydrocarbons starts at the catalyst particle surface. Atomic carbon from the decomposition starts to dissolve into the particle and additional metal from the gas phase is added. Therefore the volume of the catalyst particle but also the carbon concentration alters. It is most likely that no stable carbon cap is formed under these conditions. Thus, a base growth mode is not likely. Nevertheless, the particle starts to grow and since the carbon shells are formed the particle elongates as well. The situation is shown in fig. 2.13(D) (section 2.2.4 on page 47). A particle or

---

[a] TEM images private communication with Dr. Christian Müller (IFW)

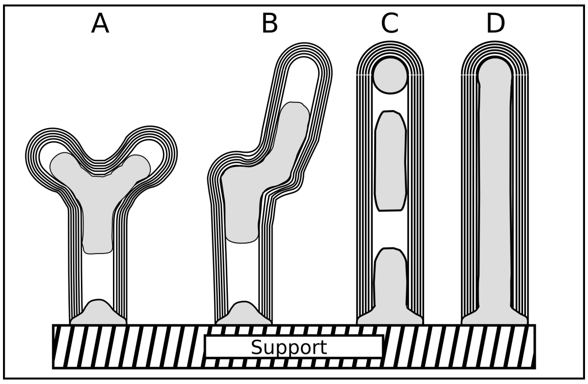

Figure 2.35: Typical morphologies and defects that have been frequently observed are sketched in this image. A) shows the branching of a CNT during growth. B) shows an empty CNT tip and a kink that is directly related to a catalyst particle, however, kinks were also formed without a particle next by. C) shows the most common case, an interruption of the filling and a spherical particle in the tip. D) shows a continuous filling.

the upper part of the existing filling allows for a tip growth mode like behavior. The complexity and diversity of possible reactions during the growth of in-situ filled CNT leads to different kinds of defects. The most frequent defects are illustrated in fig. 2.35. The occurrence of branches fig. 2.35(A) is a consequence of a too high supply rate of catalyst (iron) material at the tip of CNT and either spherical or v-shaped particle form. The upper edges of the v-shaped particle often act as new catalytic active sites and as long as more carbon is added the formation process of CNT can continue. In addition, in-situ transport measurements inside TEM have shown, that branches indeed are often continuous with respect to the filling [138]. That means that no closed cap forms and the new CNT are not added from the gas phase but grow directly from the catalyst particle.

A particle on the tip of a forming CNT, as it is shown in fig. 2.11(B), could also allow for a base growth mode like process. This can lead to the formation of an empty CNT part as it is shown in fig. 2.35(B). Especially the upper parts of CNT show this behavior. Since the particle covers itself with carbon, the growth process stops because no catalytically active particle is available any more. The kink itself fig. 2.35(B) is formed similar to the branch, however only one edge gives rise to further CNT formation.

As the filling is formed, it might happen, that due to surface tension a part of the already existing filling at the top of the CNT departs forming a separated catalyst particle. This particle could either increase in volume due to the further addition of filling material or it just leads to the formation of an empty CNT section. The former would lead to another separated filling section as the middle part of the CNT in fig. 2.35(C) shows. The latter corresponds to the upper part of the CNT in fig. 2.35(C). As the spherical particel indicates, this part is most likely formed by a tip growth mode. It is proposed that interruptions in the filling occur due to separation of smaller fractions from an already existing filling. An indication for the splitting of the filling due to the ratio between the surface and volume energy has been observed in transport measurements [138]. During the transport small fractions separated from longer fillings and formed spheres. However, the empty section might also be formed in a tip growth mode if a small part of the metal nanowire separates from the rest. In that case the formation of the filling can start again, if the supply with metal increases again.

A continuous filling fig. 2.35(D) occurs if the appropriate amount of iron and carbon is available at the CNT forming site. The constant adding of filling material and carbon leads to the formation of a continuous filling. Within the proposed mechanism the growth of the walls and the filling occur at the same rate. Since this is not very likely, a continuous filling depends on optimal process conditions. Excess carbon would lead to empty CNT while excess iron would form large particles that prevent the CNT formation. If there is a sufficient supply rate of metal catalyst material the filling grows at the same rate as the carbon shells. In that case the tip of the CNT is closed by a catalyst particle during the growth process (comp. fig. 2.11(B)). At the end of the process a fullerene-like cap will be formed (comp. fig. 2.35(D)).

From the discussion it is concluded, that the tip growth mode is the dominating mode in the formation of in-situ iron-filled CNT. The growth can switch between base and tip growth mode depending on whether the catalyst particle on top remains anchored to the already existing structure or if a small amount departs. However, that is in contrary to other explanations [101, 120]. In the cited literature the tip growth mode was only discussed as a secondary mode after the growth of the CNT was finished and new CNT were formed on top. Here it is described how the tip growth can explain the typical morphology of filled CNT without assuming the rather unlikely occurrence of an open tip or diffusion of liquid-like particles inside of existing tube on relatively large length scales [65, 139].

Which predictions can be expected from the combined growth mode of the VLS mechanism? The mass flow and resulting supply rate of the filling material is a crucial parameter in the formation of in-situ filled CNT. Different morphologies may be obtained by tuning the carbon to iron ratio. Excess carbon would lead to partially filled CNT. However, kinks and branches can not be ruled out but it was shown, that material that was grown at higher temperatures possessed a higher crystallinity and thus less defects. All discussed defects are strongly correlated to the amount of the metal catalyst (iron) in the gas atmosphere of the reactor. The experimental results suggest, that a high concentration increases the probability of a defect formation. If the mass flow is to high, the volume of the catalyst particle at the tip increases and a spherical or v-shaped defect is formed. If the mass flow is low the particle volume does not increase and only the decomposition of hydrocarbons and the precipitation of carbon as CNT shells occurs. A deficiency of catalytic active metal leads to the formation of unfilled CNT. Only if sufficient metal is added at the same rate as the carbon for the shells a CNT with a continuous filling will be formed.

2.4 Synthesis of iron carbide filled CNT

2.4.1 Experiments

As mentioned in the previous chapter 2.3 CNT can be synthesized by using the liquid source thermal CVD. The employed setup for the aerosol based LSCVD process is presented in fig. 2.36. The setup consisted of three main parts. The first was a self developed external reservoir for the precursor solution ($\boxed{\text{A}}$ in fig. 2.36). The second part was the nebulizer nozzle. The feeding of the nebulizer nozzle (Meinhardt) with the precursor solution was controlled by a valve (E in fig. 2.36). The third part was the quartz tube reactor with the furnace.

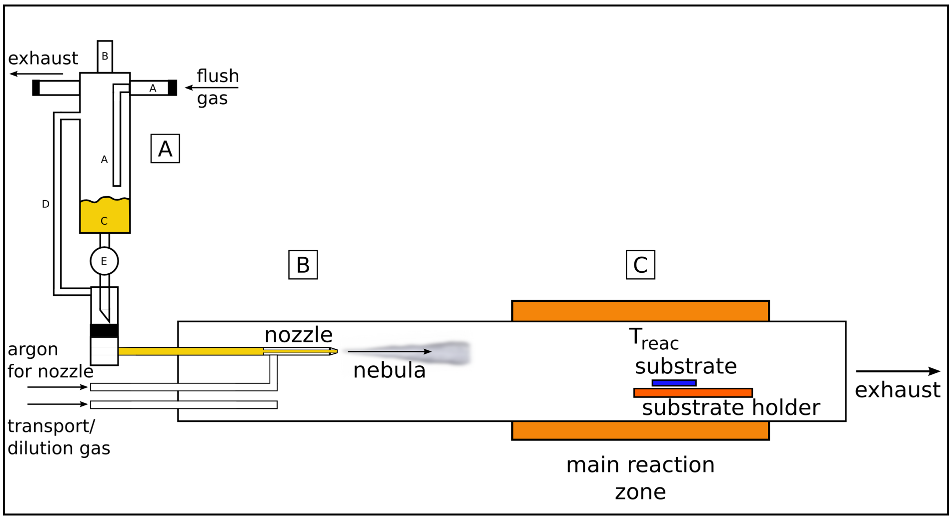

Figure 2.36: The setup for the aerosol based thermal CVD consists of a reservoir $\boxed{\text{A}}$, a nebulizer nozzle $\boxed{\text{B}}$ and the reaction furnace $\boxed{\text{C}}$. The reservoir can be flushed with an inert gas (A). The precursor liquid is introduced into the reservoir through the grind (B) and stored in the reservoir (C). (D) denotes the pressure compensation tube. For the reaction process the liquid flows through the valve (E) into the feeding tube of the nebulizer.

The LSCVD synthesis of iron carbide filled CNT was carried out at atmospheric pressure. For the growth of CNT, silicon substrates with 1 µm of thermal silicon oxide covered with 10 nm of aluminum [85] and 0.5 nm of iron as catalyst on top were employed.

The following steps were performed during an experiment. First, the precursor solution was prepared by dissolving 60 mg ferrocene in 1 ml 1,2-dichlorobenzene ($C_6H_4Cl_2$) [30]. Second, the precursor solution was stored in the reservoir and the setup was flushed with argon. The argon entered the setup through the inlet (A). Afterwards the argon flowed through the flue (exhaust) and the pressure compensation tube (D). The nozzle was flushed with argon as well. After the flushing step the furnace was heated and as it has reached the set point temperature the valve (E) was opened. A fast Ar gas flow (see fig. 2.36) generated a vacuum at the tip of the nozzle and the solution was sucked into the feeding tube of the nebulizer. The pressure compensation tube (D) prevented the formation of a lower vacuum in the reservoir than at the nozzle tip. The nozzle was operated with an argon gas flow of 300 sccm and generated a fine nebula of the precursor solution. In order to dilute the nebula and ensuring an efficient transfer of the precursor into the reaction zone, an additional gas mixture was added (see fig. 2.36). An additional gas flow of 300 sccm hydrogen and 400 sccm argon was fed into the oven, respectively. The average gas velocity in the furnace depends on the cross section. For a given volume flow ($\dot{\mathrm{V}}_{\mathrm{gas}}$) and cross section ($\mathrm{A}_{\mathrm{furn}}$) the velocity $\mathrm{v}_{\mathrm{gas}}$ can be calculated

$$v_{gas} = \frac{\dot{V}_{gas}}{A_{furn}} \tag{2.11}$$

From $\mathrm{v}_{\mathrm{gas}}$ the average retention period of a gas volume in a certain region of the furnace can be calculated. With an inner furnace diameter of 3.4 cm and a total gas flow of 1000 sccm, the average gas velocity amounts to $94\,\frac{\mathrm{cm}}{\mathrm{min}}$ at room temperature. Therefore the average retention period of a gas volume of $1.0\,\mathrm{cm}^3$ in a section of$\approx$0.1 cm in length was $\approx$0.07 s. For the CNT growth, the oven temperature was set to 830 °C for a reaction time of 10 min. In order to stop the growth process the valve (E) was closed and the nebula generation was finished by interrupting the argon gas supply. At the end the furnace was slowly cooled down to room temperature.

2.4.2 Results and discussion

After the synthesis the morphology of the CNT shells and the magnetic properties of the filling of single CNT were investigated.

2.4.2.1 Structure and synthesis

The CVD synthesis according to the preparation method and parameters described above resulted in multi-walled CNT films on substrates as well as the inner furnace wall. The iron carbide filled CNT were investigated using a 300 kV transmission electron microscope[2]. In order to prepare samples for TEM studies, as-grown CNT were dispersed and thoroughly sonicated in acetone. This dispersion was dropped on a potassium bromide single crystal and the resulting hydrophobic nanotube film was floated off by distilled water and collected on a standard copper TEM grid. Additionally, small parts of the substrate with the as-grown material were placed vertically into a special TEM holder. Furthermore, electron backscattered diffraction (EBSD) measurements

---

[2] TEM, FEI Tecnai F30

were performed in a scanning electron microscope[3] equipped with a HKL Channel 5 detector.

A high fraction of the CNT contained single crystal iron carbide nanowires (fig. 2.37). However, for a vast and statistically validated study the amount of material was too little. The outer diameter of the nanotubes ranged from 20 nm to 60 nm. The average values of the carbon shell thickness 5 ± 2 nm were smaller than values reported for iron-filled CNT [28, 29]. SEM studies revealed a typical CNT length in the range of 10 µm to 40 µm and continuous iron carbide fillings of several hundred nanometers length. Smaller iron carbide particles inside CNT were previously reported [140–143]. In fig. 2.38, a high resolution TEM micrograph of a CNT section with an iron carbide filling is presented. The inset shows the Fourier transform of the partial image of the filling, revealing lattice parameters corresponding to Fe_3C. This was observed for more than 90 percent of the filled CNT investigated in this particular study. Complementary EBSD measurements confirmed the tube filling to be Fe_3C. Larger spherical particles were identified as α-Fe, as visible in fig. 2.37. Furthermore it was found, that the [010] axis of Fe_3C was generally aligned parallel to the nanotube axis leaving the [001] axis to point perpendicular to the nanotube axis.

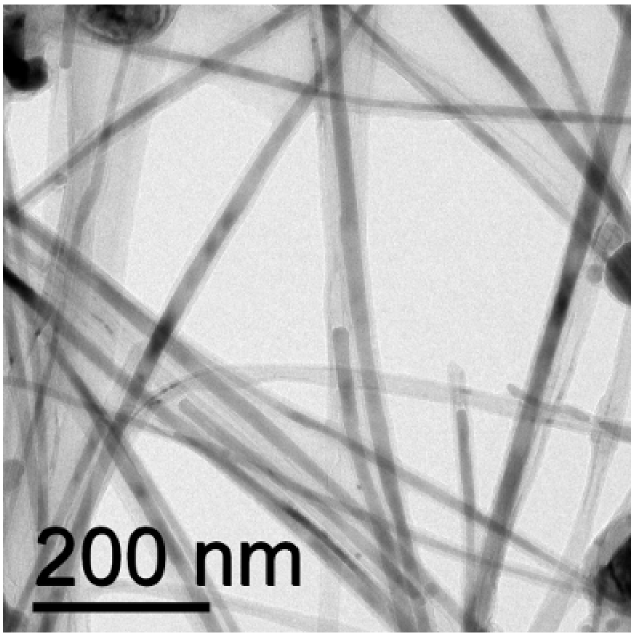

Figure 2.37: TEM image of iron carbide filled CNT. The typical outer diameter is 35 nm. Iron containing particles are visible.

A possible explanation for the preferred orientation of the iron carbide filling is the interaction between the carbon shells and the filling. The shell puts a pressure on the filling [61, 65] inducing a stress. If the elastic modulus E_b of the anisotropic orthorhombic system is larger than E_a and E_c the crystal might orient itself to minimize the stress.

---

[3] LEO 1530 FEG

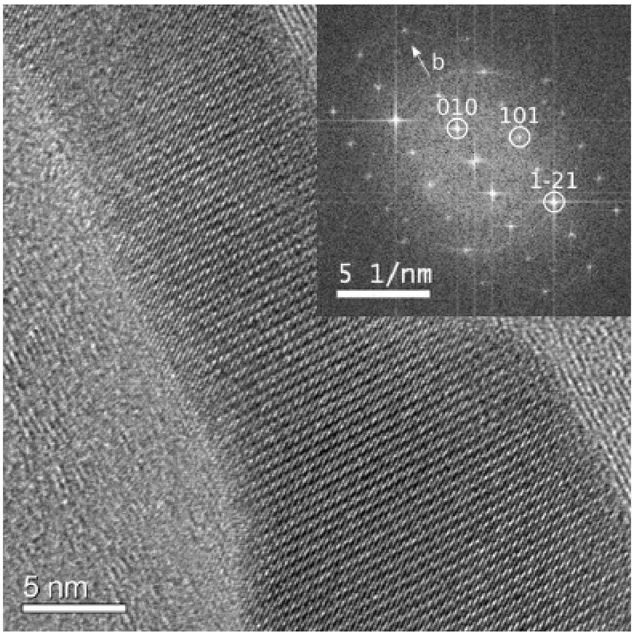

Figure 2.38: High resolution TEM image of a CNT showing the crystal structure of the filling. The inset shows the respective Fourier transform corresponding to Fe_3C.

The synthesis of iron-filled CNT based on solid powder ferrocene was previously reported 2.3. In most cases a dominating $\alpha-$Fe phase of the filling was found [28, 58]. Using iron as the catalyst, a metastable iron carbide can be formed as intermediate phase during the growth of carbon nanotubes. The role of iron carbide during the CNT formation was, e.g., investigated and discussed by Schaper et al. [141], who observed the segregation of graphene layers out of iron carbide by in-situ TEM measurements at 875 °C. The metastability of iron carbide is associated with its positive enthalpy of formation. Calculations by Shein et al. [144] and experiments by Meschel et al. [145] yield values of $21.2\,\frac{\mathrm{kJ}}{\mathrm{mol}}$ and $4.7\,\frac{\mathrm{kJ}}{\mathrm{mol}}$, respectively. The thermodynamic instability implies that the formation is only possible in a non-equilibrium process. In order to stabilize the iron carbide phase the presence of other Fe phases [146] or inclusion in confining structures such as multi-walled carbon nanotubes [142] are required.

In the experiments performed in the present study, ferrocene was dissolved in an organic 1,2-dichlorobenzene solvent. An increase of the concentration of reactive carbon species for the formation of CNT in contrast to experiments using solely ferrocene as a precursor was anticipated [28]. Wang et al. [30] and the present study used comparable precursor solutions. However, the major phase of the CNT filling differs. In contrast to the Fe_3C found in this work, Wang et al. reported $\alpha-$Fe and $\gamma-$Fe filling. The different results may partly be explained by the difference in which the precursor solution was brought into the reactor. In the present work, the solution was directly sprayed into the reaction zone, whereas Wang et al. fed the precursor solution into a preheater zone where it was evaporated. This and other differences of the experimental setup might led to the observed differences in the obtained products.

The basic chemical reaction of ferrocene and 1,2-dichlorobenzene in the presence of hydrogen during the growth process is given in eq. 2.12. However, the equation is not stoichiometrically balanced. The presence of hydrogen promotes the decomposition of ferrocene [57] and also the formation of benzene and hydrogen chloride (HCl) from 1,2-dichlorobenzene.

$$\begin{aligned} 2\,\mathrm{Fe(C_5H_5)_2} + 4\,\mathrm{C_6H_4Cl_2} + \mathrm{H_2} \xrightarrow{T=800\,^{\circ}\mathrm{C}} 2\,\mathrm{Fe} + 3\,\mathrm{Cl_2} + \mathrm{n}\,C \quad &+ \quad \mathrm{m\,C}_k\mathrm{H}_l + \mathrm{C_6H_6} \\ &+ \quad 2\,\mathrm{HCl} \end{aligned} \tag{2.12}$$

The formation of hydrogen chloride was experimentally confirmed by measuring the pH-value of the exhaust gas. Below $T_{\mathrm{reac}} = 430\,^{\circ}\mathrm{C}$ no change in the color of the unitest paper has been observed. Above this temperature the unitest paper turned dark red, indicating the formation of gaseous HCl. The reactions of iron and chlorine can be described by the following equations fig. 2.13.

$$\begin{aligned} 2\,\mathrm{Fe} + 3\,\mathrm{Cl_2} \quad &\rightarrow \quad 2\,\mathrm{FeCl_3} \\ 2\,\mathrm{FeCl_3} \quad &\xrightarrow{T>220\,^{\circ}\mathrm{C}} \quad \mathrm{Fe_2Cl_6} \\ \mathrm{Fe_2Cl_6} \quad &\xrightarrow{T>750\,^{\circ}\mathrm{C}} \quad 2\,\mathrm{FeCl_2} + \mathrm{Cl_2} \end{aligned} \tag{2.13}$$

whereas an iron-chloride dimer forms (second row in eq. 2.13) which easily sublimates at the given temperature range of 800 °C to 850 °C. These reactions reduced the amount of iron for the formation of iron-filled CNT and it is likely that smaller catalyst particles were formed. Which in its turn led to the formation of thinner CNT [30]. Furthermore, the iron carbide, that is often found as a transition state of the catalyst particle [141], is much more stable than iron particles against reactions with chlorine. This may have led to an enrichment of iron carbide as filling phase.

There were likely two different effects that led to the formation of thin walled CNT. The first was the etching effect of the chlorine due to its reactions with carbon. The second was the reaction of chlorine directly with iron. Actually, using an organic solvent increased the carbon to iron ratio and filled CNT with a large number of carbon shell could be expected. However, it was anticipated that 1,2-dichlorobenzene did not act as an efficient carbon source in the formation process of CNT in the present work. The inertness of the stable aromatic molecule under the given synthesis conditions was verified by experiments using solely 1,2-dichlorobenzene as carbon precursor. Substrates of alumina with a thin iron layer as catalyst were used ($\mathrm{Al} = 10\,\mathrm{nm}$, $\mathrm{Fe} = 1\,\mathrm{nm}$). The amount and composition of gas mixture and the reaction temperature were kept constant. Only the formation of CNT-like structures on the substrates, as shown in fig. 2.39, but no deposition of carbon structures at the inner wall of the insert tube has been observed. From these results it has been concluded, that the carbon for

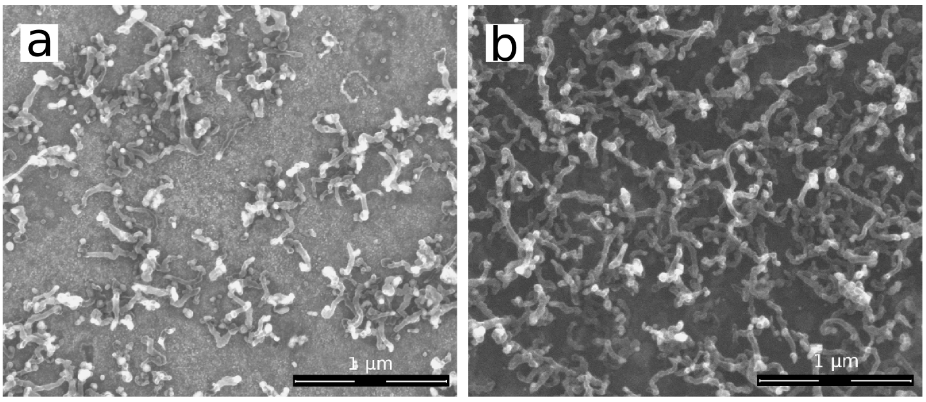

Figure 2.39: Results of experiments were solely 1,2-dichlorobenzene was used as precursor. a) T_{reac} = 800 °C and b) T_{reac} = 830 °C

the formation of the CNT shells was primarily supplied by the ferrocene rather than the 1,2- dichlorobenzene. Only a small increase of the reactive carbon species had to be taken into account. The relatively inert organic molecule 1,2- dichlorobenzene could be used as an inert solvent for the LSCVD.

2.4.2.2 Magnetic properties of iron carbide filled CNT

In order to facilitate MFM measurements, individual CNT had to be preselected. This was achieved by using oxidized silicon substrates with distinct gold markers allowing for the localization of separated CNT during scanning electron microscope[4] investigations. First, to obtain the necessary separated CNT, as-grown CNT were sonicated in ethanol to remove them from the substrate. To ensure homogeneity, the obtained dispersion was stirred with a mechanical stirrer[5] for approximately three minutes. Immediately afterwards, a small drop of the dispersion was applied to a silicon substrate with unique gold markers using a micro pipette. Single CNT were localized and imaged by means of SEM investigations, where their position relative to the marker system was mapped. For the MFM studies, the corresponding markers could then be located with the optical microscope, attached to the MFM setup.

For the stray field studies two different MFM devices were employed. The initial measurements were performed using an atmospheric pressure MFM[6] in lift mode. Prior to the scan, conventional silicon AFM probes coated with 50 nm of CoCrTa alloy were magnetized along the tip axis. To improve the resolution and avoid a hysteretic tip sample interaction, a vacuum high-resolution MFM[7] with a low moment probe was

---

[4] SEM, FEI Nano-SEM

[5] IKA Ultra-Turrax

[6] Veeco DI3100

[7] hr-MFM, Nanoscan

additionally employed. To exclude topographic and other external influences on the acquired data, scans were repeated with reversed tip magnetization. Thus, only the magnetic contribution to the frequency shift is inverted while non-magnetic interactions remain constant. MFM measurements were performed on iron carbide filled CNT. Fig. 2.40 shows SEM (fig. 2.40 a,b) and MFM images (fig. 2.40 c,d) of four partially filled nanotubes. Two of the CNT are nearly completely filled, as visible in the backscattered electron image (fig. 2.40 b). The MFM measurements were conducted under vacuum conditions with a low moment hard magnetic tip. For opposite tip magnetization the MFM maps in fig. 2.40 c and fig. 2.40 d reveal an inverted contrast [66].

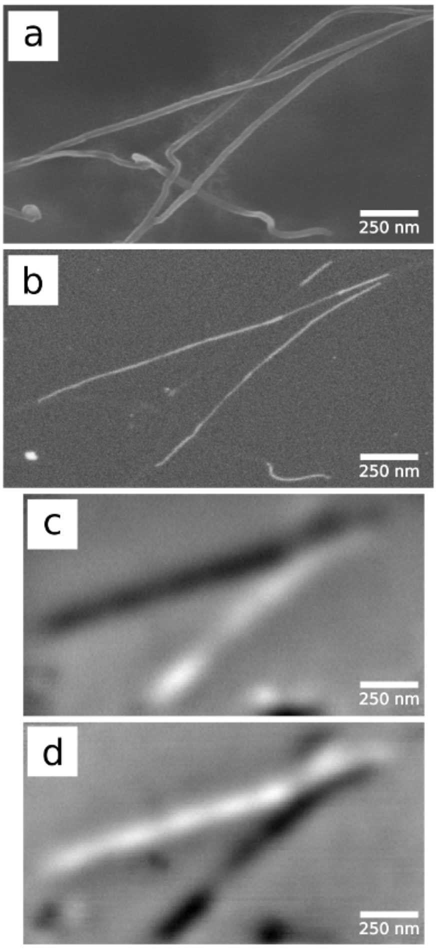

Figure 2.40: Four partially filled CNT. (a) secondary electron SEM image; (b) backscattered electron SEM contrast to emphasize the iron containing filling; (c) and (d) MFM images, the magnetization of carbide nanowires normal to the tube axis is visible. The contrast inversion is the result of the reverse tip magnetization (d) [66].

This confirms the magnetic stray field as the origin of the measured signal. The magnetic contrast is rather homogeneous along the wires indicating a remanent single domain magnetization perpendicular to the tube axis. For separated monocrystalline nanowires, it should be emphasized that such a magnetization state has not yet been reported. During the measurement, neither the sample nor the tip magnetization changed.

In addition, atmospheric condition MFM measurements employing a high moment probe were performed using the MFM in lift-mode^{TM}. A section of a Fe_3C-filled nanotube is shown in fig. 2.41. The direction of magnetization is perpendicular to the nanotube axis in the image plane. However, now various magnetization changes of the carbide nanowires caused by hysteretic and non-hysteretic magnetic tip sample interactions are visible. Some scan lines show signatures of a continuous change of the nanowire's magnetization orientation (A in fig. 2.41) or even magnetization jumps (B in fig. 2.41). Furthermore, magnetization reversals between subsequent MFM lift-mode^{TM} scan lines are visible that may have occurred during the topographic low distance scan in tapping mode (C in fig. 2.41).

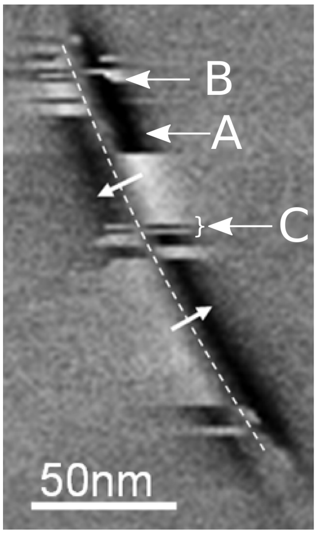

Figure 2.41: MFM phase shift image of a filled section of a nanotube. White represents repulsive and black represents attractive interactions respectively. The direction of magnetization (as indicated by arrows crossing the dashed line) lies perpendicular to the nanotube axis (dashed line) in the image plane. It can easily be seen that the direction of magnetization switches direction several times while scanning the tube [66].

The easy magnetization axis usually points along the wire axis due to the high aspect ratio. A spontaneous or remanent magnetization perpendicular to the wire axis has been observed only in electrodeposited multilayered nanowires [147, 148], but not in ferromagnetic single crystal nanowires. Iron carbide (cementite) forms an orthorhombic crystal structure with an unit cell containing 12 iron and 4 carbon atoms which corresponds to the chemical formula of Fe_3C. There are two possible configurations for the carbon atom arrangement: prismatic and octahedral [149]. The prismatic arrangement offers the lowest total energy as well as a magnetocrystalline anisotropy being one order of magnitude higher than for the octahedral environment. The lattice parameters are $a = 0.4526\,\text{nm}$, $b = 0.5087\,\text{nm}$ and $c = 0.6744\,\text{nm}$ where by convention the c-axis corresponds to the longest lattice parameter. By first principal density functional theory, the c-axis is predicted to be the magnetic easy axis, with an energy gain relative to the hard b-axis of $9.8 \times 10^5\,\text{J/m}^3$. This is supported by experiment values of $6.97 \times 10^5\,\text{J/m}^3$ at 20.4 K and $3.94 \times 10^5\,\text{J/m}^3$ at 290 K [150].

Since it is hard to calculate the domain configuration of a magnetic nanowire, the critical size of a single domain iron carbide sphere is calculated in order to illustrate the problem. However, this is only a rough approximation [151, 152]. Using $A = 8.7 \times 10^{-12}\,\text{J/m}$ for the exchange constant [153], a saturation magnetization of $M_s = 9.8 \times 10^5$ A/m, and a magnetocrystalline anisotropy of $k_2 = 1.18 \times 10^5$ J/m^3 (easy-mid), a critical diameter of 60 nm was obtained. Since the diameters of the nanowires investigated in the present study are below 60 nm a single domain magnetic configuration is reasonable.

The observation of the magnetic easy axis perpendicular to the Fe_3C wire axis (fig. 2.40) might be explained by considering the anisotropy contributions. According to calculations by Arzhnikov et al. [149], the magnetocrystalline easy axis of Fe_3C is the c-axis. The TEM investigations presented above (fig. 2.38) show that the c-axis is about perpendicular to the wire axis. There is good correspondence between the orientation of the nanowires' remanent magnetization (fig. 2.40) and the expected magnetocrystalline anisotropy. However, the shape anisotropy contribution must be also considered. Using the room temperature saturation magnetization of Fe_3C ($M_s = 9.8 \times 10^5$ A/m) [154], the shape anisotropy energy density K_s of elongated Fe_3C ellipsoids of revolution yields 3.06×10^5 J/m^3. The magnetocrystalline anisotropy energy constant of the magnetic hard axis K_b of Fe_3C amounts to 3.94×10^5 J/m^3 [150]. This value is the difference of the orthorhombic b and c axes energies, i.e., the magnetic hard and easy axes. Hence, the ratio of shape versus crystalline anisotropy energy density is 0.7, indicating that the crystal anisotropy dominates. Nevertheless, the substantial shape anisotropy contribution of elongated iron-carbide nanowires may control the magnetization reversal. Assuming a homogeneous reversal as described by coherent rotation two different paths of magnetization reversal might be considered: (i) magnetization rotation in the a-c plane (via the magnetocrystalline mid-hard axis) and (ii) rotation in the b-c plane (via the magnetocrystalline hard b-axis supported by the shape anisotropy). The energy barrier is 1.18×10^5 J/m^3 in process (i) [150] and 0.88×10^5 J/m^3 in process (ii). The latter is simply the difference between K_b and K_s of Fe_3C. Thus, rotation in the b-c plane might be preferred. However, even small deviations from the given energy constants by, e.g., temperature changes or by deviations from the ideal shape may support a magnetization reversal via rotation in the a-c plane. The anisotropy field related to an effective b-c plane barrier is 1.4×10^5 A/m which is much smaller than the respective field of a long iron nanowire. The relatively small anisotropy field of the carbide nanowires under investigation allows tip-induced switching by high-moment MFM probes as shown in fig. 2.41.

Single crystal iron-carbide nanowires contained in multi-walled CNT have been prepared by aerosol-based thermal chemical vapor deposition. Investigations by transmission electron microscopy reveal the crystallographic [010] axis of the orthorhombic Fe_3C nanowires to be predominantly aligned along the nanotube axis. Despite the high aspect ratio of the Fe_3C nanowires, magnetic force microscopy measurements imply single domain behavior with the easy magnetic axis of the nanowires perpendicular to the wire axis. In agreement with the structural results, these findings show that the magnetic behavior is dominated by the magnetocrystalline anisotropy contribution, causing the easy axis to be along the [001] direction [66].

3 Mechanical characterization of carbon nanotubes

3.1 Approaches for description of mechanical properties of carbon nanotubes

Carbon nanotubes represent a new class of nano materials with a very high mechanical strength and stiffness while at the same time possessing a very low density. The high strength is related to the structure of CNT (sec. 1.1.1) and different methods have been used to describe and explore their properties. CNT are relatively large *molecules* that can reach high aspect ratio. Although the diameters are only several nanometers, the length can reach several microns and aspect ratio even above 1000 were found. CNT are a challenge to both theoretical description and experimental investigation.
The structure of single-walled CNT has been modeled by density functional theory (DFT) for small structures that contain only several hundreds of atoms [155–157]. Larger single-walled CNT were simulated by different types of molecular dynamics (MD) [158–165], but also multi-walled CNT have been simulated. The usability of bridged CNT as nano resonators was discussed by Li et al. [166] on the basis of molecular dynamic simulations using a frame-like structure for the CNT and a type of Lennard-Jones potential for the interaction between adjacent layers. However, long single-walled CNT with a high aspect ratio and multi-walled CNT can only be handled at high computational costs. A possibility of tackling this difficulty is the usage of multi-scale methods that have been developed for treating most of the CNT as a continuum and where only local structure details are simulated by MD or DFT [164, 165, 167–169]. The applicability of continuum mechanics for describing the mechanical properties of carbon nanotubes is especially important for the simulation of larger compounds, but also for the evaluation of experimental data. Also the simulation of the usability of CNT in complex setups such as in sensor and actuator applications often requires the modeling of their properties by continuum mechanics. However, more and more details of the structure at atomic scale will be considered in future as the computational power

increases [167, 169].

The in-plane stiffness of carbon nanotube structures is very high and elastic modulus values between 0.5 TPa to 5.5 TPa have been predicted for single-walled CNT [159, 170–172]. Values in the range between 0.1 TPa to 5.0 TPa have also been reported from experiments [170, 173, 174]. However, the experimental data are most often evaluated using continuum mechanic models. Whereas the physical properties of CNT such as electrical and thermal conductivity are in general explored by atomistic and molecular models, there is an attempt to describe the mechanical behavior in terms of classical continuum mechanics. However, the transferability of the methods and assumptions of classical continuum mechanics to nano- and mesoscopic systems like carbon nanotube is not self-evident. Therefore, the possibility to describe a CNT by these methods needed to be investigated. In continuum mechanics the definition of the elastic modulus as a material property bases on the assumption of a spatial uniformity of the material, provided that at least in an average the material properties exhibit translational invariance [17]. In contradiction, speaking of elastic modulus in connection with carbon nanotubes is ambiguous. A singular CNT lacks of translational invariance in the transverse direction, which is therefore not a material, but rather a structural member [17]. A rather natural description of a single-walled CNT in terms of continuum mechanics would be a thin elastic shell. A multi-walled CNT could then be described by a stack of nested coaxial single-walled CNT with increasing diameter and constant interlayer spacing c, but again with no translational invariance in the radial direction. Both, single- and multi-walled CNT are basically *structures* and care must be taken when speaking of material properties of carbon nanotubes [17]. The assumption of the transferability of a tube like structure and using continuum mechanics to model the structure of carbon nanotubes, consisting of homogeneous material, has been widely discussed in literature [165, 170, 175–179]. Several authors developed an equivalent continuum model that links between the molecular description of nano structures and the macroscopic behavior of classical structural mechanics [61, 163]. The challenge in the description of the material properties at nanoscale is the interlink between the atomic description and its continuum counterpart [164]. Chang et al. [164] developed analytical methods to link the parameters of a molecular mechanical model to the continuum (structural) mechanics expressions. As it turned out a single-walled CNT can be assumed as a solid shell with a cross section and a finite very small shell thickness. To accomplish this linkage the molecular potential energy E_{pot} of the nanostructures is represented by the mechanical strain energy of a representative volume element of a continuum model [180]. The definition of the elastic modulus E in classical structural mechanics is given by eq. 3.1.

$$E = \frac{1}{V}\frac{\partial^2 E_{pot}}{\partial \epsilon^2} \tag{3.1}$$

Where V is the volume and ϵ is the strain. However, applying this definition to molecular structures such as carbon nanotubes is only possible for a strain ϵ directed in the axial direction [17]. Furthermore, the relevant volume of a CNT is given by the constituent graphitic layers and is therefore not well defined. The volume $V = L\,A$ of the tube is composed of the tube length L and the cross section A. It is ambiguous since the cross section area A can be chosen in several relatively arbitrary ways. Consequently, the elastic modulus E is not exactly defined but also depends on the cross section definition. In order to eliminate this problem, the intrinsic elastic energy of a nanotube is better characterized by the energy change not per volume but per area S of the constituent graphitic layer(s) as it is defined by eq. 3.2 [17].

$$C = \frac{1}{S}\frac{\partial^2 E_{pot}}{\partial\epsilon^2} = \frac{1}{L\int dl}\frac{\partial^2 E_{pot}}{\partial\epsilon^2} \tag{3.2}$$

The area S is given by the tube length L and the sum of the circumferential length of all shells l and since $S = L\,l$ is well defined C is unambiguous. Taking a similar approach Hernandez et al. [161] avoided the definition of an effective single-walled CNT layer thickness by relating the Young modulus to the perimeter of the tube. While the partial derivative of the total energy at zero strain in all directions except along ϵ yields an elastic stiffness similar to graphite, assuming a free-boundary (no lateral traction on the nanotube) gives the elastic modulus E. In the latter case, the nanotube's elastic modulus can be recovered as $E = C\,/\,h$ with $E = C\int dl\,\frac{1}{A}$ and $A = \int dl\,h$, where h denotes the wall thickness. But the non-unique choice of the cross section thickness h has to be kept in mind [17]. For single-walled CNT an effective bending stiffness was defined that is not directly related to continuum mechanics in order to consider the non-continuous nature of single-walled CNT. However, the definition of an appropriate wall thickness remains a challenging task [181]. While the definition of the thickness as the interplane distance of graphene sheets in graphite is widely used [61, 156, 170], also other values such as 0.066 nm [159] and 0.1 nm [172] for the effective thickness were suggested. The assumption of an effective layer thickness of 3.4 Å as an *ad-hoc* assumption is only possible in case of a simple stretch deformation [160]. Tu et al. [182] performed local density approximation model and classical elastic shell theory simulations on both single-walled and multi-walled CNT. An effective shell thickness of 0.75 Å has been found. The authors reported a rather high Young modulus for single-walled CNT of 4.7 TPa and also found, that the Young modulus of multi-walled CNT decreases with increasing wall thickness, i.e., the number of carbon shells. Thus, the Young modulus is also a function of the number of shells. They considered multi-walled CNT up to 100 carbon layers. However, the authors also stated that the description of CNT is on the borderline between quantum mechanics and classical bulk material methods. In contrast to these results Li and Chou et al. [180, 183] found that the Young modulus of multi-walled CNT is slightly higher compared to single-walled CNT and both are higher than for graphite, which is generally accepted to be 1.02 TPa [170]. From scanning force microscopy on both single- and multi-walled CNT it was concluded that the elastic modulus of multi-walled CNT is higher than that of single-walled CNT [184]. However, using thermal excitation of carbon nanotubes an average elastic modulus of 1.25 ± 0.45 TPa for single-walled CNT has been found [170]. The insensitivity of the Young modulus of single-walled CNT and multi-walled on the helicity, the radius, and the number of shells was reported as well [160]. However, recent data reveal a dependency of the Young modulus on these parameters [165, 167, 185, 186].

Besides the discussion about the appropriate shell thickness further effects have to be considered in the case of multi-walled CNT. In order to assume a CNT as a solid wall cylinder, slip between adjacent carbon shells should not be of importance [187]. Actually, the assumption of a tube with a continuous wall of thickness h is only valid if slip between adjacent layers can be ruled out [176], and it has been shown, that in this case the classical definition of the bending stiffness D of an elastic shell

$$D = \frac{E\,h^3}{12\,(1 - \nu^2)} \tag{3.3}$$

is valid, where h again denotes the wall thickness, ν the Poisson ratio and E the in-plane Young modulus. The expression in eq. 3.3 leads to an ambiguous D due to its dependency on h. Therefore, a further expression for the bending stiffness denoted by K has been defined (eq. 3.4), where κ denotes the curvature and L the length of the bent CNT.

$$K = \frac{1}{L}\,\frac{\partial^2 E_{pot}}{\partial \kappa^2} = C \int y^2 \, dl \tag{3.4}$$

In the case of a CNT with several constituent layers the integration on the right hand side goes over the cross-section length of each layer and y is the layer distance from the neutral axis [17]. In experiments at the nano scale it is in principle difficult to distinguish between the influence of the geometry and the elastic modulus of the material. Only the stiffness $E\,A$ can be measured, whereas A is the cross section of the structure.

Despite the enormous progress which has been made in the field of simulation of mesoscopic systems the evaluation of experimental data is still a challenge. In most cases the CNT under investigation are considered as solid tubes and continuum elastic theory is used for the evaluation of the data [174, 186, 188, 189]. For the evaluation of the experimental data the CNT are often approximated as hollow cylinders with a circular ring cross section that is defined by the outer and inner diameter [170, 173, 174, 188, 190].

However, this is a rough approximation that is caused by the limited information about the sample which can be obtained about nano scale materials. For the description of multi-walled CNT different methods exist. On the basis of the description of single-walled CNT as shells with a small hence finite wall thickness h, multi-walled CNT are described as stacks of nested single-walled CNT. Each shell within the multi-walled CNT is represented by a single-walled CNT [176, 179]. Each single-walled CNT is connected to its next neighbors by van der Waals forces. Following the knowledge about graphite the force is often deduced from the so called Brenner-Potential [155, 191]. This potential leads to a force with repulsive and attractive properties. The elastic modulus is not a real bulk property in this case. Each single-walled CNT has the same elastic modulus $E = C / h$ but its bending stiffness is also defined by the diameter of the particular shell. The behavior of such a system depends on the interaction between the shells and the total number of shells involved. While this model is a good representation of the micro structure of a multi-walled CNT, it is hardly measurable by experiments. Therefore, especially multi-walled CNT are often described by a continuum mechanics model. The tube like structure is defined by the outer and inner diameter of the multi-walled CNT. The elastic modulus is a bulk property in this case, since the CNT wall is considered as a bulk material. Even though the effective thickness of a single-walled CNT has to be handled with care, the bending stiffness for multi-walled CNT can be estimated from classical bending stiffness formula quite well [176].

Buckling and rippling mode of CNT

A CNT can neither be treated as a molecule nor as a structurally homogeneous material. While molecules have a defined structure, real CNT in general have defects and thus are not a defined type of molecule. They are mesoscopic objects and continuum theories can only be applied with care in order to describe their properties [17].

In their static and dynamic bending experiments, Poncharal et al. [188] found a diameter dependent behavior of multi-walled CNT. If a nanotube is deflected orthogonally to its long axis the shape of the cross section is changed to an oval with its short half axis in parallel to the deflection direction. On the upside of the tube (i.e. opposite to the deflection) there is plain strain while on the downside of the tube, where it is under compression, another structural change is very often found. A wave-like distortion is formed locally reducing the compression induced stress. The observed phenomena has been called *buckling* or *rippling* mode and is related to intrinsic bending instabilities of the carbon nanotube structure. Therefore, the authors introduced the term effective bending modulus into the discussion about the elastic modulus of CNT [188]. Buckling has been reported for single-walled and multi-walled CNT [158, 159]. Beyond a critical curvature buckling pattern emerge, as result of the bending, which can either be a single kink or a periodic pattern in correlation with a specific buckling wavelength λ_b. Falvo et al. [192] used AFM for the deformation and imaging of CNT that lay on flat substrates. A certain part of particular CNT was measured before and during bending and the correlation between the curvature and the buckling of CNT was evident. It was found that buckling appears with a characteristic interval, independent of their absolute position along the tube and is related to a high curvature. This suggests, that the buckling reduces curvature-induced stress, is reversible, intrinsic to the nanotube and not mediated by defects [192]. The buckling behavior allows CNT to reversibly survive large deformations. By applying a thin shell elastic model to each single CNT within a stack of nested CNT and combining the separate CNT by van der Waals forces, Pantano et al. [193] modeled the bending behavior of multi-walled CNT in good agreement with experimental data [194]. The apparent softening of multi-walled CNT was also reported for dynamic resonant bending [17, 188, 195]. Rippling is a special case of buckling where a periodic and spacial extended wave-like pattern forms [195, 196]. Rippling can not be described by continuum linear models. From their theoretical discussion Liu et al. [195] concluded that rippling can be found for CNT with outer diameters $\geq$15 nm which is also in good agreement to the experimental results of Poncharal et al. [188]. The *basal* plane distance remains almost 0.34 nm in state of rippling. These findings suggest, that the effective elastic modulus and in particular its reduction depends on the occurrence of a critical bending deflection and curvature.

3.1.1 Experimental methods

The measurement of the mechanical properties of nano scaled materials is quite challenging and different methods have been employed.

Tensile Tests

Most of the simulations deal with explicit tensile load [162]. In order to obtain the elastic properties of a material a sample with a defined geometry is necessary. The most simple experiment is a tensile test performed on a rod-like sample with a homogeneous and simple cross section. In the one dimensional case the change in length divided by the initial length is the strain ϵ of the sample. The elastic or Young modulus E is the proportional factor between the applied stress and the resulting strain.

$$\sigma = E\,\epsilon \tag{3.5}$$

Pulling and compression experiments were conducted in order to determine the elastic modulus and fracture strength of CNT [197, 198]. Yu et al. [197] used a soft and a relatively stiff conventional AFM cantilever to measure the deflection and corresponding load of the CNT. It was found by experiment and simulation that for strains larger than 2% the load transfer from the outermost layer to the inner tubes begin to cease. The reason might be the weak van der Waals interactions between adjacent layers. It is often assumed that tensile load is only born by the outermost layer based on the observed sword-in-sheath fracture mechanism. However, the exact load applied during experiments is often not known due to the lack of proper force detecting systems at the nanoscale [199]. In contrast to tensile tests the bending of the sample often allows for larger amplitudes and thus a higher sensitivity of the measurement. Bending experiments are therefore convenient especially for high strength materials. During a bending the sample is compressed on one side and stretched on the other.

Static Bending

In the static bending method a static load is applied to a one- or two-side clamped beam and from the known force and deflection, the material properties can be deduced. By an AFM measurement the outer diameter and the length of a CNT can be gained and force versa distance measurements allow for the calculation of the effective bending modulus by evaluating the corresponding beam model. Especially for multi-walled CNT a drawback is the unknown inner diameter. In order to evaluate the model, assumptions about the mounting of the CNT to the support have to be done. Static AFM bending measurements on bundles of single-walled CNT gave an effective bending modulus in range of 0.6 TPa to 1.0 TPa [174]. The static bending requires samples with separated CNT that lie cross holes [200] or bars separated by trenches [186]. The elastic modulus of multi-walled CNT was measured by acquiring force-displacement curves using an AFM [186]. CNT were aligned on top of a bar structure from a solution by using AC dielectrophoresis. The elastic modulus exhibited a strong diameter dependence. Thinner multi-walled CNT with an outer diameter of ≈10 nm possessed a elastic modulus two orders of magnitude higher than thicker multi-walled CNT with outer diameter above 20 nm. The bending modulus of a suspended beam can be set equal to the elastic modulus if the influence of shear can be neglected [186]. This is possible if the suspended length is large in comparison to the diameter of the beam. For the evaluation of experimental data a homogeneous beam cross section has been assumed [186].

Dynamic Bending

In the dynamic bending methods the CNT are mostly cantilevered on a support which can be either an as-grown substrate [170, 188] or CNT are picked off a substrate and attached to some kind of tip [36]. In some cases the CNT are placed on the edge of a substrate by dielectrophoresis [201]. The excitation can be achieved using thermal heating to excite a vibration of the sample inside a transmission electron microscope [170, 173]. Applying an electric field is another possibility which results in an excitation force [188, 190]. Assuming a harmonic excitation, the force acting on the CNT is given by eq. 3.6.

$$\begin{aligned} F(t) &= \alpha\,\beta\,[\Delta V + V_s + V_d\,\cos(\omega\,t)]^2 \\ &= \alpha\,\beta\,[(\Delta V + V_s)^2 \\ &+ 2\,(\Delta V + V_s)\,V_d\,\boxed{\cos(\omega\,t)} \\ &+ \frac{1}{2}\,V_d^2\,\boxed{\cos(2\,\omega\,t)} + \frac{1}{2}\,V_d^2] \end{aligned} \tag{3.6}$$

Where V_d is the driving amplitude, V_s is a DC offset voltage and ΔV is a potential that occurs due to differing workfunctions of the CNT and electrode material. The parameters α and β depend on the experimental setup and are defined by the capacitance of this specific setup. Also mechanical excitation [189, 201] of CNT has been performed.

3.1.2 Beam models

As the previous section has shown, the simple beam model also called *Euler-Bernoulli beam model* (EBM) can be applied to slender beams with a relative high aspect ratio even at the nanoscale [179, 202]. The derivation of the simple beam model is based on the assumption of a slender beam with an arbitrary cross section that is exposed to an external vertical load $f(x,t)$. In order to get a mathematical expression for the differential equation of a vibrating beam, a small volume element with all relevant quantities acting on it is considered. The shear forces $Q(x,t)$ and moments $M(x,t)$ and the external load acting on the beam element are shown in fig. 3.1.

For the derivation of a description a beam in pure flexure is considered. After cutting out a small beam section the relevant vertical forces (eq. 3.7) and moments (eq. 3.8) can be written down.

$$\left[Q(x,t) + \tfrac{\partial Q(x,t)}{\partial x}\mathrm{d}x\right] - Q(x,t) + f(x,t)\mathrm{d}x = m(x)\mathrm{d}x\,\frac{\partial^2 y(x,t)}{\partial t^2} \tag{3.7}$$

Where m is mass density per unit length and Q denotes the vertical shear force. The

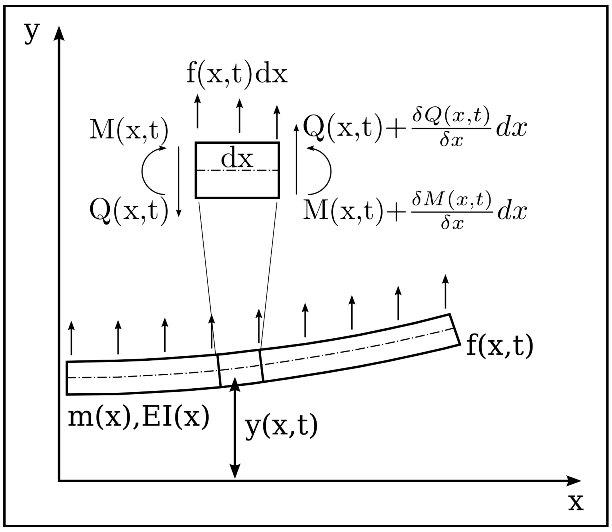

Figure 3.1: Basic assumptions for the derivation of the simple beam model [203].

influence of torque associated with the inertia torque is ignored here.

$$\left[M(x,t) + \tfrac{\partial M(x,t)}{\partial x}\,\mathrm{d}x\right] - M(x,t) + \left[Q(x,t) + \tfrac{\partial Q(x,t)}{\partial x}\,\mathrm{d}x\right]\mathrm{d}x + f(x,t)\,\mathrm{d}x\,\frac{\mathrm{d}x}{2} = 0 \tag{3.8}$$

After canceling all terms that include higher order derivations in eq. 3.8 a simplified expression eq. 3.9 results.

$$\frac{\partial M(x,t)}{\partial x} + Q(x,t) = 0 \tag{3.9}$$

A form for the equation of motion is obtained by eq. 3.10.

$$-\frac{\partial^2 M(x,t)}{\partial x^2} + f(x,t) = m(x)\,\frac{\partial^2 y(x,t)}{\partial t^2} \tag{3.10}$$

The relation between the bending moment and the resulting bending deformation is defined by eq. 3.11.

$$M(x,t) = E\,I(x)\,\frac{\partial^2 y(x,t)}{\partial x^2} \tag{3.11}$$

Inserting eq. 3.11 into eq. 3.10 the differential equation for the flexural vibration of a bending bar is given by eq. 3.12.

$$-\frac{\partial^2}{\partial x^2}\left[E\,I(x)\,\tfrac{\partial^2 y(x,t)}{\partial x^2}\right] + f(x,t) = m(x)\,\frac{\partial^2 y(x,t)}{\partial t^2}, \quad 0 < x < L \tag{3.12}$$

This forth order differential equation has to be solved with respect to the boundary conditions. A rigidly clamped beam with a slope equal to zero at $x = 0$ is given by the following boundary conditions

$$y(x,t)\big|_{x=0} = 0, \quad \frac{\partial y(x,t)}{\partial x}\bigg|_{x=0} = 0 \tag{3.13}$$

A so called hinged condition is given by

$$y(x,t)\big|_{x=0} = 0, \quad E\,I(x)\,\frac{\partial^2 y(x,t)}{\partial x^2}\Big|_{x=0} = 0 \tag{3.14}$$

This boundary condition is important for beams which are supported at least at two positions. A special situation is the assumption of a torsion spring like behavior of the beam at $x = 0$.

$$y(x,t)\big|_{x=0} = 0, \quad E\,I(x)\,\frac{\partial^2 y(x,t)}{\partial x^2}\Big|_{x=0} = \alpha\,\frac{\partial y(x,t)}{\partial x}\Big|_{x=0} \tag{3.15}$$

While this boundary condition is not frequently found in text books it is in particular interesting for the evaluation of experimental data, since a rigid clamping of the beam under experimental investigation is often not realized [191, 204]. The boundary conditions at the *free end* of the beam at $x = L$ are given by

$$E\,I(x)\,\frac{\partial^2 y(x,t)}{\partial x^2}\Big|_{x=L} = 0, \quad \frac{\partial}{\partial x}\left[E\,I(x)\,\tfrac{\partial^2 y(x,t)}{\partial x^2}\right]\Big|_{x=L} = 0 \tag{3.16}$$

While the first expression in eq. 3.16 represents the fact that the free end can not bear a moment, the second equation represent zero shear forces at the free end.

For dynamic resonant vibration experiments the corresponding eigenvalue problem has to be solved. Considering the free vibration state, which corresponds to the assumptions $f(x,t) = 0$, the solution becomes separable in space and time.

$$y(x,t) = Y(x)\,F(t) \tag{3.17}$$

Since the time dependency $F(t)$ is a harmonic function denoting its frequency with ω and inserting this ansatz into eq. 3.12 gives

$$\frac{\mathrm{d}^2}{\mathrm{d}x^2}\left[E\,I(x)\,\tfrac{\mathrm{d}^2 Y(x)}{\mathrm{d}x^2}\right] = \omega^2\,m(x)\,Y(x), \quad 0 < x < L \tag{3.18}$$

This eigenvalue problem can be solved for the given boundary conditions. In case of a homogeneous cross section and material properties in the interval $0 < x < L$ the equation can be simplified further.

$$\frac{\mathrm{d}^4 Y(x)}{\mathrm{d}x^4} - \beta^4\,Y(x) = 0, \quad \beta^4 = \frac{\omega^2\,m}{E\,I} \tag{3.19}$$

Where $E\,I$ represents the bending stiffness. The general solution for eq. 3.19 is given by

$$Y(x) = C_1\,\sin(\beta\,x) + C_2\,\cos(\beta\,x) + C_3\,\sinh(\beta\,x) + C_4\,\cosh(\beta\,x) \tag{3.20}$$

The eigenvalue β has to be solved accordingly to the boundary conditions. In the case of a free vibrating beam, that is clamped only to one side, the characteristic equation is given by

$$\cos(\beta\,L)\,\cosh(\beta\,L) \;=\; -1 \tag{3.21}$$

whereas solutions of this equation can only be obtained numerically. The first three eigenvalues are $\hat{\beta}_1 \;=\; 1.875$, $\hat{\beta}_2 \;=\; 4.694$ and $\hat{\beta}_3 \;=\; 7.855$ with $\hat{\beta}_j \;=\; \beta_j\,L$.

The Euler-Bernoulli beam model is often called the *simple beam theory* which assumes that the rotation of each small beam element is insignificant compared to its vertical translation. It can only be applied to slender beams and small deflections. Consequently, the ratio between the length and the diameter of the beam should be greater than 50 [203, 205]. It is also assumed that shear in the material is very low in relation to the bending deformation and can be neglected. However, if the aspect ratio for the beam under consideration is below 30, other models that consider shear have to be used [206]. If shear effects and rotational moment of inertia have to be considered a more general beam model, intensively studied and introduced by Timoshenko [207, 208], has to be applied. It is therefore often called the Timoshenko beam model, which is of a more general nature. Two coupled partial differential equations are necessary in that case. The free vibrating Timoshenko beam is given by [206]

$$\rho\,A\,\omega^2\,y(x) \;-\; K\,G\,A\left(\tfrac{\mathrm{d}\phi}{\mathrm{d}x} \;-\; \tfrac{\mathrm{d}^2 y(x)}{\mathrm{d}x^2}\right) \;=\; 0 \tag{3.22}$$

$$E\,I\,\tfrac{\mathrm{d}^2\phi}{\mathrm{d}x^2} \;-\; K\,G\,A\left(\phi \;-\; \tfrac{\mathrm{d}y(x)}{\mathrm{d}x}\right) \;+\; \rho\,I\,\omega^2\,\phi \;=\; 0 \tag{3.23}$$

where y is the transverse displacement, ϕ the slope of the cross section due to pure bending without shear deformation, x the axial coordinate, I the second moment of area of cross-section, A the cross-sectional area, ρ the mass density per unit volume, K the shear correction factor, E the Young's modulus, G the shear modulus and ω the circular frequency of the beam.

3.1.3 Special beam cases

Besides atomistic descriptions continuum mechanics is still very attractive especially for meso- and nanoscopic systems since the complex behavior of the material is reduced to a number of specific characteristic quantities, such as the Young modulus E or the shear modulus G. Furthermore, knowledge about the natural frequency and mode shape can reveal defect information, as the presence and location of a structural feature [30] and to some extend the severity of the damage.

For the evaluation of experimental data of nanowires and also for their usage in applications, knowledge about the influence of structural peculiarities [30] and mounting conditions [209] on the bending and vibrational behavior is mandatory. In theoretical studies, structural defects are often expressed by a torsion spring [30], whereas the elastic properties of the mounting are often modeled by a combination of torsion, lateral and vertical springs [209].

The shift of the natural frequency as a consequence of non-rigid mounting conditions has been shown and discussed by Ding et al. [204] for crystalline boron nanowires. At first, the nanowires were attached to the substrate by using solely adhesion forces. Since the stability of these connections was weak, additional carbon was deposited by electron beam induced deposition (EBID). By comparing the first mode eigenfrequency of the nanowire before and after the EBID process an increase of the eigenmode frequency has been observed. After a deposition time of approximately 30 minutes a saturation of the eigenfrequency was found. This was related to a stiffening of the clamping, approaching a rigid-like clamping condition. A non-rigid rather elastic mounting reduces the first eigenmode frequency. Since the carbon deposition also leads to a reduction of the effective beam length and thus an increase of the resonance frequency, Ding et al. [204] assumed, that the over all stiffening was much higher than could be expected from the shortening alone. The increase of the resonance frequency was mainly effected by the stiffening of the clamping. However, the deposited carbon might still be softer than the CNT but its bending stiffness might exceed the one of the CNT. Due to the complex morphology of micro- and nanoscaled beams, numerous deviations from a simple homogeneous and rigid clamped beam situation have been studied theoretically [209].

Volume defects might be expressed by a torsion spring. If the defect location is very close to the clamping, it has to be treated as a torsion spring. If the defect location is somewhere within the structure and its properties are not too great a difference from its surrounding an effective elastic modulus for the whole structure can be assumed [205].

Another interesting feature are point masses attached to a cantilevered beam [205]. This is in particular important for usage of nanowires as micro balances for the detection of very small mass [201]. The frequency shift of the first and second eigenmode frequency as function of amount and position of a point mass has been theoretically discussed by Wang et al. [205]. Their findings are shown in fig. 3.2. While f_i is the system frequency with the point mass attached, F_i denotes the frequency of an ideal simple beam. The ratio $\frac{a}{l}$ gives the relative position of the point mass along the beam. Within their studies a perfectly rigid boundary condition was assumed. Depending on the mass repartition the eigenmode frequencies are differently affected. The second eigenmode frequency is reduced more than the first eigenmode frequency, if a point like mass is located in the middle or close to the clamping point of the vibrating beam. It is also affected, if the mass is close to the free end but less than the first eigenmode frequency. The latter is mostly affected if the mass is at the free end. In general, if the mass is

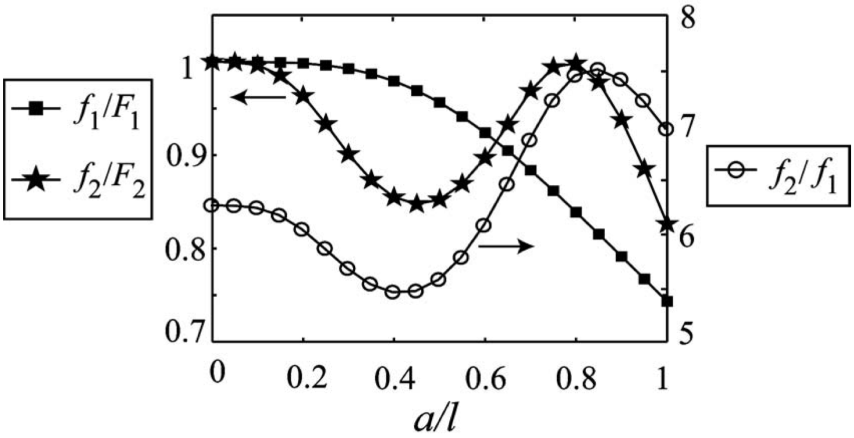

Figure 3.2: Resonant frequency shifts of the first and second eigenmode as a function of the point mass position [205].

located in the area with the highest amplitude than it has the highest influence on the corresponding eigenmode frequency. For a point mass m that is 20 % of the total beam mass M, the authors found that the frequency ratio $\frac{f_2}{f_1}$ is within the range of 5.5 to 7.5 depending on the mass point position [205]. In comparison, for an ideal homogeneous, one side clamped beam a frequency ratio $\frac{f_2}{f_1}$ of about 6.3 is expected.

3.2 Experiments

In the following sections the experimental setups for the measurement of the mechanical properties of the iron-filled CNT, used in the present work, are presented. Thereafter, the results are presented and discussed. The elastic properties of CNT were measured by two different methods. At first a dynamic resonant bending and at second a static bending method have been employed.

3.2.1 Sample preparation

For the measurement of the elastic properties of single CNT an adequate sample preparation is required. For both, the dynamic resonant and the static bending method a one side clamped CNT could be used. To prepare the samples, the as grown wafer were broken into smaller pieces. Such a piece was then glued to a sample holder. The sample was positioned such as the substrate surface was in parallel with the electron beam inside the SEM. Thus, the breaking edge could be directly investigated. Consequently, the CNT film itself was aligned perpendicular to the incident beam and thus the morphology of CNT became visible.

As substrates tapered tungsten wires were utilized. The tips were produced by wet electro chemical etching. A 2 molar NaOH solution was used and an electrical voltage of 2 V to 3 V at 0.01 A to 0.05 A has been applied. The etch process resulted in tapered tips with radii in the range of 10 nm to 1000 nm. Often the etching process produced an tungsten oxide layer on the surface of the tip. Since this isolating material can cause problems during the sample preparation and imaging of the attached CNT, the oxide layer was etched away by hydrofluoric acid treatment. The etching duration of each tip in a 37% HF was 3 minutes.

The steps of the sample preparation are illustrated in fig. 3.3. The sample preparation has been performed in a SEM equipped with a micromanipulater (Kleindiek). The etched tungsten tip was attached to a sample holder and mounted on the micromanipulator. Then the tip was carefully approached to the breaking edge of the sample. As the tip was close by a previously specified CNT, the tip was approached further. The contact with the selected CNT was visualized by using the internal vibration mode of the manipulator. In the next step the CNT was glued to the wire by the deposition of amorphous carbon. In the microscope atmosphere contained hydrocarbons were cracked by the electron beam and deposited on the exposed area. If necessary, the carbon concentration was increased by adding highly volatile hydrocarbons such as paraffin, whose usage has been reported in literature [210]. Since the deposition conditions depend on the selected acceleration voltage and beam current, appropriate

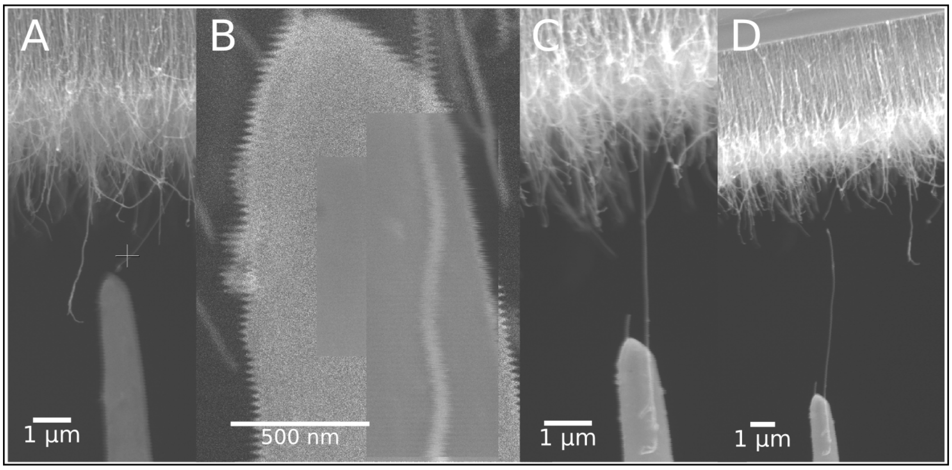

Figure 3.3: Preparation of a free standing CNT as a prerequisite for bending experiments. Step A: Tungsten tip approaching a free standing CNT. Step B: Large magnification of the mounting area for fixation of the CNT by amorphous carbon deposition. Step C: Tip with attached CNT is carefully retracted. Step D: Single free standing CNT ready for measurements.

parameters had to be found. An acceleration voltage of 10 kV was selected together with a beam current of 10 pA. After the glueing the tip with the mounted CNT was carefully withdrawn. This step was critical, since both the stability of the mounting and the maximum possible tensile load for CNT had to be higher than the contact of the CNT to the substrate. This was often not the case. Either the mounting was not stable enough or the CNT broke next to the mounting. In the former case the deposition condition needed to be adjusted. A successful sample preparation resulted in free standing one side clamped CNT that could be processed further.

3.2.2 Determination of length and diameter

The knowledge of the *beam* length is necessary for the evaluation of the elastic modulus, especially in case of the resonant dynamic bending method [189]. In order to measure the length of the CNT, the tungsten wire together with the attached CNT was rotated inside the SEM by defined angles. The rotation axis coincides with the x-axis in fig. 3.4 which is defined here to be in parallel with the projection of CNT long axis into the focus plane. For the rotation either the stage of the SEM was tilted or the rotation extension of the micromanipulator was utilized. In the SEM only the projection of the CNT is visible, thus the true length of the CNT is unknown. Directly from the image only the projection onto the x-axis and the y-axis can be measured. There is also a projection of the CNT onto the yz-plane. Even though the projection onto the151 yz-plane is unknown, it is a constant of rotation around the x-axis. If the sample is

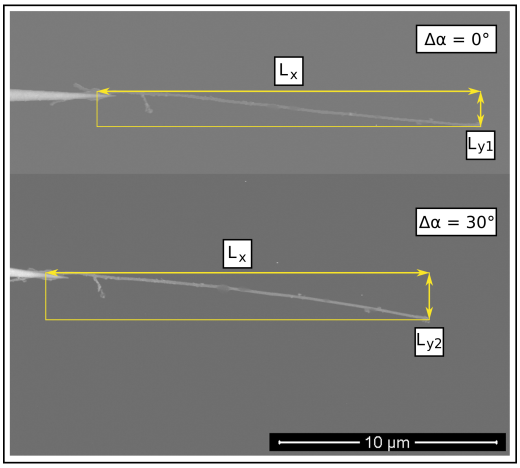

Figure 3.4: Method for the length measurement of an one side suspended CNT.

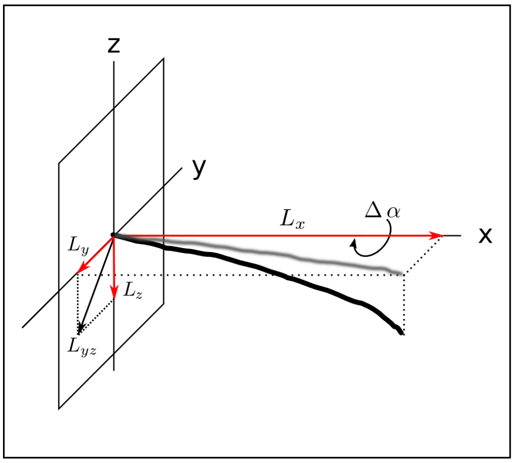

Figure 3.5: Sketch of the projection of a CNT onto the xy- xz- and yz-plane. The black curve represents the CNT and light grey is the visible projected length.

rotated by a known angle, the projection L_{yz} can be calculated by eq. 3.24.

$$\begin{aligned} L_{y1} &= L_{yz}\cos\alpha \\ L_{y2} &= L_{yz}\cos(\alpha + \Delta\alpha) \\ L &= \sqrt{L_x^2 + L_{yz}^2} \end{aligned} \tag{3.24}$$

Whereas α is an unknown angle of the CNT relative to the xy-plane and $\Delta\alpha$ is the known angle of rotation. L_{y1} and L_{y2} are the projections of the CNT onto the y-axis before and after the rotation, respectively. These three equations 3.24 can be used to calculate the total length of the CNT. In order to increase the accuracy of the length measurement the same process was conducted for at least three rotation angles between 15° to 90°. For highly curved CNT such as shown in fig. 3.24 this method was also used to find the position with the largest projection onto the y-axis. In that case, the full length was calculated from piecewise measuring the length of the CNT along the curve and applying eq. 3.24. The orientation with the maximized y-projection was also used for mounting the sample for the subsequent bending experiments.

The diameter of each CNT investigated was determined inside SEM by measuring the diameter at ten different positions along the CNT length. For the analysis of the experimental data the average diameter value was used. When possible the diameter was additionally determined from TEM micrographs.

3.2.3 Resonant dynamic bending

The dynamic resonant bending method requires a periodic excitation source. The excitation can either be electrical [188, 190] or mechanical [201].

The electrical excitation was achieved by using a counter electrode and applying an AC voltage between the sample and the electrode. This method requires a sufficiently high conductivity of both the sample and the contact between the CNT and the tungsten wire. An advantage is the possibility to perform also static bending of the CNT by applying a DC voltage [188]. Especially in the SEM the high field strength between the sample and the counter electrode led to disturbances of the electrons and imaging is seriously disturbed. The setup for the excitation by AC voltage is shown in fig. 3.6. A micromanipulator was used to bring the tungsten tip with the CNT sample into proximity of the counter electrode. An AC voltage was applied between the CNT and the counter electrode using a signal generator (Stanford Research System, Model DS345). In eq. 3.6 two harmonic terms can be identified. The amplitude of the first term (blue in eq. 3.6 on page 93) depends on the DC offset voltage V_s and can be set to zero if the condition $V_s = -\Delta V$ is satisfied. In that case no excitation caused by this term can be found. On the other side the second term (red in eq. 3.6) only depends on the driving voltage. A resonant excitation of the CNT can be found if $2\,\omega_{elec} = \omega^{res}$. That means, if the electrical frequency ω_{elec} is half of the mechanical resonance frequency ω^{res} an eigenmode vibration occurs. In that case the vibration amplitude is not sensitive to the DC offset voltage. By checking these two conditions the origin of the excitation can be ruled out and the mechanical eigenfrequency of the CNT can be measured independently by two different excitation frequencies. Due to the second term in eq. 3.6 (red) the first as well as the second eigenmode can be excited by an excitation frequency that is half of the mechanical eigenfrequency of the CNT. While this reduces the necessary frequency that has to be provided by the function generator it was found that the driving voltage was often to low for an excitation of the second eigenfrequency. Even though the power was increased by using a power amplifier the higher voltages lead to significant image distortions, which is shown in fig. 3.7. Furthermore, the resonance frequency also depends on the applied voltage [211] and

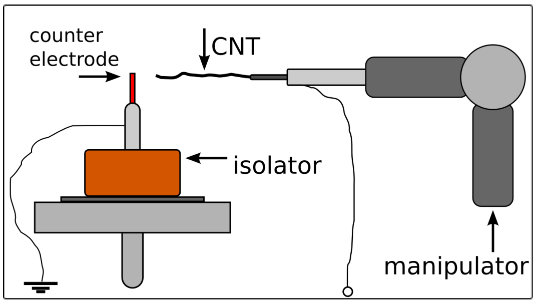

Figure 3.6: Setup for the electrical excitation of CNT vibration.

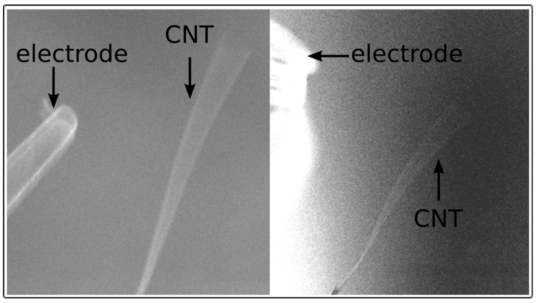

Figure 3.7: Counter electrode and vibrating CNT. On the right side disturbance of the image caused by the electrical field between electrode and CNT is shown.

very small excitation voltages have to be used. To avoid these problems a new setup, that enables a mechanical excitation of the CNT vibration, was set up.

The mechanical excitation was achieved by employing a shear piezo actuator. The sketch of the setup is shown in fig. 3.8. A driving voltage was applied between the front side and back side electrode of the actuator. This voltage led to a mechanical movement of the piezo crystal. In order to avoid charging disturbances during imaging, the sample holder was grounded to the stage of the microscope. The back side electrode of the shear actuator was attached to the ground plate using conducting silver. A small aluminum cylinder with a length of 3 mm and a diameter of 2 mm, was used as specimen holder for the tungsten nanowires. In order to prevent an electrical contact of the front side electrode with the cylinder, an isolating glass substrate was glued in between. The cylinder itself was grounded to the microscope stage to avoid charging of the sample during imaging. The orientation of the actuator allowed the excitation of the sample vibration perpendicular to the electron beam.

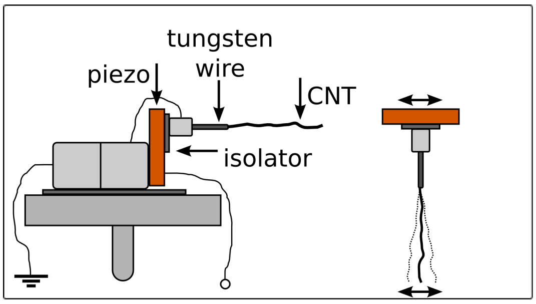

Figure 3.8: Setup for the mechanical excitation of CNT vibration.

After the length measurement the samples were mounted to the shear actuator by glueing the tungsten wire into a small aluminum cylinder using conducting silver. The excitation was driven by a signal generator (Stanford Research System, Model DS345). The signal generator could deliver frequencies in the range 0.01 kHz to 30.0 MHz and a driving voltage of 10 V. The setup was especially suitable for SEM measurements due to less disturbance of the electrons used for imaging. In order to measure the free resonant vibrating state of the sample the frequency was manually tuned and the amplitude of the sample evaluated from the images taken. The improvement of the image quality as a consequence of the mechanical excitation allowed for the evaluation of the envelope of the resonant vibrating state to gain further experimental information.

Further improvements of the experimental setup should include an automated frequency and amplitude detection system in order to measure the dynamics of the vibration behavior of the sample.

Dynamic vibration experiments have also been performed inside of a TEM. Besides the structure of the CNT, the fixation of the CNT to the tungsten wire was investigated in detail. The typical mounting of a CNT onto a tungsten wire is shown in fig. 3.9. The most important aspects of the mounting in conjunction with the bending experiments are shown. On the right side it shows the onset of the free standing CNT with a thin cover of amorphous carbon. Also other features of in-situ iron-filled CNT, such as spherical particles on the surface and a short iron nanowire inside the CNT core are shown. Besides the tip of the tungsten wire also the amorphous carbon deposition that glues the CNT to the tip is clearly visible. It has been observed by TEM investigations that the vibrating CNT moves elastically within the amorphous carbon deposition, indicating that the mounting is not perfectly stiff.

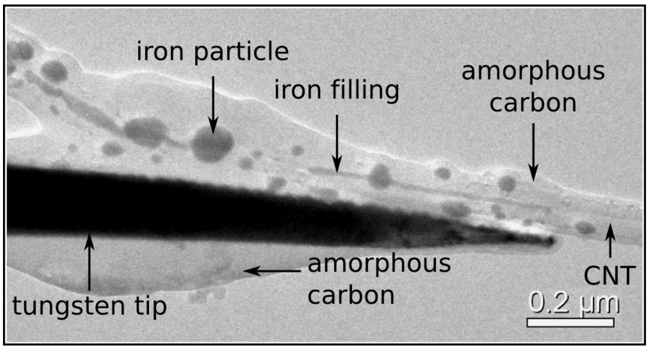

Figure 3.9: Typical mounting condition of a CNT. On the right side the onset of the free standing CNT is visible. Also the tungsten wire and the amorphous carbon deposition can be seen, and furthermore iron particles on the surface and a small part of iron filling.

The structure of CNT has been investigated inside TEM in order to obtain information about the carbon shell structure, the iron filling and deposition of amorphous carbon on the CNT surface. The outer and inner diameter was measured from TEM micrographs. As an example of special structural features, a volume defect is shown in fig. 3.10. It includes all relevant effects such as a complex morphology of the filling and thereby affected shape of the carbon shells. Furthermore, it shows the deposition of an unusually high amount of amorphous carbon on the surface of the CNT. Some of the carbon was previously deposited during imaging.

3.2.4 Static bending

Another method for measuring the elastic bending modulus of carbon nanotubes is the static bending. In the present work a setup that combines the advantages of force deflection measurement of conventional AFM with the advantages of TEM imaging was developed. Static bending was achieved by using a conventional AFM cantilever and a TEM nanomanipulator (Nanofactory). The setup for the static bending method

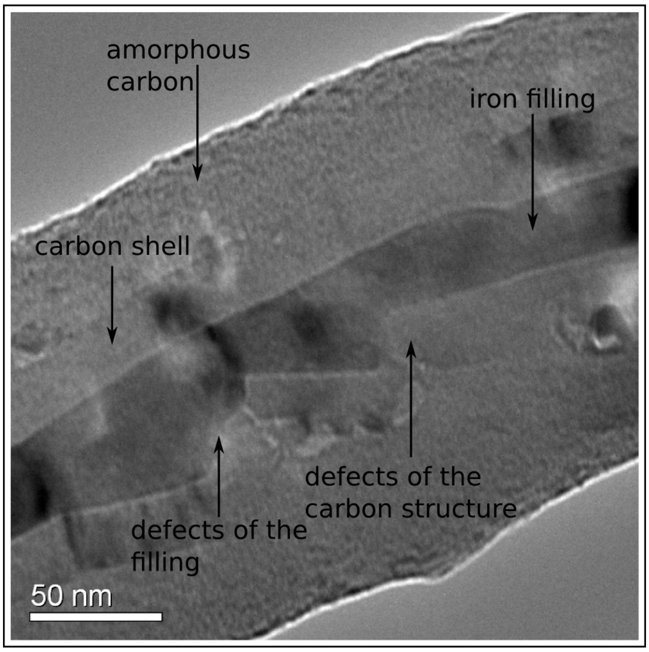

Figure 3.10: Typical large volume defects of an iron-filled CNT. The micrograph shows the shape of the filling and the carbon shells as well as amorphous carbon deposition.

is shown in fig. 3.11. In preparation of the experiment a conventional conducting AFM cantilever with a known spring constant was mounted onto a small isolating glass substrate with the cantilever tip almost in the center of the working area (eucentric focus) of the transmission electron microscope. The cantilever itself was grounded to avoid charging during imaging. The tungsten tip with a free standing carbon nanotube was mounted to the sample holder of the TEM nanomanipulator. By using the piezo scanner which can move in the x-,y- and z-direction the sample was attached to the cantilever tip, whereas it has been checked that the tip of the tungsten wire and the cantilever tip were approximately in the same focus plane. After the CNT snapped into contact with the cantilever tip it was affixed by deposition of amorphous carbon using a concentrated electron beam. No force has been applied to the carbon nanotube until then.

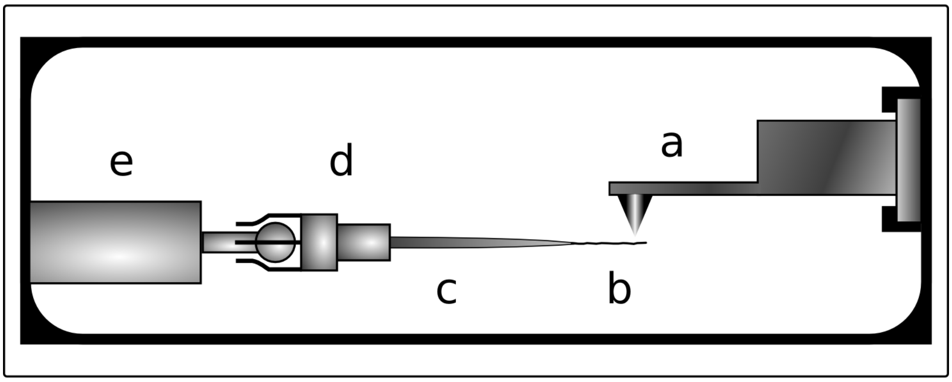

Figure 3.11: Sketch of the experimental setup for static bending inside TEM. a) cantilever with known spring constant, b) CNT sample attached to c) a tungsten nanowire as sample holder, d) sample holder TEM and e) piezo actuator head.

The cantilever was placed such as the bending of the CNT could be observed directly in the focus plane of the TEM. From the cantilever deflection and its known spring constant the applied force could be calculated. Before a force was applied a sequence of micrographs was taken in order to obtain the initial curvature of the unloaded state of the CNT under investigation. Using this curvature information the shape of the bending curve of the loaded state could be extracted afterwards. The principle of the experiment is shown in fig. 3.12. In $\boxed{\text{A}}$ no force was applied to the CNT. The amorphous carbon deposition that pinned the CNT onto the tungsten wire and the cantilever tip respectively is illustrated. After the initial state of the complete CNT has been recorded, an image of the initial position of the cantilever tip relative to the image border was taken. For the following micrographs all imaging conditions, in particular the magnification and focus, were kept constant and only the beam shift was used when necessary. To apply a force to the CNT the tip holder with the CNT sample was moved against the cantilever. Thus the cantilever was deflected and the CNT bent as it is shown in fig. 3.12 $\boxed{\text{B}}$. After the movement of the nanomanipulator was completed, the displacement of the cantilever tip d_{Cant} was measured relative to the image boundary again. It was crucial, that the field of vision did not change, since the boundaries were used to determine the tip position between the actual and the previous state. This required the maintenance of the imaging parameters so that the image frame border was at the very same position and only the cantilever tip relative to the boundary moved. Ensuring these requirements the acting force after each step was obtained from $F_i = k_{Cant} \sum\limits_i d_{Canti}$ where k_{Cant} is the known spring constant of the cantilever. The bending curve of the CNT under different load was measured. Before each increase of the applied force an image of the previous tip position was taken. After

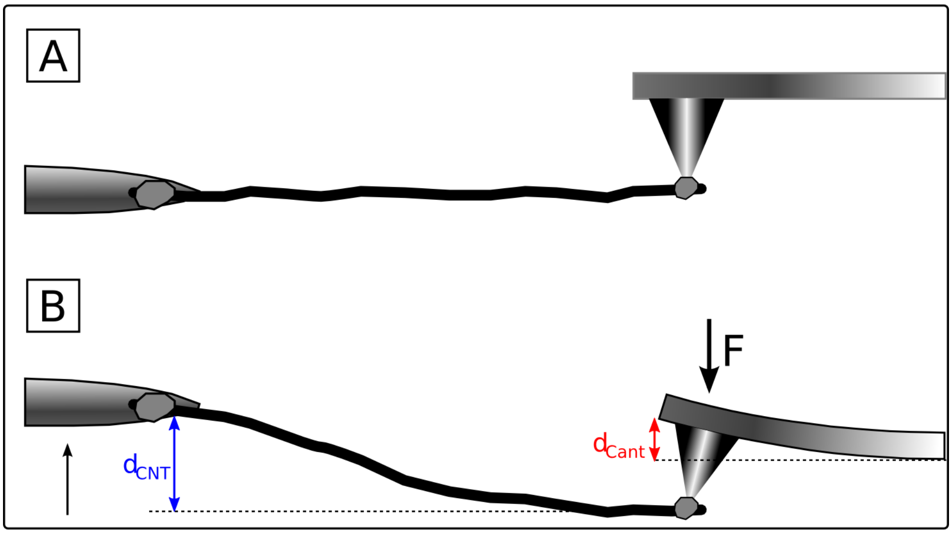

Figure 3.12: Principle of static bending inside a TEM

the force was increased the cantilever position was measured within the same frame again and afterwards a sequence of micrographs of the bent CNT were captured. By carefully reconstructing of the total image of the CNT the overall bending curve has been extracted.

The deflection of the free end of the CNT d_{CNT} was obtained by superimposing the image of the unloaded CNT and the actual loaded state which is shown in fig. 3.13. By superposing the tungsten wire side of the initial unloaded and the actual loaded state exactly one on top of each other, the deflection of the side where the force was applied (*free end*) could be obtained. This value was necessary for the formulation of the boundary conditions in the model.

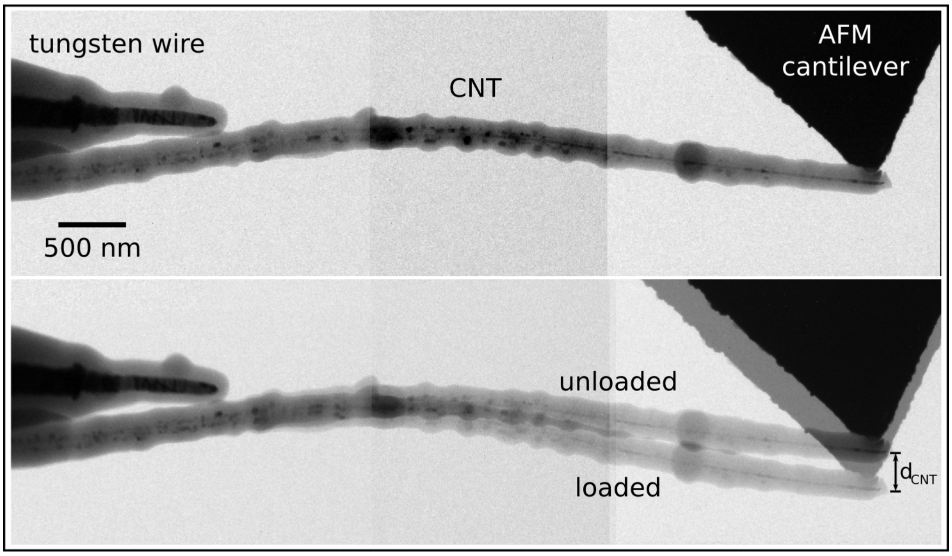

Figure 3.13: Deflection of the free end due to the acting force.

In order to extract the real bending curve shape the curvature of the unloaded CNT was subtracted from each CNT bending curve under load. Afterwards, the Euler-Bernoulli beam model was fitted to these data.

$$\frac{\partial^2}{\partial x^2}\left(E\,I\,\frac{\partial^2 y}{\partial x^2}\right) - \sigma\,A\,\frac{\partial^2 y}{\partial x^2} = -w \tag{3.25}$$

where $w = \frac{F}{L}$ is the linear force density. The second term on the left hand side denotes any axial forces which may act on the nanotube. For the sake of simplicity these were omitted and the experiments were conducted in a way to ensure that this assumption was reasonable. The boundary conditions depend on the particular properties of the fixation points. No deflection was assumed at the left side of the beam where it was mounted to the tungsten wire. The *free end* deflected as a consequence of the applied load but due to the amorphous carbon clamping a non zero bending moment was assumed. The corresponding boundary conditions can be formulated like this

$$\begin{aligned} y(x)|_{x=0} &= 0 \\ E\,I\,\frac{\partial^2 y}{\partial x^2}|_{x=0} &= \alpha_1 \frac{\partial y}{\partial x}|_{x=0} \\ E\,I\,\frac{\partial^2 y}{\partial x^2}|_{x=L} &= -\alpha_2 \frac{\partial y}{\partial x}|_{x=L} \\ \frac{\partial}{\partial x}\,(E\,I\,\frac{\partial^2 y}{\partial x^2})|_{x=L} &= F \end{aligned} \tag{3.26}$$

Therefore the shape of the bending curve differs from that of a simple beam with a concentrated load acting on the free end.

3.3 Results and discussion

Before the results of the measurement of the mechanical properties will be presented, a short remark on the selection of the CNT for the investigation should be given. The up-taking of CNT by sharply etched tungsten wires or cantilever tips requires a free standing reachable section of the CNT. Therefore, taking such CNT from an as-grown sample prefers mostly straight aligned representatives. Often these CNT have less defects in their structure and are also filled with extended iron nanowires. These CNT are required and used for the preparation of magnetic force microscopy probes [36, 54].

3.3.1 Static bending

Static bending of micro- and nanostructures inside TEM is a convenient method to measure the material properties while also gaining information about structural details. In the following section the measurement of elastic properties of iron-filled CNT is shown based on an example.

In fig. 3.14 the full length of an iron-filled CNT is presented, which corresponds to the CNT shown in fig. 3.13. Further structural details of the CNT are shown in fig. 3.15. The CNT was almost completely filled with a continuous iron nanowire with a total length of 14 µm. Only a length of 2 µm close to the mounting point was unfilled. The BSE contrast of the filling is shown in the upper right part of fig. 3.14. In the upper left part of the figure details of the mounting area are presented. Unfortunately, a part of the CNT broke off during the nanomanipulator infiltration into the TEM, thus only a short part of ≈5 µm remained for the static bending measurement. After the static bending experiment, a part of the amorphous carbon broke off when pulling back the CNT from the cantilever tip and the actual diameter of the CNT became visible. The outer diameter of the CNT could be determined as 70 nm.

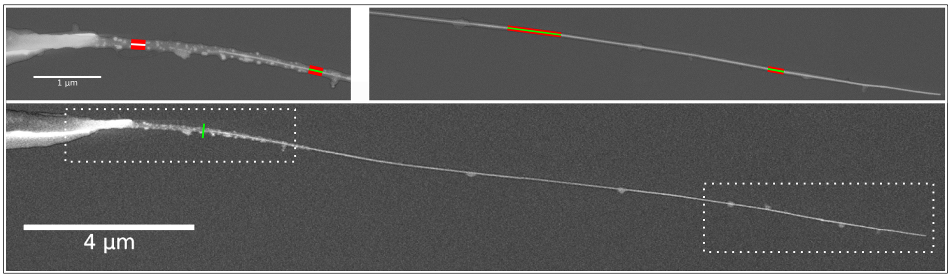

Figure 3.14: The bottom part shows a carbon nanotube with a long and continuous iron filling. The CNT is about 16 µm long and the filling is about 14 µm. In the upper left corner, the section of the CNT is shown, which was measured by the static bending method.

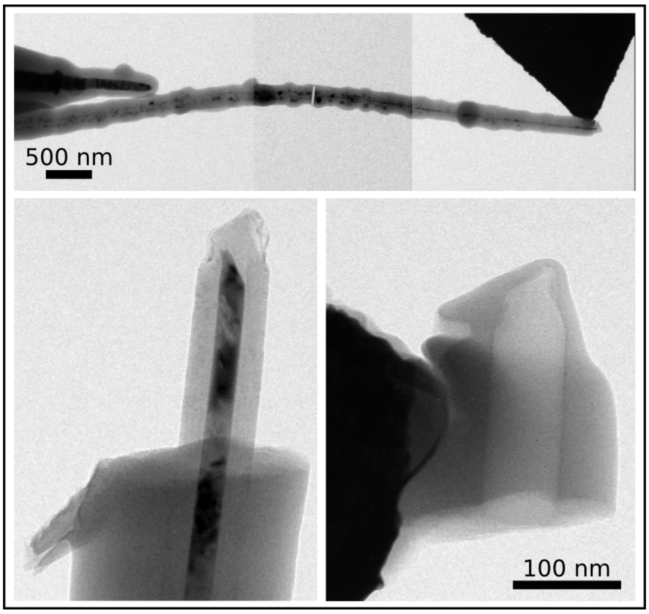

Figure 3.15: Structural details of the CNT. The lower two images show part of the CNT structure and the corresponding amorphous coating attached to the cantilever tip.

The spring constant of the cantilever was measured by the thermal vibration excitation method [212]. Considering the geometry of the gold coated silicon nitride cantilever a spring constant of ≈4.2 $\frac{\mathrm{N}}{\mathrm{m}}$ was found. In fig. 3.16 four representative bending curves of the CNT and the corresponding fits for each load applied are shown. The forces were in the range of 0.6 µN to 4.0 µN and the resulting deflections of the *cantilever end* in the range of 288 nm to 1351 nm.

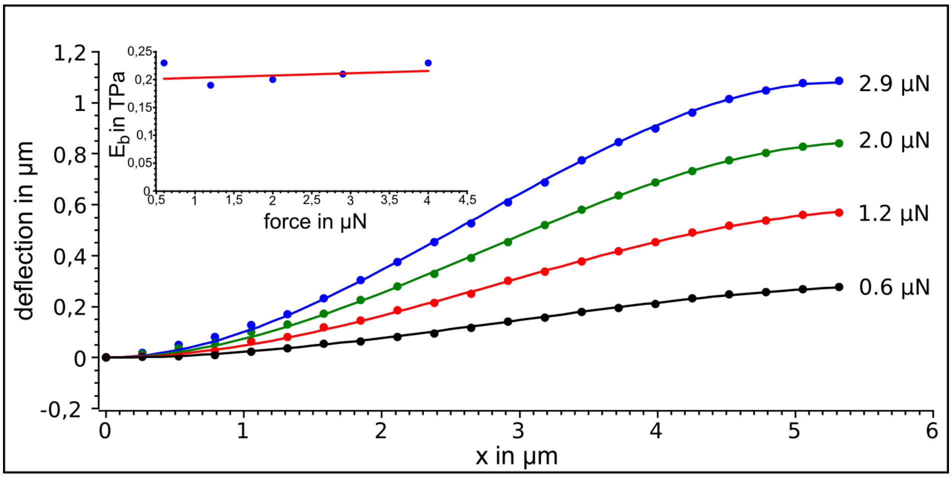

Figure 3.16: Static bending curve of a CNT for different loads. The inset shows the elastic modulus and the corresponding forces.

Since the CNT was mounted by amorphous carbon deposition on both sides of the CNT, the elastic properties of these connections needed to be considered. In that case two torsion spring constants α_1 and α_2 were introduced. In the inset of fig. 3.16 the effective elastic bending modulus versus the corresponding applied force is shown. The obtained E_b values are below the average value for forces in the range of 1 µN to 3 µN indicating that a small compressive stress was applied to the CNT. For a higher force of 4 µN the E_b increases above the average which might be the consequence of a tensile stress within the CNT.

The cross section of the beam consists of the iron filling, the CNT shells and the amorphous carbon deposition. Referring to eq. 3.33, only the effective bending stiffness can be measured in a bending experiment. The elastic modulus of iron is at least one order of magnitude smaller than that expected for the CNT. Also the diameter of the filling is small in comparison to the CNT diameter. Therefore the contribution of the filling can be neglected. The elastic properties of the amorphous carbon are unknown. Assuming a very low elastic modulus for the amorphous carbon a CNT diameter of 70 nm can be used. In that case an elastic modulus of about 20 TPa would have been obtained for the CNT. However, this value is unreasonable high. Unfortunately, for this particular sample the elastic properties of the amorphous carbon can not be determined. Thus, in a second approach the whole carbon structure was considered as pristine carbon shells and a value of 240 nm for the outer diameter was assumed. In that case an effective elastic modulus of $\mathrm{E_b} = 0.22 \pm 0.04\,\mathrm{TPa}$ was found. This value is a lower estimate for the elastic modulus. However, it has to be stressed, that with this specific experiment the E_b of the pristine shells could not be revealed. This particular CNT in full length without amorphous carbon contamination was measured by dynamic bending as well and an effective elastic modulus of 0.57 TPa was found (compare tab. 3.2 in section 3.3.2.6).

For high sensitive measurements the spring constant of the cantilever should be in the same range as that of the sample (CNT) measured. Since axial forces were not considered in the used model a brief discussion of their influence on the bending behavior and the estimated elastic bending modulus is given here. A tensile or compressive stress might occur if the applied force does not only act perpendicular but also has a component in the direction of the beam axis. The movement of the cantilever tip and also the CNT free end proceed on curved paths. Depending on the deflection amplitude of the cantilever the distance between the tungsten and cantilever tip can change. If, e.g., a soft cantilever in relation to the stiffness of the CNT is used the cantilever tip tilts towards the CNT resulting in a force component in parallel to the x-axis. If there is a compressive stress, the CNT experiences an additional bending moment and appears less stiff. In the simplified model the bending and thus the curvature of the beam is only expressed by the effective elastic modulus. In the case of compression of the CNT, mainly at small deflections, the used model leads to an underestimation of the elastic bending modulus. On the contrary, a tensile stress causes stiffening and the CNT would seem more rigid due to the reduced curvature. If this tensile effect is not taken into account it results in an overestimation of the elastic modulus. In the present experiments there was evidence for a *stiffening* of the CNT at higher forces and deflections, as it is visible in the inset in fig. 3.16. The value of the elastic modulus rises with increasing deflection, indicating the incidence of tensile stress. Also a reduced E_b has been found for lower forces, which might be a consequence of compression. However, no axial stress has been considered in the present evaluation. A more detailed investigation should consider tensile forces. The experimental challenge is the simultaneous measurement of axial and vertical forces in AFM and especially inside TEM where only the bending of the CNT and cantilever within the focus plane can be measured.

Besides the static bending of CNT inside a TEM employing an AFM cantilever another approach was used [213]. Due to the high magnetic field of about 2.16 T of the objective lens system at the position of the sample inside a TEM, a lorenz force is acting on the CNT, if a current is flowing through it. The force per unit length is almost homogeneous. By these static bending experiments again the importance of the consideration of the elastic mounting properties has been confirmed. Furthermore, inhomogeneities of the CNT cross section originating from amorphous carbon deposition were resolved and reasonable values for the elastic modulus of the CNT as well as for the amorphous carbon have been deduced.

The advantage of both static bending methods is the knowledge about the quantity of the load acting on the structure. Furthermore, in case of low contact resistance both methods might also be suitable for combining electrical and mechanical measurements on the same sample. A combination of Lorentz force excitation and a soft conducting contact mode cantilever might be used to measure also tensile forces and the impact of axial stress on the electrical and mechanical behavior of CNT.

3.3.2 Resonant dynamic bending

The main method for the investigation of the mechanical properties of iron-filled CNT within this work was the resonant dynamic bending method. This method is capable to measure the mechanical properties such as the bending stiffness, from which the elastic modulus can be deduced. It also gives information about the possible vibrational behavior of the investigated CNT in comparable application setups such as probes for scanning probe microscopy and actuators.

3.3.2.1 Amplitude versus frequency

The vibrational amplitude versus frequency was measured in order to obtain the resonance frequency. In fig. 3.17 at the bottom part the resting state and in the upper part the first resonant vibrational state of a CNT is shown. The amplitudes were obtained by taking SEM images of vibrational states at several driving frequencies.

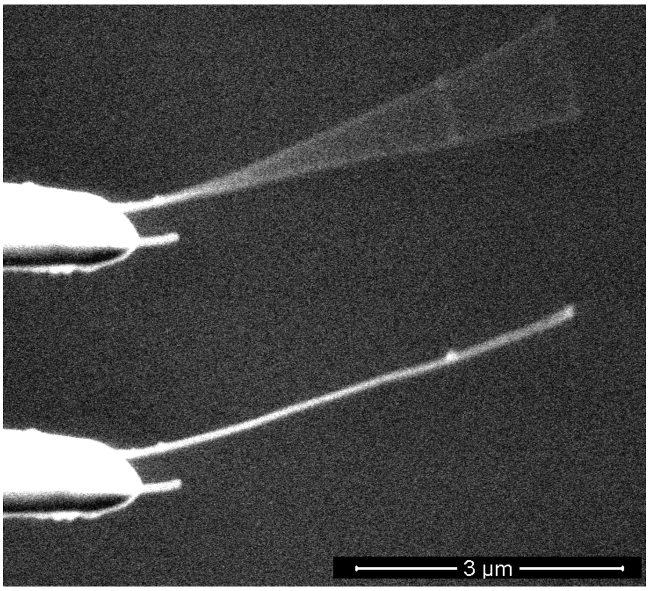

Figure 3.17: The vibration state of an excited CNT and the resting state of a CNT are shown.

However, only the projection of the vibrational amplitude into the imaging plane of the SEM could be measured for each excitation frequency. An example of the amplitude versus the excitation frequency is presented in fig. 3.18. The change of the vibration plane of a CNT is shown in the upper part of this figure. The five images show the transition from the resonant excitation of one main axis to the other main axis via intermediate states with elliptical trajectories of the free end. The two resonance frequency peaks shown in fig. 3.18 might be explained by two different influencing factors. One reason are the non-isotropic properties of the CNT clamping generated by amorphous carbon deposition. Another could be a non- circular cross section of the CNT. Even though an elliptical cross section could not be measured inside SEM, the observation of two adjacent resonance peaks suggests an elliptical cross section. Within this particular discussion the presence of a torsion spring like mounting of the CNT is not regarded. Assuming an elliptical beam cross section the resonance frequency of each peak is given by

$$\begin{aligned} \nu_1^D &= \frac{1}{2\pi}\frac{\hat{\beta}_1^2}{L^2}\sqrt{\frac{E\,I_D}{m}} = \frac{1}{2\pi}\frac{\hat{\beta}_1^2}{L^2}\sqrt{I_D}\sqrt{\frac{E}{\rho\,A}} \\ \nu_1^d &= \frac{1}{2\pi}\frac{\hat{\beta}_1^2}{L^2}\sqrt{\frac{E\,I_d}{m}} = \frac{1}{2\pi}\frac{\hat{\beta}_1^2}{L^2}\sqrt{I_d}\sqrt{\frac{E}{\rho\,A}} \end{aligned} \tag{3.27}$$

The elastic modulus E, the cross section area and the mass density m are identical for both main axis. The moment of inertia for an elliptical cross section depends on the bending direction relative to the large or small major axis. If D and d denote the length of the large and small major axis respectively, the moments of inertia are given

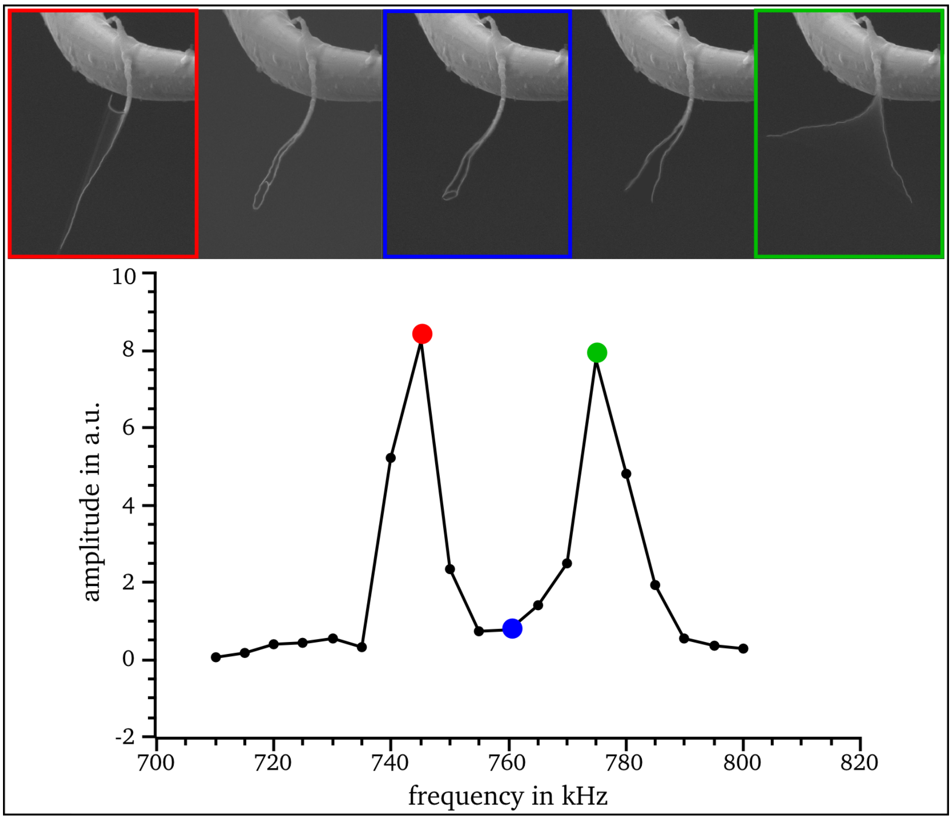

Figure 3.18: The figure presents the amplitude projected into the imaging plane of the SEM. The amplitude of the main axes vibration at different excitation frequencies and elliptical trajectories as transition states are visible.

by

$$
\begin{aligned}
I_D &= \frac{\pi}{4} D^3 d \\
I_d &= \frac{\pi}{4} D d^3
\end{aligned}
\tag{3.28}
$$

where I_D is the moment of inertia of the larger and I_d of the smaller outer main axis respectively. Inserting the expressions from eq. 3.29 into eq. 3.28 the following relation can be found

$$
\frac{\nu_1^D}{\nu_1^d} = \frac{\sqrt{I_D}}{\sqrt{I_d}} = \frac{D}{d} \tag{3.29}
$$

The frequency ratio is proportional to $\sqrt{\frac{I_D}{I_d}}$. Since the mounting of the sample resulted in a random orientation of the two main axes relative to the excitation plane, both axes have been excited in the experiments but with slightly different resulting amplitudes. Thus a frequency ratio of two peaks of fundamental modes related to the two main axes being close to each other gives evidence for an almost circular cross section. The data of the CNT shown in fig. 3.18 suggested only a small deviation of the cross section shape from a circle, which is reflected by the ratio between the two

eigenfrequencies $\frac{\nu_1^{res,D}}{\nu_1^{res,d}} = 1.04$.
As already mentioned above, another even more significant reason to explain the occurrence of two resonance frequencies might be the amorphous carbon deposition of the mounting. The stiffness of the amorphous carbon might be highly anisotropic depending on the deposition conditions. The elastic properties of the deposited carbon are also influenced by the energy of the electrons [210] from the microscope electron beam. The electron energy as well as the electron dose on the backside of the CNT is lower than on top and on the sides of the CNT resulting in anisotropic properties. In general it should be assumed that the amorphous carbon is much less stiff than the CNT itself, which might be the origin for several of the observed effects that are discussed in this work.

In some cases the data of the amplitude versus frequency could not be fitted by a single Lorentzian-shape function. An example is shown in fig. 3.21. The shoulders, such as shown in fig. 3.21, were observed and may indicate a second main axis vibration with a slightly different resonance frequency. A linear combination of two Lorentzian-shape functions was used for the data evaluation. If the corresponding peak frequencies are close to each other the cross section is assumed to be almost circular. In the case of two separated signals the peak corresponding to the resonance frequency resulting in the higher amplitude has been evaluated.

3.3.2.2 Q-factor

The Q-factor is a quantity used to describe the quality of vibrating systems regarding their damping. It is defined by the ratio between the resonance frequency divided by the full width of frequency at half maximum energy eq. 3.30. It measures how much energy of a vibrating system is stored in relation to the energy dissipation in one oscillation cycle. The Q-factor is an important quantity for the description of vibrational behavior of a CNT.

$$Q = \frac{\nu_0}{\Delta\nu} \tag{3.30}$$

The $\Delta\nu$ for the Q-factor was obtained by getting the full width at the maximum amplitude value divided by $\sqrt{2}$ from the fit of the amplitude-frequency measurement. Strictly speaking the Q-factor can only be obtained if the correlation between the amplitude and the exciting frequency shows a Lorentzian-like behavior. In the case of the complex vibration behavior of iron-filled CNT this was not always fulfilled. A large distribution of Q-factors in the range 70 to 800 has been found for iron-filled CNT. Typical examples are shown in fig. 3.19 and fig. 3.20. In the first example, the evaluation of the amplitude as a function of the excitation frequency gave a resonance frequency of $\nu_0 = 2731\,\text{kHz}$ together with a band width of $\Delta\nu = 3.8\,\text{kHz}$ which resulted in a quality factor of 718. The second example shows a resonance frequency of $\nu_0 = 353\,\mathrm{kHz}$ together with a band width of $\Delta\nu = 2.7\,\mathrm{kHz}$ which resulted in a quality factor of 131.

A more complicated relation between the driving frequency and the amplitude is shown in fig. 3.21. In such case no Q-factor has been determined. Since the data points were measured manually the vibration behavior was measured with poor resolution. In order to gain detailed information a more sophisticated experimental setup, that allows for automatic sweeping of the frequency and measurement of the vibration amplitude should be used for further study.

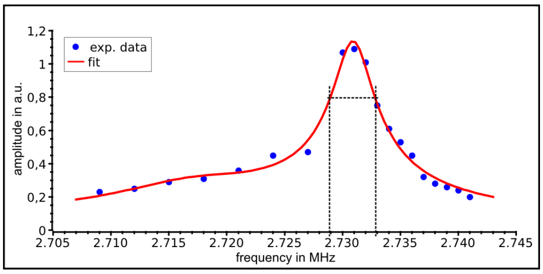

Figure 3.19: Amplitude versus frequency and frequency range that has been used to determine the Q-factor of 718 of the CNT.

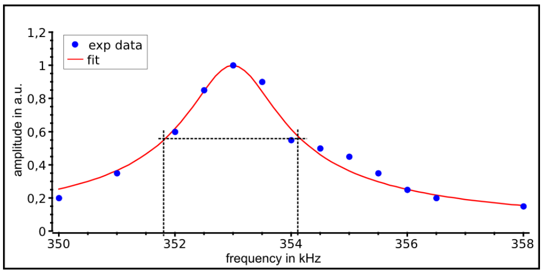

Figure 3.20: Amplitude versus frequency and frequency range that has been used to determine the Q-factor of 131 of the CNT.

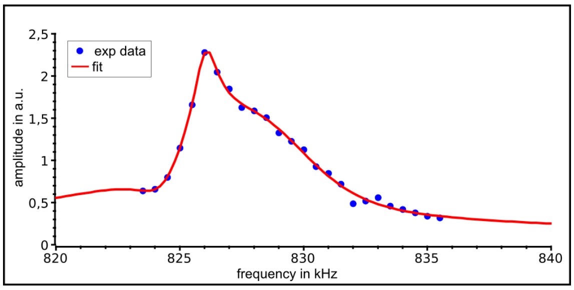

Figure 3.21: Non symmetric shape of the amplitude as function of the driving frequency. The data was fitted by a linear combination of three Lorentzian-shaped functions.

The low Q-factor of multi-walled CNT might be explained by structural defects within the carbon structure [214]. In the concept of continuum mechanics they might be interpreted as *bulk defects*. Ono et al. reported a Q-factor of 800 for oscillation of CNT under high vacuum conditions [214]. Contaminants on the CNT surface were desorbed by heating in vacuum and a decrease of energy loss has been observed. However, the Q-factor remained below 1000 and suggested bulk defects as the origin of the energy loss. The Q-factor is related to the energy dissipated during the vibration of the system. Several mechanisms result in energy loss during vibration such as intrinsic internal friction, acoustic emission from a support or via air, friction at the surface and thermoelastic loss [214]. The latter is a type of internal friction and occurs in vibrating structures since generated heat leads to spatially limited areas with higher and lower temperature that can not reach thermal equilibrium [215, 216]. An irreversible heat flow leads to additional energy dissipation. However, this loss mechanism scales with the size of the structure and is less important in nanoscale objects [215]. An alternating thermal current is driven by the time dependent thermal gradient within the structure. The surface friction effect was identified to be important in the vibration of silicon nanoneedles. Internal friction, especially due to internal defects and their dynamics within the microstructure of the CNT is thought to be the most important energy loss mechanism [214, 216]. Amorphous carbon layers of several nanometers on the surface of the CNT might contribute to the energy loss as well. As shown in fig. 3.1 the extension and compression of a structure during bending of the beam is highest on the upper and lower surface, respectively. Thus, the deformation and strain of the CNT itself is smaller than that of the amorphous layer. The higher the deformation, the higher is the dissipation of energy and more heat can be generated within the amorphous carbon structure [217]. Thus, the low Q-factor of the iron-filled CNT might be partly related to the existence of amorphous carbon.

Nevertheless, in literature small Q-factor far below 1000 have also been reported for MWCNT grown by arc discharge (Q=500) [188] and thermal CVD (200-800) [214] and (115) [218]. Sazonova et al. [178] found Q-factors in the range of 40 to 200 for single-walled and double-walled CNT. The resonance frequencies were between 3 MHz to 200 MHz. Other authors reported Q-factors in the range of 150 for multi-walled CNT and 2500 for single-walled CNT [188, 219, 220]. However, no information about the existence of amorphous carbon was reported.

Due to the thickness of the amorphous carbon and its formation during the synthesis it might be considered as an intrinsic effect and not as surface defect in the present study. As mentioned in the synthesis chapter, the formation of amorphous carbon during the synthesis of in-situ iron-filled CNT is often inevitable. Thus, the iron-filled CNT possess a layer of amorphous carbon that contributes to the energy loss and can be thought of as an internal defect. However, no annealing experiments have been performed. But a discrimination between adsorbates and internal defects is not clearly possible, since the heating removes the adsorbates but also heals defects in the structure [214, 221]. For very small structures with a high surface to volume ratio such as CNT it is difficult to distinguish between pure surface and bulk defects. Also clamping losses can not be ruled out, especially when considering, that the mounting is not perfectly rigid but elastic.

3.3.2.3 Resonance frequency

A homogeneous, simple vibrating beam has a set of characteristic eigenfrequencies given by eq. 3.31, which depends on the geometry, the mass and elastic properties of the material.

$$\nu_j = \frac{1}{2\,\pi}\,\frac{\hat{\beta}_j^2}{L^2}\,\sqrt{\frac{E_b\,I}{m}} \tag{3.31}$$

Where $\hat{\beta}_j$ is the mode depended dimensionless eigenvalue, L is the length, m is the mass per unit length, I the bending moment of inertia of the beam cross section and E the elastic bending modulus of the beam material. Resonant dynamic bending methods are often used to determine material properties in the case of a known and defined geometry. Assuming a homogeneous beam with a circular ring cross section ($I = \frac{\pi}{64}\,(d_o^4 - d_i^4)$), homogeneous material density across its whole length ($m = \rho\,A$, $A = \frac{\pi}{4}\,(d_o^2 - d_i^2)$), the eigenfrequency is given by eq. 3.32

$$\nu_j = \frac{1}{8\pi}\,\frac{\hat{\beta}_j^2}{L^2}\,\sqrt{d_o^2 + d_i^2}\,\sqrt{\frac{E_b}{\rho}} \tag{3.32}$$

In most cases the CNT can be assumed as a homogeneous beam. However, the cross section in case of the material of the present study can be more complex. In general three different contributions have been found. The carbon shell structure itself, the filling and often an amorphous carbon layer were observed. Since all three contributions are symmetrical around the centerline of the beam their contributions to the total bending stiffness EI_n can be summed up according to the rule of Steiner (eq. 3.33).

$$I_{ni} = I_{si} + A_i\,a_i^2 \tag{3.33}$$

Where I_n is the moment of inertia relative to the off-centroid n-axis which has the distance a_i relative to the axis that goes through the centroid of I_s which in turn is the moment of inertia relative to this centroid axis. The beam cross section area is denoted by A_i. The total moment of inertia I_n is the sum of all partial moments of inertia (eq. 3.34).

$$I_n = I_{n1} \pm I_{n2} \pm I_{n3} \pm \ldots \tag{3.34}$$

Since all three cross sections have the same reference axis, that is furthermore located in the center of mass of the corresponding cross section no additional term $A_i\,a_i^2$ has to be considered, because all a_i^2 are zero. With eq. 3.35 the total bending stiffness of the filled CNT can be expressed by

$$E_n I_n = E_{CNT} I_{CNT} + E_{fill} I_{fill} + E_{aC} I_{aC} \tag{3.35}$$

The influence of the mass per unit length to the resonance frequency can be obtained in a similar way according to eq. 3.36.

$$\begin{aligned} m_n &= m_{CNT} + m_{fill} + m_{aC} \\ &= \rho_{CNT}\, A_{CNT} + \rho_{fill}\, A_{fill} + \rho_{aC}\, A_{aC} \end{aligned} \tag{3.36}$$

For the density of the CNT a value of 2200 kg/m^3 and for the iron filling a density of 7874 kg/m^3 has been assumed. According to Wang et al. [222] a density of 2000 kg/m^3 was used for the amorphous carbon. However, also values in the range 1800 kg/m^3 to 2100 kg/m^3 were reported.

The presence of amorphous carbon on the surface of the CNT increases both the outer diameter and the mass. While its contribution to the enhancement of the bending stiffness has to be considered due to the significant impact of the outer diameter on the moment of inertia, the effect on the mass is rather low. Especially in comparison with the mass influence of the iron filling the mass of the amorphous carbon is a minor contribution. Even though the inner diameter was relatively small the high density of iron, that is approximately three times higher than the density of graphite, leads to a significant contribution of the filling mass to the resonance frequency and can not be neglected. An empty CNT of the same length and carbon structure but without an iron filling would have a much higher resonance frequency, thus for a given geometry of the CNT the mass of the filling reduces the resonance frequency. The mass of the filling is especially important if it is located close to the free end of the vibrating CNT. The mass density m of the filling was calculated by $\rho_{Fe}\,\frac{\pi}{4}\,d_i^2$ where d_i is the inner diameter of the CNT. As shown in fig. 3.14 long and aligned CNT were most often filled with extended iron nanowires. Nevertheless, small interruptions or unfilled sections can not be ruled out. Furthermore, the distribution of amorphous carbon is also not always homogeneous along the CNT surface. It was often concentrated in the vicinity of the mounting, where it contributes to both the stiffness of the beam but also to the elastic properties of the mounting. Strictly speaking each inhomogeneity such as interruptions of the filling or local depositions of amorphous carbon actually limits the simple application of eq. 3.32 and requires the segmentation of the beam into sections with constant properties. Each section is connected to its environment by either natural or boundary conditions. The treatment of such a multisegment system can easily become quite elaborate to be analytically solved and for more detailed studies numerical methods should be used.

3.3.2.4 Resonance frequency shift

The resonance frequency of a vibrating CNT depends on the length, the bending stiffness and the mass. There are several reasons for a frequency shift of a vibrating beam and a discrimination of the competitive effects is hardly possible [216].

A downward resonance frequency shift was more often observed during the conducted experiments. In that case the deposition of additional contaminations from the microscope atmosphere on the surface of the CNT was the dominating effect. In order to show the frequency shift due to the formation of a localized mass as consequence of a local mass deposition, amorphous carbon has been deposited at the tip of a CNT. In fig. 3.22 the drift of the resonance frequency versus time and the corresponding CNT are shown. The total imaging time for this CNT was 120 min and the deposition of amorphous carbon was clearly visible. In order to investigate the influence of the mass deposition, every three minutes the resonance frequency was measured. In case of the upper curve in fig. 3.22 the CNT was measured every three minutes and in between the CNT was not exposed to the electron beam. Thus the mass deposition and corresponding frequency shift could directly be related to the imaging time which was approximately 20 min, that is almost one minute per point. The total frequency shift was 31 kHz. The lower curve in fig. 3.22 was obtained by a permanent exposure to the e-beam. Therefore, the CNT was exposed to the electron beam for 60 min. The significant higher frequency shift was 100 kHz and thus about three times higher. In total a layer of approximately 60 nm thickness was deposited on the tip of the CNT.

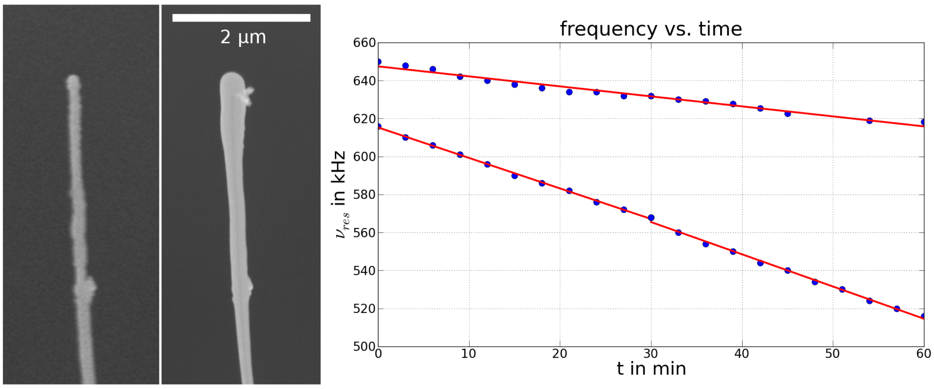

Figure 3.22: Resonance frequency shift due to mass deposition. The upper curve shows the deposition behavior without permanent imaging of the CNT. The lower curve shows the frequency shift for a permanent observation.

Especially if the amorphous carbon is located close to the free end of the vibrating CNT the resonance frequency of the first mode would be reduced. Consequently, the imaging time was kept as short as possible and furthermore a low pressure inside the SEM was maintained. Since the deposition rate of gaseous carbon is smaller for high e-beam energy an acceleration voltage above 15 kV was chosen. However, at higher electron energy the strength of the deposited material increases [115].

In the case of an adsorption of material a reduction of the resonance frequency due to the increase of the vibrating mass can be expected. However, assuming the adsorption of amorphous carbon on the surface of a CNT the resonance frequency might even rise, if the influence of the increasing moment of inertia exceeds the influence of the additional mass. In fig. 3.23 a simulation of the resonance frequency shift as a function of increasing outer diameter is shown. If the additional material has nearly the same elastic properties and density as the vibrating beam, the resonance frequency will always increase (blue curve in fig. 3.23). The red curve represents the case of an diameter increase due to an amorphous carbon layer with a lower elastic modulus in comparison to a diameter growth with the same properties (blue). In a certain diameter range the resonance frequency drops down due to the higher beam mass. When the diameter increases further, its contribution to the bending stiffness dominates the resonance frequency behavior. In the present experiments a downward shift of the resonance frequency has been observed.

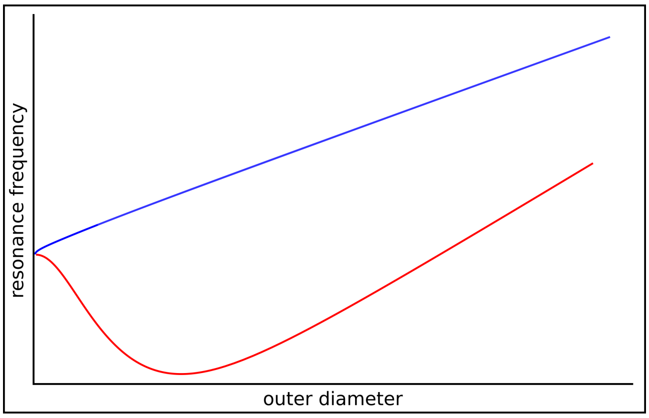

Figure 3.23: Simulation of resonance frequency shift due to increase of the outer diameter and mass deposition. The blue curve shows the increase of the outer diameter due to material with the same properties as the original beam. The red curve shows the deposition behavior for material with different material properties than the beam, especially a lower elastic modulus.

3.3.2.5 Resonance frequency ratio

A vibrating beam possesses different modes, each with a characteristic eigen frequency, which depends on the geometry, the material and the boundary conditions. For an ideal homogeneous, one side clamped beam a resonance frequency ratio $\frac{\nu_2}{\nu_1}$ of 6.3 between the second and first eigenmode is expected. In the present work only the first two eigenmodes were considered.

In fig. 3.24 the resting state of a completely iron-filled CNT together with its first and second resonant eigenmode vibration is presented. The resonance frequency of the first eigenmode was 747 kHz and of the second eigenmode 3182 kHz. The resonance frequency ratio of this particular iron-filled CNT was 4.25. The envelope of the first vibrating eigenmode in fig. 3.24 (middle position) was fitted using the Euler-Bernoulli beam model as shown in fig. 3.25 . The assumed elastic properties of the clamping have been considered by using a torsion spring like formulation of the corresponding boundary condition as given by eq. 3.15. For the elastic clamping a torsion spring constant $\alpha = 4.2 \times 10^{-12} \, \frac{\mathrm{N\,m}}{\mathrm{rad}}$ was found. The resonance frequency ratios of several

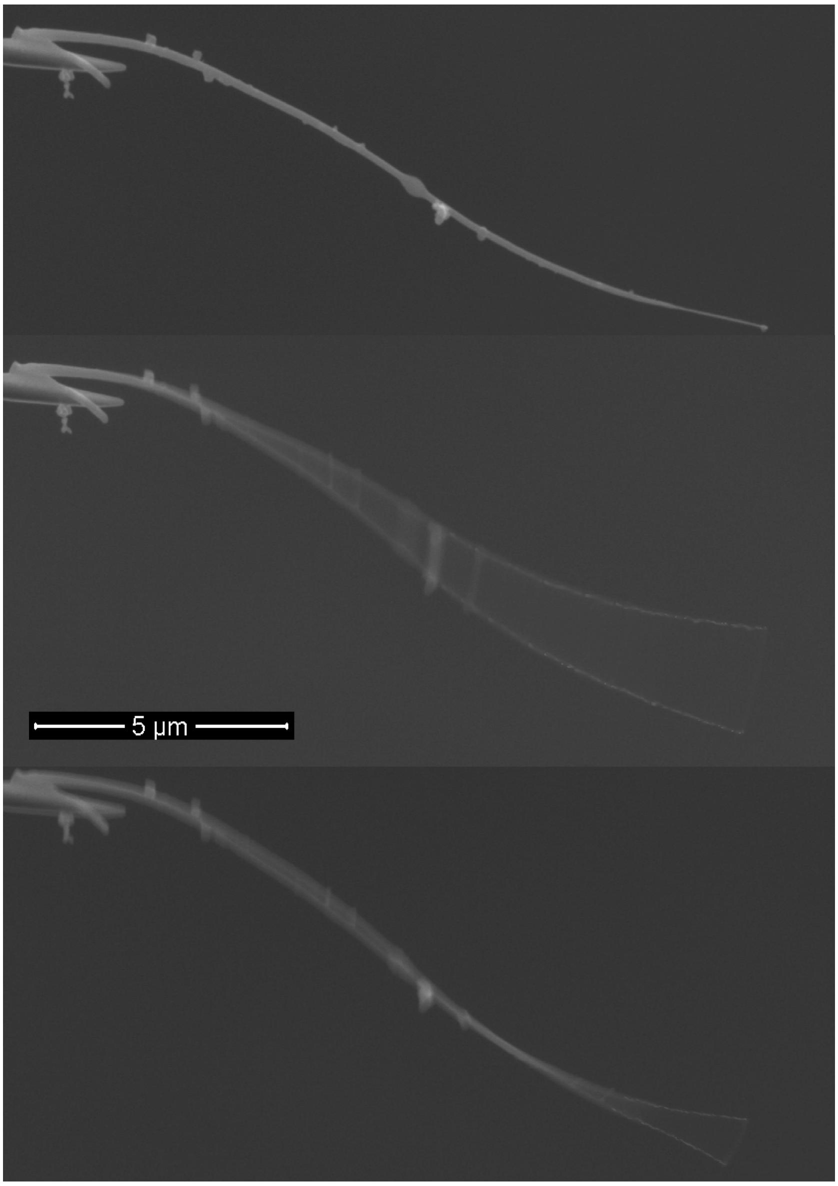

Figure 3.24: Vibration of an iron-filled CNT. The upper part shows the resting state. In middle the first eigenmode and at the bottom the second eigenmode vibration is shown. The resonance frequency was 747 kHz for the first mode and 3182 kHz for the second mode.

iron-filled CNT investigated in the present work are presented in tab. 3.2 on page 133 and were below the expected value of 6.3.

The evaluation of the bending curve of the resonant vibrating state furthermore indicated the elastic properties of the CNT mounting, since a non-zero slope in the vicinity of the mounting area was frequently observed within this work. The fit of the bending curve supports the experimental observation related to the elastic mounting properties as mentioned before and shown in fig. 3.9. In addition, the curvature of the bending curve deviated from that of the ideal simple Euler Bernoulli beam which is illustrated in fig. 3.29 and will be discussed in detail in 3.3.2.6.

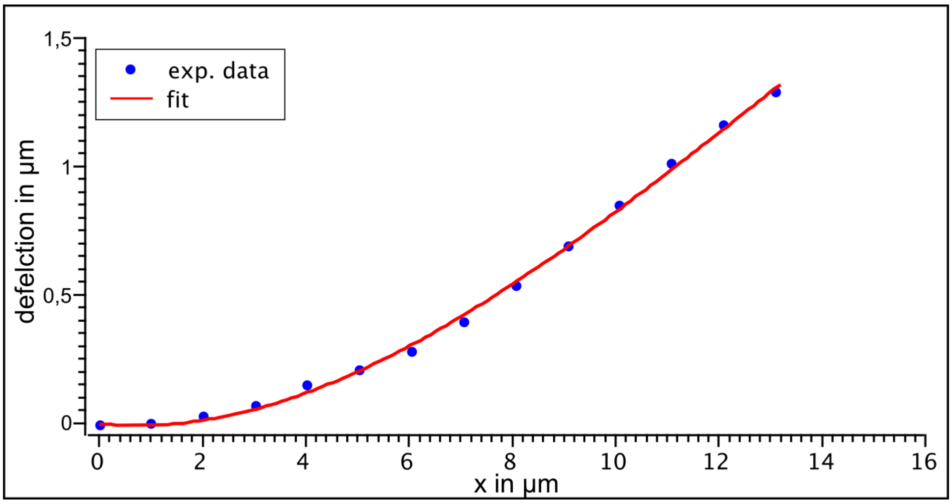

Figure 3.25: Envelope of vibrating bending curve of the CNT corresponding to fig. 3.24.

The presence of localized masses could be a reasonable explanation for a reduced resonance frequency ratio. Depending on the amount and position of a localized mass, it has been shown, that the resonance frequency ratio can be lower or higher in comparison to an ideal homogeneous beam [205]. For a point mass that was 20 % of the total beam mass it was found, that the resonance frequency ratio is in the range of 5.5 to 6.3, if the position of the point mass is between the mounting point and the half beam length (fig. 3.2 on page 98). If the point mass is somewhere between the half beam length and the beam tip, the resonance frequency ratio was in the range of 6.3 to 7.5. Within their work Wang et al. [205] were focussed on the effect of a small point mass but also indicated, that localized defects might have similar effects on the vibration behavior of CNT. If an attached localized mass is the origin of the frequency shift the bending stiffness of the CNT itself is not changed but the kinetic behavior during the oscillation is affected. In some rare cases a distribution of particles was found, as shown in fig. 3.30, but these particles were not attributed by the used analytic model. In the present work the influence of point masses was not explicitly considered since in the majority, localized mass accumulations of iron particles were not observed. Nevertheless, diameter variations of the iron filling inside of the CNT could lead to a point like mass distribution. Especially for CNT revealing a non-continuous and inhomogeneous iron filling a model that considers the influence of localized masses would be useful for further studies.

The properties of the clamping of the CNT to the support did also have an influence on the vibration properties and thus the resonance frequency ratio. The clamping properties of CNT used in the experimental setup were described by the boundary conditions of the model of the vibrating beam. The solution eq. 3.20 of the eq. 3.19

satisfies the boundary conditions eq. 3.13 and therefore the slope has to be zero at $x = 0$ which is in the vicinity of the clamping point. The elastic properties of the clamping can be explained by a boundary condition eq. 3.15, which enables a finite slope of the curve at $x = 0$. The proportional constant α in eq. 3.15 is called torsion spring constant. The resonance frequency ratio is a function of the elastic properties of the beam clamping. A non rigid clamping reduces the first mode eigenfrequency whereas the second mode eigenfrequency is less affected. For that reason the eigenfrequency ratio $\frac{\nu_2^{res}}{\nu_1^{res}}$ increases above 6.3 which would be the theoretical frequency ratio for a rigidly clamped beam. The measurements of in-situ iron-filled CNT often revealed a frequency ratio lower than this value. Since the elastic properties of the mounting can not explain a reduced frequency ratio, another effect has to be considered as the origin of the reduced frequency ratios.

When the envelope of a vibrating CNT was evaluated it was found, that in some cases a homogeneous beam could not be fitted. In fig. 3.26 the shape of a long iron-filled CNT and its first and second eigenmode vibrations are shown. The shape of the initial non vibrating state was measured, since the shape of the CNT was not a perfectly aligned beam. In order to obtain the shape of the bending curve, the shape of the resting CNT was subtracted from the envelope of the first eigenmode. In fig. 3.27 the data points and an Euler-Bernoulli beam model fit are shown. The data of the envelope of the first eigenmode vibrating state could be fitted by a homogeneous beam model only up to a partial length of approximately 10 µm. At a length of ≈10 µm a significant deviation between the data points and the fit was visible. A frequency ratio of 4.75 was found for this CNT. The kink in the shape of the envelope curve suggested the existence of a dominating localized large volume defect in the structure of the CNT in the last third of the tube length close to its free end. An example of such a localized large volume defect is shown in fig. 3.10 in section 3.2.3. It locally weakens the strength of the CNT and can be described as a local inhomogeneity of the bending stiffness $E\,I$ that consists of the elastic modulus E and the moment of inertia I. The rather complex in-situ filling process during the CNT formation might have led to localized volume defects in the carbon shell structure of the CNT. Such defects do have an influence on the properties of the CNT and hence on their vibration behavior. In the case of volume defects the effective bending stiffness of the CNT is reduced. Different types of defects lead to different response in the vibration behavior of CNT. As yet, no genuinely suitable model for the treatment of volume defects and their influence on the resonance frequency has been found [205]. But the description of such a defect by a torsion spring has been suggested [205] as an first approach.

In order to understand the influence of such a local defect and the elastic properties of the clamping on the vibrational behavior of a CNT, numerical simulations of a

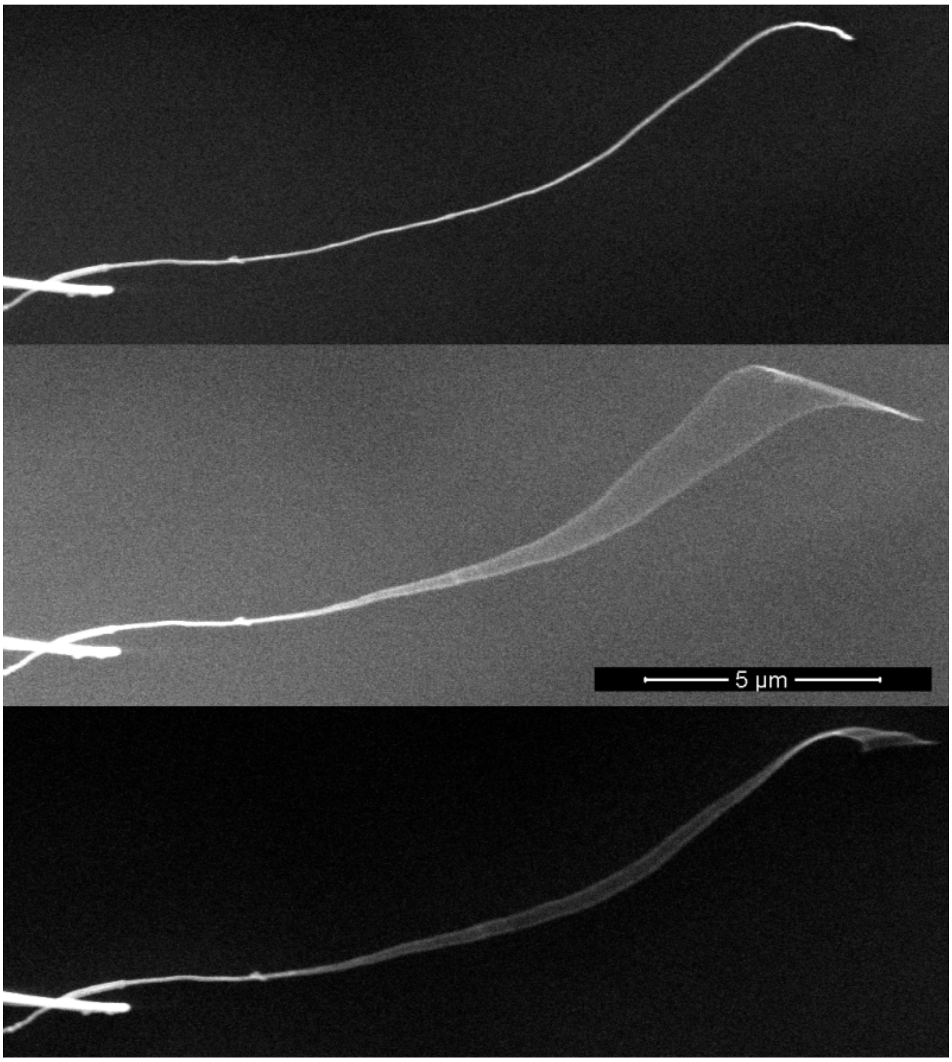

Figure 3.26: Vibration of a long iron-filled CNT. Top shows the non vibrating state. In middle the first eigenmode and at the bottom the second eigenmode vibration is presented.

representative model system were conducted. An Euler Bernoulli beam with an elastic mounting and additional volume defect within the structure was simulated. Whereas the properties of the mounting were kept constant in the case of the defect containing simulations, the strength and the position of the defect were varied. The parameters used for the simulation are given in tab. 3.1. The black curve in fig. 3.28 represents a continuous and homogeneous beam without an additional defect. In that case the x-axis represents the strength of the mounting, expressed by its elastic modulus. It shows, that the frequency ratio clearly increases if the mounting becomes softer.

In the case of the red, green and blue curve the x-axis represents the strength of the defect at constant beam cross section. For the mounting an elastic modulus of 1 GPa was chosen. As it can be read off fig. 3.28 a dominating defect (blue) close to the mounting, that would be the first third of the beam, results in an even larger increase

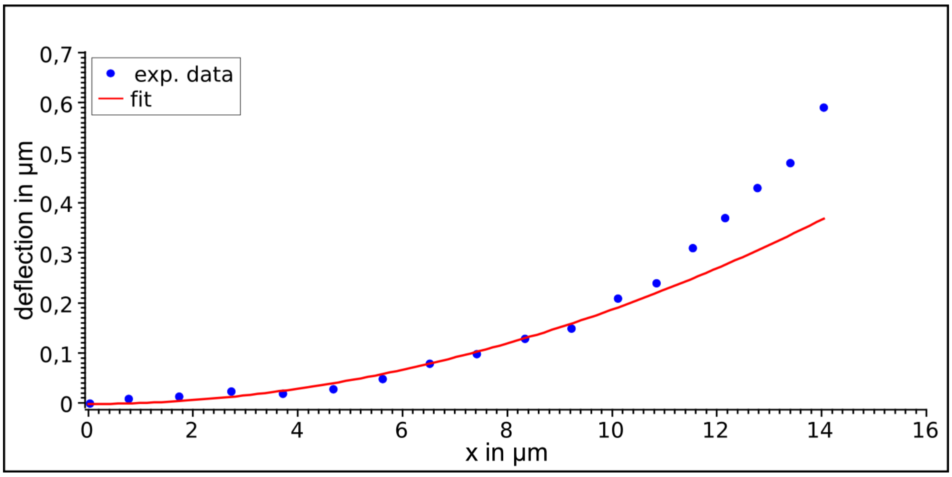

Figure 3.27: The envelope of the vibrating bending curve of the CNT corresponding to fig. 3.26. Only a part of the data could be fitted by a homogeneous beam model. The last third of the beam could not be fitted.

Table 3.1: Parameter of the numeric simulation of the influence of elastic mounting and defects on the vibration behavior of iron-filled CNT.

Parameter	Value	Dimension
Length of CNT	15	μm
Outer diameter	90	nm
Inner diameter	30	nm
Elastic modulus of CNT	100	GPa
Length of defect	0.1	μm
Elastic modulus of defect	0.01 - 100	GPa
Length of amorphous mounting	1	μm
Diameter of amorphous mounting	270	nm
Elastic modulus of amorphous mounting	1 - 100	GPa

of the frequency ratio in comparison to the homogeneous beam (black). If the defect is in the middle of the structure (green), it depends on its strength whether the frequency ratio is above or below the value of 6.3. Only if the defect is in between the half beam length or even more close to the free end of the vibrating beam (red), a continuous decrease of the frequency ratio can be found for a diminishing strength of the defect. That shows, that the frequency ratio depends on the defect strength and its position. With increasing stiffness of the defect and increasing stiffness of the mounting all cases approach to the value of 6.3. However, for a finite stiffness of the mounting that can not be considered as perfectly rigid the frequency ratio will remain above 6.3.

The simulation results, especially the red curve in fig. 3.28, can explain the experimental results of the particular CNT shown in fig. 3.26 and the corresponding envelop data in fig. 3.27. The assumption appears to be supported, that the presence of a localized volume defect within the vicinity of the free end in combination with an elastic

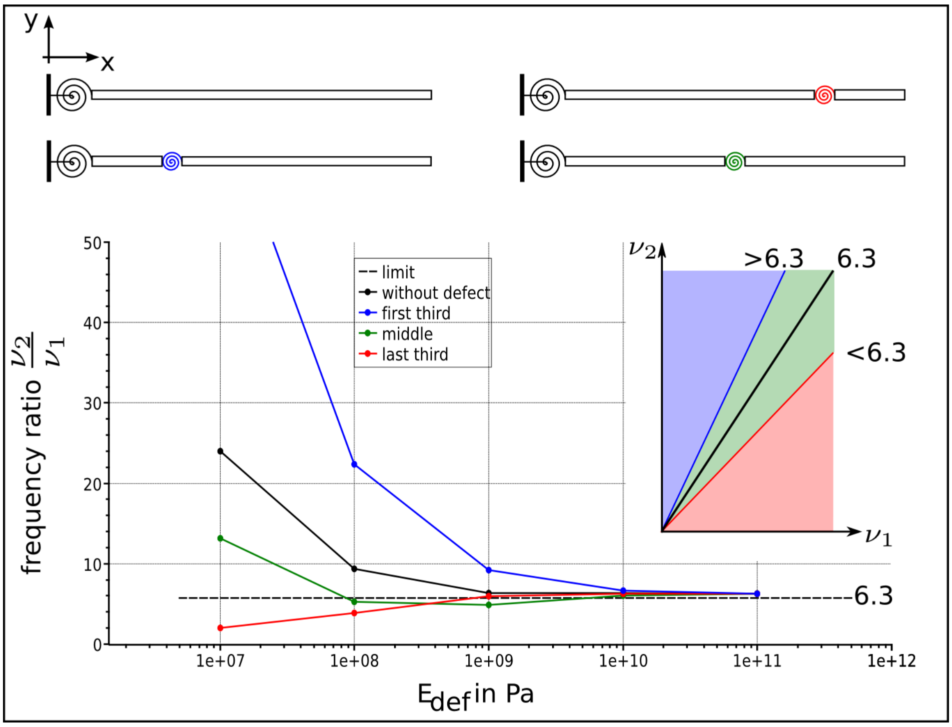

Figure 3.28: Influence of defect strength and position on the resonance frequency ratio. The colors corresponds to the different beam cases, while the x-axis represents either the strength of the mounting (black) or of the defect.

mounting is one reason for the reduced resonance frequency ratio, which was 4.75 for this particular CNT. From the discussed influence of the mounting and defect properties on the frequency ratio it was also understandable, that in some cases no vibration of the second eigenmode was observable. That was especially the case for short CNT possessing a high first eigenmode frequency and furthermore a high elastic modulus, i.e., a low defect density, and no additional dominating volume defect. In combination with an elastic mounting the frequency ratio might have been clearly above 6.3 and thus the second eigenmode frequency could not be observed during the experiments, due to a limited maximum excitation frequency of the function generator.

Of course, other structural inhomogeneities such as diameter variation and non continuous filling will also affect the vibration behavior. The evaluation of the envelope curve of the resonant vibrating state reveals further information about the investigated structure, that can not be obtained from evaluating the resonance frequency alone. By using the resonance frequency expression eq. 3.31 only an effective elastic modulus can be obtained in the case of an inhomogeneous beam structure. The envelope curve contains spatially resolved information and can be used to obtain the elastic modulus of the beam structure even if it includes localized inhomogeneities. Also the elastic properties of the mounting become only visible by evaluating the envelope curve which is vividly shown in fig. 3.29 (page 130) in the following section 3.3.2.6 about the determination of the elastic modulus.

All resonance frequency ratios found within the present work were less than 6.3. Reduced resonance frequency ratios for unfilled multi-walled CNT such as 5.68 and 4.18 have also been reported in literature [188, 190]. These are surprising and unexpected results for ideal homogeneous vibrating beams (CNT). Furthermore, for an elastic mounting of an one-side clamped vibrating CNT a resonance frequency ratio above 6.3 is expected. A part of the experimental results within this work gives clear evidence for the presence of elastic mounting properties, which has also been revealed in a previous work [213]. The reduced resonance frequency ratio could be explained by the presence of a point mass [205]. Another possible explanation for a reduced resonance frequency ratio is based on the presence of a localized volume defect within the CNT structure near the middle or in the vicinity of the free end of the *vibrating beam* as shown by the green and red curve in fig. 3.28. The morphology of the as grown CNT as shown, e.g., in fig. 2.32 on page 70, indicates the defect enriched structure of the CNT close to the substrate surface. The middle part of the CNT show off less defects, whereas the tip of the CNT again possess a higher defect density. Due to the sample preparation method the upper part is connected to the tungsten tip and the lower part becomes the tip of the free standing CNT and consequently the part with the high defect density is close to the free end. This might explain why in most of the measurements a reduced resonance frequency ratio has been found.

The special structure of multi-walled CNT gives evidence for a further effect which could cause a reduced ratio. Even though most of the experimentally investigated multi-walled CNT can be regarded as slender beams, when looking at the high aspect ratio above 100, it is still possible, that the Timoshenko beam model has to be considered [223], due to shear effects within the structure during bending [193]. However, for a homogeneous beam this model can not explain resonance frequency ratios below 4.0 [224]. Due to the complex structure of in-situ iron-filled CNT a combination of all above mentioned effects can not be excluded.

3.3.2.6 Determination of elastic modulus of iron-filled CNT

The purpose of the dynamical bending experiments was to gain knowledge about the elastic modulus of in-situ iron-filled CNT, which is an important material property. Its knowledge is necessary to predict the mechanical behavior of this type of CNT.

After describing the evaluation procedure based on selected examples, the experimental results will be presented and a discussion about the obtained elastic modulus in relation to the literature follows.

In order to obtain the elastic modulus of the CNT from the dynamic bending method the resonance frequency and the geometry had to be determined. The geometry in particular the length, the outer and inner diameter were measured from SEM and TEM micrographs.

The evaluation of eq. 3.31 is a widely used procedure [188, 190, 218]. It was also applied to a number of CNT within the present work. The results are presented in the upper part of tab. 3.2. In order to obtain additional information on the vibration behavior and mechanical properties of iron-filled CNT the evaluation of the envelope of the resonant vibrating state of the CNT was added to state of the art approaches. Thereby, further knowledge about the bending behavior and in particular about the elastic mounting properties of the CNT become available.

After the length measurement, compare section 3.2.2, the curvature of the resting state of the CNT was determined. Thereafter, the presumed resonance frequency of the particular CNT was estimated from its measured diameter and length according to eq. 3.32. The precise resonance frequency was then obtained from the amplitude versus frequency data as described in 3.3.2.2. The data points of the CNT curvature and envelope of the resonant bending state were taken from the images of the resting state and the resonant vibrating state, respectively. These two sets of data points, containing the relevant information of the bending state, were deduced for each investigated CNT. However, the CNT were not perfectly aligned beams rather than possessed a certain curvature, visible in particular in the resting state. In order to get the *real* bending curve of the particular CNT, the data of the resting state were subtracted from the data of the resonant vibrating state. The resulting bending curve was afterwards fitted, using the Euler Bernoulli beam model implemented in *Mathematica*. By solving the boundary condition eq. 3.15 an expression for the torsion spring constant α was obtained, which was inserted into eq. 3.20. The free unknown parameters $\beta = f(E)$ and C_i of eq. 3.20 were determined by a non-linear fit.

As discussed earlier, the mounting was in general not perfectly rigid but rather showed an elastic behavior. Thus, it was necessary to modify the boundary conditions accordingly. An example of a particular CNT bending curve is shown in fig. 3.29. The amplitude versus frequency measurement of this CNT revealed a resonance frequency of 2731 kHz and a Q-factor of 718. Regarding only the resonance frequency eq. 3.31 and a theoretically expected $\hat{\beta} = 1.875$ an elastic bending modulus of $\mathrm{E_b} = 0.24\,\mathrm{TPa}$ was obtained. In the next step the envelope of the resonant vibrating state was considered. Without the torsion spring assumption the model could only poorly fit the data of the envelope, since the finite non zero slope at the mounting was not taken into account. This fact is illustrated by the green curve in fig. 3.29, which shows a higher curvature than the data points demand and consequently gives a lower elastic modulus. In that case the effective elastic bending modulus is $\mathrm{E_b} = 0.22\,\mathrm{TPa}$ and $\hat{\beta} = 1.932$. This gave only a small difference to the previous case, where only the resonance frequency was

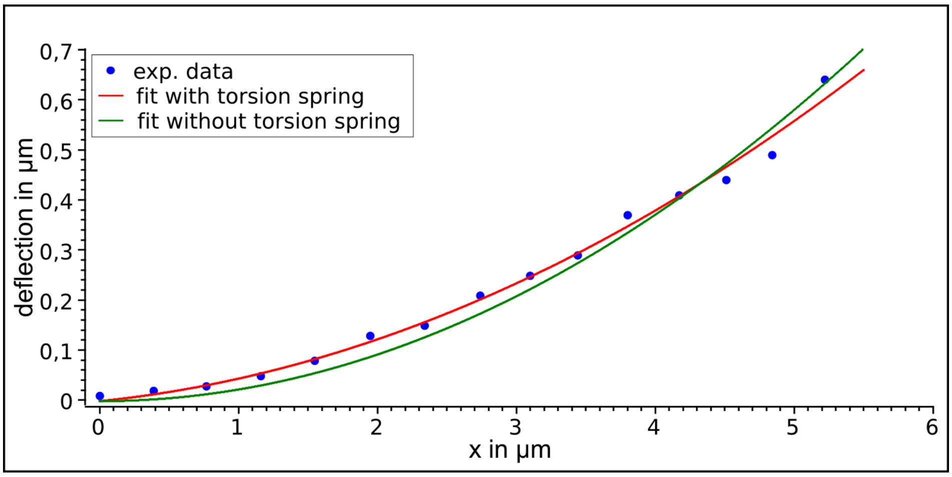

Figure 3.29: Envelope of an oscillating CNT. The red curve shows the fit assuming a torsion spring like mounting. The green curve is the fit assuming a perfectly rigid clamping.

regarded.

Considering the elastic properties of the mounting by a torsion spring constant α provided an additional parameter, that took the finite slope of the envelope near the mounting into account. Consequently, the model represented by the red curve in fig. 3.29 fitted the data better and gave a significantly higher effective elastic bending modulus of $\mathrm{E_b} = 0.35\,\mathrm{TPa}$. For $\hat{\beta}$ a value of 1.891 was found which is somewhat higher than 1.875. For the torsion spring constant $\alpha = 2 \times 10^{-12}\,\frac{\mathrm{N\,m}}{\mathrm{rad}}$ was obtained which indicates a rather high stiffness of the mounting.

This example vividly shows, that assuming the two options, a zero slope at the mounting point or evaluating only the resonance frequency, gives significantly different results. Thus, the elastic mounting conditions can only be neglected, if the mounting is either perfectly rigid or its stiffness is very high in comparison to the stiffness of the CNT. Due to the expected high stiffness of CNT this is usually not fulfilled. However, the assumption of elastic properties of the mounting requires the evaluation of the envelope of the resonant vibrating state by fitting the particular bending curve. Furthermore, the modified model of a simple beam can only be used without restrictions, if the elastic properties of the CNT are sufficiently homogeneous along the full beam length.

However, due to the complex morphology of iron-filled CNT and amorphous carbon deposition during sample preparation this assumption is not always fulfilled. In fig. 3.30 the structure of a completely iron-filled CNT and a corresponding schematic sketch are shown. The attached structures on the CNT surface consisted of carbon deposited during the formation process but were not filled with iron. Thus, no significant influence of these masses on the vibration behavior was expected. At the left side a part of the tungsten wire can be seen and also an amorphous carbon deposition of an approximate length of 2 µm. The amorphous carbon deposition in the vicinity of the mounting locally increases the outer diameter and therefore enhances the bending stiffness. The sketch in fig. 3.30 shows the different parts, whereas the slanting hatched area represents the amorphous carbon, which is represented by the torsion spring in the model and the horizontal hatched area the CNT, respectively. The back scattered electron contrast at the bottom of fig. 3.30 revealed, that the CNT shown here was continuously filled with iron. In fig. 3.31 the fit of the experimental data with the analytical model is shown. An elastic modulus $E_b = 0.52\,\mathrm{TPa}$ and a $\hat{\beta} = 1.948$ was obtained. The value of $\hat{\beta}$ was higher than the theoretically expected 1.875. The torsion spring constant α was $\approx 9 \times 10^{-13}\,\frac{\mathrm{N\,m}}{\mathrm{rad}}$, which suggested a rather soft mounting of this particular CNT. This gave evidence for a low elastic modulus of the amorphous carbon deposition. Since the underlying model assumed a homogeneous beam, the analytical fit function could not explicitly account for the influence of the amorphous carbon deposition in the vicinity of the mounting point. However, the slope of the envelope supports the assumption of elastic mounting properties and no discontinuities in the curve shape were observable. The two discussed examples show the relevant features, that were found during the investigations.

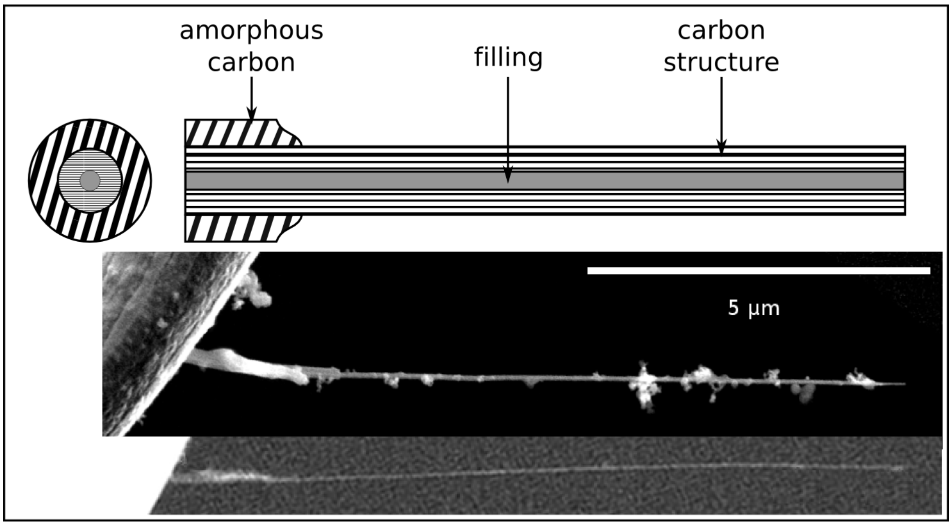

Figure 3.30: Structure of a completely iron filled CNT and a corresponding model structure. The amorphous carbon deposition around the mounting can be seen. The carbon structures on the surface were not filled with iron. At the bottom the BSED contrast is shown revealing the iron filling.

The results of the dynamic bending experiments on in-situ iron-filled CNT, in order to gain information about their vibration behavior and elastic modulus, are presented in tab. 3.2. In the upper part the experimental results are shown assuming a rigid clamping and the validity of a homogeneous beam model. These results are based on the evaluation of the resonance frequency only and do not contain information about

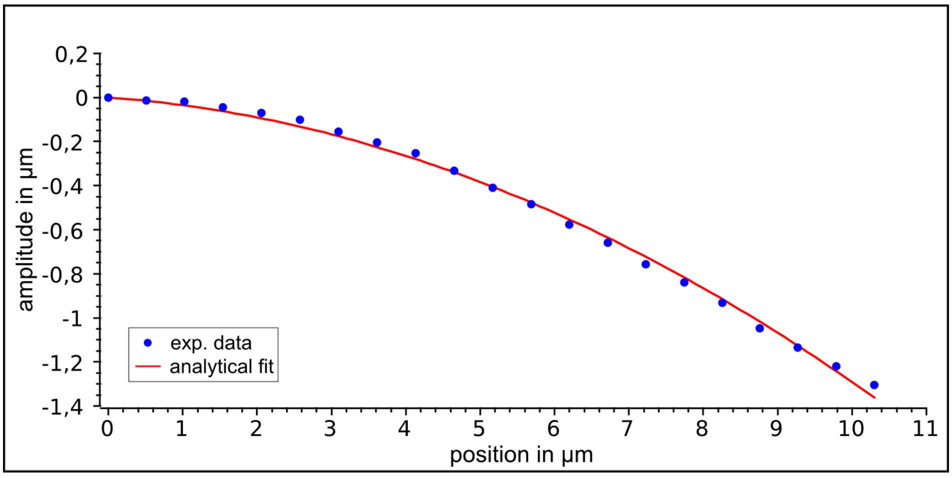

Figure 3.31: Experimental data and analytical fit of the envelope of the CNT shown in fig. 3.30. An effective elastic bending modulus of $E_b = 0.52\,\text{TPa}$ was found.

the envelope of the resonant vibrating state. In the lower part experimental results are presented, in which the envelope curve of the free resonant vibrating state has been evaluated. This led to modified values for the elastic modulus E_b. In the cases where both, the first and the second eigenmode were measured, the corresponding frequency ratio is given. The data in line 16 belongs to the CNT shown in fig. 3.26 and is an exception. Because of the kink, only a part of approximately 10 µm was considered in the fitting process. The parameter $\hat{\beta}_1$ was calculated by eq. 3.32 and deviates significantly from the other $\hat{\beta}_1$ values. The measured CNT were grown on the same type of substrate and using the same argon gas flow and pressure. Some samples (line no. 8, 10 and 16 in tab. 3.2) were grown at a reduced precursor mass flow. In order to show the effect of the boundary condition modification, the average elastic modulus of the investigated samples was evaluated. For the upper part in tab. 3.2 an average of $E_b = 0.45 \pm 0.33\,\text{TPa}$ $(\bar{E}_1)$ and for the lower part $E_b = 0.41 \pm 0.11\,\text{TPa}$ $(\bar{E}_2)$ was determined. It should be emphasized, that the standard deviation was much lower in the case of the advanced evaluation method, in which the resonance frequency and the envelope have been considered.

Although the average values seemed quite similar, a significance test in the framework of a TUKEY-test has been performed in order to test that there was no significant deviation of the mean values. As primary hypothesis no deviation of the mean values $(\bar{E}_1)$ and $(\bar{E}_2)$ was assumed. Since the p-value was 0.7 and much higher than the significance level $\alpha = 0.05$ this hypothesis could not be rejected. Due to the limited number of investigated CNT the conclusiveness of this test is limited, as it requires a minimum sample size of 30 for the comparison of data sets with such a high difference of the standard deviation.

Table 3.2: Geometry, parameter $\hat{\beta}_1$, number of shells (nos), resonance frequency ν_i^{res} and the effective elastic bending modulus E_b for a number of iron-filled CNT.

Nr.	L	d$_o$	d$_i$	nos	$\hat{\beta}_1$	ν_1^{res}	ν_2^{res}	$\frac{\nu_2^{res}}{\nu_1^{res}}$	E_b
	μm	nm	nm			kHz	kHz		TPa
1	16.23	90	23	98	1.875	325.00	-	-	0.12
2	18.90	74	20	80	1.875	204.00	-	-	0.13
3	18.17	119	39	118	1.875	454.40	-	-	0.21
4	18.50	106	35	104	1.875	509.90	-	-	0.39
5	21.70	103	25	115	1.875	334.00	-	-	0.64
6	17.60	104	34	103	1.875	774.00	-	-	0.82
7	11.84	90	27	79	1.875	1632.00	-	-	0.90
8	21.49	69	23	68	1.290	90.50	296.00	3.27	0.23
9	16.35	122	33	130	1.974	747.60	3182.00	4.25	0.29
10	5.27	48	16	47	1.891	2731.00	-	-	0.35
11	19.05	130	28	150	1.844	585.30	-	-	0.36
12	16.38	147	27	176	1.914	1107.00	-	-	0.46
13	16.80	179	32	216	1.197	510.00	1183.00	2.32	0.47
14	15.44	112	33	116	1.816	826.00	4613.00	5.58	0.48
15	10.39	60	20	59	1.948	1141.00	-	-	0.52
16	14.04	90	20	103	0.741	146.00	694.00	4.75	$0.53^\star$
17	17.48	104	24	117	1.635	545.00	2196.00	4.03	0.57

At this point it should also be mentioned, that in the first case, i.e., the upper part of the table tab. 3.2, where no elastic mounting properties were considered, a lower mean elastic modulus than in the lower part would have been expected. However, the evaluation of the CNT shown in fig. 3.29 on page 130 revealed, that the value of the elastic modulus was significant higher if the elastic mounting properties were taken into account. The same phenomena was reported for quasi-static bending experiments [213]. Despite the differences between the individual in-situ iron-filled CNT investigated in the present work, the reduced standard deviation indicated, that a narrow range of the elastic modulus values for this class of material exists. The consideration of the elastic mounting properties by evaluating the envelope of the free vibrating CNT in combination with the resonance frequency clearly gave more reliable results for the elastic modulus.

Tu et al. [182] investigated MWCNT up to 100 carbon shells theoretically and calculated an elastic modulus of 1.04 TPa. Also other authors [161] obtained an elastic modulus of 1 TPa. Although values above 1 TPa such as 1.8 TPa and 1.3 TPa have been reported [173, 225] the experimentally obtained values for MWCNT are in general below 1 TPa.

An analytical solution of the differential equation 3.12 can only be found for special cases such as a homogeneous bending stiffness $E\,I$ or some simple zero dimensional deviations. However, in many situations this requirement is not fulfilled and the

4th order differential equation of the problem can only be solved numerically. In this particular case, the solution depends on the known geometry and resonance frequency, whereas the torsion spring constant α and the effective elastic bending modulus E_b are directly obtained from the data fitting. Furthermore, the elastic modulus of the amorphous carbon deposition can be obtained, if it is inhomogeneousely distributed along the CNT surface. In order to fit the envelope data of a beam with an inhomogeneous cross section, an additional numerical method has been used. Each change of the beam geometry or material property actually requires the introduction of a separate beam section with homogeneous properties. Depending on the number of inhomogeneities the number of sections might get quite large. For each section the beam equation has to be solved, whereas the sections are connected with each other by natural boundary conditions. Due to the special geometry of the CNT another modeling approach can be used. The total area moment of inertia is given by eq. 3.34. The total bending stiffness is given by eq. 3.35, whereas each moment of inertia is weighted by the corresponding elastic modulus. The contribution of the amorphous carbon to the total bending stiffness, as a consequence of the change of the cross section, was weighted by a Fermi-function (eq. 3.37) that returns function values in the interval $[0\,,\,1] = \{f(x) \in R\,|\,0 \leq f(x) \leq 1\}$.

$$f(x) = \frac{1}{\exp(\frac{x-d}{c}) + 1} \tag{3.37}$$

While the parameter d defines the point where the function returns $\frac{1}{2}$, the parameter c controls steepness of the function around $x = d$. The beam is not divided into sections but special features such as the amorphous carbon deposition can be weighted by one or zero which is comparable to switching the particular feature on or off. This can be achieved by multiplying the corresponding contribution of the feature to the total cross section along the tube axis with the Fermi-function. By using this method one differential equation, that represents the whole CNT including the inhomogeneities of the cross section and material, is obtained. This method can in principle also be used to encounter for the influence of filling sections, if the filling is not continuous.

Applying both the analytical and numerical method to a homogeneous, almost completely iron-filled CNT, which is shown in fig. 3.14 on page 109, confirmed their usability. In the first case the analytical method containing the parameter β, the torsion spring constant α and the amplitude C has been applied to the data shown in fig. 3.32. The fit revealed a $\hat{\beta} = 1.635$ and from eq. 3.32 an effective elastic bending modulus $\mathrm{E_b} = 0.57\,\mathrm{TPa}$ was determined.

In the second case the 4th-order differential equation was directly fitted to the data as shown in fig. 3.33 and from that an effective elastic modulus $\mathrm{E_b} = 0.55\,\mathrm{TPa}$ was obtained.

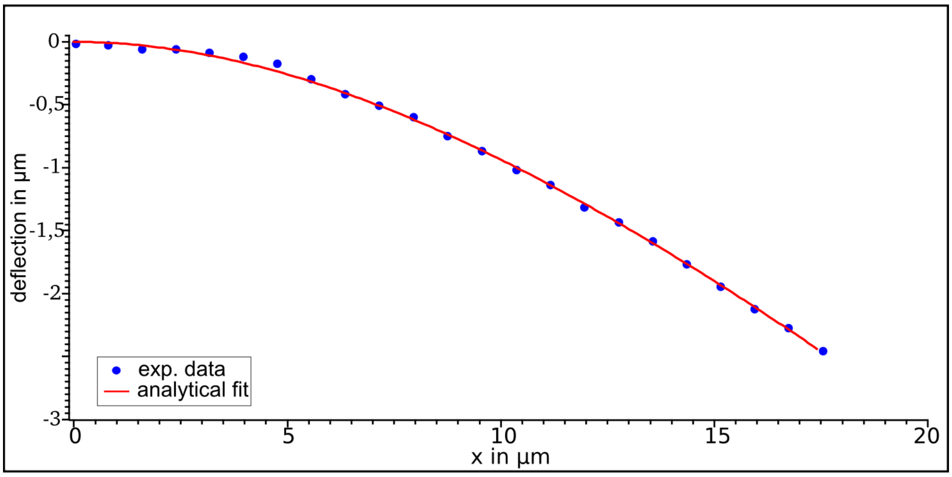

Figure 3.32: Fit of the envelope data with the analytical expression. An effective elastic bending modulus of $E_b = 0.57\,\mathrm{TPa}$ was found.

Thus, the elastic modulus obtained in both cases is almost the same regarding the differences between the two fitting approaches. However, for comparison a $\hat{\beta} = 1.648$ was calculated from the resonance frequency expression eq. 3.32, which is very close to the value found by the analytical fitting method. This is a remarkable compliance, attributable to the homogeneous properties of this particular CNT. Although the CNT possessed an amorphous carbon deposition in the vicinity of the mounting, it turned out, that it did not increase the bending stiffness but was actually the origin of the elastic mounting properties. Both methods gave a value of the torsion spring constant of about $1.0 \times 10^{-12}\,\frac{\mathrm{N\,m}}{\mathrm{rad}}$ and thus the clamping could not be considered as rigid. This also supported the assumption, that the amorphous carbon was the origin of the elastic properties of the mounting.

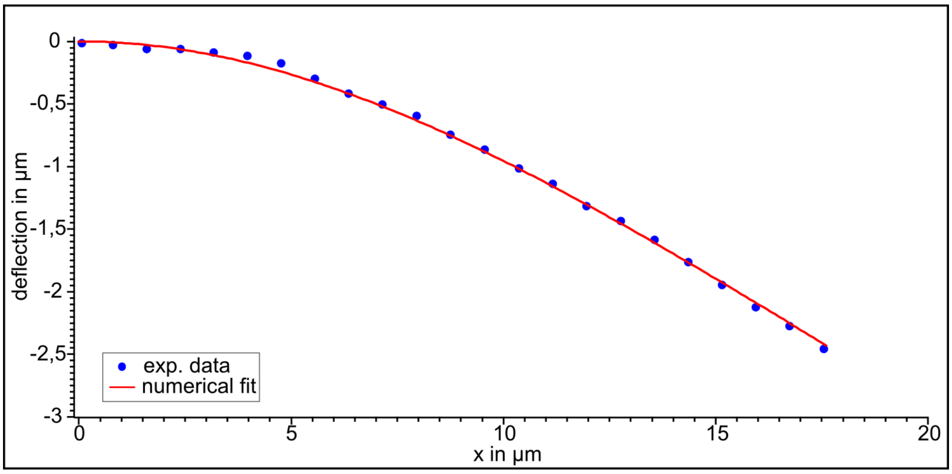

Figure 3.33: Fit of the envelope with the numerical expression. An effective elastic bending modulus of $E_b = 0.55\,\mathrm{TPa}$ was found.

However, fig. 3.35 shows an example, where the analytical and numerical approach revealed different results. The analytical fit of this CNT was already presented in fig. 3.31, whereas the numerical fit is shown in fig. 3.34. Using a value of $c = 1.0 \times 10^{-9}$ m, which corresponds to a smooth decline in eq. 3.37, a good fit has been obtained. In that case a value for the amorphous carbon of $E_{am} = 0.6$ GPa was found, suggesting a rather soft amorphous carbon deposition on the CNT surface. The effective elastic modulus of the CNT was $E_b = 0.21$ TPa which is about half the value that was found by fitting the data with the analytical model. Furthermore, a relatively high value for the torsion spring constant α of $\approx 1.0 \times 10^{-9}\,\frac{\mathrm{N\,m}}{\mathrm{rad}}$ was obtained, indicating a rather high stiffness of the mounting. Thus, the slope of the curve was flat in the vicinity of the mounting point.

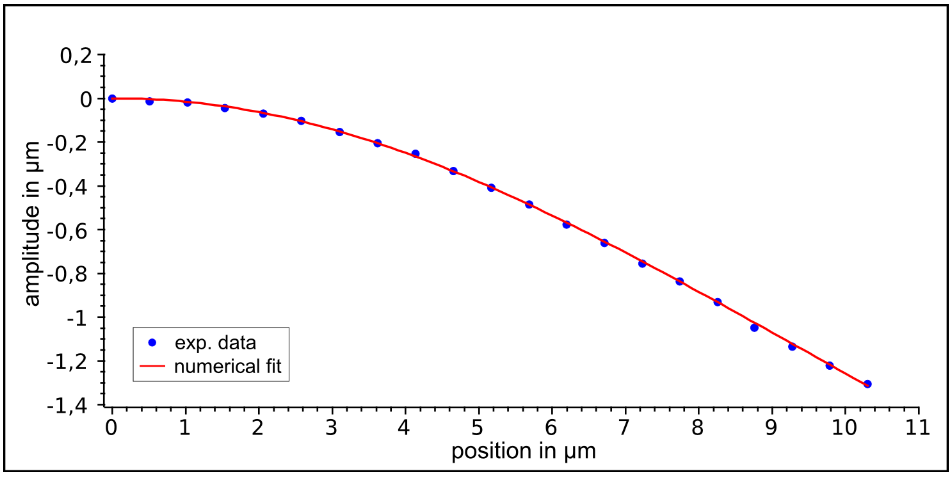

Figure 3.34: Experimental data and numerical fit. The elastic modulus of the CNT was $E_b = 0.21$ TPa.

The direct comparison of the analytical fit (green curve) and numerical fit (red curve) is shown in fig. 3.35. It is obvious, that in the former case a much higher slope than in the latter case was obtained at the mounting point. However, the curvature in the analytical case is lower, which is reflected by the higher effective elastic bending modulus. The analytical model was not capable to consider the local influence of the amorphous carbon to the overall bending stiffness of the CNT. Therefore, the effective elastic bending modulus might have been overestimated, if the stiffening, that results from the deposition of amorphous carbon was not taken into account as it is shown by this example. It can be concluded, that the numerical fit (red curve in fig. 3.35) gave a reliable result and the effective elastic bending modulus E_b of this particular CNT is about 0.21 TPa.

The conducted examinations suggest, that more detailed studies of the influence of amorphous carbon and inhomogeneities of the CNT structure should be performed. Even though it has been shown that continuum mechanics can be used also for

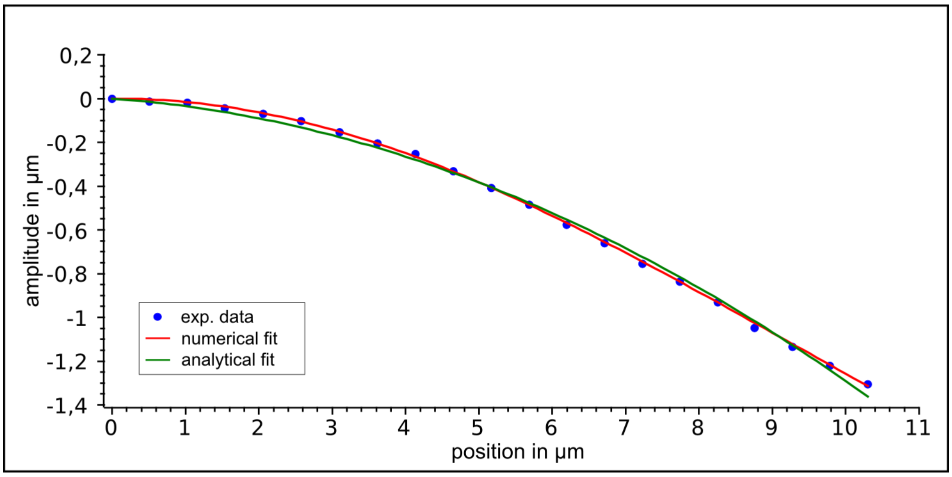

Figure 3.35: Comparison of the analytical and numerical fit. The numerical approach gave a better fit and an elastic bending modulus $E_b = 0.21\,\text{TPa}$. The analytical fit gave $E_b = 0.52\,\text{TPa}$.

mesoscopical systems, such as CNT, their complicated and often complex structure has to be regarded. Sophisticated models, that reflect special features of CNT are necessary. A better agreement between experiments and theory will be achieved. Whether a certain behavior of CNT found in experiments related to the internal structure or the boundary conditions effects can only be determined, if the data evaluation reflects the experiment in more detail. The comparison between different features and methods of evaluation in the case of in-situ iron-filled CNT illustrates this aspect vividly.

3.3.3 Influence of the parameters

In the following section the experimental results of the present work are compared and discussed with literature, mainly focussing on multi-walled CNT grown by thermal CVD.

Influence of the length

Due to the high aspect ratio, the CNT length measurement is not straight forward. The length is a critical parameter and its value is often underestimated for two reasons: First, only the projection of the real length can be measured which is always smaller than the real length. Second, due to screening effects or uncertainties of the exact mounting point position a shorter length is measured. The exact anchoring point is often not visible [209]. The free standing part of the length of a micrometer long beam can in principle be measured with good accuracy, whereas a large uncertainty with respect to the exact clamping point exists [188, 209]. Consequently, the beam length contains a certain systematic uncertainty. The length enters with the power of four into the formula of E_b (eq. 3.38).

$$E_b = \frac{64\,\pi^2\,\rho_T\,\nu_j^2 L^4}{(d_o^2 + d_i^2)\,\hat{\beta}_j^4} \tag{3.38}$$

While in the present work the length of free standing CNT was measured either by using the tilt functionality of the the SEM stage or by using the rotational extension of the micromanipulator inside SEM, Poncharal et al. [188] rotated the stage of the TEM in order to get at least two projections of the CNT for the length estimation. However, while the length unsureness due to an unknown angle between the CNT and the focus plane can be corrected the above mentioned uncertainties remain. To show the effect of the length uncertainty onto the elastic modulus eq. 3.38 was evaluated with the initial length as it was measured only from one image and with the corrected length. Referring to the CNT line number 10 in tab. 3.2, in the first case $\mathrm{E_b} = 0.26\,\mathrm{TPa}$ corresponding to a length of 4.89 µm were found. In the second case $\mathrm{E_b} = 0.35\,\mathrm{TPa}$ were obtained, using the corrected length of 5.22 µm. This clearly shows, that the elastic modulus is underestimated if only the projected length is used.

All methods, in literature as well as in the present work, that have been applied to determine the elastic modulus have in common, that the length has a high impact on the obtained value. In experiments often the exact mounting point can not be determined due to screening by amorphous carbon deposition or by shadowing by sample itself [188, 190]. In case of AFM measurements it is also often uncertain where the CNT is actually clamped and where the unsupported part begins. Furthermore, the CNT might also be supported by other structures such as other CNT or dirt below the sample. These problems can only be minimized to a certain level but should always be considered. Zeng et al. [209] suggested the introduction of an additional support with known properties in order to reduce the uncertainties of an undefined clamping position. However, the suggested solution is not suitable for experimental implementation since such an additional support would introduce a number of new unknown properties to the experiment. Furthermore, it is not obvious that a certain mounting point exists [226].

Another issue is the curvature of the CNT. Most nanotubes investigated experimentally in this work but also in the literature [188–190, 201] are no straight aligned but possess a certain curvature. This leads to an additional uncertainty about the real length of the measured CNT. Due to the curvature the length is often underestimated as it is measured from the anchoring point to the tip. The measurement of CNT deposited onto specially prepared substrates can be advantageous [174, 186]. In that case the CNT were dispersed in an organic solvent and a small amount dropped to the surface of either a porous substrate [174] or an especially prepared line grid [186]. In the latter case the CNT were additionally orientated perpendicular to the lines using dielectrophoresis forces as consequence of an applied electrical field. Only a small part of the CNT across a hole or trench is unsupported and can be bent. The rest of the CNT is anchored to the substrate surface. If the hole diameter or the trench width is given also the free length of the CNT is known. Furthermore, such a short beam section of several hundred nanometers can be considered as straight aligned.

As a consequence of the challenges regarding the length measurement, the investigation of the elastic bending modulus by resonant dynamic bending often gives an underestimated value. It is therefore stated, that in most cases the given values for the effective elastic bending modulus in tab. 3.2 can be considered as a lower boundary estimation.

Influence of the cross section geometry

The bending stiffness $E\,I$ of a beam consists of the material properties represented by the elastic modulus E and the bending moment of inertia I which is defined by the geometry. The elastic modulus can only be extracted if the cross section of the beam is known. Although in general the cross section of a CNT can be approximated by a circular ring, the cross section of an in-situ iron-filled CNT is not that simple. In fig. 3.36 the most relevant features of an iron-filled CNT are sketched. The amorphous carbon in section A originates from the mounting process, whereas the amorphous carbon in section B was formed during the CNT growth process. The filling might be interrupted as it is shown in section D. In section E an additional iron particle is attached to the surface. In a model each part should be described as beam section with homogeneous properties. At the nanoscale not all inhomogeneities might be known, nevertheless the elastic modulus is influenced by these unknown properties and only an effective elastic bending modulus E_b can be obtained.

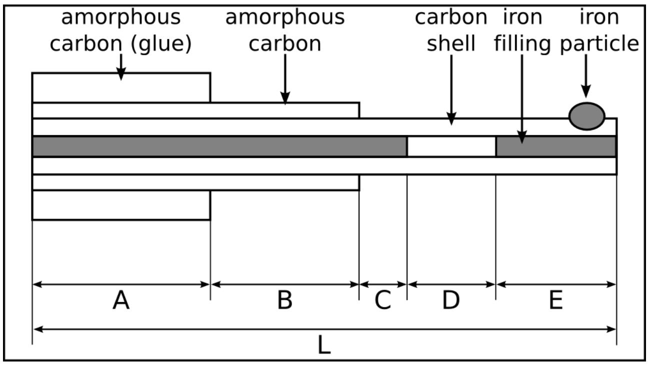

Figure 3.36: Typical inhomogeneities and different possibilities of cross sections of in-situ filled CNT.

A thickening of the CNT cross section especially in the region of the highest bending moment in the immediate vicinity of the mounting point, such as in section A, results in a higher effective bending stiffness. This implies a higher overall E_b, if the influence of the specific geometry in this particular beam section is not considered. An amorphous carbon deposition, as indicated in section B in fig. 3.36, can either lead to an over- or underestimation of the elastic modulus of the investigated CNT. If amorphous carbon, with a strength that is almost one order of magnitude lower than that of the graphitic carbon shells, is located in the surrounding to the mounting area of the CNT, the resonance frequency increases due to additional stiffening of the vibrating structure. Thereby it is assumed, that the density of amorphous carbon is similar to graphite. The consequences of these assumptions were already shown in fig. 3.23 on page 121. If not explicitly considered the elastic modulus is overestimated.

In the present work and in literature two main sources of the amorphous carbon at the CNT surface are discussed. Amorphous carbon is often formed during the synthesis of CNT by chemical vapor deposition. Carbon from the pyrolytic decomposition of the precursor deposits on the graphitic CNT shell during the formation process [103, 114]. Another source results from the treatment and storage of CNT in organic solvents. The deposition of CNT from an organic solution results in the deposition of carbon contaminations at the full length of the CNT [174, 186]. If the samples are only measured by AFM or SEM it is not possible to distinguish between the highly graphitic CNT structure and contaminations. This information can only be obtained by TEM measurements.

In principle, bending experiments can not distinguish between different contributions of the composed cross section if it is homogeneous along the nanowire length. Only if significant inhomogeneities exist and the bending curve is spatially resolved, the contributions of different parts of the cross section to the overall bending stiffness can be resolved. If a CNT is completely covered by amorphous carbon its contribution to the total bending stiffness can not be concluded in comparison to the contribution of the graphitic shells. For the same reason the contribution of the iron filling to the bending stiffness can not be discriminated in the case of a continuous filling.

The following example of a vibrating CNT, completely covered by amorphous carbon, illustrates this problem. If no distinction is made between the CNT shells and the amorphous carbon a low elastic modulus of 0.07 TPa has been found, whereas for this particular CNT no torsion spring was taken into account. In the first step (point $\boxed{\text{A}}$ in fig. 3.37) the complete outer diameter of 179 nm was regarded as the graphitic shells of the CNT, according to SEM measurements. In the next step (point $\boxed{\text{B}}$ in fig. 3.37) the CNT diameter (d_{CNT}) was reduced to 86 nm as it was measured by TEM. For the elastic modulus of the amorphous carbon $\mathrm{E_b} = 50\,\mathrm{GPa}$ has been assumed [210]. Due to the reduced *effective* diameter of the CNT the elastic modulus increased to 0.49 TPa. In that case the soft amorphous carbon does not significantly contribute to the bending stiffness. If the amorphous carbon is not considered at all (point $\boxed{\text{C}}$ in fig. 3.37) the elastic modulus decreases a little bit because the CNT appears lighter.

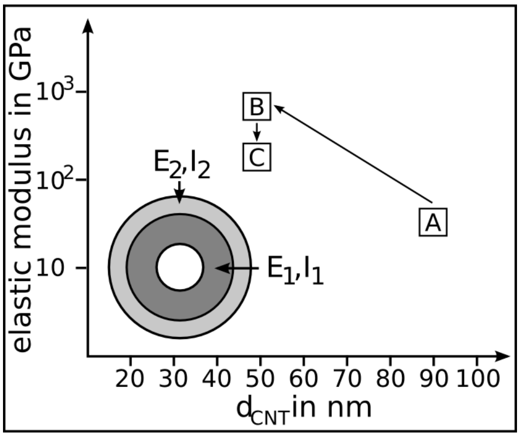

Figure 3.37: Change of elastic modulus if the composition of the cross section consists of graphite and amorphous carbon.

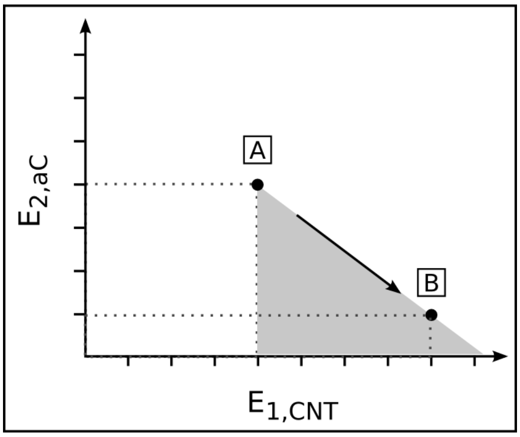

Figure 3.38: Elastic modulus of graphite and amorphous carbon

An approximation for the evaluation of the elastic modulus of CNT can be performed in the following way. At first, a CNT with a known outer diameter but unknown properties of the cross section is considered. Furthermore, it is assumed that there is a non-uniformity in material properties of the cross section. From the resonance frequency and the given geometry the elastic modulus E_{tot} can be calculated. Now the cross section is artificially divided into two sections with the same elastic properties ($E_{tot}\,I_{tot} = E_1\,I_1 + E_2\,I_2$, with $E_1 = E_2$). This is equal to point $\boxed{\text{A}}$ in fig. 3.38. If $E_2 = 0$ than $E_1 = E_{tot}$ and $I_1 = I_{tot}$. If an amorphous carbon layer is assumed the colored area in fig. 3.38 is valid whereas $E_{CNT} > E_{aC}$. However, from pure bending the ratio between the two elastic moduli can not be determined. But a value for the amorphous carbon can be estimated from literature such as 60 GPa [210]. Taking this value a new value for the elastic modulus of the CNT can be calculated using eq. 3.39.

$$E_b = \frac{E_{aC}\,(d_{aC}^4 - d_o^4)}{(d_i^4 - d_o^4)} + \frac{64\,\pi^2\,\nu_j^2\,L^4\,(-d_{aC}^2\,\rho_{aC} + d_o^2\,(\rho_{aC} - \rho_T) + d_i^2\,(-\rho_F + \rho_T))}{(d_i^4 - d_o^4)\,\beta_j^4} \tag{3.39}$$

Where ρ_{aC} and d_{aC} are the cross section and outer diameter of the amorphous carbon deposition, respectively. An upper estimate for the elastic modulus is obtained by calculating E_b based on the measured CNT diameter not considering the amorphous carbon layer. On the contrary, a lower estimate is found by assuming the full diameter of the CNT. The amorphous carbon increases the outer diameter and therefore the bending stiffness but its elastic modulus is almost one order of magnitude lower. Thus the elastic modulus of the carbon shells seems to be much lower. The value for E_b obtained by considering the E_{aC} should be within this range. Without any further information the contribution of two or more different materials to the cross section and thus the bending stiffness can not be resolved. As given by eq. 3.35 on page 118 the total bending stiffness is a linear sum of the individual cross section contributions and in case of a continuous iron nanowire inside its particular influence can not be revealed. For that reason only an effective elastic modulus for the complete cross section can be determined. However, due to the small inner diameter, hence lower elastic modulus of the iron filling in comparison to the elastic modulus of CNT by at least one order of magnitude, a minor contribution to the overall bending stiffness can be assumed. Furthermore, due to the synthesis conditions an amorphous carbon layer is often deposited on the surface of thermally grown CNT, whereby its thickness is not always precisely known [103, 114]. The elastic modulus of such an amorphous carbon layer can be one or two orders of magnitude lower than that of CNT and, as before, its particular contribution to the overall bending stiffness can not be identified. By assuming, that the outer diameter equals the thickness of the CNT shells, the outer diameter of the *real* CNT is overestimated and consequently the effective elastic bending modulus of the shells is underestimated.

Influence of the mounting properties

As shown in 3.3.2.6 the mounting properties do have a significant influence on the vibrating behavior of the CNT and the determination of the elastic modulus. In order to measure the CNT properties the sample has to be prepared. As presented in the immediately preceding section, CNT are often dispersed in organic liquids and dropped onto the substrate surface [174, 186]. The properties of the CNT-anchoring to the substrate are partly influenced by this organic carbon contaminations at the CNT surface. An individual CNT can also be clamped to a sharp wire tip by the deposition of amorphous carbon [189, 201, 218, 219]. In that case the carbon contamination is more localized. The latter sample preparation method was used in the present work. Within a typical exposure time of 10 min in the present study, gaseous carbon compounds from the microscope atmosphere diffused along the CNT and condensed at the surface. However, since this material was not exposed directly its structure was soft. Values below 1 GPa are reasonable for this material. On the contrary, measurements on amorphous carbon that was directly exposed to the electron beam revealed values above 10 GPa [210]. Depending on the elastic properties of the amorphous carbon deposition and its geometric dimensions a rather stiff clamping can be achieved.

In fig. 3.39 three different experimentally found cases are presented. In case A the CNT is mounted to the wire in a small localized area. This situation is schematically illustrated in fig. 3.40 A_1 and A_2. The CNT is embedded in a small amount of amorphous carbon and its elastic properties can be expressed by a torsion spring constant. This can be explained by the movement of the CNT within the soft material. In that case the well localized amorphous carbon deposition did not lead to an additional stiffening of the structure. The evaluation revealed a torsion spring constant of $\approx 1.0 \times 10^{-12}\,\frac{\mathrm{N\,m}}{\mathrm{rad}}$. In some situations amorphous carbon was also deposited on the surface of the CNT in the vicinity of the mounting point. This is shown in fig. 3.39 case B. Consequently, the diameter of the vibrating beam was enhanced in this particular area. The torsion spring constant in this case was $\approx 1.0 \times 10^{-9}\,\frac{\mathrm{N\,m}}{\mathrm{rad}}$. This situation is sketched in fig. 3.40 B using a torsion spring in combination with a section of an increased outer diameter. The situation in fig. 3.39 C represents an almost perfectly rigid clamping condition.

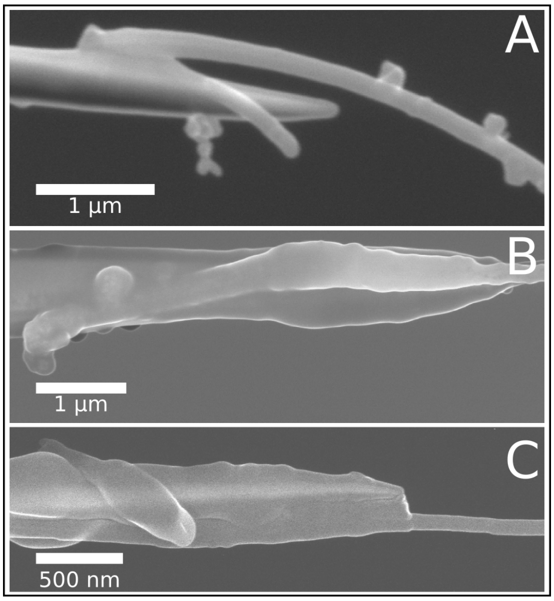

Figure 3.39: Case A shows a situation where the CNT is glued to the tungsten wire and a torsional spring constant was used to model the elastic properties of the glue. In case B the torsion spring represents the elastic properties of the amorphous carbon, which was in part also deposited in the vicinity of the mounting point. In case C a small part of the CNT was completely embedded in amorphous carbon with a high bending stiffness. In that case also a high torsion spring constant was found.

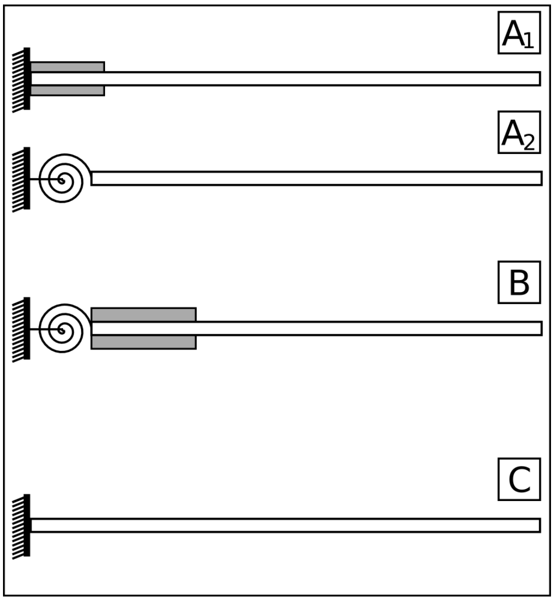

Figure 3.40: Different mounting cases. Case A_1 considers relatively soft amorphous carbon. Its properties can be expressed using a torsion spring model (case A_2). Case B consists of a torsion spring and additional amorphous carbon. Case C corresponds to the ideal case where CNT clamping can be considered as perfectly rigid and no significant additional carbon is deposited on the CNT surface.

The CNT was completely embedded in amorphous carbon with a high elastic modulus in comparison to case A and B. A high torsion spring constant of $\approx 1.0 \times 10^{-7}\,\frac{\mathrm{N\,m}}{\mathrm{rad}}$ have been found in this case.

All situations, in particular case A and C, can be described by a modified Euler Bernoulli beam model, which considers the elastic properties of the clamping. In case B the consideration of a separate section for the region with the amorphous carbon deposition might be useful. More complex situations could be modeled by numeric models. The evaluation of the envelope of the free vibrating state took the special features of the CNT structure into account. The examples shown in this section emphasize the need for considering the properties of the mounting.

Most of the experimental data in literature and also in this work were evaluated using the Euler Bernoulli beam model. Depending on the experimental situation the boundary conditions have to be adapted accordingly. For microbeams, especially silicon based cantilevers, this has been theoretically and experimentally done [209, 227, 228]. In their review Gibson et al. [191] raised the question whether the assumption of a torsion spring like boundary condition is feasible at the nano scale and in particular for CNT. As shown above, the results of the present work suggest that the influence of amorphous carbon should not be underestimated and that its elastic properties have to be considered. The evaluation of the material properties of the CNT under investigation is influenced by the boundary conditions of the sample. The vibration behavior and material properties can only be understood if the mounting properties are considered. If not, the elastic modulus might be highly underestimated, since the only parameter of the model to encounter for the slope and curvature would be the elastic modulus. However, the elastic modulus is actually only related to the bending of the beam. It is therefore stated, that in most cases the given values for the effective elastic bending modulus can be considered as a lower boundary estimation. The elastic modulus of the CNT investigated in the present work might even be higher than the values given in tab. 3.2.

Rippling and buckling mode

Besides the influence of structural defects and disorder which are discussed later, there is also an intrinsic property of CNT that might result in a reduced effective bending stiffness. It is known from slender beams and thin-shell structures, especially tubes, that the so called rippling or buckling bending mode appears, if a critical load is imposed. Depending on the material properties either extended wave-like distortions or one or more kinks arise. As mentioned before in section 3.1 on page 86, in particular single-walled carbon nanotubes can be considered as a thin shell structure in the framework of continuum mechanics [17, 179]. But also multi-walled CNT show, due to the nested shell structure, the tendency to ripple [188]. This is especially related to the relatively low van der Waals interaction force between adjacent layers in highly crystalline multi-walled CNT. In fig. 3.41 an example of a rippling pattern is shown that was obtained by electrostatic bending of a CNT achieving a high curvature [188]. Poncharal et al. [188] reported the reduction of the effective elastic bending modulus down to ≈0.2 TPa for multi- walled CNT with an outer diameter above 12 nm. It was later on also supported by theoretical investigations, that only CNT with a certain outer diameter tend to ripple [195, 196]. Liu et al. [195] applied a model to the data

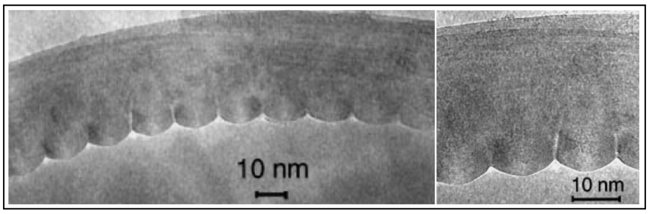

Figure 3.41: Formation of a rippling pattern for a CNT highly bent by electrostatic forces [188]. Such patterns show a characteristic wavelength λ. They only occur on the compression side of the beam and reduce the energy due to inner planar stress.

of [188] containing the concept of a critical load and corresponding critical curvature of the loaded structure, above which rippling is energetically favorable in order to reduce in-plane stress. The data and model curve are presented in fig. 3.42. However, in agreement with Poncharal et al. it was indicated that the CNT have to exceed a certain outer diameter. Even though the experimental data suggested a critical diameter of 12 nm it is not known up to now, whether this is the critical diameter for MWCNT. It was suggested by the authors of both groups [188, 195], that rippling patterns are energetically favorable with increasing outer diameter and number of carbon shells. But they also suggested, that defects in the shell structure, which lead to interactions between adjacent layers might hinder the formation of rippling patterns and lead to an increase of the effective bending stiffness.

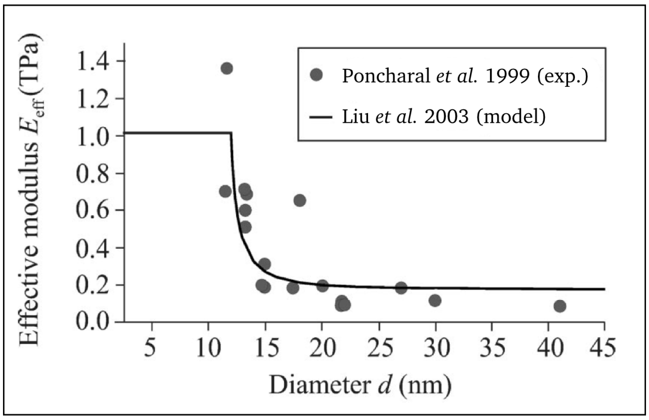

Figure 3.42: Relation between outer diameter and elastic modulus for multi-walled CNT grown by arc discharge [195]. The experimental data [188] was fitted by a model that encounters for the occurrence of the rippling mode of the CNT structure.

For an one-side clamped homogeneous CNT the formation of such a rippling pattern is expected in the region where the highest bending moment occurs. A rippling pattern can be considered as an energy or load dependent defect. It locally reduces the bending stiffness of the CNT. In a dynamic bending experiment the resonance frequency of the *beam* correlates with both, the defect position and its specific elastic properties. The resonance frequencies of the first and second eigenmode as well as their ratio are sensitive to the position and number of distinct defects. Hence, a number of defect types can be seen in the shape of vibration curve. Rippling is a phenomena with a periodically extended manifestation. It might be considered as a kink-like defect that influences the bending stiffness and thus the resonance frequency of the beam structure. The appearance of such a defect would depend on the amplitude of the dynamic excitation or static external load, respectively. However, the amplitude during the vibration experiments were most likely too low for the occurrence of the rippling mode in the present work as well as in literature [188].

Rippling was not observed in the present work. Neither the dynamic nor the static bending experiments inside TEM showed the formation of rippling patterns. However, due to the large outer diameter of the CNT in the present work, rippling would have been likely to occur. Based on the experimental knowledge it is assumed, that because of the defects within the CNT shells adjacent layers were interlinked. This might have prevented the formation of rippling patterns even at high amplitudes during bending as was also indicated in literature [188].

The rippling and buckling behavior of CNT is not completely understood up to now. However, at least two conditions have to be fulfilled: 1.) a certain critical outer diameter has to be exceeded and 2.) a critical load has to be imposed that leads to a critical curvature of the bent CNT. Kuzumaki et al. [229] investigated the buckling behavior of MWCNT and concluded that a CNT can only bent without changes in bonding, which was called the rippling mode later on, up to a certain critical curvature. Further bending and increase of the curvature requires a change of the bonding state from sp^2 to sp^3, which was called the buckling mode. Several groups performed simulations either based on molecular dynamics [17] or continuum mechanics [193, 195]. It was found, that multi-walled CNT with high crystallinity prefer rippling, whereas a higher defect density, especially interlinks between adjacent layers might have a higher energy barrier against rippling. For that reason, for multi-walled CNT grown by thermal CVD not such a obvious dependency on the outer diameter has been found [201, 218], which is also shown in fig. 3.46 where literature data and the results of the present work are shown. The higher defect density within the shells reduces their strength but due to interlinks the overall stiffness might increase and rippling is more unlikely to occur. It is possible that in some cases multi-walled CNT with a certain defect density are favorable to high crystalline CNT. Due to the formation process, in-situ iron-filled CNT possess a variety of defects that might increase the overall effective bending stiffness of the CNT synthesized and measured in the present work.

Influence of defects

The effective bending stiffness of carbon nanotubes depends, besides on the geometry, especially on the structural properties of the carbon shells and in particular their defects. There are different kinds of defects which have to be considered in this type of material.

The first kind are defects within the carbon structure that can be expected for all multi-walled CNT grown by thermal CVD. During the CNT formation process point defects are formed which lead to disorder within the graphene structure of the carbon shells. It can be assumed that these defects are homogeneously distributed along the CNT resulting in some kind of defect density, which in its turn influences the material properties. This results in an effective elastic modulus that is characteristic for the investigated material.

The second type are larger volume defects. These extended structural defects have their origin in the formation process of the CNT as well. Also unfilled CNT show several long range structural defects such as spiral formation and kinks [218, 219]. Additional defects such as branches and spherical catalyst particle inclusions result in a larger variability of defects in case of in-situ iron-filled CNT. These defects can extend into large volumes up to several hundred nanometers and contribute to the effective bending stiffness, which, e.g., is reflected in the CNT vibrational behavior. If such a large volume defect exist within the CNT it might be called a dominating defect. With a more advanced experimental setup its presence and position along the tube axis might be found by evaluating the frequency ratio and the envelope curve. As it was discussed earlier the frequency ratio changes as a function of the defect position and strength.

The third type are adsorbents on the surface of the material. These depositions can have different origins. Amorphous depositions can be formed during the synthesis [28, 31] and their formation can hardly be prevented. Another part might originate from the sample preparation where amorphous carbon is used as glue for the fixation of the CNT. Although only a very small area is exposed to the electron beam, carbon may diffuse in the gas phase to some extend and adsorb at the CNT surface. Furthermore, the imaging process itself leads to the deposition of amorphous carbon on the sample. Thus, during the measurement of the resonance frequency itself further carbon might be adsorbed by the surface.

The material investigated in the present work was not homogeneous. The material properties along the radius varied from highly graphitic and crystalline graphene shells to amorphous carbon deposits. In the following section possible correlations between the structure and the elastic modulus will be discussed.

Thinner CNT should show a better structural quality than thicker CNT. Low elastic moduli in the range of (1 GPa to 100 GPa) were reported for CNT grown by thermal CVD [174]. Higher moduli were found for double and quadruple-walled CNT [230]. Their bending behavior is similar to that reported for single-walled CNT. Thin multi-walled CNT have higher elastic modulus than thicker [222]. In tensile tests multi-walled CNT actually did act like single-walled CNT as the inner shells did not contribute to the elastic properties due to the low van der Walls interaction forces (shear forces) between adjacent shells [231]. The diameter dependence of the elastic modulus of multi-walled CNT in bending experiments reflects also diameter-dependent material

properties. When grown in CVD, thinner multi-walled CNT are structurally superior to the thicker tubes [186]. It was suggested, that the formation process of the CNT is reflected in the elastic properties of the material. The link between the metastable catalyst model and the elastic properties of the resulting CNT was discussed by Lee et al. [186]. A diameter-dependent variation of the elastic modulus was suggested to be a strong evidence for a metastable catalyst growth model [186]. Helveg et al. [232] did observe numerous morphological changes of the catalyst suggesting its instability during the formation process.
Gao et al. [219] assumed point defects in the CNT structure to be responsible for the reduction of the elastic modulus to values as low as 2.2 GPa. The CNT were grown by thermal CVD and possessed a high point defect density. Since the defect distribution was considered to be homogeneous along the CNT, the usage of a continuum beam model was claimed to be applicable. Large volume defects were also investigated but no influence on the overall behavior was found [219]. The CNT was considered to be homogeneous even though structural inhomogeneities were found and the mounting has been assumed to be perfectly rigid. A reduction of the elastic modulus of CNT due to defects was also claimed by Xia et al. [233]. The authors found different values for the axial and radial elastic modulus of SWCNT by hydrostatic pressure simulation (classical MD). Furthermore, the elastic modulus depends on the strain that is applied. With greater strain the CNT become softer [233]. No multi-walled CNT were simulated and thus the influence of shell interaction was not investigated.

Salvetat et al. [200] proposed a correlation between the degree of disorder and the elastic modulus, which is shown in fig. 3.43. For material with a low disorder (type A) a high elastic modulus can be expected, whereas in the case of increasing disorder (type B and type C) the elastic modulus might be low.
It may be assumed, that in case of a homogeneous defect density no dependence between the elastic modulus and the outer diameter exists. For each type of homogeneous material the elastic modulus is not a function of the diameter as it is shown in fig. 3.44. Data of both, homogeneous low defect density material as the arc-discharge CNT (type A), but also homogeneous material possessing a higher defect density as the CVD-grown CNT (type B) should show almost no diameter dependency [174]. As it was reported for arc-discharge material [174], no dependence on the outer diameter was found which is anticipated for very homogeneous material [186].
With increasing disorder the elastic modulus might be more dependent on the diameter especially if the defect density is not a constant along the radius of the CNT cross section. Also the occurrence of large volume defects influences the elastic modulus. In the case of a very high disorder, the elastic modulus might be within a broader range of values. Nevertheless, if the defect density is homogeneous and constant along the

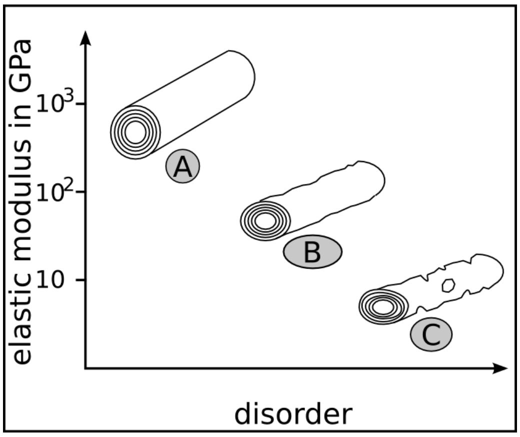

Figure 3.43: Correlation between degree of disorder and expected average for the elastic modulus after [200]. (A) low, (B) medium and (C) high defect density

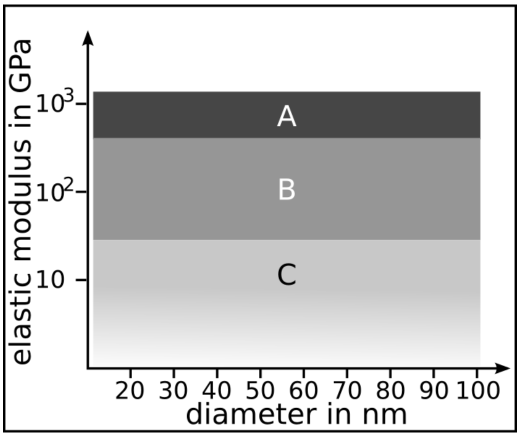

Figure 3.44: Elastic modulus is a function of the disorder but not of the outer diameter. Variations in the elastic modulus only occur if the defect density is not a constant along the diameter.

radius the elastic modulus might be small (type C) but should not strongly depend on the diameter.

However, if CNT with large diameters are grown by catalytic thermal CVD the probability of defect formation especially in the outer shells is high [186, 218]. Gaillard et al. [218] performed studies on MWCNT grown by thermal CVD. Material grown from three different types of precursors have been investigated. As their data in fig. 3.45 suggest, the elastic modulus of CNT depends on the growing conditions such as the precursor material and the temperature. But for the same growth conditions and within one particular type of precursor only a minor dependence on the diameter of the CNT was observed. Even though the diameter of this material was 2 to 6times higher than the largest CNT measured in [186], the elastic moduli found in [218] are much higher especially for thicker CNT. Nevertheless, in both cases it is assumed,

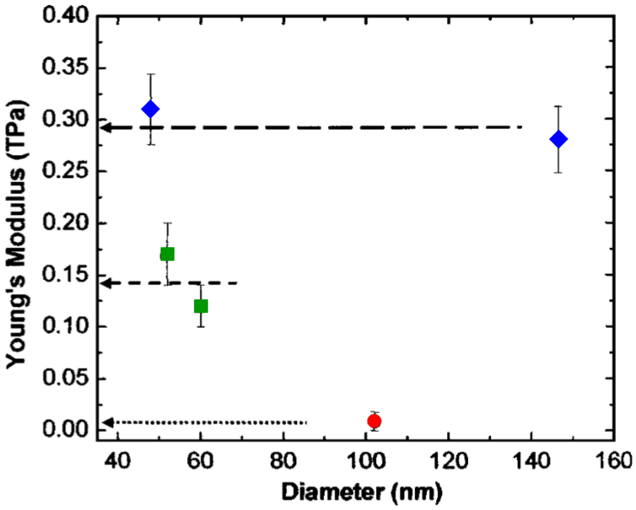

Figure 3.45: Elastic moduli for CNT grown by thermal CVD employing different precursors [218]. The blue rhombs corresponds to trimethylamine (TMA), the green squares to xylene and the red circle to melamine, respectively.

that the reduction of the elastic modulus is related to the defect density. Gaillard et al. [218] presumed that the elastic bending modulus of CNT is relatively more sensitive to defects of the carbon shells than to the diameter. The higher the defect density, the lower the elastic bending modulus of the CNT is. The authors further agreed, that the defect density increases with the number of shells and is strongly related to the growth conditions. Due to the higher concentration of material involved in the formation of thicker CNT the possibility of defect formation increases. In principle, also thick CNT with a high elastic modulus and low defect density can be obtained.

In the present work the material was produced by thermal CVD based on ferrocene as precursor. Due to the growth conditions the materials structure and morphology was inhomogeneous. This is reflected by the fact, that a certain range of elastic moduli was found tab. 3.2, even though the diameter distribution is relatively small in comparison to Gaillard et al. [218]. This shows that the material obtained by the in-situ filling process possesses a defect density that is comparable to other multi-walled CNT grown by thermal CVD. The origin of the defects which are formed during synthesis was discussed in chapter 2.3 on page 48 about the synthesis. Besides major defects such as kinks and spherical particle inclusions, a certain defect density within the carbon shells can be assumed.

The values obtained for the elastic modulus within the present work in comparison to literature [174, 186, 218] are shown in fig. 3.46. The material investigated by static bending using AFM [174, 186] might also have carbon contamination on top of the surface as a result of the dispersion of the CNT. This deposition might lead to an increase of the outer diameter, however, this material has a significant lower elastic modulus than highly crystalline carbon shells. In that case the increase of the diameter and the strong decrease of the elastic modulus might also be explained by an overestimation of the CNT diameter. The data marked with ■ represent results of the present work assuming elastic properties of the mounting by introducing a torsion spring as boundary condition. The mean elastic modulus for these data points is $E_b = 0.41\,\text{TPa}$ with a standard deviation of 0.11 TPa. There is no obvious dependence of the effective elastic modulus on the outer diameter as it is shown in fig. 3.46. Also measurements reported in literature did not reveal a clear functional relationship [173, 174]. However, a dependence of the elastic modulus as a function of the outer diameter can be discussed for the data of Poncharal et al. [188] and Lee et al. [186]. A sharp drop of the elastic modulus around 15 nm was observed in both cases. As it can be expected for the elastic modulus as a material property, it is not a function of the diameter. However, since each CNT is an individual and the CNT are from different samples, the morphology and thus the defect density has still an impact on the elastic properties and different values for the elastic modulus can be expected.

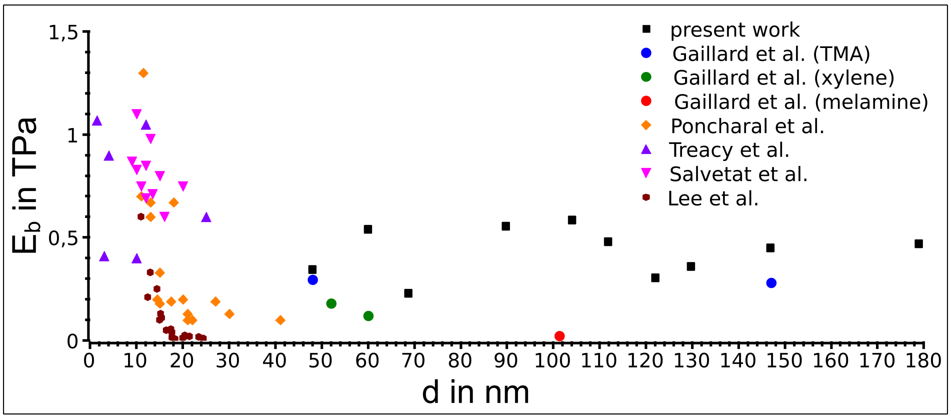

Figure 3.46: Elastic moduli of multi-walled CNT versus the outer diameter. Data points marked with ■ represents data of iron-filled CNT measured in this work, assuming elastic properties of the mounting. One additional data point (purple upwards triangle) with the coordinates (3,1.9) is not shown [173].

3.3.4 CNT as sensors and actuators

CNT have been proven to be a suitable material for raster scanning probes such as AFM [234] and MFM probes [54]. A sufficient high bending stiffness of the CNT structure is one important requirement for a successful application of carbon nanotubes as free standing probes for raster scanning microscopy. Therefore, especially for using iron-filled CNT as probes for MFM a high bending stiffness is mandatory, since the magnetic filling should be several microns in length which requires a stable and stiff carbon structure for its protection. The usage of CNT as free standing probes for AFM applications is limited by the stiffness of the CNT. It was found that only very short single-walled CNT below 100 nm can be used for non-contact AFM [8]. The issue with SWCNT is the low lateral bending stiffness due to the small outer diameter (≈1 nm). Also the diameter of a multi-walled CNT-tip should be as small as possible in order to ensure a high lateral resolution. A thin walled cap also ensures a close distance between the sample surface and the magnetic moment of the nanowire inside of the CNT providing good sensitivity. In case of a rough surface also the unsupported length of the CNT should be long enough to measure the surface features with substantial inclines. The spring constant of the iron-filled CNT is within the range $0.0008\,\frac{\mathrm{N}}{\mathrm{m}}$ to $0.0131\,\frac{\mathrm{N}}{\mathrm{m}}$ for measured elastic moduli in the range 0.06 TPa to 0.9 TPa. In tab. 3.3 the expected deflection of CNT with a free length of 10 µm or 20 µm and an elastic modulus of 0.1 TPa or 0.1 TPa for a static vertical force of 0.001 nN is given.

During the MFM measurements few of the CNT could neither be used for a topography nor for a magnetic contrast imaging. It might be that either the bending stiffness of the CNT or the stiffness of the mounting was too small. A number of CNT was successfully used for both, measurement of the topography and the magnetic information. Thus, it was shown that the produced material is suitable for the production of MFM probes based on CNT filled with α-iron as ferromagnetic material. The iron-filled CNT have been proven as probes for MFM imaging applications [35, 36, 54]. The magnetic moment of the filling might also be used for actuator applications. A magnetic dipole, such as a ferromagnetic filling section inside of a CNT, experiences a force $\vec{F} = (\vec{m}\,\nabla)\,\vec{B}$ and a torque $\vec{T} = \vec{m} \times \vec{B}$ when exposed to an inhomogeneous magnetic field. In a sensor application the CNT might be fixed on one or even two sides and thus it can only bend but not translate. In a first approximation the torque $\vec{T}$ results in a bending of the CNT while the force $\vec{F}$ is compensated by the fixation. CNT filled with ferromagnetic material could be used for magneto (electro) mechanical systems such as actuators and sensors.

Table 3.3: Expected deflection of CNT for a static vertical force of 0.001 nN.

L in μm	d_o	d_i	E_b in TPa	defl. in nm
20	30	10	0.1	680
			0.4	170
10	100	30	0.1	0.68
			0.4	0.17

In order to achieve a higher sensitivity in future, the stiffness of the CNT has to be lowered. This could be achieved in general by reducing the number of encapsulating carbon shells but also by local weakening of the CNT structure using etching methods.

Summary and outlook

An industrial application of CNT requires the understanding of the growth mechanism and the control of the synthesis process parameters. In case of single- and double-walled CNT the chirality and thus electrical properties are the most interesting properties. The research objective is the controlled synthesis of CNT with the desired properties. Albeit multi-walled CNT generally show metallic electrical behavior, the formation of defined properties such as diameter, number and crystallinity of the shells is required as well. The most promising synthesis approaches are CVD and laser ablation techniques which evolved successfully during the last two decades. However, due to the extensive parameter space the nucleation and growth process are not fully understood, yet. In conjunction with filled CNT in addition to the shell formation the filling process has to be understood in order to control the distribution and dimension of the filling. Different models have been proposed in literature, but many open questions still remain.

Chapter 2 of the present work dealt with the synthesis of iron-filled CNT. In this thesis all experiments and the discussion about the growth process were conducted with respect to the demands of magnetic force microscopy probes. Since the impact of reaction temperature has been investigated in previous works [132, 133], the present thesis focused on the temperature profile of the furnace, the aluminum layer of the substrate, the precursor mass flow and their impact on the morphology of in-situ iron-filled CNT. By selecting appropriate process parameters for the temperature, sample position, gas flow and by controlling the precursor mass flow, CNT with a continuous filling of several microns in length were obtained.

Existing growth models have been analyzed and controversially discussed in order to explain the formation of typical morphologies of in-situ filled CNT. In this work a modified growth model for the formation of in-situ filled CNT has been suggested that is based upon a model introduced by Kunadian et al. [120]. The combined-growth-mode model is capable to explain the experimental results. Experiments which were conducted in consideration of the assumption of this model, especially the role of the precursor mass flow, resulted in the formation of long and continuous iron nanowires encapsulated inside multi-walled CNT. The modified growth model and the synthesis results showed, that besides the complexity of the parameter interaction, a control of

the morphology of in-situ iron-filled CNT is possible.
In addition to the established solid state CVD method a liquid source CVD employing 1,2-Dichlorobenzene as organic solvent and dissolved ferrocene as precursor was performed. As an unexpected result it was found, that a significant part of the CNT was filled with iron-carbide [66]. The synthesis conditions and chemical reactions that might be the reason for the occurrence of the iron carbide phase were discussed in section 2.4.
In order to further investigate the implications of the proposed combined-growth-mode model a two-parted precursor evaporator is suggested. The possibility of two different subsequently or even alternately provided precursors can be used to study the filling process. The sequence of the filling material could be examined and the found material sequence and its constitution should reveal whether the model could predict the experimental results. In addition, a setup with two or more precursor sources could also be used for growing CNT filled with alloys.

In chapter 3 the measurements of mechanical properties of in-situ iron-filled CNT were presented. Two different experimental methods and setups were established, whereby one enabled a static bending measurement inside a TEM and another a dynamical excitation of flexural vibration of CNT inside SEM, which was the preferred method. For the first time mechanical properties and in particular the effective elastic modulus E_b of in-situ iron-filled CNT were determined basing on the Euler-Bernoulli beam model. This continuum mechanic model can be applied to describe the mechanical properties of CNT and especially MWCNT in consideration of the restriction that CNT represent a macro molecular structure built of nested rolled-up graphene layers. For evaluation and determination of the elastic modulus the envelope of the resonant vibrating state was evaluated by fitting the EBM to the experimental data. The experiments also showed clearly, that at the nanoscale the properties of sample attachment have to be taken into account. Thus, instead of a rigid boundary condition a torsion spring like behavior possessing a finite stiffness was used to model an one side clamped CNT. The extended data evaluation considering the elastic boundary conditions resulted in an average elastic modulus of $\mathrm{E_b} = 0.41 \pm 0.11\,\mathrm{TPa}$. The low standard deviation gives evidence for the homogeneity of the grown material. To some extend a correlation between the formation process, the consequent morphology and the mechanical properties has been discussed. The obtained results prove the usability of this material as free standing tips for raster scanning microscopy and especially magnetic force microscopy. The developed methods provide the basis for further investigations of the CNT and the understanding of mechanical behavior in greater detail.

Besides the successful usage as MFM tips, iron- or iron-carbide filled CNT synthesized in the present thesis formed the basis for several other fundamental research activities.

The electrical current induced transport of the filling material was investigated inside a TEM [235]. The extended iron nanowires of several microns in length enabled investigations on their magnetic properties. The switching behavior of single encapsulated iron nanowires by micro hall microscopy was investigated [236]. The magnetic properties of iron- and iron-carbide filled CNT employing the MFM were investigated [237]. For Fe_3C nanowires it has been shown that the magnetic crystalline anisotropy of this material can have a larger influence on the magnetic configuration than the shape anisotropy [66]. The research done on and with this material underlined its great potential for the usage as magnetic field sensors [36, 42, 54, 238, 239].
An one or two side clamped CNT can be considered as a cantilever beam, which enables future fields of application. Especially iron-filled CNT can be thought of as an excellent material for magnetic nano electro mechanical system (magnetic NEMS). Magnetometry measurements of an encapsulated ferromagnetic nanowire directly using the CNT itself as the cantilever have been performed [42]. These experiments presented the proof of principle, that CNT filled with ferromagnetic material can be used as sensors for magnetic stray fields. Also actuators based on this material might be built in future. However, this demands further experiments and more detailed results. A faster and automatic vibration detection setup should be utilized in order to increase the potential of the magnetic CNT oscillators. Furthermore, more complex models of the particular CNT under investigation should be used taking the special characteristics such as diameter variations and composed cross sections into account. Regardless of the preparation method of the setup construction, a detailed study of boundary conditions will be inevitable. However, it also provides the possibility to taylor a device with a desired behavior, especially if the bending stiffness is too high. A soft and elastic mounting might provide the possibility of a magnetic switch at micro- or nanoscale.

Carbon nanotubes with additional magnetic properties due to ferromagnetic filling or adhered particles will provide the basis for many interesting future applications as they step out from the laboratory into applied science and engineering.

Bibliography

[1] S. Iijima. Helical microtubeles of graphitic carbon. *Nature*, 354(7):56–58, 1991.

[2] R. Klingeler, S. Hampel, and B. Buechner. Carbon nanotube based biomedical agents for heating, temperature sensoring and drug delivery. *Int. J. Hyperthermia*, 24:496–505, 2008.

[3] S. Hampel, D. Kunze, D. Haase, K. Kraemer, M. Rauschenbach, M. Ritschel, L. Leonhardt, J. Thomas, S. Oswald, V. Hoffmann, and B. Buechner. Carbon nanotubes filled with a chemotherapeutic agent: a nanocarrier mediates inhibition of tumor cell growth. *Nanomedicine 3*, 2:175–182, 2008.

[4] A. Vyalikh, A. Wolter, S. Hampel, D. Haase, M. Ritschel, A. Leonhardt, H.-J. Grafe, A. Taylor, K. Kraemer, B. Buechner, and R. Klingeler. A carbon-wrapped nanoscaled thermometer for temperature control in biological environments. *Nanomedicine 3*, 3:321–327, 2008.

[5] Y. Krupskaya, C. Mahn, A. Parameswaran, A. Taylor, K. Krämer, S. Hampel, A. Leonhardt, M. Ritschel, B. Büchner, and R. Klingeler. Magnetic study of iron-containing carbon nanotubes: Feasibility for magnetic hyperthermia. *J. Magn. Magn. Mater.*, 321:4067–4071, 2009.

[6] S. Y. Chou, M. S. Wei, P. R. Krauss, and P. B. Fisher. Single-domain magnetic pillar array of 35 nm diameter and 65 gbits/in^2 density for ultrahigh density quantum magnetic storage. *J. Appl. Phys.*, 76:6673–6675, 1994.

[7] P. Avouris, B. Bhushan, K. von Klitzing, H. Sakaki, and R. Wiesendanger. *Applied Physics of Carbon Nanotubes.* Springer, 2005.

[8] E. S. Snow, P. M. Campbell, and J. P. Novak. Single-wall carbon nanotube atomic force microscope probes. *Appl. Phys. Lett.*, 80:2002–2004, 2002.

[9] F. Wolny. *Magnetic properties of individual iron filled carbon nanotubes and their application as probes for magnetic force microscopy.* PhD thesis, TU Dresden, 2011.

[10] M. Dresselhaus, G. Dresselhaus, and P. Avouris. *Carbon Nanotubes: Synthesis, Structure, Properties and Applications.* Number 80 in Topics in Applied Physics. Springer, 2002. ISBN 3-549-41086-4.

[11] R. Saito, G. Dresselhaus, and M. S. Dresselhaus. *Physical Properties of Carbon Nanotubes.* Imperial College Press: London, 1998.

[12] A. Jorio, G. Dresselhaus, and M. S. Dresselhaus, editors. *Carbon Nanotubes.* Springer, 2008.

[13] L. Liu, C. S. Jayanthi, M. Tang, S. Y. Wu, T. W. Tombler, C. Zhou, L. Alexseyev, J. Kong, and H. Dai. Controllable reversibility of an sp^2 to sp^3 transition of a single wall nanotube under the manipulation of an afm tip: A nanoscale electromechanical switch? *Phys. Rev. Lett.*, 84(21):4950–4953, 2000.

[14] H. Kataura, Y. Kumazawa, Y. Maniwa, I. Umezu, S. Suzuki, Y. Ohtsuka, and Y. Achiba. Optical properties of single-wall carbon nanotubes. *Synth. Met.*, 103:2555–2558, 1999.

[15] R. Saito and H. Kataura. Optical properties and raman spectroscopy of carbon nanotubes. *Top. Appl. Phys.*, 80:213–247, 2001.

[16] J. Hone. Phonons and thermal properties of carbon nanotubes. *Top. Appl. Phys.*, 80:273–286, 2001.

[17] B. I. Yakobson and P. Avouris. Mechanical properties of carbon nanotubes. *Top. Appl. Phys.*, 80:287–327, 2001.

[18] L. Forró and C. Schönenberger. Physical properties of multi-wall nanotubes. *Top. Appl. Phys.*, 80:329–391, 2001.

[19] M. C. Hersam. Progress towards monodisperse single-walled carbon nanotubes. *Nat. Nanotechnol.*, 3:387–394, 2008.

[20] A. Bianco, K. Kostarelos, and M.Prato. Applications of carbon nanotubes in drug delivery. *Curr. Opin. Chem. Biol.*, 9:674–679, 2005.

[21] V. Raffa, G. Ciofani, O. Vittorio, V. Pensabene, and A. Cuschieri. Carbon nanotube-enhanced cell electropermeabilisation. *Bioelectrochemistry*, 79(1):136–141, 2010.

[22] M. S. Strano, C. A. Dyke, M. L. Usrey, P. W. Barone, M. J. Allen, H. Shan, C. Kittrell, R. H. Hauge, J. M. Tour, and R. E. Smalley. Electronic structure control of single-walled carbon nanotube functionalization. *Science*, 301:1519–1522, 2003.

[23] Y.-L. Hsin, J.-Y. Lai, K. C. Hwang, S.-C. Lo, F.-R. Chen, and J. Kai. Rapid surface functionalization of iron-filled multi-walled carbon nanotubes. *Carbon*, 44:3328–3335, 2006.

[24] O. Byl, J. Liu, and J. John T. Yates. Etching of carbon nanotubes by ozonesa surface area study. *Langmuir*, 21:4200–4204, 2005.

[25] C.-C. Hu, J.-H. Su, and T.-C. Wen. Modification of multi-walled carbon nanotubes for electric double-layer capacitors: Tube opening and surface functionalization. *J. Phys. Chem. Solids*, 68:2353—-2362, 2007.

[26] J. Zhang, H. Zou, Q. Qing, Y. Yang, Q. Li, Z. Liu, X. Guo, and Z. Dus. Effect of chemical oxidation on the structure of single-walled carbon nanotubes. *J. Phys. Chem. B*, 107:3712–3718, 2003.

[27] A. Taylor, Y. Krupskaya, K. Krämer, S. Füssel, R. Klingeler, B. Büchner, and M. P. Wirth. Cisplatin-loaded carbon-encapsulated iron nanoparticles and their in vitro effects in magnetic fluid hyperthermia. *Carbon*, 48:2327–2334, 2010.

[28] A. Leonhardt, S. Hampel, C. Müller, I. Mönch, R. Koseva, M. Ritschel, D. Elefant, K. Biedermann, and B. Büchner. Synthesis, properties, and applications of ferromagnetic-filled carbon nanotubes. *Chem. Vap. Deposition*, 12:380–387, 2006.

[29] S. Hampel, A. Leonhardt, D. Selbmann, K. Biedermann, D. Elefant, C. Müller, T. Gemming, and B. Büchner. Growth and characterization of filled carbon nanotubes with ferromagnetic properties. *Carbon*, 44:2316–2322, 2006.

[30] W. Wang, K. Wang, R. Lv, J. Wei, X. Zhang, F. Kang, J. Chang, Q. Shu, Y. Wang, and D. Wu. Synthesis of fe-filled thin-walled carbon nanotubes with high filling ratio by using dichlorobenzene as precursor. *Carbon*, 45(5):1127–1129, 2007.

[31] U. Weissker, S. Hampel, A. Leonhardt, and B. Büchner. Carbon nanotubes filled with ferromagnetic materials. *MDPI Materials*, 3:4387–4427, 2010.

[32] A. Fert and L. Piraux. Magnetic nanowires. *J. Magn. Magn. Mat.*, 200:338–358, 1999.

[33] D. J. Sellmyer, M. Zheng, and R. Skomski. Magnetism of fe, co and ni nanowires in self-assembled arrays. *J. Phys.: Condens. Matter*, 13:433–460, 2001.

[34] L. Sun, Y. Hao, C.-L. Chien, and P. C. Searson. Tuning the properties of magnetic nanowires. *IBM J. Res. Dev.*, 49:79, 2005.

[35] A. Winkler, T. Mühl, S. Menzel, R. Kozhuharova-Koseva, S. Hampel, A. Leonhardt, and B. Büchner. Magnetic force microscopy sensors using iron-filled carbon nanotubes. *J. Appl. Phys.*, 99:104905–5, 2006.

[36] F. Wolny, U. Weissker, T. Mühl, A. Leonhardt, S. Menzel, A. Winkler, and B. Büchner. Iron-filled carbon nanotubes as probes for magnetic force microscopy. *J. Appl. Phys.*, 104(6):064908–5, 2008.

[37] R. Skomski. Nanomagnetics. *J. Phys.: Condens. Matter*, 15:R841–R896, 2003.

[38] Y. Endo, H. Fujimoto, S. Kumano, Y. Matsumura, I. Sasaki, Y. Kawamura, and M. Yamamoto. Study on the magnetization reversal process in a magnetic nanowire and a magnetic dot observed by magnetic field sweeping magnetic force microscopy measurements (invited). *J. Appl. Phys.*, 103:07D918–6, 2008.

[39] J. Yuan, W. Pei, T. Hasagawa, T. Washiya, H. Saito, S. Ishio, H. Oshima, and K.-i. Itoh. Study on magnetization reversal of cobalt nanowire arrays by magnetic force microscopy. *J. Magn. Magn. Mater.*, 320(5):736–741, 2008.

[40] T. Mühl, D. Elefant, A. Graff, R. Kozhuharova, A. Leonhardt, I. Mönch, M. Ritschel, P. Simon, S. Groudeva-Zotova, and C. M. Schneider. Magnetic properties of aligned fe-filled carbon nanotubes. *J. Appl. Phys.*, 93(10):7894–7896, 2003.

[41] P. Banerjee, F. Wolny, D. V. Pelekhov, M. R. Herman, K. C. Fong, U. Weissker, T. Mühl, Y. Obukhov, A. Leonhardt, B. Büchner, and P. C. Hammel. Magnetization reversal in an individual 25 nm iron-filled carbon nanotube. *Appl. Phys. Lett.*, 96:252505–3, 2010.

[42] S. Philippi, U. Weissker, T. Muhl, A. Leonhardt, and B. Buchner. Room temperature magnetometry of an individual iron filled carbon nanotube acting as nanocantilever. *J. Appl. Phys.*, 110(8):084319–5, 2011.

[43] K. Lipert, F. Kretzschmar, M. Ritschel, A. Leonhardt, R. Klingeler, and B. Büchner. Non-magnetic carbon nanotubes. *J. Appl. Phys.*, 2009.

[44] C. Prados, P. Crespo, J. M. Gonzalez, A. Hernando, J. F. Marco, R. Gancedo, N. Grobert, M. Terrones, R. M. Walton, and H. W. Kroto. Hysteresis shift in fe-filled carbon nanotubes due to γ-fe. *Phys. Rev. B*, 65:113405–4, 2002.

[45] Y. Li, P. Xiong, S. von Molnár, Y. Ohno, and H. Ohno. Magnetization reversal in elongated fe nanoparticles. *Phys. Rev. B*, 71:214425–6, 2005.

[46] W. Wernsdorfer, E. B. Orozco, B. Barbara, K. Hasselbach, A. Benoit, D. M. an B. Doudin, J. Meier, J. E. Wegrowe, J. P. Ansermet, N. Demoncy, H. Pascard, N. Demoncy, A. Loiseau, L. Francois, N. Duxin, and M. P. Pileni. Mesoscopic effects in magnetism: Submicron to nanometer size single particle measurements. *J. Appl. Phys.*, 81:5543, 1997.

[47] Y. C. Sui, R. Skomski, K. D. Sorge, and D. J. Sellmyer. Nanotube magnetism. *Appl. Phys. Lett.*, 84(9):1525–1527, 2004.

[48] R. O'Barr and S. Schultz. Switching field studies of individual single domain ni columns. *J. Appl. Phys.*, 81(8):5458–5460, 1997.

[49] Y. Henry, K. Ounadjela, L. Piraux, S. Dubois, J.-M. George, and J.-L. Duvail. Magnetic anisotropy and domain patterns in electrodeposited cobalt nanowires. *Eur. Phys. J. B*, 20:35, 2001.

[50] D. Rugar, H. J. Mamin, P. Guethner, S. E. Lambert, J. E. Stern, I. McFadyen, and T. Yogi. Magnetic force microscopy general-principles and application to longitudinal recording media. *J. Appl. Phys.*, 68(3):1169–1183, 1990.

[51] J. J. Saenz, N. Garcia, P. Grutter, E. Meyer, H. Heinzelmann, R. Wiesendanger, L. Rosenthaler, H. R. Hidber, and H. J. Gunterodt. Observation of magnetic forces by the atomic force microscope. *J. Appl. Phys.*, 62(10):4293–4295, 1987.

[52] P. Grutter, D. Rugar, and H. J. Mamin. Magnetic force microscopy of magnetic-materials. *Ultramicroscopy*, 47(4):393–399, 1992.

[53] U. Hartmann. The point dipole approximation in magnetic force microscopy. *Phys. Lett. A*, 137(9):475–478, 1989.

[54] F. Wolny, U. Weissker, T. Mühl, M. U. Lutz, C. Müller, A. Leonhardt, and B. Büchner. Stable magnetization of iron filled carbon nanotube mfm probes in external magnetic fields. *J. Phys. Conf. Ser.*, 200:112011–4, 2010.

[55] P. M. Ajayan and S. Iijima. Capillarity-induced filling of carbon nanotubes. *Nature*, 361:333–334, 1993.

[56] J. Bao, Q. Zhou, J. Hong, and Z. Xu. Synthesis and magnetic behavior of an array of nickel-filled carbon nanotubes. *Appl. Phys. Lett.*, 81(24):4592–4594, 2002.

[57] L. M. Dyagileva, V. P. Mar'in, E. I. Tsyganova, and G. A. Razuvaev. Reactivity of the first transition row metallocenes in thermal decomposition reaction. *J. Organomet. Chem.*, 175(1):63–72, 1979.

[58] C. Müller, D. Golberg, A. Leonhardt, S. Hampel, and B. Büchner. Growth studies, tem and xrd investigations of iron-filled carbon nanotubes. *Phys. Status Solidi A*, 203:1064–1068, 2006.

[59] R. Andrews, D. Jacques, A. M. Rao, F. Derbyshire, D. Qian, X. Fan, E. C. Dickey, and J. Chen. Continuous production of aligned carbon nanotubes: a step closer to commercial realization. *Chem. Phys. Lett.*, 303(5-6):467–474, 1999.

[60] R. Kamalakaran, M. Terrones, T. Seeger, P. Kohler-Redlich, M. Rühle, Y. A. Kim, T. Hayashi, and M. Endo. Synthesis of thick and crystalline nanotube arrays by spray pyrolysis. *Appl. Phys. Lett.*, 77(21):3385–3387, 2000.

[61] X. Zhang, A. Cao, B. Wei, Y. Li, J. Wei, C. Xu, and D. Wu. Rapid growth of well-aligned carbon nanotube arrays. *Chem. Phys. Lett.*, 362(3-4):285–290, 2002.

[62] A. G. Nasibulin, A. Moisala, D. P. Brown, H. Jiang, and E. I. Kauppinen. A novel aerosol method for single walled carbon nanotube synthesis. *Chem. Phys. Lett.*, 402:227–232, 2005.

[63] C. Deck and K. Vecchio. Growth of well-aligned carbon nanotube structures in successive layers. *J. Phys. Chem. B*, 109(25):12353–12357, 2005.

[64] M. Mayne, N. Grobert, M. Terrones, R. Kamalakaran, M. Rühle, H. W. Kroto, and D. R. M. Walton. Pyrolytic production of aligned carbon nanotubes from homogeneously dispersed benzene-based aerosols. *Chem. Phys. Lett.*, 338(2-3):101–107, 2001.

[65] C. P. Deck and K. Vecchio. Growth mechanism of vapor phase cvd-grown multi-walled carbon nanotubes. *Carbon*, 43(12):2608–2617, 2005.

[66] U. Weissker, M. Löffler, F. Wolny, M. U. Lutz, N. Scheerbaum, R. Klingeler, T. Gemming, T. Mühl, A. Leonhardt, and B. Büchner. Perpendicular magnetization of long iron carbide nanowires inside carbon nanotubes due to magnetocrystalline anisotropy. *J. Appl. Phys.*, 106(5):054909–5, 2009.

[67] K. Kuwana and K. Saito. Modeling cvd synthesis of carbon nanotubes: Nanoparticle formation from ferrocene. *Carbon*, 43:2088–2095, 2005.

[68] R. Kozhuharova, M. Ritschel, D. Elefant, A. Graff, I. Mönch, T. Mühl, C. Schneider, and A. Leonhardt. (fe$_x$co$_{1-x}$)-alloy filled vertically aligned carbon nanotubes grown by thermal chemical vapor deposition. *J. Magn. Magn. Mater.*, 290:250–253, 2005.

[69] M. H. G. Jacobs, P. J. Van Ekeren, and C. G. De Kruif. The vapour pressure and enthalpy of sublimation of ferrocene. *J. Chem. Thermodyn.*, 15(7):619–623, 1983.

[70] L. A. Torres-Gómez, G. Barreiro-Rodríquez, and F. Méndez-Ruíz. Vapour pressures and enthalpies of sublimation of ferrocene, cobaltocene and nickelocene. *Thermochimica Acta*, 124:179–183, 1988.

[71] V. N. Emel'yanenko, S. P. Verevkin, O. V. Krol, R. M. Varushchenko, and N. V. Chelovskaya. Vapour pressures and enthalpies of vaporization of a series of the ferrocene derivatives. *J. Chem. Thermodyn.*, 39(4):594–601, 2007.

[72] R. Sen, A. Govindaraj, and C. N. R. Rao. Carbon nanotubes by the metallocene route. *Chem. Phys. Lett.*, 267(3-4):276–280, 1997.

[73] C. N. R. Rao, R. Sen, B. C. Satishkumar, and A. Govindaraj. Large aligned-nanotube bundles from ferrocene pyrolysis. *Chem. Commun.*, 15:1525 – 1526, 1998.

[74] X. Gui, J. Wei, K. Wang, W. Wang, R. Lv, J. Chang, F. Kang, J. Gu, and D. Wu. Improved filling rate and enhanced magnetic properties of fe-filled carbon nanotubes by annealing and magnetic separation. *Mater. Res. Bull.*, 43:3441–3446, 2008.

[75] X. Gui, K. Wang, W. Wang, J. Wei, X. Zhang, R. Lv, Y. Jia, Q. Shu, F. Kang, and D. Wu. The decisive roles of chlorine-contained precursor and hydrogen for the filling fe nanowires into carbon nanotubes. *Mater. Chem. Phys.*, 113:634–637, 2009.

[76] R. L. Vander Wal, T. M. Ticich, and V. E. Curtis. Substrate-support interactions in metal-catalyzed carbon nanofiber growth. *Carbon*, 39(15):2277–2289, 2001.

[77] A.-C. Dupuis. The catalyst in the ccvd of carbon nanotubes—a review. *Prog. Mater Sci.*, 50:929–961, 2005.

[78] Y. Chen, J. Huang, J. Hu, C. Yang, and W. Kang. Synthesis of single-walled carbon nanotubes produced using a three layer al/fe/mo metal catalyst and their field emission properties. *Carbon*, 45(15):3007–3014, 2007.

[79] P. Kappen, B. Halstead, A. Rider, P. J. Pigram, and N. Brack. Multi-walled carbon nanotubes grown from chemical vapor: Links between atomic near range order and growth parameters. *J. Phys. Chem. C*, 113:4307–4314, 2009.

[80] A. M. Molenbroek, S. Helveg, H. Topsoe, and B. S. Clausen. Nano-particles in heterogeneous catalysis. *Top Catal.*, 52:1303–1311, 2009.

[81] H. Endo, K. Kuwana, K. Saito, D. Qian, R. Andrews, and E. A. Grulke. Cfd prediction of carbon nanotube production rate in a cvd reactor. *Chem. Phys. Lett.*, 387(4-6):307–311, 2004.

[82] H. T. Ng, B. Chen, J. E. Koehne, A. M. Cassell, J. Li, J. Han, and M. Meyyappan. Growth of carbon nanotubes: A combinatorial method to study the effects of catalysts and underlayers. *J. Phys. Chem. B.*, 107:8484–8489, 2003.

[83] C. Müller, S. Hampel, D. Elefant, K. Biedermann, A. Leonhardt, M. Ritschel, and B. Büchner. Iron filled carbon nanotubes grown on substrates with thin metal layers and their magnetic properties. *Carbon*, 44:1746–1753, 2006.

[84] Y. Mo, A. Kibria, and K. Nahm. The growth mechanism of carbon nanotubes from thermal cracking of acetylene over nickel catalyst supported on alumina. *Synth. Met.*, 122:443–447, 2001.

[85] H. Hongo, F. Nihey, T. Ichihashi, Y. Ochiai, M. Yudasaka, and S. Iijima. Support materials based on converted aluminum films for chemical vapor deposition growth of single-wall carbon nanotubes. *Chem. Phys. Lett.*, 380(1-2):158–164, 2003.

[86] I. K. Song, W. J. Yu, Y. S. Cho, G. S. Choi, and D. Kim. The determining factors for the growth mode of carbon nanotubes in the chemical vapour deposition process. *Nanotechnology*, 15:590–595, 2004.

[87] C. Müller, A. Leonhardt, S. Hampel, and B. Büchner. Diameter controlled growth of iron-filled carbon nanotubes. *Phys. Status Solidi B*, 243:3091–3094, 2006.

[88] S. Iijima, P. M. Ajayan, and T. Ichihashi. Growth model for carbon nanotubes. *Phys. Rev. Lett.*, 69(21):3100–3103, 1992.

[89] S. Sinnott, R. Andrews, D. Qian, A. Rao, Z. Mao, E. Dickey, and F. Derbyshire. Model of carbon nanotube growth through chemical vapor deposition. *Chem. Phys. Lett.*, 315:25–30, 1999.

[90] G. Y. Zhang and E. G. Wang. Cu-filled carbon nanotubes by simultaneous plasma-assisted copper incorporation. *Appl. Phys. Lett.*, 82(12):1926–1928, 2003.

[91] M. S. Kabir, R. E. Morjan, O. A. Nerushev, P. Lundgren, S. Bengtsson, P. Enoksson, and E. E. B. Campbell. Fabrication of individual vertically aligned carbon nanofibres on metal substrates from prefabricated catalyst dots. *Nanotechnology*, 17(3):790–794, 2006.

[92] I. Mönch, R. Kozhuharova-Koseva, M. Rümmeli, D. Elefant, T. Gemming, R. Kaltofen, A. Leonhardt, T. Schäfer, and B. Büchner. Selective growth of vertically aligned fe-filled carbon nanotubes on oxidized silicon substrates. *J. Phys. Conf. Ser.*, 61:815–819, 2007.

[93] S. Esconjauregui, C. M. Whelan, and K. Maex. The reasons why metals catalyze the nucleation and growth of carbon nanotubes and other carbon nanostructures. *Carbon*, 47(3):659–669, 2009.

[94] J. Gavillet, J. Thibault, O. Stéphan, H. Amara, A. Loiseau, C. Bichara, J. P. Gaspard, and F. Ducastelle. Nucleation and growth of single-walled nanotubes: The role of metallic catalysts. *J. Nanosci. Nanotechnol.*, 4(4):346–359, 2004.

[95] F. Schouten, O. Gijzeman, and G. Bootsma. Interaction of methane with ni(111) and ni(100); diffusion of carbon into nickel through the (100) surface; an aes-leed study. *Surf. Sci.*, 87(1):1–12, 1979.

[96] M. Audier, A. Oberlin, and M. Coulon. Crystallographic orientations of catalytic particles in filamentous carbon; case of simple conical particles. *J. Cryst. Growth*, 55(3):549–556, 1981.

[97] R. R. Vanfleet and J. M. Mochel. Thermodynamics of melting and freezing in small particles. *Surf. Sci.*, 341(1-2):40–50, 1995.

[98] A. Loiseau and F. Willaime. Filled and mixed nanotubes: from tem studies to the growth mechanism within a phase-diagram approach. *Appl. Surf. Sci.*, 164(1):227–240, 2000.

[99] J. Wen, Z. Huang, D. Wang, J. Chen, S. Yang, Z. Ren, J. Wang, L. Calvet, J. Chen, J. Klemic, and M. Reed. Growth and characterization of aligned carbon nanotubes from patterned nickel nanodots and uniform thin films. *J. Mater. Res.*, 16:3246–3253, 2001.

[100] A. Loiseau, J. Gavillet, F. Ducastelle, J. Thibault, O. Stephan, P. Bernier, and S. Thair. Nucleation and growth of swnt: Tem studies of the role of the catalyst. *C. R. Phys.*, 4(9):975–991, 2003.

[101] C. Müller, A. Leonhardt, M. C. Kutz, H. Reuther, and B. Büchner. Growth aspects of iron-filled carbon nanotubes obtained by catalytic chemical vapor deposition of ferrocene. *J. Phys. Chem. C*, 113:2736–2740, 2009.

[102] A. Leonhardt, M. Ritschel, R. Kozhuharova, A. Graff, T. Mühl, R. Huhle, I. Mönch, D. Elefant, and C. M. Schneider. Synthesis and properties of filled carbon nanotubes. *Diamond Relat. Mater.*, 12(3-7):790–793, 2003.

[103] A. Leonhardt, M. Ritschel, D. Elefant, N. Mattern, K. Biedermann, S. Hampel, C. Müller, T. Gemming, and B. Büchner. Enhanced magnetism in fe-filled carbon nanotubes produced by pyrolysis of ferrocene. *J. Appl. Phys.*, 98(7):074315–5, 2005.

[104] K. Kuwana, H. Endo, K. Saito, D. Qian, R. Andrews, and E. A. Grulke. Catalyst deactivation in cvd synthesis of carbon nanotubes. *Carbon*, 43(2):253–260, 2005.

[105] K. Kuwana, T. Li, and K. Saito. Gas-phase reactions during cvd synthesis of carbon nanotubes: Insights via numerical experiments. *Chem. Eng. Sci.*, 61(20):6718–6726, 2006.

[106] K. Kuwana and K. Saito. Modeling ferrocene reactions and iron nanoparticle formation: Application to cvd synthesis of carbon nanotubes. *Proceedings of the Combustion Institute*, 31(2):1857–1864, 2007.

[107] C. Singh, M. S. P. Shaffer, and A. H. Windle. Production of controlled architectures of aligned carbon nanotubes by an injection chemical vapour deposition method. *Carbon*, 41(2):359–368, 2003.

[108] O. A. Nerushev, M. Sveningsson, L. K. L. Falk, and F. Rohmund. Carbon nanotube films obtained by thermal chemical vapour deposition. *J. Mater. Chem.*, 11:1122–1132, 2001.

[109] K. Hernadi, A. Fonseca, J. B. Nagy, D. Bernaerts, and A. A. Lucas. Fe-catalyzed carbon nanotube formation. *Carbon*, 34(10):1249–1257, 1996.

[110] W. Wasel, K. Kuwana, P. T. Reilly, and K. Saito. Experimental characterization of the role of hydrogen in cvd synthesis of mwcnts. *Carbon*, 45(4):833–838, 2007.

[111] C. Ducati, I. Alexandrou, M. Chhowalla, J. Robertson, and G. A. J. Amaratunga. The role of the catalytic particle in the growth of carbon nanotubes by plasma enhanced chemical vapor deposition. *J. Appl. Phys.*, 95(11):6387–6391, 2004.

[112] M. Kumar and Y. Ando. Chemical vapor deposition of carbon nanotubes: A review on growth mechanism and mass production. *J. Nanosci. Nanotechnol.*, 10(6):3739–3758, 2010.

[113] P. T. Reilly and W. B. Whitten. The role of free radical condensates in the production of carbon nanotubes during the hydrocarbon cvd process. *Carbon*, 44(9):1653–1660, 2006.

[114] Z. Y. Juang, J. F. Lai, C. H. Weng, J. H. Lee, H. J. Lai, T. S. Lai, and C. H. Tsai. On the kinetics of carbon nanotube growth by thermal cvd method. *Diamond Relat. Mater.*, 13(11-12):2140–2146, 2004.

[115] F. Ding, K. Bolton, and A. Rosen. Iron-carbide cluster thermal dynamics for catalyzed carbon nanotube growth. *J. Vac. Sci. Technol. A*, 22(4):1471–1476, 2004.

[116] R. S. Wagner and W. C. Ellis. Vapor-liquid-solid mechanism of single crystal growth. *Appl. Phys. Lett.*, 4(5):89–90, 1964.

[117] R. T. K. Baker. Nucleation and growth of carbon deposits from the nickel catalyzed decomposition of acetylene. *J. Catal.*, 26:51–62, 1972.

[118] R. T. K. Baker. Catalytic growth of carbon filaments. *Carbon*, 27:315–323, 1989.

[119] S. Hofmann, G. Csanyi, A. C. Ferrari, M. C. Payne, and J. Robertson. Surface diffusion: The low activation energy path for nanotube growth. *Phys. Rev. Lett.*, 95:036101–4, 2005.

[120] I. Kunadian, R. Andrews, D. Qiana, and M. P. Mengüc. Growth kinetics of mwcnts synthesized by a continuous-feed cvd method. *Carbon*, 47(2):384–395, 2009.

[121] Y.-K. Kwon, Y. H. Lee, S.-G. Kim, P. Jund, D. Tománek, and R. E. Smalley. Morphology and stability of growing multiwall carbon nanotubes. *Phys. Rev. Lett.*, 79(11):2065–2068, 1997.

[122] Y. H. Lee, S. G. Kim, and D. Tománek. Catalytic growth of single-wall carbon nanotubes: An ab initio study. *Phys. Rev. Lett.*, 78:2393–2396, 1997.

[123] F. Ding, K. Bolton, and A. Rosén. Nucleation and growth of single-walled carbon nanotubes: A molecular dynamics study. *J. Phys. Chem. B*, 108:17369–17377, 2004.

[124] M. B. Nardelli, C. Brabec, A. Maiti, C.Roland, and J. Bernholc. Lip-lip interactions and the growth of multiwalled carbon nanotubes. *Phys. Rev. Lett.*, 80:313–316, 1998.

[125] M. B. Nardelli, C. Roland, and J. Bernholc. Theoretical bounds for multiwalled carbon nanotube growth. *Chem. Phys. Lett.*, 296(5-6):471–476, 1998.

[126] J.-C. Charlier, H. Amara, and P. Lambin. Catalytically assisted tip growth mechanism for single-wall carbon nanotubes. *ACS Nano*, 1(3):202–207, 2007.

[127] F. Ding, A. Rosen, and K. Bolton. Molecular dynamics study of the catalyst particle size dependence on carbon nanotube growth. *J. Chem. Phys.*, 121(6):2775–2779, 2004.

[128] R. Kozhuharova, M. Ritschel, D. Elefant, A. Graff, A. Leonhardt, I. Mönch, T. Mühl, and C. M. Schneider. Synthesis and characterization of aligned fe-filled carbon nanotubes on silicon substrates. *J. Mater. Sci.*, 14:789–791, 2003.

[129] X. Ma, Y. Cai, X. Li, and S. Wen. Growth and microstructure of co-filled carbon nanotubes. *Mater. Sci. Eng., A*, A 357:308–313, 2003.

[130] R. Kozhuharova, M. Ritschel, I. Mönch, T. Mühl, and A. Leonhardt. Selective growth of aligned co-filled carbon nanotubes on silicon substrates. *Fuller. Nanotub. Car. N.*, 13:347–353, 2005. Fuller. Nanotub. Car. N. = Fullerenes, Nanotubes and Carbon Nanostructures.

[131] N. Grobert, M. Terrones, A. Osborne, H. Terrones, W. Hsu, S. Trasobares, Y. Zhu, J. Hare, H. Kroto, and D. Walton. Thermolysis of c_{60} thin films yields ni-filled tapered nanotubes. *Appl. Phys. A*, 67(5):595–598, 1998.

[132] R. H. Koseva. *Aligned ferromagnetic filled carbon nanotubes on oxidized silicon substrates.* PhD thesis, TU Dresden, 2006.

[133] C. Müller. *Grundlegende Untersuchungen zum CVD-Wachstum Fe-gefüllter Kohlenstoff-Nanoröhren.* PhD thesis, Technischen Universität Dresden, 2007.

[134] A. Burcat and M. Dvinyaninov. Detailed kinetics of cyclopentadiene decomposition studied in a shock tube. *Int. J. Chem. Kinet.*, 29(7):505–514, 1997.

[135] G. J. M. Dormans. Omcvd of transition metals and their silicides using metallocenes and (di) silane or silicon tetra-bromide. *J. Cryst. Growth*, 108(3-4):806–816, 1991.

[136] C. Müller, D. Elefant, A. Leonhardt, and B. Büchner. Incremental analysis of the magnetization behavior in iron-filled carbon nanotube arrays. *J. Appl. Phys.*, 103:034302, 2008.

[137] J. S. Chickos and J. William E. Acree. Enthalpies of sublimation of organic and organometallic compounds. 1910–2001. *J. Phys. Chem. Ref. Data*, 31(2):537–698, 2001.

[138] M. Löffler. *Nanomanipulation and In-situ Transport Measurements on Carbon Nanotubes.* PhD thesis, IFW Dresden, 2009.

[139] B. Zheng, C. Lu, G. Gu, A. Makarovski, G. Finkelstein, and J. Liu. Efficient cvd growth of single-walled carbon nanotubes on surfaces using carbon monoxide precursor. *Nano Lett.*, 2(8):895–898, 2002.

[140] J. Cheng, X. Zhang, F. Liu, J. Tu, Y. Ye, Y. Ji, and C. Chen. Synthesis of carbon nanotubes filled with fe_3c nanowires by cvd with titanate modified palygorskite as catalysts. *Carbon*, 41(10):1965–1970, 2003.

[141] A. K. Schaper, H. Hou, A. Greiner, and F. Phillipp. The role of iron carbide in multiwalled carbon nanotube growth. *J. Catal.*, 222:250–254, 2004.

[142] D. Golberg, M. Mitome, C. Müller, C. Tang, A. Leonhardt, and Y. Bando. Atomic structures of iron-based single-crystalline nanowires crystallized inside multi-walled carbon nanotubes as revealed by analytical electron microscopy. *Acta Mater.*, 54:2567–2576, 2006.

[143] H. Hou, A. K. Schaper, Z. Jun, F. Weller, and A. Greiner. Large-scale synthesis of aligned carbon nanotubes using fecl3 as floating catalyst precursor. *Chem. Mater.*, 15(2):580–585, 2003.

[144] I. Shein, N. Medvedeva, and A. Ivanovskii. Electronic and structural properties of cementite-type m_3x (m = fe, co, ni; x = c or b) by first principles calculations. *Physica B*, 371:126–132, 2006.

[145] S. Meschel and O. Kleppa. Standard enthalpies of formation of some 3d transition metal carbides by high temperature reaction calorimetry. *J. Alloys Compd.*, 257(1-2):227–233, 1997.

[146] A. Schneider. Iron layer formation during cementite decomposition in carburising atmospheres. *Corros. Sci.*, 44:2353–2365, 2002.

[147] G. P. Heydon, S. R. Hoony, A. N. Farleyy, S. L. Tomlinsony, M. S. Valeray, K. Attenboroughz, and W. Schwarzacherz. Magnetic properties of electrodeposited nanowires. *J. Phys. D: Appl. Phys.*, 30:1083–1093, 1997.

[148] L. Belliard, J. Miltat, A. Thiaville, S. Dubois, J. Duvail, and L. Piraux. Observing magnetic nanowires by means of magnetic force microscopy. *J. Magn. Magn. Mater.*, 190:1–16, 1998.

[149] A. K. Arzhnikov, L. V. Dobysheva, and C. Demangeat. Structural peculiarities of cementite and their influence on magnetic characteristics. *J. Phys.: Condens. Matter*, 19(19):196214–, 2007.

[150] P. Blum and R. Pauthenet. Etude ferromagnetique de la cementite polycrystalline et monocristalline. *Compt. Rend.*, 237:1501, 1953.

[151] S. Blundell. *Magnetism in Condensed Matter.* Oxford University Press, 2007.

[152] R. O'Handley. *Modern Magnetic Materials, Principles and Applications.* John Wiley & Son, Inc, 2000.

[153] W. Lottermoser, A. K. Schaper, W. Treutmann, G. Redhammer, G. Tippelt, A. Lichtenberger, S.-U. Weber, , and G. Amthauer. ^{57}fe mössbauer spectroscopy on multiwalled carbon nanotubes with metal filling. *J. Phys. Chem. B*, 110:9768–9771, 2006.

[154] F. Stäblein and K. Schroeter. Die bestimmung der magnetischen sättigung von eisencarbid. *Z. anorg. Ch.*, 174:193, 1928.

[155] D. H. Robertson, D. W. Brenner, and J. W. Mintmire. Energetics of nanoscale graphitic tubules. *Phys. Rev. B*, 45(21):12592–12595, 1992.

[156] D. Sanchez-Portal, E. Artacho, J. M. Soler, A. Rubio, and P. Ordejon. Ab initio structural, elastic, and vibrational properties of carbon nanotubes. *Phys. Rev. B*, 59(19):12678–12688, 1999.

[157] G. Van Lier, C. Van Alsenoy, V. Van Doren, and P. Geerlings. Ab initio study of the elastic properties of single-walled carbon nanotubes and graphene. *Chem. Phys. Lett.*, 326(1-2):181–185, 2000.

[158] S. Iijima, C. Brabec, A. Maiti, and J. Bernholc. Structural flexibility of carbon nanotubes. *J. Chem. Phys.*, 104(5):2089–2092, 1996.

[159] B. I. Yakobson, C. J. Brabec, and J. Bernholc. Nanomechanics of carbon tubes: Instabilities beyond linear response. *Phys. Rev. Lett.*, 76(14):2511–2514, 1996.

[160] J. P. Lu. Elastic properties of single and multilayered nanotubes. *J. Phys. Chem. Solids*, 58(11):1649–1652, 1997.

[161] E. Hernandez, C. Goze, P. Bernier, and A. Rubio. Elastic properties of c and bxcynz composite nanotubes. *Phys. Rev. Lett.*, 80(20):4502–4505, 1998.

[162] T. Belytschko, S. P. Xiao, G. C. Schatz, and R. S. Ruoff. Atomistic simulations of nanotube fracture. *Phys. Rev. B*, 65(23):235430–8, 2002.

[163] G. M. Odegard, T. S. Gates, L. M. Nicholson, and K. E. Wise. Equivalent-continuum modeling of nano-structured materials. *Compos. Sci. Technol.*, 62(14):1869–1880, 2002.

[164] T. Chang and H. Gao. Size-dependent elastic properties of a single-walled carbon nanotube via a molecular mechanics model. *J. Mech. Phys. Solids*, 51(6):1059–1074, 2003.

[165] K.-T. Lau, M. Chipara, H.-Y. Ling, and D. Hui. On the effective elastic moduli of carbon nanotubes for nanocomposite structures. *Composites Part B*, 35(2):95–101, 2004.

[166] C. Li and T.-W. Chou. Vibrational behaviors of multiwalled-carbon-nanotube-based nanomechanical resonators. *Appl. Phys. Lett.*, 84(1):121–123, 2004.

[167] D. Qian, G. J. Wagner, W. K. Liu, M.-F. Yu, and R. S. Ruoff. Mechanics of carbon nanotubes. *Appl. Mech. Rev.*, 55:495–533, 2002.

[168] S. Zhang, S. L. Mielke, R. Khare, D. Troya, R. S. Ruoff, G. C. Schatz, and T. Belytschko. Mechanics of defects in carbon nanotubes: Atomistic and multiscale simulations. *Phys. Rev. B*, 71:115403–12, 2005.

[169] G. C. Schatz. Using theory and computation to model nanoscale properties. *PNAS*, 104:6885–6892, 2007.

[170] A. Krishnan, E. Dujardin, T. W. Ebbesen, P. N. Yianilos, and M. M. J. Treacy. Young's modulus of single-walled nanotubes. *Phys. Rev. B*, 58(20):14013–14019, 1998.

[171] T. Vodenitcharova and L. C. Zhang. Effective wall thickness of a single-walled carbon nanotube. *Phys. Rev. B*, 68(16):165401–4, 2003.

[172] L. Zhang and C. Wang. Effective wall thickness of single-walled carbon nanotubes for multi-scale analysis: the problem and a possible solution. *IUTAM Symposium on Modelling Nanomaterials and Nanosystems*, pages 53–61, 2009.

[173] M. M. J. Treacy, T. W. Ebbesen, and J. M. Gibson. Exceptionally high young's modulus observed for individual carbon nanotubes. *Nature*, 381:678–680, 1996.

[174] J.-P. Salvetat, G. A. D. Briggs, J.-M. Bonard, R. R. Bacsa, A. J. Kulik, T. Stöckli, N. A. Burnham, and L. Forró. Elastic and shear moduli of single-walled carbon nanotube ropes. *Phys. Rev. Lett.*, 82(5):944–947, 1999.

[175] K. Sohlberg, B. G. Sumpter, R. E. Tuzun, and D. W. Noid. Continuum methods of mechanics as a simplified approach to structural engineering of nanostructures. *Nanotechnology*, 9:30–36, 1998.

[176] C. Q. Ru. Effective bending stiffness of carbon nanotubes. *Phys. Rev. B*, 62(15):9973–9976, 2000.

[177] C. Q. Ru. Degraded axial buckling strain of multiwalled carbon nanotubes due to interlayer slips. *J. Appl. Phys.*, 89(6):3426–3433, 2001.

[178] V. Sazonova, Y. Yaish, H. Ustunel, D. Roundy, T. A. Arias, and P. L. McEuen. A tunable carbon nanotube electromechanical oscillator. *Nature*, 431(7006):284–287, 2004.

[179] A. Pantano, D. M. Parks, and M. C. Boyce. Mechanics of deformation of single- and multi-wall carbon nanotubes. *J. Mech. Phys. Solids*, 52(4):789–821, 2004.

[180] C. Li and T.-W. Chou. A structural mechanics approach for the analysis of carbon nanotubes. *Int. J. Solids Struct.*, 40(10):2487–2499, 2003.

[181] V. N. Popov, V. E. Van Doren, and M. Balkanski. Elastic properties of single-walled carbon nanotubes. *Phys. Rev. B*, 61(4):3078–, 2000.

[182] Z.-c. Tu and Z.-c. Ou-Yang. Single-walled and multiwalled carbon nanotubes viewed as elastic tubes with the effective young's moduli dependent on layer number. *Phys. Rev. B*, 65(23):233407–4, 2002.

[183] C. Li and T.-W. Chou. Elastic moduli of multi-walled carbon nanotubes and the effect of van der waals forces. *Compos. Sci. Technol.*, 63(11):1517–1524, 2003.

[184] J. Muster, M. Burghard, S. Roth, G. S. Duesberg, E. Hernandez, and A. Rubio. Scanning force microscopy characterization of individual carbon nanotubes on electrode arrays. *J. Vac. Sci. Technol. B*, 16(5):2796–2801, 1998.

[185] R. S. Ruoff, D. Qian, and W. K. Liu. Mechanical properties of carbon nanotubes: theoretical predictions and experimental measurements. *C. R. Physique*, 4:993–1008, 2003.

[186] K. Lee, B. Lukic, A. Magrez, J. W. Seo, G. A. D. Briggs, A. J. Kulik, and L. Forró. Diameter-dependent elastic modulus supports the metastable-catalyst growth of carbon nanotubes. *Nano Lett.*, 7(6):1598–1602, 2007.

[187] C. Y. Wang, C. Q. Ru, and A. Mioduchowski. Axially compressed buckling of pressured multiwall carbon nanotubes. *Int. J. Solids Struct.*, 40(15):3893–3911, 2003.

[188] P. Poncharal, Z. L. Wang, D. Ugarte, and W. A. de Heer. Electrostatic deflections and electromechanical resonances of carbon nanotubes. *Science*, 283:1513–1516, 1999.

[189] L. Calabri, N. Pugno, W. Ding, and R. Ruoff. Resonance of curved nanowires. *J. Phys.: Condens. Matter*, 18:2175–2183, 2006.

[190] Z. L. Wang, P. Poncharal, and W. A. de Heer. Nanomeasurements of individual carbon nanotubes by in situ tem. *Pure Appl. Chem.*, 72:209–219, 2000.

[191] R. F. Gibson, E. O. Ayorinde, and Y.-F. Wen. Vibrations of carbon nanotubes and their composites: A review. *Compos. Sci. Technol.*, 67(1):1–28, 2007.

[192] M. R. Falvo, G. J. Clary, R. M. Taylor, V. Chi, F. P. BrooksJr, S. Washburn, and R. Superfine. Bending and buckling of carbon nanotubes under large strain. *Nature*, 389:582, 1997.

[193] A. Pantano, M. C. Boyce, and D. M. Parks. Nonlinear structural mechanics based modeling of carbon nanotube deformation. *Phys. Rev. Lett.*, 91(14):145504–4, 2003.

[194] C. Bower, R. Rosen, L. Jin, J. Han, and O. Zhou. Deformation of carbon nanotubes in nanotube–polymer composites. *Appl. Phys. Lett.*, 74(22):3317–3319, 1999.

[195] J. Z. Liu, Q. Zheng, and Q. Jiang. Effect of bending instabilities on the measurements of mechanical properties of multiwalled carbon nanotubes. *Phys. Rev. B*, 67(7):075414–8, 2003.

[196] J. Z. Liu, Q. Zheng, and Q. Jiang. Effect of a rippling mode on resonances of carbon nanotubes. *Phys. Rev. Lett.*, 86(21):4843–4846, 2001.

[197] M.-F. Yu, O. Lourie, M. J. Dyer, K. Moloni, T. F. Kelly, and R. S. Ruoff. Strength and breaking mechanism of multiwalled carbon nanotubes under tensile load. *Science*, 287:637–640, 2000.

[198] B. G. Demczyk, Y. M. Wang, J. Cumings, M. Hetman, W. Han, A. Zettl, and R. O. Ritchie. Direct mechanical measurement of the tensile strength and elastic modulus of multiwalled carbon nanotubes. *Mater. Sci. Eng., A*, 334(1-2):173–178, 2002.

[199] M. Wang, I. Kaplan-Ashiri, X. Wei, R. Rosentsveig, H. Wagner, R. Tenne, and L. Peng. In situ tem measurements of the mechanical properties and behavior of ws<sub>2</sub> nanotubes. *Nano Research*, 1(1):22–31, 2008.

[200] J. P. Salvetat, J. M. Bonard, N. H. Thomson, A. J. Kulik, L. Forró, W. Benoit, and L. Zuppiroli. Mechanical properties of carbon nanotubes. *Appl. Phys. A*, 69:255–260, 1999.

[201] M. Nishio, S. Sawaya, S. Akita, and Y. Nakayama. Carbon nanotube oscillators toward zeptogram detection. *Appl. Phys. Lett.*, 86(13):133111–3, 2005.

[202] J. Yoon, C. Q. Ru, and A. Mioduchowski. Vibration of an embedded multiwall carbon nanotube. *Compos. Sci. Technol.*, 63(11):1533–1542, 2003.

[203] L. Meirovitch. *Elements of Vibration Analysis.* McGraw-Hill, 1975.

[204] W. Ding, L. Calabri, X. Chen, K. M. Kohlhaas, and R. S. Ruoff. Mechanics of crystalline boron nanowires. *Compos. Sci. Technol.*, 66(9):1112–1124, 2006.

[205] M. Wang, X. Zhang, M. W. Lu, and Y. Liu. Effect of defects on resonance of carbon nanotubes as mass sensors. *Appl. Phys. Lett.*, 88(11):113513–3, 2006.

[206] C. Wang, V. Tan, and Y. Zhang. Timoshenko beam model for vibration analysis of multi-walled carbon nanotubes. *J. Sound Vib.*, 294(4-5):1060–1072, 2006.

[207] S. P. Timoshenko. Lxvi. on the correction for shear of the differential equation for transverse vibrations of prismatic bars. *Philosophical Magazine Series 6*, 41(245):744–746, 1921.

[208] S. P. Timoshenko. X. on the transverse vibrations of bars of uniform cross-section. *Philosophical Magazine Series 6*, 43(253):125–131, 1922.

[209] D.-J. Zeng and Q.-S. Zheng. Resonant frequency-based method for measuring the young's moduli of nanowires. *Phys. Rev. B*, 76(7):075417–7, 2007.

[210] W. Ding, D. A. Dikin, X. Chen, R. D. Piner, R. S. Ruoff, E. Zussman, X. Wang, and X. Li. Mechanics of hydrogenated amorphous carbon deposits from electron-beam-induced deposition of a paraffin precursor. *J. Appl. Phys.*, 98(1):014905–7, 2005.

[211] J. Gaillard, M. J. Skove, R. Ciocan, and A. M. Rao. Electrical detection of oscillations in microcantilevers and nanocantilevers. *Rev. Sci. Instrum.*, 77(7):073907–5, 2006.

[212] T. R. Albrecht, P. Grütter, D. Horne, and D. Rugar. Frequency modulation detection using high-q cantilevers for enhanced force microscope sensitivity. *J. Appl. Phys.*, 69:668–673, 1991.

[213] M. Löffler, U. Weissker, T. Mühl, T. Gemming, and B. Büchner. Robust determination of young's modulus of individual carbon nanotubes by quasi-static interaction with lorentz forcesrobust determination of young's modulus of individual carbon nanotubes by quasi-static interaction with lorentz forcesrobust determination of young's modulus of individual carbon nanotubes by quasi-static interaction with lorentz forces. *Ultramicroscopy*, 111:155–158, 2011.

[214] T. Ono, H. Miyashita, and M. Esashi. Electric-field-enhanced growth of carbon nanotubes for scanning probe microscopy. *Nanotechnology*, 13(1):62–64, 2003.

[215] B. H. Houston, D. M. Photiadis, M. H. Marcus, J. A. Bucaro, X. Liu, and J. F. Vignola. Thermoelastic loss in microscale oscillators. *Appl. Phys. Lett.*, 80(7):1300–1302, 2002.

[216] P. Mohanty, D. A. Harrington, K. L. Ekinci, Y. T. Yang, M. J. Murphy, and M. L. Roukes. Intrinsic dissipation in high-frequency micromechanical resonators. *Phys. Rev. B*, 66(8):085416–15, 2002.

[217] Y. Kogure. Simulation of mechanical damping in nanostructures. *J. Alloys Compd.*, 355:188—-195, 2003.

[218] J. Gaillard, M. Skove, and A. M. Rao. Mechanical properties of chemical vapor deposition-grown multiwalled carbon nanotubes. *Appl. Phys. Lett.*, 86(23):233109–3, 2005.

[219] R. Gao, Z. L. Wang, Z. Bai, W. A. de Heer, L. Dai, and M. Gao. Nanomechanics of individual carbon nanotubes from pyrolytically grown arrays. *Phys. Rev. Lett.*, 85(3):622–625, 2000.

[220] S. T. Purcell, P. Vincent, C. Journet, and V. T. Binh. Tuning of nanotube mechanical resonances by electric field pulling. *Phys. Rev. Lett.*, 89(27):276103–4, 2002.

[221] J. Yang, T. Ono, and M. Esashi. Surface effects and high quality factors in ultrathin single-crystal silicon cantilevers. *Appl. Phys. Lett.*, 77(23):3860–3862, 2000.

[222] Z. L. Wang, R. P. Gao, P. Poncharal, W. A. de Heer, Z. R. Dai, and Z. W. Pan. Mechanical and electrostatic properties of carbon nanotubes and nanowires. *Mater. Sci. Eng., C*, 16(1-2):3–10, 2001.

[223] M. Wang, L.-M. Peng, J. Wang, and Q. Chen. Shaping carbon nanotubes and the effects on their electrical and mechanical properties. *Adv. Funct. Mater.*, 16(11):1462–1468, 2006.

[224] H. B. Seon M. Han and T. Wei. Dynamics of transversely vibrating beams using four engineering theories. *J. Sound Vib.*, 255:935–988, 1999.

[225] E. W. Wong. Nanobeam mechanics: Elasticity, strength, and toughness of nanorods and nanotubes. *Science*, 277:1971–1974, 1997.

[226] Y. Chen, M. Conway, and J. Fitzgerald. Carbon nanotubes formed in graphite after mechanical grinding and thermal annealing. *Appl. Phys. A*, 76(4):633–636, 2004.

[227] X. Chen, S. Zhang, G. J. Wagner, W. Ding, and R. S. Ruoff. Mechanical resonance of quartz microfibers and boundary condition effects. *J. Appl. Phys.*, 95(9):4823–4828, 2004.

[228] J. Wang and P. Qiao. Vibration of beams with arbitrary discontinuities and boundary conditions. *J. Sound Vib.*, 308(1-2):12–27, 2007.

[229] T. Kuzumaki, T. Hayashi, H. Ichinose, K. Miyazawa, K. Ito, and Y. Ishida. In-situ observed deformation of carbon nanotubes. *Philos. Mag. A*, 77(6):1461–1469, 1998.

[230] B. Lukić, J. W. Seo, R. R. Bacsa, S. Delpeux, F. Béguin, G. Bister, A. Fonseca, J. B. Nagy, A. Kis, S. Jeney, A. J. Kulik, and L. Forró. Catalytically grown carbon nanotubes of small diameter have a high young's modulus. *Nano Lett.*, 5(10):2074–2077, 2005.

[231] G. Zhang, D. Mann, L. Zhang, A. Javey, Y. Li, E. Yenilmez, Q. Wang, J. P. McVittie, Y. Nishi, J. Gibbons, and H. Dai. Ultra-high-yield growth of vertical single-walled carbon nanotubes: Hidden roles of hydrogen and oxygen. *PNAS*, 102(45):16141–16145, 2005.

[232] S. Helveg and P. L. Hansen. Atomic-scale studies of metallic nanocluster catalysts by in situ high-resolution transmission electron microscopy. *Catal. Today*, 111(1-2):68–73, 2006.

[233] Y. Xia, M. Zhao, Y. Ma, M. Ying, X. Liu, P. Liu, and L. Mei. Tensile strength of single-walled carbon nanotubes with defects under hydrostatic pressure. *Phys. Rev. B*, 65(15):155415–7, 2002.

[234] C. Bernard, S. Marsaudon, R. Boisgard, and J.-P. Aim´e. Competition of elastic and adhesive properties of carbon nanotubes anchored to atomic force microscopy tips. *Nanotechnology*, 19:035709–10, 2008.

[235] M. Löffler, U. Weissker, T. Mühl, T. Gemming, J. Eckert, and B. Büchner. Current-induced mass transport in filled multiwalled carbon nanotubes. *Adv. Mater.*, 23(4):541—-544, 2010.

[236] K. Lipert, S. Bahr, F. Wolny, P. Atkinson, U. Weissker, T. Muhl, O. G. Schmidt, B. Buchner, and R. Klingeler. An individual iron nanowire-filled carbon nanotube probed by micro-hall magnetometry. *Appl. Phys. Lett.*, 97(21):212503–3, 2010.

[237] M. U. Lutz, U. Weissker, F. Wolny, C. Müller, M. Löffler, T. Mühl, A. Leonhardt, B. Büchner, and R. Klingeler. Magnetic properties of α-fe and fe$_3$c nanowiress. *J. Phys. Conf. Ser.*, 200:072062–4, 2010.

[238] F. Wolny, T. Mühl, U. Weissker, K. Lipert, J. Schumann, A. Leonhardt, and B. Büchner. Iron filled carbon nanotubes as novel monopole-like sensors for quantitative magnetic force microscopy. *Nanotechnology*, 21:435501–5, 2010.

[239] F. Wolny, Y. Obukhov, T. Mühl, U. Weißker, S. Philippi, A. Leonhardt, P. Banerjee, A. Reed, G. Xiang, R. Adur, I. Lee, A. Hauser, F. Yang, D. Pelekhov, B. Büchner, and P. Hammel. Quantitative magnetic force microscopy on permalloy dots using an iron filled carbon nanotube probe. *Ultramicroscopy*, 111(8):1360–1365, 2011.

Versicherung

Die von Uhland Weißker vorgelegte Arbeit *Synthesis and mechanical properties of iron-filled carbon nanotubes* wurde unter der Betreuung von Prof. Dr. B. Büchner am *Leibniz Institut für Festkörper- und Werkstoffforschung Dresden e.V.* angefertigt.

Ich versichere hiermit an Eides statt, dass ich die vorliegende Arbeit ohne die unzulässige Hilfe Dritter und ohne Benutzung anderer als der angegebenen Hilfsmittel geschrieben habe. Die aus fremden Quellen direkt oder indirekt übernommenen Gedanken sind als solche gekennzeichnet. Die Arbeit wurde bisher weder im In- noch im Ausland in gleicher oder ähnlicher Form einer anderen Prüfungsbehörde vorgelegt. Des Weiteren erkenne ich die Promotionsordnung der TU Dresden an.

....

Dresden, den

Acknowledgements

My special gratitude I would like to express to Prof. Bernd Büchner for the opportunity to write my thesis on iron-filled carbon nanotubes at the IFW and to learn a lot about the synthesis and properties of these fascinating structures.

My gratitude also goes to Dr. Thomas Mühl, who supervised my work in a very constructive and encouraging way. He always discussed my questions and to him I owe the insight into the physics of carbon nanotubes and magnetic nanostructures. Furthermore, I want to thank him for the proof-reading of this thesis.

I want to thank Dr. Albrecht Leonhardt for his supervision and useful discussions regarding the chemical aspects of the synthesis of iron-filled CNT.

I like to thank Prof. Cuniberti from the Technical University Dresden for his willingness to act as a referee.

I want to thank Prof. Seifert for his helpful suggestions for the investigation of filled CNT.

At this point I also thank Dr. Christine Täschner for sharing her experience about CVD and related chemical problems and the proof-reading of this thesis. I also thank Dr. Christian Müller for his introduction about the synthesis of iron-filled CNT.

The imaging and experiments with CNT with the SEM would have not been successful without the suggestions and technical help of Dr. Siegfried Menzel to whom I am very grateful. I also like to thank Dr. Thomas Gemming and Dr. Jürgen Thomas for the introduction to the TEM and scientific support and discussion. For the thin film and other substrate preparation I want to thank Dr. Ingolf Mönch, Barbara Eichler and Rainer Kaltofen.

My special thanks goes to all my colleagues, especially Dr. Markus Löffler for his support at the TEM and the interesting discussions about many physical properties of CNT and related topics. I also thank Dr. Franziska Wolny and Matthias Lutz to whom I own a deeper understanding of the magnetic force microscopy and the magnetic properties of iron nanowires. Moreover, I thank Stefan Philippi for his discussions about mechanical and magnetic properties of iron- filled CNT. I thank Dr. Silke Hampel, Dr. Diana Maier, Dr. Franziska Schäffel, Dr. Danny Haberer, Dr. Daniel Grimm, Dr. Mark Rümmeli, Dr. Kamil Lipert, Dr. Niels Scherbaum, Dr. Danny Baumann, Martin Engel and Dr. Vyacheslav Khavrus for all scientific and non-scientific discussed topics. I also would like to thank Dr. Ute Queitsch for her engagement and resolute leadership of the IFW choir and the fun we had on stage.

I also want to thank Monika Siegert, Gesine Kreutzer, Dietmar Meiler, Rico Pohl and Verena Wrengel who helped me with the practical work in the synthesis lab. And I thank all people of the IFW workshop who always support the research competent and reliable.

And last but not least special thanks go to Kerstin Höllerer and Manja Maluck for their help regarding all administrative questions.

Finally, I want to thank my family and friends for all their love and support. I especially dedicate this work to my father and my sister, who had always full confidence into me but unfortunately could not witness this moment.